Density functional theory calculations for understanding gas conversion reactions on single metal atom embedded carbon-based nanocatalysts

Proefschrift ingediend tot het behalen van de graad van doctor in de wetenschappen: chemie aan de Universiteit Antwerpen, te verdedigen door

Parisa Nematollahi

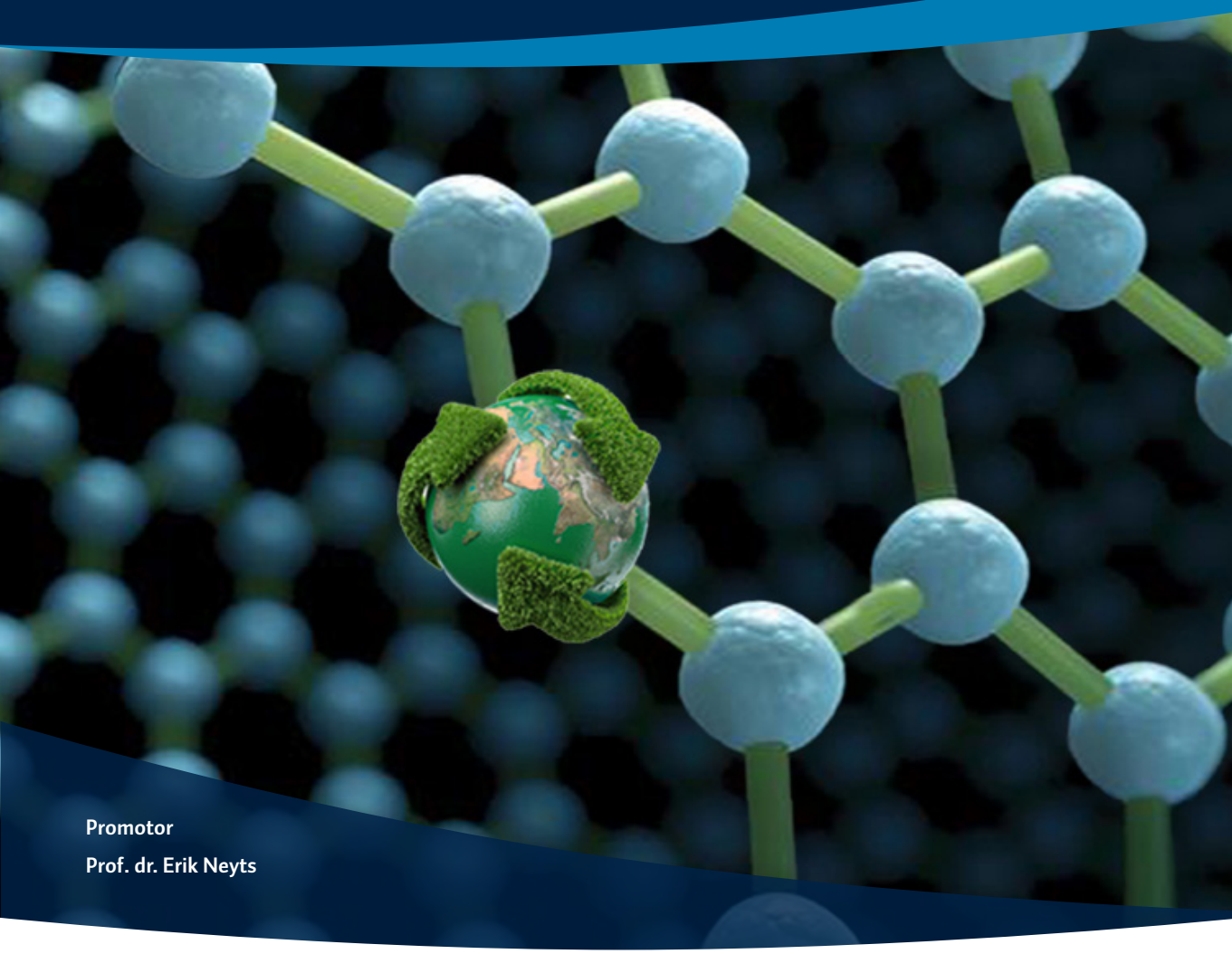

Promotor

Prof. dr. Erik Neyts

Faculteit Wetenschappen
Departement Chemie
Antwerpen 2020

Universiteit Antwerpen

Faculteit Wetenschappen
Departement Chemie

Density functional theory calculations for understanding gas conversion reactions on single metal atom embedded carbon-based nanocatalysts

---

Dichtheidsfunctionaal berekeningen voor het begrijpen van gasconversiereacties op metaal-gemodificeerde koolstofgebaseerde nanokatalysatoren

Proefschrift ingediend tot het behalen van de graad van
Doctor in de Wetenschappen: Chemie
aan de Universiteit Antwerpen, te verdedigen door

Parisa Nematollahi

Promotor
Prof. Dr. Erik Neyts

Antwerpen, 2020

Members of the Jury:

Chair

Prof. dr. Bart Partoens, Universiteit Antwerpen, Belgium

Supervisors

Prof. dr. Erik Neyts, Universiteit Antwerpen, Belgium

Secretary

Prof. dr. Vera Meynen, Universiteit Antwerpen, Belgium

Members

Prof. dr. Annemie Bogaerts, Universiteit Antwerpen, Belgium

Prof. dr. Geoffrey Pourtois, IMEC

Prof. dr. Pascal Brault, Université d'Orléans, France

Contact Information

Parisa Nematollahi

University of Antwerp

Department of Chemistry

CDE, D.B.230

2610 Antwerpen, Belgium

Pn.comchem@gmail.com

Nematollahi.par@gmail.com

To the one who wished to see this moment,
the one I wish was alive to see this moment...,
my father, Prof. Faramarz Nematollahi

To the one whose only heartfelt wish has
always been my success...,
my mother, Fatemeh Ebrahimi

Acknowledgment

*I would like to express my deepest gratitude to my supervisor, **Prof. Erik Neyts**, for his unlimited support during my Ph.D. and his guidance to go a step forward in the world of science, for helping me reach one of my goals, becoming a Ph.D. in Chemistry. Erik, I profoundly appreciate your trust in me from the time I started working in your group, your advice and your indelible smile that always invited me to stay calm, the freedom you gave me, allowed me to overcome the obstacles I have encountered during the past years, Thank you! I would like to express my appreciation to **Prof. Annemie Bogaerts** for her immediate back-up support, consideration, and advice. Also, I would like to thank **Prof. Vera Meynen** for her kindness and willingness to help others find their way, for her technical advice about the industrial workflow and of course, safety issues!*

*I would like to express my especial thanks to our collaborators from Notre Dame University, **Prof. William Schneider**, who gave me the opportunity of working in his group. I learned a lot from my hosts there, especially, **Dr. Hanyu Ma**. Hanyu, I want to thank you for your endless patience and for providing me the situation that I could learn from you, for the discussions during and after my stay, and for the nice collaboration. I would also like to express my appreciation to my friends **Dr. Shuguang Zhang** who always helped me during my research stay at Notre Dame University, and others **Yujia Wang**, **Anshuman Goswami, Neha Mehra, Zhenghang Zhao,** and **Jeonghyun Ko**. I further thank my colleagues in the PLASMANT group, especially my office mates, **Dr. Charlotte Vets**, my best friend, and **Yannick Engelmann**. Charlotte, thank you for helping me out starting work on supercomputers. Charlotte, in tough situations or in our joyful moments I will miss our talks. I wish you all the best of luck in your career and life. Additional thanks to Yannick for our scientific discussions. For all administrative and technical help, I will thank **Luc Van't dack**, a valuable treasure in our group. Without him, we would experience many more problems than we currently do. Luc, we are lucky to have you in our group, you are so patient that I can hardly find a person like you with your permanent smile. You always help people solving their problems in a second, ignoring your priorities for a while. Also, I will thank my friends **Fabiana Quiroz** and **Ingrid swenters,** for their hard work and support in the administrative part, and **Karel Venken**, our ICT man, for his utmost efforts to support everyone in the same way, providing a faster and updated technical working environment. With you people, I experienced perfect moments in the PLASMANT group.*

*Finally, I must express my special gratitude to my husband, **Bahador**, for his unconditional support. I confess that he makes all my difficult moments a piece of cake for me. Bahador, you are my only supporter and lifelong companion that always encouraging me to go to higher levels. Without you, I could not make it. Thank you.*

Summary

Since the industrial revolution, the global air and sea temperature has increased significantly because of the rise in the concentration of greenhouse gases. Therefore, extensive research has been done to either minimize the carbon emission from the exhaust of automobiles, petrochemical, agricultural and chemical industries, or reduce the current high levels of greenhouse gases, by converting them into carbon-neutral fuels or other value-added industrial chemicals.

Conventional metal catalysts for these processes have their own disadvantages. While their reactivity is beneficial, some of them, e. g. noble metals, are typically rare, expensive and require high reaction temperatures (e. g., 350-570°C on a PdO surface [1]). Therefore, lots of efforts have been done to solve these downsides by replacing them with other catalysts. In the past decades, huge effort was devoted to the synthesis and application of nanocatalysts in different fields of science. Amongst different types of nanocatalysts, single individual metal atoms anchored to graphene-based materials is of great interest not only because they are environmentally friendly, but also because they are cost-effective and they surpass conventional catalysts in terms of having a high specific activity with a considerably reduced amount of metals.

In this thesis I tried to clarify the detailed reaction mechanisms of direct conversion of methane to methanol, along with CO and NO oxidation to CO_2 and NO_2 on two types of tailored nanocatalysts, i.e., graphene, and boron carbon nitride (BC_2N) nano-flakes at ambient conditions. Exploring these detailed characteristics and mechanisms is done using computer simulations, more specifically, density functional theory (DFT) calculations. Tailoring the surface is done by adding single atoms (Ni, Co, and Si) or heteroatoms like nitrogen into different materials including defective graphene, and BC_2N nano-flakes. The potential energy surface (PES) is then provided for each catalytic reaction to find the most probable reaction pathway.

In all of the cases, first, we address the question of whether tuning the surface of nanomaterials by introducing defects or single metal atom can increase its catalytic activity. To achieve this, we calculate the adsorption, diffusion, formation, and cohesive energy of the adsorbed-single metal atom into the defective nanocatalyst to find whether the modified surface is stable enough to start the catalytic reaction. Our results show that tailoring the nanomaterial surfaces will increase their stability toward agglomeration and diffusion of doped-single metal atoms on their surfaces.

Second, we address the adsorption behavior of gas species on the modified nanocatalysts. We calculate the (co)-adsorption and dissociation of gas species on each nanocatalyst. According to our studies, the co-adsorption of gas species on the catalyst is preferred over their individual adsorption, but the adsorption energy of each gas species will determine the priority of which species will first cover the active sites of

the surface. Third, we address a set of chemical reactions for the catalytic methane or CO oxidation over the used nanocatalyst. We propose a detailed reaction mechanism, provide the corresponding pathways, and analyse the energetic and thermodynamic properties of each reaction individually. Our studies demonstrate that tuning the structure of the nanocatalysts will significantly increase their catalytic activity toward oxidation or reduction of methane, CO, NO, and NO_2 gases, respectively.

In a comparative investigation explained in Chapter 3, we studied the reaction and activation energies of M and MN_4 embedded graphene (M=Ni and Si) on methane conversion to methanol. Two different spin states, singlet and triplet, are considered for the studied systems. According to the thermodynamic results, the conversion of methane to methanol is energetically favourable at ambient conditions. The calculated barriers in the triplet state are significantly lower than those in the singlet state. We found that Si-G with the preferred triplet spin multiplicity shows better catalytic activity for methane oxidation due to the lower energy barriers and higher configurational stability of the obtained configurations.

Different reaction mechanisms of CO oxidation catalyzed by the Si atom embedded defective BC_2N nanoflake (Si-BC_2NNF) and nanotube (Si-BC_2NNT) is reported in Chapter 4. We also investigate the curvature effect on the CO oxidation reaction on a finite-sized armchair (6, 6) Si-BC_2NNT. Two possible pathways are considered for the CO oxidation: $O_{2(g)} + CO_{(g)} \rightarrow O_{2(ads)} + CO_{(ads)} \rightarrow CO_{2(g)} + O_{(ads)}$ and $O_{(ads)} + CO_{(g)} \rightarrow CO_{2(g)}$ in which the first and second reaction proceeds via the Langmuir-Hinshelwood (LH) and Eley–Rideal (ER) mechanism, respectively. By increasing the tube diameter, the energy barrier increases due to the strong adsorption energy of the O_2 molecule. We conclude that Si-BC_2NNF could catalyze CO oxidation more efficiently than Si-BC_2NNT.

Chapter 5 focusses on the healing of two different N-vacancies in BCN nanoflakes and nanotubes. Various N-vacancies are considered: the vacancy site is surrounded by either three B-atoms (NB) or by two B- and one C-atom (NBC). Then, the formed N-vacancy boron carbon nitride nanoflake (NV-BC_2NNF) and nanotube (NV-BC_2NNT) is "healed" by a NO molecule and used as a support for the removal of two toxic gas molecules, NO and CO. Although both NB and NBC vacancy BC_2NNF showed a better reactivity toward the removal of adsorbed atomic oxygen with NO and CO molecule, NBC vacancy BC_2NNF shows better catalytic activity in O-removal by a second NO molecule thanks to the lower energy barrier compared to the NB vacancy case.

In Chapter 6 we investigated the effects of heteroatom-doping (in this case, nitrogen) into the Co atom embedded single vacancy and di-vacancy graphene flake (Co-SV-G and Co-dV-G) on methane oxidation to methanol using two different oxidants, i.e., N_2O and O_2. Our DFT results suggest a two-step method for methanol formation on CoN_3-G using N_2O as an oxygen-donor. The N_2O molecule adsorbs dissociatively on CoN_3-G, providing atomic oxygen for catalysing the oxidation reaction. Furthermore, we

investigated the adsorption (CH_x, x=0-4) and dehydrogenation (CH_x, x=1-4) process of methane on CoN_3-G. We found that the adsorption energy of CH_4, CH_3, CH_2, CH, and C on CoN_3-G increases by reducing the number of hydrogen atoms. In the dehydrogenation process, all pathways start from the C-H cleavage ($CH_x \longrightarrow CH_{x-1} + H$) Dehydrogenation of methane to methyl is the more preferred reaction thanks to the lower energy barrier. Therefore, the C-C coupling of two-methyl group to ethane is easiest, passing via an energy barrier of 0.45 eV.

Samenvatting

Sinds de industriële revolutie is de wereldwijde lucht- en zeetemperatuur aanzienlijk gestegen door de toename van de concentratie van broeikasgassen. Daarom is er uitgebreid onderzoek gedaan om ofwel de koolstofuitstoot van de uitlaatgassen van de auto-, petrochemische, landbouw- en chemische industrie te minimaliseren, ofwel de huidige hoge niveaus van broeikasgassen te verminderen door ze om te zetten in koolstofneutrale brandstoffen of andere industriële chemicaliën met een toegevoegde waarde.

Conventionele metaalkatalysatoren voor deze processen hebben hun specifieke nadelen. Hoewel hun hoge reactiviteit gunstig is, zijn ze doorgaans zeldzaam en duur en vereisen ze hoge reactietemperaturen (e. g., 350-570°C op een PdO surface [1]). Daarom wordt veel onderzoek verricht naar de mogelijke toepassing van nieuwe katalysatoren. In de afgelopen decennia is veel aandacht besteed aan de synthese en toepassing van nanokatalysatoren. Van de verschillende soorten nanokatalysatoren zijn afzonderlijke metaalatomen die verankerd zijn in materialen op basis van grafiet van groot belang, niet alleen omdat ze milieuvriendelijk zijn, maar ook omdat ze kosteneffectief zijn en conventionele katalysatoren overtreffen in termen van een hoge specifieke activiteit en de benodigde hoeveelheid materiaal.

In dit proefschrift heb ik geprobeerd de gedetailleerde reactiemechanismen van de omzetting van methaan naar methanol, alsook van CO en NO naar CO_2 en NO_2, te onderzoeken, op twee soorten op maat gemaakte nanokatalysatoren, namelijk grafeen, en boorcarbon nitride (BCN). Deze studies zijn gebeurd met behulp van computersimulaties, en meer in het bijzonder met dichtheidsfunctionaliteitstheorie (DFT). Het op maat maken van het oppervlak gebeurt door het toevoegen van een enkel atoom (Ni, Co, of Si) of enkele heteroatomen zoals stikstof in verschillende materialen zoals grafeen en BC_2. Het potentiële energieoppervlak (PES) wordt dan voor elke katalytische reactie berekend om het meest waarschijnlijke reactiepad te vinden.

In alle gevallen wordt eerst de vraag gesteld of het afstemmen van het oppervlak van het nanomateriaal door het introduceren van defecten of een enkel metaalatoom de katalytische activiteit kan verhogen. Om dit te weten te komen berekenen we de adsorptie, diffusie, vorming en cohesieve energie van het geadsorbeerde-metaalatoom systeem in de defecte nanokatalysator om te bepalen of het gewijzigde oppervlak stabiel genoeg is met betrekking tot agglomeratie en diffusie van de doterende metaalatomen.

Ten tweede hebben we het adsorptiegedrag van gassen op de gemodificeerde nanokatalysatoren bestudeerd. Hiervoor berekenen we de (co)-adsorptie en dissociatie van gassen op ieder van de onderzochte nanokatalysatoren. Volgens onze studies heeft de co-adsorptie van gassen op de katalysator de voorkeur boven hun individuele adsorptie, maar de adsorptie-energie van elke gassoort zal de prioriteit bepalen van

welke soort eerst de actieve sites van het oppervlak zal bedekken.

Ten derde bestuderen we een reeks chemische reacties voor de katalytische oxidatie van methaan (CO) enerzijds en CO_2 reductie anderzijds op de gebruikte nanokatalysator. Op basis van deze berekeningen, stellen we een gedetailleerd reactiemechanisme voor, geven de overeenkomstige routes aan en analyseren we de energetische en thermodynamische eigenschappen van elke reactie afzonderlijk. Onze studie toont aan dat het afstemmen van de structuur van de nanokatalysatoren hun katalytische activiteit aanzienlijk zal verhogen in de richting van respectievelijk oxidatie of reductie van methaan, CO of CO_2.

In een vergelijkend onderzoek, uitgelegd in hoofdstuk 3, hebben we de reactie- en activeringsenergieën van M en MN_4 ingebed in grafeen (M=Ni en Si) op de methaanconversie naar methanol bestudeerd. Twee verschillende spintoestanden, singlet en triplet, worden in aanmerking genomen voor de bestudeerde systemen. Volgens de thermodynamische resultaten is de omzetting van methaan in methanol energetisch gunstig onder omgevingscondities. De berekende barrières in de triplettoestand zijn significant lager dan die in de singlettoestand. We vonden dat Si-G met de geprefereerde triplet spin multipliciteit een betere katalytische activiteit voor methaanoxidatie vertoont door de lagere energiebarrières en de hogere structurele stabiliteit van de verkregen configuraties.

In hoofdstuk 4 rapporteren we verschillende reactiemechanismen voor CO oxidatie gekatalyseerd door een Si atoom ingebed in een defecte BC_2N nanoflake (Si-BC_2NNF) en nanobuisje (Si-BC_2NNT). We onderzoeken ook het krommingseffect op de CO-oxidatiereactie op een eindige armchair (6, 6) Si-BC_2NNT. Voor de CO oxidatie worden twee mogelijke routes overwogen: $O_{2(g)} + CO_{(g)} \rightarrow O_{2(ads)} + CO_{(ads)} \rightarrow CO_{2(g)} + O_{(ads)}$ en $O_{(ads)} + CO_{(g)} \rightarrow CO_{2(g)}$ waarbij de eerste en tweede reactie respectievelijk via het Langmuir-Hinshelwood (LH) en Eley-Rideal (ER) mechanisme verloopt. Door het vergroten van de buisdiameter neemt de energiebarrière toe door de sterke adsorptie-energie van O_2. We concluderen dat Si-BC_2NNF de CO-oxidatie efficiënter kan katalyseren dan Si-BC_2NNT.

Hoofdstuk 5 richt zich op het helen van twee verschillende N-vacatures in BCN nanoflakes en nanobuisjes. Verschillende N-vacatures worden beschouwd: wordt de vacatureplaats omgeven door drie B-atomen (NB), ofwel door twee B- en één C-atoom (NBC). Vervolgens wordt de gevormde N-vacature-boorcarbon nitride nanoflake (NV-BC_2NNF) en nanobuisje (NV-BC_2NNT) geheeld door een NO-molecuul en zo gebruikt voor de verwijdering van twee toxische gasmoleculen, NO en CO. Hoewel zowel NB- als NBC-vacature-BC_2NNF een betere reactiviteit vertoonde voor de verwijdering van geadsorbeerd atomair zuurstof met NO en CO, vertoont NBC-vacature-BC_2NNF een betere katalytische activiteit in O-verwijdering door een tweede NO molecuul dankzij de lagere energiebarrière in vergelijking met de NB vacature.

In hoofdstuk 6 hebben we de effecten van heteroatoom dotering (in dit geval stikstof) in de Co ingebedde vacature en di-vacature grafeen (Co-SV-G en Co-dV-G) op oxidatie van methaan tot methanol onderzocht met behulp van twee verschillende oxidanten, namelijk N_2O en O_2. Onze DFT-resultaten suggereren een tweestapsproces voor methanolvorming op CoN_3-G met N_2O als zuurstofdonor. N_2O adsorbeert dissociatief op CoN_3-G en levert atomair zuurstof hetgeen de oxidatiereactie katalyseert. Verder onderzoeken we ook het adsorptieproces (CH_x, x=0-4) en de dehydrogenering (CH_x, x=1-4) van methaan op CoN_3-G. We vonden dat de adsorptie-energie van CH_4, CH_3, CH_2, CH, en C op CoN_3-G toeneemt door het verminderen van het aantal waterstofatomen. In het dehydrogeneringsproces starten alle reactiepaden met C-H splitsing ($CH_x \longrightarrow CH_{x-1} + H$). Dehydrogenering van methaan tot methyl is de geprefereerde reactie dankzij de lage energiebarrière. Daarom zal de C-C-koppeling van de twee-methylgroepen tot ethaan gemakkelijk verlopen, via een energiebarrière van 0,45 eV.

Table of contents

List of Abbreviations

BCN	Boron carbon nitride
DFT	Density functional theory
SV	Single vacancy
dV	di-vacancy
MV	Multiple vacancy
PES	Potential energy surface
SANCs	Single metal atom nanocatalyst
TM	Transition metal
MN-G	Metal coordinated nitrogen doped graphene
N-G	Nitrogen-doped graphene flake
ORR	Oxygen reduction reaction
BCNNT	BCN-nanotube
BC_2NNS	BC_2N nanosheet
BC_2NNF	BC_2N nanoflake
SW	Stone wales
LH	Langmuir-Hinshelwood
ER	Eley-Rideal
QM	Quantum mechanics
HF	Hartree Fock
TF	Thomas-Fermi
HK	Hohenberg-Kohn
LDA	Local density approximation
GGA	Generalized gradient approximation
PBE	Perdew-Burke-Ernzerhof
MO	Molecular orbital
AO	Atomic orbital
STO	Slater type orbital

GTO	Gaussian type orbital
DZ	Double zeta
ECP	Effective core potential
VWN	Vosko, Wilk and Nusair functional
IS	Initial state
TS	Transition state
FS	Final state
MS	Intermediate state
IRC	Intrinsic reaction coordinate
NBO	Natural bond orbital
EDD	Electron density difference
ZPE	Zero point energy
DOS	Density of states
TDOS	Total density of states
PDOS	Partial density of states
BSSE	Basis set superstition error
MEP	Minimum energy pathway
DOMM	Direct oxidation of methane to methanol
OER	Oxygen evolution reaction
TOF	Turnover frequency
TON	Turnover number

Chapter 1

Single metal atom embedded graphene-based nanocatalysts (SANCs)

When one dares to try, rewards are not guaranteed but at least it is an adventure.

Andrew K. Geim

Andrew K. Geim *Konstantin Noroselov*

Carbon is a versatile compound that can be used in several technological processes. This is due to the ability of carbon atoms to bond with each other in different ways, forming linear, planar, and tetrahedral bonding arrangements which lead to the production of materials with a large range of properties. The physicochemical characteristics of the formed materials including e. g. conductivity, surface area, and surface chemistry can be tailored for specific applications. One- and two-dimensional carbon-based nanomaterials show unique mechanical and electronic properties for various types of applications. One of the most effective methods to tailor the electronic properties of these nanomaterials is introducing defects, doping singlet metal atoms, or heteroatoms into their hexagonal carbon network. In this thesis, the properties of three tailored carbon-based nanomaterials, i.e. boron carbon nitride (BCN) flakes, graphene flake, and carbon nanotube (CNT) were chosen and their catalytic activity toward gas conversion was studied in detail. This chapter consists of two parts: first, a brief overview is presented the geometric structure, properties, and the modification methods of the mentioned nanomaterials. The second part relates to the application of the modified nanostructures in gas conversion. The computational methods used in this thesis will be discussed in chapter 2 and the results are discussed in chapters 3 to 6. I will finish this thesis with the general conclusion and a summary of future research topics.

1.1 SANCs for gas conversion

With depleting resources and environmental concerns regarding climate change, energy conversion technologies are regarded as promising pathways for developing clean energy devices [2]. Therefore, either minimizing the carbon emission from the exhaust of automobiles, petrochemical, agricultural and chemical industries, or reducing the current high levels of greenhouse gases by converting them into carbon-neutral fuels (i.e., syngas, formic acid or methanol) or other value-added industrial chemicals is of great importance.

Recently, due to limitations in downsizing metal morphology, the concept of single-metal atom nanocatalysts (SANCs) [3] emerged and has been used in several applications since it increases the exposed atom efficiency along with its exceptional physical and chemical properties [4, 5]. Compared with bulk metals, SANCs have shown better activity and selectivity thanks to the strong interaction between the single metal atom and the graphene-based support which shifts the partially occupied *d* states of the metal atom to the Fermi level [6]. However, the high free energy of single metal atoms leads to metal aggregation, and therefore, the preparation of SANCs remains challenging [7].

The catalytic activity of the SANCs can be tuned by tailoring the local coordination environments around the single metal atom. For instance, various investigations indicated that single metal atom doped graphene exhibits outstanding catalytic activity in various catalytic reactions [8-11]. This can be related to the exceptional properties of graphene such

as its huge surface-to-volume ratio, large thermal and mechanical stability as well as low-cost and high flexibility. These properties make it an ideal carbonic support for single metal atoms or clusters doping in heterogeneous catalysis [12, 13].

In the following section, I provide a short history of the basic structure and properties of the used nanocatalysts and the applied tuning methods.

1.1.1 Monolayer graphene sheet

1.1.1.1 Structure and properties

The high reactivity of metal catalysts is of great importance, although some of them are rare, expensive and require high reaction temperatures. For instance, it is reported by Chen et al. [14] that at 600°C and atmospheric pressure, the bimetallic Cu–Fe catalysts exhibit high and stable catalytic activity up to 120 h. Consequently, there is a continuous search for finding a costless and environmentally friendly catalyst with high activity toward gas conversion. For instance, the calculated turnover frequency (TOF) for CO_2 reduction to CO on Ni-doped N-embedded graphene is of 2700 to 4600 h^{-1}, reported by Su et al[15]. Graphene, with its quite unique electronic, optical, thermal, and mechanical properties [16] is considered for a wide range of applications such as memory devices [17-19], energy storage [20], solar cells [21, 22], and sensors [23, 24]. Owing to the outstanding geometry, electronic, thermal, and mechanical properties of graphene, a lot of research is carried out on this material in both experimental and theoretical investigations.

Graphene is a single-layer sheet of sp^2 carbon in a hexagonal arrangement. This sp^2 hybridization leads to a trigonal planar structure with the formation of a σ bond between carbon atoms with a C-C bond length of 1.42 Å. This C-C bond is between the single C-C bond in ethane (1.54 Å) and the double C=C bond in ethylene (1.34 Å) and is responsible for the stability of the lattice structure of graphene [25]. Graphene can be regarded as the building block of all carbon allotropes with the exception of the diamond. It can be wrapped up into 0D fullerenes, rolled into 1D carbon nanotubes (CNTs), or stacked into 3D graphite [26] (see Figure 1-1).

An important characteristic of single-layer graphene is its impressive mechanical properties, which are attributed to the high stability of the sp^2 bonds that form the hexagonal lattice [25]. Overlap of the remaining p_z orbital on each carbon atom with neighboring carbon atoms produces a filled band of π orbitals, called the valence band and an empty band of π^* orbitals known as the conduction band. The valence and conduction bands touch at the Brillouin zone corners thus making graphene a zero-bandgap semiconductor with spectacular electronic properties that are not present in bulk graphite [27]. Another important reason for the interest in graphene is its electron transport property, as well as the most unusual thermal conductivity that has ever been found in any material, which originates from the unique electronic and structural features of graphene.

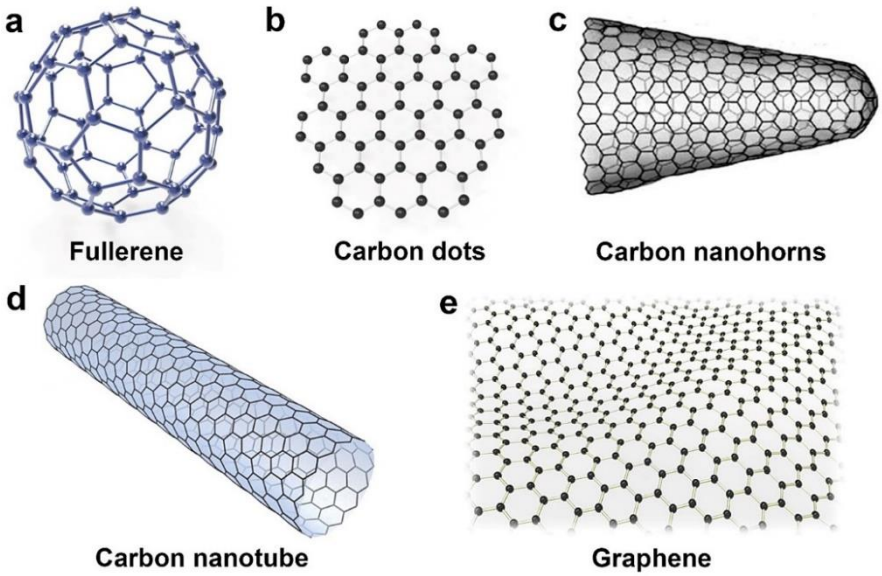

Figure 1-1. Schematic models of various carbon nanomaterials [28]

1.1.1.2 Surface modifications

Tailoring the graphene sheet by introducing defects [29, 30], or heteroatoms (e.g., N, B, P) [31] into the structure of graphene is often found to speed up catalytic reactions on the surface [32, 33] and modulate the electronic properties of the catalyst [34-37].

1.1.1.2.1 Defects in graphene

Although a pristine graphene sheet has unique electronic and mechanical properties, the formation of various structural defects during growth, separation, or fabrication processes affects the performance of graphene-based devices. However, the existence of such structural defects results in considerable benefits in some applications [38].

Defects in graphene classify into two main categories: (i) point defects including the stone-wales defect (Figure 1-2a), single vacancy (SV) (Figure 1-2b) and multiple vacancy (MV) defects (Figure 1-2c); (ii) one-dimensional defects such as dislocation-like defects, i.e., line defects, or defects at the edges [39].

According to theoretical and experimental investigations, topological point defects in the basal plane of graphene can lead to the opening of the bandgap [40, 41]. These defects locally increase the reactivity of the structure and allow adsorption of other atoms on the graphene surface [39].

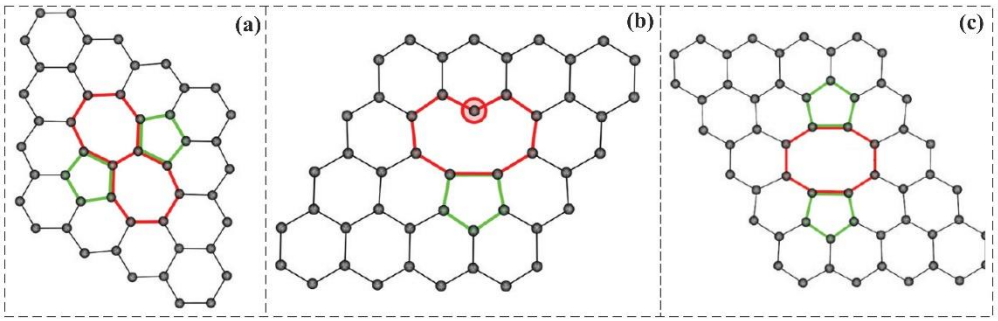

Figure 1-2. Schematic view of (a) stone-wales defect SW(55-77), (b) single vacancy defect, and (c) multi-vacancy (MV) defect in graphene sheet [39].

1.1.1.2.2 Chemical doping of graphene

One method to tune the bandgap of graphene is doping, i.e., the addition of electron donors (n-type) or acceptors (p-type) into the graphene lattice[42, 43]. This is a well-known procedure in semiconductor technology. The motivation of doping is to control the type and concentration of the charge carriers.

Substitutional N-doping. Substitutional doping with e.g. B, P, S, and N [44-46] to the graphene vacancies can enhance its catalytic reactivity [47-49]. N-doped graphene (N-graphene) has been one of the most broadly studied doping models. Since the electronegativity of nitrogen (χ = 3.04) is larger than that of C (χ = 2.55), the introduction of N into graphene sheets modifies its local electronic structure. It is well established (shown in Figure 1-3) that the incorporation of N atoms into the graphene matrix can lead to three main "types" of N, including graphitic N with direct substitution structure, pyridinic N and pyrrolic N structures [50]. According to the recent studies, the pyridinic N-C bonding can efficiently change the band structure and catalytic activity of N-doped graphene materials [51, 52].

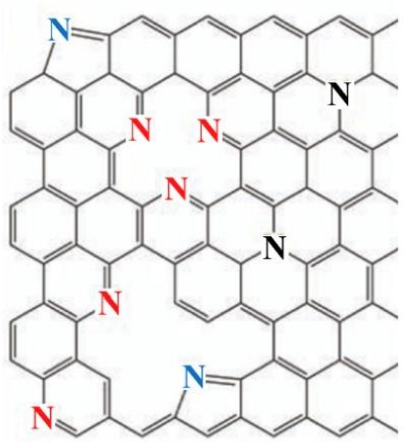

Figure 1-3. Various configurations of N atoms doped graphene [53]

Transition metal and metalloid substitutional doping. Transition metals (TM) retain partially filled d- or f-orbitals, and have been extensively explored in various fields of material chemistry due to their excellent electrical conductivity, and catalytic activity [54]. In the last decades, doping graphene with TM atoms such as Fe [55, 56], Ni [57, 58], noble metals like Pt [59, 60], Pd [61, 62], and metalloids like Si [63-66] has attracted a lot of attention. In Si-doping, the Si-3p orbitals strongly couple with the 2p orbitals of the connected C atoms above and below the Fermi level (E_F), suggesting a very strong interaction between the Si atom and C-vacancy. The binding energies of the TM-doped vacancy complexes are in the range of 2–8 eV. In addition, the high energy barrier for TM migration on the graphene surface indicates the stable trapping of substitutional impurities that might allow for engineering of the position of metal atoms with atomic precision [67]. The improvement of electric conductivity and flexibility of tuning the electric structure results from the strong covalent bonds between the dopant atom and the carbon atoms of the graphene sheet [68, 69]. Experimental studies also confirmed the existence of strong binding between defect sites and metallic impurities which makes the metal embedded graphene stable enough to be used in catalytic reactions [70, 71].

Metal-doped heteroatom embedded graphene. It has been reported that metal coordinated N-doped graphenes (MN-G) can enhance the chemical reactivity of graphene due to their lower cost, higher durability, and catalytic activity. Recently, it was found that pyridinic-N can better anchor TM atoms in comparison to other types of N-G, due to its higher configurational and energetic stability and catalytic activity [72, 73]. These nanomaterials can be easily synthesized [74-76] and used in molecular sensors [77, 78], bio-sensing applications [79], metal-free oxygen reduction catalysis (ORR) [80, 81], CO oxidation reactions [82-85], and in lithium batteries [86-88] (see Figure 1-4). Different factors have a considerable effect on the activity and stability of metal-doped nitrogen embedded graphene (MN_x-G) like the synthesis procedures and conditions, the type of carbonic support, the type of transition metal, and N-containing precursors [89, 90]. MN_4-G is found to be thermodynamically more stable [91, 92] than MN_3-G or MN_2-G [93, 94]. Recently, Yeager et al. [95] found that metal cations coordinated by pyridinic nitrogen-doped at the defect sites of graphitic carbon are the active sites for ORR in alkaline and acid electrolytes. In a theoretical investigation [83], the catalytic activity of SiN_4 co-doped graphene is investigated as a metal-free catalyst for the oxidation of CO.

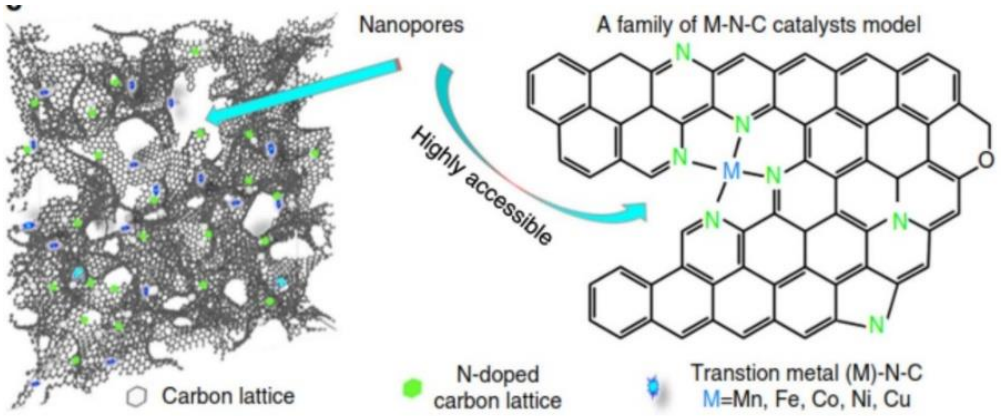

Figure 1-4. (left) Visualization, porosity, and illustration of the M–N–C catalyst. (Right) Materials model and a schematic local structure [96]

1.1.2 Carbon nanotubes

1.1.2.1 Structures and properties

Carbon nanotubes (CNTs) are known as one of the best examples of novel nanostructures derived by bottom-up chemical synthesis approaches. The electronic properties of "ideal" carbon nanotubes depend on both the width of the graphene sheet (diameter of the tube) and the way it is folded (chirality of the tube). This is specified by introducing the so-called chiral indices (n, m)[97, 98] (see Figure 1-5). CNTs are attractive substrates in heterogeneous catalytic processes owing to their ability to be easily tailored to meet specific needs.

The electronic properties of a nanotube range between being metallic and semiconductor and follow a general rule: if (n - m) is a multiple of 3, then the tube exhibits metallic behavior, while if (n - m) is *not* a multiple of 3, then the tube exhibits a semiconducting behavior. CNTs can be single-walled CNTs (SWCNTs), double-walled CNTs (DWCNTs) or multi-walled CNTs (MWCNTs) [99]. Due to their highly porous and hollow structure, large specific surface area, low mass density, and strong interaction between CNTs and pollutant molecules, they attract scientific interest in various areas, such as biosensors, molecular devices, removal of hazardous pollutants from gas streams and nanoelectronic devices [100-103].

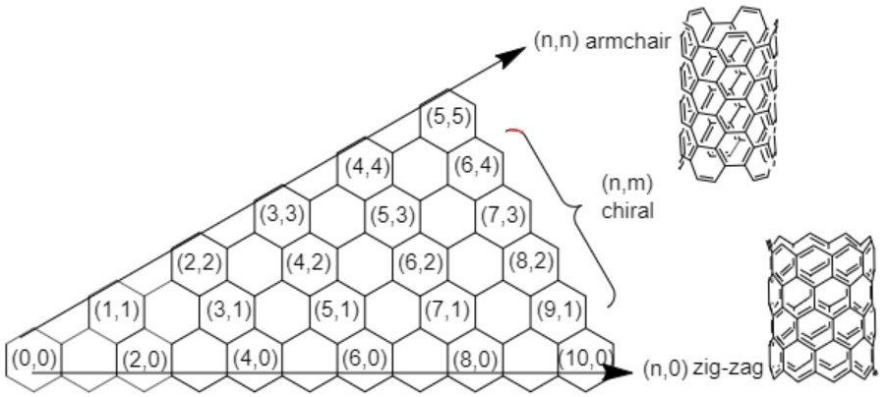

Figure 1-5. Schematic view of possible wrapping of the two-dimensional graphene sheet into tubular forms.

1.1.2.2 Surface modifications

1.1.2.2.1 Defects in CNTs

The introduction of defects in the carbon network of CNTs is an interesting way to modify their intrinsic properties and to create new potential nanodevices. Defects such as pentagons, heptagons, or vacancies are found to tune the electronic properties of these nanosystems. One of the common ways which lead to the production of interesting, highly defective nanostructures and also to the coalescence of nanotubes within a rope is irradiation processes. According to the experimental microscopic observations[104], during controlled electron irradiation of isolated single-wall nanotubes, a drastic shrinkage of the nanosized cylinders occurs. In the uniform irradiation conditions, atom removal from the irradiated nanotubes occurs slowly as long as the irradiation persists. Atom loss creates vacancies that could cluster into larger holes in the structure. The removal of carbon atoms from the hexagonal network of the CNT creates a number of carbon atoms with unsaturated valence orbitals. Therefore, the system will become energetically unstable due to the dangling bonds associated with these defects. On the other hand, the excess energy arising from the unsaturated valence orbitals promotes reconstructions local to the vacancy, forming energetically more stable configurations. For instance, each of the single- and di-vacancy defects has two possible reconstructed configurations, symmetric or asymmetric with respect to the axial direction of the CNT, as shown in Figure 1-6. These reconstructions lead to dimensional changes local to the defects.

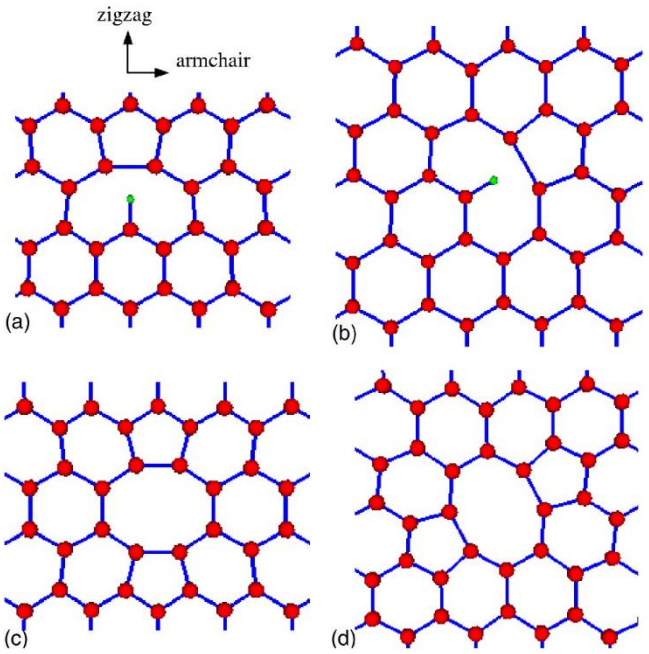

Figure 1-6. Single- and di-vacancy defects; (a) single-atom vacancy, symmetric, (b) single-atom vacancy, asymmetric. (c) di-atom vacancy, symmetric. (d) di-atom vacancy, asymmetric. In the single-vacancy cases, a hydrogen atom is included to saturate the system[105]

1.1.2.2.2 Chemical doping of CNTs

To improve the performance of doped carbon catalysts, some researchers have investigated the addition of metal or heteroatom species to enhance the performance of the tube surface. Chemical doping of CNTs is an attractive option for a wide range of potential applications. The new generation of nanoelectronics based on nanotubes will require *n*- and *p*-doping for diode and transistor construction. Chemical doping of CNTs introduces additional electronic states around the Fermi level, making the doped nanotubes attractive candidates for enhanced electron emission.

Substitutional N doping. In 2009, Y. Tang et al. [106] synthesized N-doped carbon nanotubes (N-CNTs) via the chemical vapor deposition (CVD) method. It is found that they are less stable than their pure carbon counterparts, breaking easily under the electron beam in the transmission electron microscope (TEM) [107] and the nitrogenized nanotubes start to gasify at a lower temperature (370°C) compared with the pure carbon nanotubes, which burn at 450°C [108]. The doping of CNTs with N atoms offers a practical way of tailoring both the physical and chemical properties of the CNTs by creating new states that modify their electronic structure [109]. N-doping creates defects on the surface of the CNTs (see Figure 1-7) and breaks its chemical inertness while preserving its electrical conductivity [110]. Since N atoms induce a positive charge on the adjacent carbon atoms, they facilitate oxygen dissociation, make the tube surface chemically active toward ORR[111] and facilitate the chemical functionalization[112, 113]. In addition, the

catalytic stability of the tube increases with the increase of N contents in N-CNTs [114].

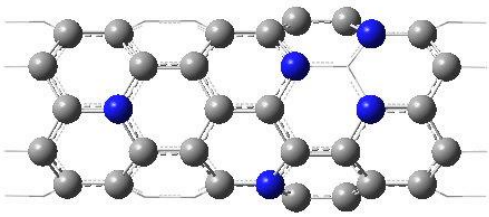

Figure 1-7. Various configurations of graphitic and pyridinic N-doped CNT

Transition metal substitutional doping. Besides N-dopant-induced defect sites in CNTs, TM-N_x-CNT has also been regarded as highly promising substitutes [115, 116] making CNTs excellent catalyst for catalytic reactions [117]. This can be related to the high surface nucleation of defective N-CNTs sites, which allow the active metal atom to anchor strongly on the support surface. For instance, compared to regular CNTs, it was shown that highly dispersed Pt nanoparticles with a smaller size (2–3 nm) and higher electrochemical Pt surface area as well as higher fuel cell performance were obtained for Pt doped-nitrogen embedded CNT [118]. Gao et al. [119] demonstrated the catalytic activity of FeN_4-CNT as a cathode catalyst for hydrogen fuel cells. Furthermore, it is shown that MnN_4-CNT has a good catalytic activity for CO oxidation at ambient condition [84].

1.1.3 Boron carbon nitride (BCN) nanostructures

Hybridization of the semi-metallic carbon and boron nitride (BN), with a wide bandgap $\geq$ 5.8 eV [120], creates another series of novel materials called boron carbon nitride (BCN or $B_xC_yN_z$) with a honeycomb structure and physical properties intermediate between those of the precursors [121]. Modification of the physical properties of these hybrids is possible by controlling their atomic compositions. It is expected that the BCN nanostructures exhibit semiconducting properties [122] similar to their bulk counterparts, which will be of great importance in nano-electronics [123, 124]. The main member of the BCN nanostructures is BCN-nanotube (BCNNT). Up to now, the BCNNTs have been synthesized in a large composition range through various methods such as electrical arc discharge [125, 126], laser ablation [127] and more recently by laser vaporization [128].

1.1.3.1 Structures and properties

Amongst the various ternary BCN systems, $C_x(BN)_y$ nanosheets and nanotubes such as BC_xN ($1<x<5$) [129, 130] have been synthesized experimentally [131, 132]. Already more than 30 years ago, the possible atomic configurations of a hexagonal BC_2N sheet (BC_2NNS) were examined using first-principles total energy calculations [121]. The geometry of the h-BC_2N is shown in Figure 1-8 and it is found to be the most stable structure. In 1996,

Watanabe et al. [133] studied the electronic properties of layered BC_2N materials by scanning tunneling spectroscopy. They reported that the layered BC_2N materials show semiconducting behavior with an energy gap of 2eV. However, according to experiments, a large variety of shapes and sizes of the C and BN patterns are existed from which the h-BC_2N compounds are used more dominantly [134]. The conductivity of the sheets having a lower carbon concentration (C < BN), is less than the sheet having a higher carbon concentration (C > BN) [135]. This can be explained theoretically; because C-B and C-N bonds are less stable than C-C and B-N bonds, it is energetically more favourable to form structures that minimize the number of the less stable bonds with respect to the more stable C-C and B-N bonds.

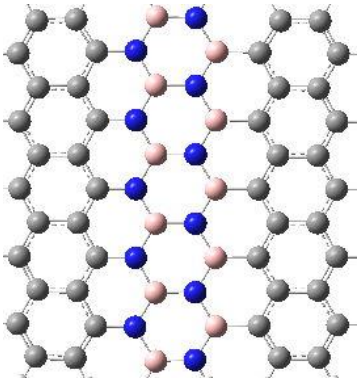

Figure 1-8. Atomic structure of the fully optimized BC_2N sheet. The pink, gray, and blue colors denote B, C, and N atoms, respectively.

The diameter of a (n, m) BC_2N nanotube (BC_2NNT) is almost twice than that of (n, m) graphite nanotube. BC_2NNT was first synthesized in 1995 by Weng-Sieh et al. [136], using an arc discharge method. Different studies have been carried out to investigate the optical and elastic properties of single-walled BC_2NNTs [137, 138]. In a theoretical study, Pan et al. [139] found that the strain energy of BC_2NNTs shows a direct relationship with the diameter of the tube, but is independent of the chirality of the tube. Wang et al. [140] investigated the structural stability and electronic properties of ultra-thin BC_2NNTs. They indicated that the stability of BC_2NNTs toward reactants is sensitive to both the number of B-N bonds and the relative ordering of the CNT and BNNT segments. All (2,2) BC_2NNTs were found to be semiconducting with tunable energy gap, whereas (4,0) BC_2NNTs can be either conducting or semiconducting.

1.1.3.2 Surface modifications

1.1.3.2.1 Defects in BCN nanostructures

Similar to graphene, in BCN nanostructures different defects can be considered. In this thesis, three point defects have been considered in BC_2N structures, i.e., C-, N-, and B- vacancies. In a theoretical investigation [141], it is mentioned that introducing the Stone Wales (SW) defect in three types of zigzag (4,0) and two types of armchair (4,4)

BC_2NNTs is energetically more preferable which leads to the enhancement of their properties.

1.1.3.2.2 Chemical doping of BCN nanostructures

Transition metal substitutional doping. It is known that by metal doping or decorating the BC_2N structure, the electrical, optical, and magnetic properties will change [142-145]. For instance, Si-doped BC_2NNT not only adsorbs formaldehyde (H_2CO) molecules strongly but also it can "sense" the presence of this molecule due to the increase in the electric conductivity of the tube [146]. Rupp et al. [147] studied the equilibrium geometry, energetic stability, and electronic properties of substitutional Si impurities in the zigzag (5,0) and armchair (3,3) BC_2NNTs. They indicated that the Si impurities in BC_2NNTs have lower formation energy compared to Si-doped CNT and BNNT. They also reported that the electronic properties of BC_2NNTs depend on the position of the Si-doping. Moreover, Wang et al. [148] reported that Li and Ca decorated BC_2NNS has a high capacity for hydrogen storage without a metal clustering problem. Qiu et al. [149] studied the effects of Ca decoration of BC_2NNS on hydrogen storage. They found that unlike the weak bond between Ca atoms and pristine BC_2N, doping boron or carbon atoms on BC_2N sheet can strengthen the Ca atoms on the BC_2N and consequently work as high-capacity hydrogen storage materials with the practically usable capacities.

1.2 Introduction to heterogeneous catalysis

Catalysis has a very wide scope of applications, some already quite old and some only very recent. There are several catalytic reactions that were practiced in the 16^{th} and 17^{th} centuries, such as the production of alcoholic beverages by fermentation, the manufacture of vinegar by ethanol oxidation, production of soap by fat hydrolysis, and the production of diethyl ether by dehydration of ethanol. Yet, we generally take catalysis as a field to have started some 283 years ago. In a short paper, J. J. Berzelius summarized his ideas on catalysis as a new force; he wrote: "*It is, then, proved that several simple or compound bodies, soluble and insoluble, have the property of exercising on other bodies an action very different from chemical affinity. By means of this action they produce, in these bodies, decompositions of their elements and different recombination of these same elements to which they remain indifferent*." [150]. He submitted his report in 1835 and it was published in 1836 [151]. He indicated that these findings could be rationally explained by the concept of catalysis. Berzelius called "catalysis" the decomposition of bodies by the catalytic force. This was the first recognition of catalysis as a wide-ranging natural phenomenon. Another definition which is still usable today is due to Ostwald (1895) [152]: "*a catalyst is a material that accelerates a chemical reaction without affecting the position of the equilibrium and thermodynamics of the reaction.*" Ostwald proposed the concept of catalysis as a universal dynamic phenomenon that was to be explained in terms of the laws of physical chemistry. His fundamental work was recognized with the Nobel Prize for chemistry in 1909.

1.2.1 What is catalysis?

Typical for catalysis is that only small quantities of the catalyst are needed (at least in relative terms)[151, 153]. According to Figure 1-9, a catalyst increases the rate of a chemical reaction by forming bonds with the adsorbents (A and B) and letting them to react with each other to make products (C). Then the products can desorb from the catalyst and it is recovered in its original form at the end of the reaction cycle.

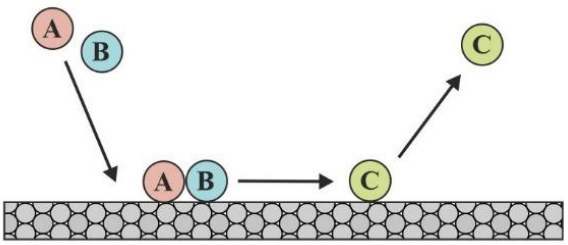

Figure 1-9. A catalytic reaction consists of different steps in which the reactants (A and B) adsorb and react with the catalyst, form the products (C) which finally detaches from the catalyst. Then, the liberated catalyst is ready to enter a new catalytic cycle

The lifetime of a catalyst, is measured by the total number of catalytic cycles that it can undergo until it needs to be replaced. Turnover number (TON) is a common value which is used in this context and denotes the total amount of product (in moles) that can be produced by a given amount (in moles) of catalyst. A highly durable catalyst enables the economic production of a larger quantity of the desired compound, before the replacement of the catalyst for starting a new cycle [151]. It is expected that single atom graphene-based nanocatalysts contribute to lower process energy consumption, with longer lifetime and enhanced possibilities to isolate and reuse the active nanomaterials. These catalysts are promising examples to illustrate the efforts toward "green chemistry".

1.3 Reactions at the catalyst surface

When a particle impinging on the surface does not immediately reflect back into the gas phase, it remains adsorbed on the surface through physisorption or chemisorption. Chemisorption involves the formation of a chemical bond between the adsorbate and the surface and thus corresponds to the creation of a true chemical bond between adsorbate and substrate. Hence, it is highly directional (in contrast to physisorption). As a result, chemisorbing species stick at specific sites and they exhibit a binding interaction that depends strongly on their exact position and orientation with respect to the surface.

Adsorption of adsorbates in their weakest form (~ 0.1 eV), with no true chemical bond between surface and adsorbate, is known as physisorption. In this mode, the bonding is rather due to the (induced) dipole moment of a (non) polar adsorbate

interacting with its own image charges in the polarizable solid, which means that the attraction is caused by a combination of Keesom (in the case of dipole interactions), and/or Debye and London dispersion interactions (in the case of induced dipole interactions) [154].

1.3.1 Surface reaction mechanisms

An additional aspect comes into play with regard to the reaction between two different species A and B to a product molecule. Two limiting cases for this process are discussed: Langmuir-Hinshelwood (LH) and Eley-Rideal (ER) mechanisms (see Figure 1-10). In the LH mechanism, suggested by Irving Langmuir in 1921 [155] and further developed by Cyril Hinshelwood [156], two molecules adsorb on neighboring sites and the adsorbed molecules undergo a bimolecular reaction. The better explanation of this mechanism is shown in Figure 1-10. In steps 1, 2, and 3, the gas species (A and B) adsorbs on the surface and interact with each other on the surface. Steps 4 and 4' represent the desorption of the product (C) but in step 4 the product forms on the surface, with a weak (strong) chemical bond, and desorbs from the surface while in step 4' the product desorbs upon its formation.

In the ER mechanism, proposed by D. D. Eley [157] and E. K. Rideal [158], only one of the molecules adsorbs , particle A, and the other one, particle B, reacts with it directly from the gas phase, without adsorbing [159]. In step 1 shown in Figure 1-9, number 1 represents the adsorption of the first gas species on the surface. In the 2, the second gas species (B) directly reacts with the pre-adsorbed species (A). Finally, the formed product (C) can be produced on the surface and then desorbs from it via step 3 while in step 3' it directly desorbs from the surface upon its formation.

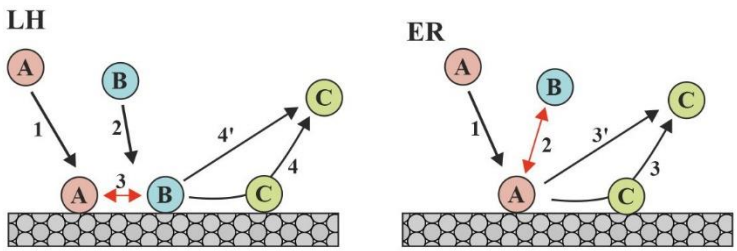

Figure 1-10. Detailed schematic representation of the existed steps in the LH and ER mechanisms

1.4 Statistical thermodynamics

1.4.1 Canonical ensemble

Equilibrium thermodynamics describes energy changes associated with the (macroscopic) state-to-state evolution of systems in equilibrium. If a system with fixed volume is kept in thermal equilibrium in contact with a heat bath at temperature T, the

system can exchange energy, and therefore, the states of the system differ in total energy. This is called the canonical ensemble. The probability density distribution of the microstates in phase space must be consistent with the constant temperature T. In experiments, it is the temperature of the environment. The energy dependence of the probability density conforms to the Boltzmann distribution.

1.4.2 The Boltzmann distribution

According to the statistical mechanics, the probability that a system in thermal equilibrium occupies a state with the energy of E_i, is proportional to exp ($-E_i/k_BT$), where k_B is the Boltzmann constant. k_BT has a dimension of energy. The exponential mentioned above is called the Boltzmann weight.

For a classical canonical ensemble with energy levels E_i the probability distribution for the level populations (P_i) is given by the Boltzmann (Gibbs) distribution [160]. Using a system of N particles that exist in *r* different states, with (i = 0, ..., r-1), the number of particles is N_i. The particles are completely independent of each other and do not interact. The probability distribution for the level populations is given by the Boltzmann distribution

$$P_i = \frac{N_i}{N} = \frac{e^{-E_i/k_BT}}{\sum_{i=0}^{\infty} e^{-E_i/k_BT}} \tag{1-1}$$

The canonical partition function applies to a canonical ensemble, in which the system is allowed to exchange heat with the environment at a fixed temperature, volume, and the number of particles. The sum over states required for normalization is known as the canonical partition function. a The partition function is a thermodynamical state function

$$Z\ (N, V, T) = \sum_{i=0}^{\infty} e^{-E_i/k_BT} \tag{1-2}$$

In Eq. 1-2, the dependence on N and V arises because these parameters influence the energy levels. The symbol Z which is used for the partition function relates to the German term “Zustandssumme”, which is a clear description of this quantity.

1.4.3 Partition functions of atoms and molecules

The partition function describes the statistical properties of a system in thermodynamic equilibrium. Almost all of the thermodynamic variables of the system, such as the total energy, free energy, entropy, and pressure, can be expressed in terms of the partition function or its derivatives. The partition function is a pure dimensionless number and is, in fact, an important mathematical tool that makes a connection between statistical mechanics and thermodynamics [161, 162]. To briefly explain

the relationships between the partition function and the thermodynamic parameters of the system, we first calculate the thermodynamic value of the total energy which is the expected value for the energy, i. e., the sum of the microstate energies weighted by their probabilities:

$$\langle E\rangle = \sum_i E_i P_i = \frac{1}{Z}\sum_i E_i e^{-\beta E_i} = -\frac{1}{Z}\frac{\partial}{\partial\beta}Z(\beta, E_1, E_2, \dots) = -\frac{\partial lnZ}{\partial\beta} \tag{1-3}$$

Or equivalently,

$$\langle E\rangle = k_B T^2 \frac{\partial lnZ}{\partial T} \tag{1-4}$$

Where Z is the partition function and $\beta = 1/k_B T$. According to the calculated thermodynamic energy from Eq. (1-3), the variance in the energy, energy fluctuation, is

$$\langle(\Delta E)^2\rangle \equiv \langle(E - \langle E\rangle)^2\rangle = \frac{\partial^2 lnZ}{\partial\beta^2} \tag{1-5}$$

1.4.4 Gibbs free energy, enthalpy, and pressure

The previously defined ensembles correspond to equilibrium states at constant volume. To make predictions for processes at constant pressure or to compute enthalpies (H = U + pV) and Gibbs free energies (G = *F* + pV) we need to compute the pressure from the partition function. The simplest way is to note that

$$p = -(\partial F/\partial V)_{T,n} \tag{1-6}$$

where *F* is the Helmholtz free energy,

$$F = U - TS = U - T\left(U/T + k_B lnZ\right) = -k_B T lnZ \tag{1-7}$$

and z is the system partition function. Thus,

$$p = k_B T\left(\partial lnZ/\partial V\right)_T \tag{1-8}$$

In Eq. (1-8) the lower index *n* indicating constant molar amount is omitted. This is permissible for the canonical ensemble, where the number of particles is constant by definition. From Eq. (1-8) it follows that

$$pV = k_B T\left(\partial lnZ/\partial lnV\right)_T \tag{1-9}$$

and

$$H = U + pV = k_B T\left[\left(\partial lnZ/\partial lnT\right)_V + \left(\partial lnZ/\partial lnV\right)_T\right] \tag{1-10}$$

And finally, with Eq. (1-8) the Gibbs free energy can be calculated as

$$G = F + pV = -k_B T \left[lnZ - \left({}^{\partial lnZ}/_{\partial lnV} \right)_T \right] \quad (1\text{-}11)$$

1.5 Applications of SANCs

1.5.1 Methane oxidation

Since the industrial revolution, the global air and sea temperature has increased because of the rise in the concentration of greenhouse gases [163]. Amongst the most important greenhouse gases are methane (CH_4), CO, NO_2, and NO. Therefore, extensive research is performed to investigate the conversion of these air pollutants into more useful chemicals, i.e., higher hydrocarbons or liquid fuels [164]. Of particular interest is the production of methanol. Traditional conversion of methane to methanol (CH_3OH) is performed by a two-step process in the industry under harsh reaction conditions such as high temperature (500-800 K) and pressure (30-200 bar) [165, 166]. Chang et al. [167] reported that nano-crystallites of nickel oxide (e.g., NiO and $NiAl_2O_4$) form with high dispersion on the surface. Also, at an optimized reaction temperature of 773 K, a maximum yield (≈ 58%) and selectivity of CH_4 (≈ 90%) is obtained. Despite the fact that it is not a cost-effective procedure, there is currently no industrially relevant alternative. Although noble metals like Ir, Pt, Rh, and Ru [168-172] are highly active toward methane conversion and are resistant to carbon formation, they are economically less attractive materials for large-scale industrial use due to their scarcity, high cost, and toxicity [173]. In an experimental investigation, Kowalczyk et al. [174] studied the effect of the support on the catalytic properties of Ru nanoparticles in CO_2 hydrogenation. They found that turnover frequencies (TOFs) of Ru-based catalysts were dependent on the Ru dispersion and the type of supports. For high metal dispersion, the following order of TOFs ($\times 10^3 s^{-1}$) for the reaction was obtained: Ru/Al_2O_3 (16.5) > $Ru/MgAl_2O_4$ (8.8) > Ru/MgO (7.9) > Ru/C (2.5). However, although metal catalysts are typically toxic and economically less attractive for large-scale industrial use [173], the conversion of methane to syngas or other useful chemicals in industries takes place in the presence of less expensive and more readily available transition metals, especially Ni, Fe or Co [175-178]. Amongst different types of catalysts, single individual metal atoms anchored to various graphene-based support materials including metal oxides [179, 180], metal-organic frameworks [181], and carbonaceous materials such as graphene-based materials [182-184] are explored as novel materials not only because they minimize material usage to meet the goal of cost-effective catalysis, but also because they surpass conventional catalysts in terms of having a high specific activity with a reduced amount of noble metals. Recently, Quinn and Choudhury [185] investigated large macrocyclic molecules, copper porphyrins, as active metal centers for the catalyzed methane oxidation to methanol.

Besides O_2, which is the major oxidizing agent of methane, N_2O is a powerful oxidizer donating oxygen for direct methane oxidation. N_2O is known as an agricultural toxic gas which may also originate from other activities like wastewater treatments, or the combustion of fossil fuels and biomass. During the last century, it is found that the global warming potential of CH_4 and N_2O are 28 and 265 times higher than that of CO_2. Therefore, investigating the conversion of these gas molecules is of great interest. Direct synthesis of CH_3OH from CH_4 at room temperature and pressure is a promising way for the industry. To date, many studies explored the direct synthesis of methanol but none of them has proven to be cost-effective. Thus, it remains a considerable challenge in the sector of methane utilization.

1.5.2 CO oxidation

Carbon monoxide (CO) is one of the major common toxic gases in the atmosphere, originating from automobile exhausts, industrial processes, and incomplete burning of fuels or petroleum products [82, 186]. This odorless, colorless, and poisonous gas is the origin of fatal diseases like anoxemia and causes various problems for both the environment and the human body [187, 188].

The oxidation of CO to other non or less harmful gases by means of noble metals, such as Au [189, 190], Pt [191], Pd [192], Rh [193] or bimetallic alloy surfaces like Pd-Ni[194], Pd-Zn [195] or Rh/Ceria [196] has been proposed as a viable abatement method. Several studies already investigated CO oxidation on metal supported catalysts [197, 198]. Qiao et al. [199] proposed that although Pt-based catalysts are important for many commercial chemical processes, their efficiency is rather low because only the surface active-site atoms are used. Therefore, they investigated the synthesis of a single-atom catalyst that consists of only single isolated Pt atoms anchored to the surfaces of iron oxide nanocrystallites. This single-atom catalyst showed excellent energetic stability and high activity for CO oxidation.

Metal nanoclusters [200, 201], or single metal atoms embedded nanostructures [202, 203] are extensively explored to reduce the reaction barrier for CO oxidation. This can be related to their quantum size effects, which make them promising materials for sensors, transistors, and energy devices [204-206]. Various studies were recently performed on the oxidation of CO over carbon-based materials [207]. For example, Tang et al. [208] studied CO oxidation over Pt-doped X- graphene sheets (X= pristine or single vacancy defective). They found that in contrast to a Pt atom on pristine graphene, a vacancy defect in graphene strongly stabilizes a single Pt atom and makes it more positively charged, which enhances the activity toward CO oxidation and reduces the CO poisoning of the platinum catalysts. Li et al. [209] studied the oxidation of CO on graphene supported Pd catalyst. In order to know the intrinsic activities of the Pd-doped graphene (Pd-G) catalyst, they normalized the turnover frequencies as the number of CO molecules reacting per active site per second. The TOF values of Pd-G at 100°C showed

that the TOF increases with the increasing op Pd loading. Also, it showed a steady state for the catalytic activity of Pd-G. For instance, a 10% Pd-G catalyst revealed good stability at a reaction temperature of 100°C and 120°C. The conversion of CO at 100°C almost kept steady around 10% throughout the 24h reaction. The conversion reaches 15% at the initial moment and after the reaction lasted for 1 h, it drops to 10% more or less and after 14 h it became lower than 9.5% gently. Moreover, they mentioned that the CO conversion at 120°C could retain 100% during the testing time. The same stability results can also be found in other catalysts like Au/TiO_2 [210].

According to the literatures, the defective and metal-doped BC_2N nanostructures have been widely used for H-storage. For instance, Gao and his co-workers reported that the hydrogen storage properties of BC_2N graphene-like sheet with the largest hydrogen adsorption energy of 0.11 eV, which is slightly dependent on the adsorption site [211]. In another study [212], BC_2N with the surface area of 1990 m^2 g^{-1} showed CO_2 adsorption of 128 wt.% at 195 K and 1 atm. At room temperature and 5 MPa, it showed 64 wt.%. CH_4 adsorption-desorption isotherms for BC_2N indicated that the uptake of CH4 is 15 wt.% at room temperature and 5 MPa and increases by 2 wt.% at 273 K. Adsorption of CH_4 increases with the increase in the surface area of BC_2N.

Chapter 2

Computational methods

A careful analysis of the process of observation in atomic physics has shown that the subatomic particles have no meaning as isolated entities, but can only be understood as interconnections between the preparation of an experiment and the subsequent measurement.

Erwin Schrödinger

Currently, density functional theory (DFT) is very popular. The key quantity is the electron density, which greatly simplifies the problem to be solved compared to wave function-based methods since it has only three dimensions, regardless of the number of electrons being considered. The basis for DFT is proved by Hohenberg and Kohn [213]. They showed that the ground state electronic energy is completely defined by the electron density. This means that there is a one-to-one correspondence between the electron density of a system and the energy. In this theory, the properties of the system are defined as functional (a prescription for producing a function from a function) of the electron density. It is one of the most used ab initio methods available, mainly because of its wide range of possible applications as well as its relative computational simplicity [214]. DFT calculations enable us to study the catalytic reactions that occur on the surface of the heterogeneous catalysts, e.g. in the fields of gas conversion and energy storage.

2.1 Quantum mechanics

Within the framework of classical mechanics, the correct description of atomic and molecular interactions is in principle not possible. It is assumed in classical mechanics that the energies involved have a continuous character instead of having a discrete character. A better description of atoms and molecules is obtained within the framework of quantum mechanics (QM). QM often gives us a more fundamental understanding of chemical processes, since it is not always possible to extract detailed information from experiments. For instance, it is possible to calculate molecular geometries, energy differences between different conformers, differences adsorption energies at different adsorption sites, find transition states in chemical reactions, and their corresponding activation barriers, as well as thermodynamic properties.

In quantum chemistry one typically tries to solve the time-independent Schrödinger equation [215]. An exact solution of the Schrödinger equation exists only for a limited number of cases such as the hydrogen atom. Thus, various approximations are introduced in order to find an estimate of the exact solution which leads to the development of various methods like Hartree-Fock (HF), DFT, and post-Hartree-Fock methods. For HF and post-Hartree-Fock methods, the wave function, which contains all possible information about a system, is used as a basic source of information, while for DFT the electron density is used.

2.1.1 Schrödinger equation

One of the problems of QM is that it quickly becomes too complex to solve for systems with more than one electron. In principle, we seek to solve the time-independent Schrödinger equation, which is the basis of all computational chemistry methods:

$$\hat{H}\Psi(\vec{r}_1, \vec{r}_2, \dots, \vec{r}_N) = E\Psi(\vec{r}_1, \vec{r}_2, \dots, \vec{r}_N) \quad (2\text{-}1)$$

where $\hat{H}$ is the Hamiltonian operator, $\Psi(\vec{r}_1, \vec{r}_2, \dots, \vec{r}_N)$ is the wave function of the many-

body system, and E is the total energy. In mathematics, this equation is called an eigen equation. Then, Ψ and E is called an eigenfunction and an eigenvalue, respectively. Ψ is a function of the electron and nuclear positions, describing an electron as a wave. It can describe the probability of the presence of electrons in a given volume element (i.e., the electron density). To obtain a relevant solution of the Schrödinger equation, Ψ should be continuous, single-valued, and normalizable with respect to the exchange of electrons. In a system consisting of n electrons and N nuclei, the Hamiltonian (in atomic units) is written as:

$$\hat{\mathrm{H}} = \hat{T}_e + \hat{T}_n + \hat{V}_{ne} + \hat{V}_{ee} + \hat{V}_{nn} \tag{2-2}$$

In Eq.(2-2), the kinetic energy operator for electrons (i), $\hat{T}_e$, and nuclei (A), $\hat{T}_n$, are written as:

$$\hat{T}_e = -\sum_{i=1}^{n} \frac{\nabla_i^2}{2} \tag{2-3}$$

$$\hat{T}_n = -\sum_{A=1}^{N} \frac{\nabla_A^2}{2m_A} \tag{2-4}$$

the Coulomb attraction between the nuclei and electrons, $\hat{V}_{ne}$, the repulsion between the electrons, $\hat{V}_{ee}$, and the repulsion between the nuclei, $\hat{V}_{nn}$, are also written as:

$$\hat{V}_{ne} = -\sum_{i=1}^{n}\sum_{A=1}^{N} \frac{Z_A}{r_{iA}} \tag{2-5}$$

$$\hat{V}_{ee} = \sum_{i=1}^{n}\sum_{j>i}^{n} \frac{1}{r_{ij}} \tag{2-6}$$

$$\hat{V}_{nn} = \sum_{A=1}^{N}\sum_{B>A}^{N} \frac{Z_A Z_B}{R_{AB}} \tag{2-7}$$

where r_{ij}, r_{iA}, and R_{AB} represents the distance between electron i and j, electron i and nuclei A, and nuclei A and B. M_A and Z_A refer to the mass and atomic number, respectively. Finally, ∇_i^2 and ∇_A^2 in Eqs.(2-3) and (2-4) represents the Laplacian operators for the i^{th} electron and A^{th} nucleus:

$$\nabla_i^2 = \frac{\partial^2}{\partial x_i^2} + \frac{\partial^2}{\partial y_i^2} + \frac{\partial^2}{\partial z_i^2} \tag{2-8}$$

However, since this Hamiltonian cannot be solved, some approximations must be made.

2.1.2 Born-Oppenheimer approximation

Taking advantage of the difference in mass of nuclei and electrons, the Schrödinger equation can be simplified. According to the Born-Oppenheimer approximation [216], the motion of atomic nuclei and electrons in a molecule can be treated separately. Since electrons are lighter than nuclei, they move much faster while nuclei can be considered stationary. Then, electrons will move in a fixed external potential due to the nuclei. In return, the nuclei will experience an average interaction with the electrons that surround them. Of course, if the nuclei are fixed in space and do not move, their kinetic energy is zero while the potential energy is merely a constant for the nucleus-nucleus repulsion. This approximation allows the decoupling of the degrees of freedom of the electrons and nuclei. Hence, we divide the many-body Hamiltonian into two parts, the nuclear, $\hat{H}_{nuc}$, and electronic, $\hat{H}_{el}$, part as follows:

$$\hat{H}_{nuc} = \hat{T}_n + \hat{V}_{nn} \tag{2-9}$$

$$\hat{H}_{el} = \hat{T}_e + \hat{V}_{ne} + \hat{V}_{ee} \tag{2-10}$$

In addition, the wave function splits into an electronic and nuclear part:

$$\Psi = \Psi_{el}(r^n, R^N).\Psi_{nuc}(R^N) \tag{2-11}$$

where the R^N is included as parameters and not as variables. However, solving the electronic Schrödinger equation is still too complex for the systems consisting of more than one electron.

2.1.3 Density Functional Theory

In a many-body system with n electrons, the electronic wave function depends on 4n variables: 3n spatial and n spin coordinates. Since the wave function has more information than needed, looking for other methods that involve fewer variables than the wave function has to calculate the energy and other properties is of great interest.

2.1.3.1 Thomas-Fermi model

Shortly after the introduction of the Schrödinger equation, Llewellyn Thomas and Enrico Fermi [217, 218] introduced the so-called Thomas-Fermi (TF) model, in which they reduce the number of variables, and use the electron density $\rho(\vec{r})$ to express the total energy, $E_{TF}[\rho(\vec{r})]$.

$$E_{TF}[\rho(\vec{r})] = C_F \int \rho(\vec{r})^{5/3} d^3\vec{r} + \int \rho(\vec{r}) - \left(- \sum_{A=1}^{M} \frac{Z_A}{|\vec{r} - \vec{r}'|} \right) d^3\vec{r} d\vec{r}' + \frac{1}{2} \iint \frac{\rho(\vec{r})\rho(\vec{r}')}{|\vec{r} - \vec{r}'|} d^3\vec{r} d\vec{r}' \tag{2-12}$$

In the TF model, three terms are represented; (I) the kinetic energy of the electrons as the non-interacting electrons in a homogeneous electron gas, (II) the electrostatic attraction between electrons and the nuclei using an external potential, $\upsilon_{ext}(\vec{r})$, as a static Coulomb potential from the nuclei, and (III) the repulsion between the electrons as a classical Coulomb repulsion. The TF neglects the exchange and correlation in its description, and since the total energy of a molecule is higher than the sum of atomic energies, it cannot describe the molecular bonding. This method is generally considered as a simple predecessor of modern DFT.

2.1.3.2 Modern density functional theory

The entire field of density functional theory rests on two fundamental mathematical theorems proved by Kohn and Hohenberg and the derivation of a set of equations by Kohn and Sham in the mid-1960s. Hohenberg and Kohn (1964) [219] proved two theorems critical to establishing DFT as a legitimate quantum chemical methodology and is of great importance for DFT.

2.1.3.2.1 The Hohenberg-Kohn existence theorem

The Hohenberg-Kohn theorem states that the ground state energy from Schrödinger's equation is a unique functional of the electron density [220]. These also determine the Hamiltonian of the system and ultimately, determine the energy of the system (E). In this theorem, the electron density $\rho(\vec{r})$ is used as the basic variable. It states that the external potential is defined uniquely, except for an additive constant, by the ground state electron density $\rho_0(\vec{r})$ which is only a function of three variables. The ground state electronic energy, E_0, can be written as a functional of $\rho_0(\vec{r})$:

$$E_0 = E[\rho_0(\vec{r})] = V_{ext}[\rho_0(\vec{r})] + T[\rho_0(\vec{r})] + V_{ee}[\rho_0(\vec{r})] \tag{2-13}$$

In this equation, the nuclear-electron attraction, $V_{ext}[\rho_0(\vec{r})]$ is known. Also, in the electron-electron interactions term, $V_{ee}[\rho_0(\vec{r})]$, only the classical part $\frac{1}{2}\int \frac{\rho(\vec{r})\rho(\vec{r}')}{|\vec{r}-\vec{r}'|} d\vec{r}d\vec{r}'$ is known. The remaining term which refers to the electronic kinetic energy, $T[\rho_0(\vec{r})]$, is unknown.

$$E[\rho_0(\vec{r})] = V_{ext}[\rho_0(\vec{r})] + F_{HK}[\rho_0(\vec{r})] = \int \rho_0(\vec{r}) V_{ext}(\vec{r}) d\vec{r} + F_{HK}[\rho_0(\vec{r})] \tag{2-14}$$

The Hohenberg-Kohn functional, F_{HK}, in only dependent on the ground state density and is independent of the external potential. Since the F_{HK} is unknown, this description cannot provide a practical way to calculate the ground state energy from the ground state electron density.

2.1.3.2.2 The Hohenberg-Kohn variation theorem

The second Hohenberg-Kohn theorem and the approach developed by Kohn and Sham make the DFT a practical tool. According to the second Hohenberg-Kohn theorem, any trial electron density function will give an energy higher than (or equal to, if it were exactly the true electron density function) the true ground state energy [221]. This theory has the consequence that in principle, the exact energy of the ground state and the ground state density can be calculated by changing the density because no density with the correct number of electrons *n* can give the total energy lower (minimum energy) than the true total energy. The second HK theorem just declares the existence of such a functional: it doesn't give any further information about its form or the way of finding it. Also, it doesn't mention anything about finding the $\rho_0(\vec{r})$ independently without first finding the wave function.

2.1.3.3 Kohn-Sham Self-Consistent Field methodology

Kohn and Sham [222] provided an explicit method to find the $\rho_0(\vec{r})$, and E_0 from $\rho_0(\vec{r})$. The above discussion emphasizes that the density determines the external potential, which determines the Hamiltonian, which in turn determines the wave function. With the Hamiltonian and wave function in hand, the energy can be computed. They introduced a fictitious reference system in which the electrons do not interact with each other and move in an effective potential, $v_{eff}(\vec{r})$, due to all the other electrons. We know from the Hohenberg-Kohn existence theorem that the external potential can be determined by $\rho_0(\vec{r})$. Once we find the density of the reference the external potential is uniquely determined. The electrons in the reference system do not interact with each other. Therefore, the Hamiltonian of the non-interacting system will be

$$\widehat{H}_s = \sum_{i=1}^{n}\left[-\frac{1}{2}\nabla_i^2 + v_{eff}(\vec{r}_i)\right] \tag{2-15}$$

The Kohn-Sham functional for a set of doubly occupied electronic states, ψ_i^{KS}, can be written as:

$$E[\rho_0(\vec{r})] = -\sum_{i=1}^{n}\left[\frac{1}{2}\langle\psi_i^{KS}|\nabla_i^2|\psi_i^{KS}\rangle\right] + \int V_{ion}(\vec{r})\rho(\vec{r})d\vec{r} + \frac{1}{2}\int\frac{\rho(\vec{r})\rho(\vec{r}')}{|\vec{r}-\vec{r}'|}d\vec{r}d\vec{r}' + E_{xc}[\rho(\vec{r})] + E_{ion}[R_n] \tag{2-16}$$

where $E_{xc}[\rho(\vec{r})]$is the exchange-correlation energy, $E_{ion}[R_n]$ is the Coulomb energy for the interactions between the nuclei for a certain complex in position R_n, and the electronic density by $\rho(\vec{r}) = \sum_{i=1}^{n}|\psi_i^{KS}|^2$. The Kohn-Sham functional will be minimized by the wave functions, and the wave functions satisfy the single particle

Kohn-Sham eigenvalue equations as follows:

$$\left\{-\frac{1}{2}\nabla^2 + V_{ion}(\vec{r}) + \int \frac{\rho(\vec{r})}{|\vec{r} - \vec{r'}|} + V_{xc}(\vec{r})\right\}\psi_i^{KS} = \varepsilon_i \psi_i^{KS} \quad (2\text{-}17)$$

where $\psi_i^{KS}$and ε_i are the wave function and energy of the ith Kohn-Sham orbital (the eigenvalue), respectively. The exchange-correlation potential is defined as:

$$V_{xc}(\vec{r}) = \frac{\delta E_{xc}[\rho(\vec{r})]}{\delta \rho(\vec{r})} \quad (2\text{-}18)$$

Since the wave-functions deatermine the electronic density, the Kohn-Sham eqution needs to be solved self-consistently. The summation of the single particle Kohn-Sham eigenvalues does not result in the total electronic energy, as this would overcount the electron-electron interactions. The exchange-correlation energy is a relatively small contribution to the total energy and it is difficult to evaluate accurately. To calculate the properties of a molecular system accurately, it is key to formulate a good approximation of the E_{xc}. There are a variety of reasonable approximations, some of which are explained in the following sections.

2.1.3.3.1 Exchange-correlation functional

Up to know, we would like to find the ground-state energy of the Schrödinger equation, but this is extremely difficult because this is a many-body problem. The results of Kohn, Hohenberg, and Sham showed that the ground state we seek can be found by minimizing the energy of an energy functional, and thus this can be achieved by finding a self-consistent solution to a set of single-particle equations. To solve the Kohn-Sham equation, we must specify the exchange-correlation function, E_{xc}. E_{xc} contains two different components: exchange and correlation. Exchange is the energy contribution resulting from the electrons being indistinguishable particles. Correlation is the energy contribution resulting from the interaction between the electrons, i.e., the extent to which the behaviour of one electron is influenced by the presence of all others. Both effects find their origin in quantum mechanics.

There is one case where this functional can be derived exactly: the uniform electron gas. In this situation, the electron density is constant at all points in space, $\rho(\vec{r})$= constant. The uniform electron gas provides a practical way to actually use the Kohn-Sham equations. To do this, the exchange-correlation potential is set at each position to be the known exchange-correlation potential from the uniform electron gas at the electron density observed at that position. This approximation uses only the local density to define the approximate exchange-correlation functional, therefore, it is called the local density approximation (LDA).

2.1.3.3.2 Local Density Approximation (LDA)

The LDA is the simplest way to approximate the exchange-correlation energy via the Kohn-Sham equations [223]. LDA uses two assumptions: (i) the local exchange-correlation energy per particle only depends on the local density (ii) the local exchange-correlation energy is equal to the exchange-correlation energy per electron of a homogeneous electron gas. Then, the total exchange-correlation energy E_{xc} is obtained by the energy per electron of a uniform electron gas with the same density at that point in space $\vec{r}$.

$$E_{xc}^{LDA} = \int \varepsilon_{xc}^{hom}(\rho(\vec{r}))\rho(\vec{r})d\vec{r} \tag{2-19}$$

where $\varepsilon_{xc}^{hom}(\rho(\vec{r}))$ represents the exchange-correlation energy per electron of the homogeneous electron gas. The quantity $\varepsilon_{xc}^{hom}(\rho(\vec{r}))$ can be calculated for every density. It is also common to split the exchange and correlation models in LDA. In this case, the exchange part represents the exchange energy of an electron in a uniform electron gas while the correlation part is determined using quantum Monte-Carlo simulations of the homogeneous electron gas, proposed by Ceperly and Alder [224].

While relatively simple and widespread application, the method has its limitations, e.g. the LDA method overestimates of binding energies and the total energies of atoms are more accurately described in the HF approximation.

2.1.3.3.3 Generalized Gradient Approximation (GGA)

In LDA the knowledge of the density is in point $\vec{r}$. In reality, the density varies in space. One way to improve the correlation functional is to make it depend not only on the local value of the density but on the extent to which the density is locally changing, i. e., the gradient of the density. This approximation is called the Generalized Gradient Approximation (GGA). In the GGA, the exchange-correlation term is a functional of both the density and its gradient. Generally, the GGA approximation improves total energies, energy barriers, atomization energies and energy differences compared to the LDA method. The E_{xc} energy is now written as

$$E_{xc}^{GGA} = \int f(\rho(\vec{r}), \nabla\rho(\vec{r}))d\vec{r} \tag{2-20}$$

which is still local but also takes into account a local variation through the gradient of the density at the same position.

Often one splits the exchange-correlation energy into an exchange and correlation part, which are modeled separately. In GGA functional, when the exchange and correlation are modeled separately, one can combine any exchange functional with any correlation functional. Since there are many ways to include information from the

gradient of the electron density in a GGA functional, there is a large number of distinct GGA functional. Some of these functional groups are derived solely from theoretical considerations such as the Perdew-Wang functional (PW91)[225] or the Perdew-Burke-Ernzerhof (PBE) [226] exchange-correlation functional. Combining B88 [227] or B98 [228] exchange functional with LYP [229] or PW91 correlation energy functional, leading to the popular BLYP or BPW91 GGAs, fall into the category of semi-empirical exchange-correlation functional groups. Another type of approximation to the exchange-correlation energy has shown great promise. These approximations [230, 231], called meta-GGAs (MGGAs) [232], require additional semi-local information such as Laplacians (the second derivative of the electron density) of the spin densities or kinetic energy densities as input and applied to atoms, molecules, surfaces, and solids. In contrast to GGA's, Meta-GGAs are explicitly orbital dependent. However, because the Kohn-Sham orbitals are functional of the density, these meta-GGAs are still density functional.

2.1.3.4 Hybrid functional

The LDA and GGA functional are quite effective in calculating the lattice parameters, atomic positions and binding energies, as well as describing the electronic structure of metals. However, a general problem when using these functional groups is that they tend to underestimate the bandgap of semiconductor materials [233]. In the early 1990s, Axel Becke demonstrated that more accurate energies could be obtained if some part of the HF exchange was included within the functional [234]. Thus, hybrid-GGA and hybrid-meta-GGA are the combinations of GGA and meta-GGA with the HF exchange term, respectively. This crucial insight is what made DFT methods accurate and consistent and enabled them to be applied to the full range of chemical problems resulting in the widespread use they see today. We call the result of such a combination a hybrid functional:

$$E_{XC}[\rho(\vec{r})] = c_{HF}\mathrm{X} + c_{DFT}E_{XC}^{pure}[\rho(\vec{r})] \tag{2-21}$$

where the constants (c) specify how much of each term is included. A famous example of these types of functional groups is the B3LYP exchange-correlation functional [235]:

$$E_x^{B3LYP} = (1 - a_0 - a_x)E_x^{LSDA} + a_0E_x^{HF} + a_xE_x^{b88} + (1 - a_c)E_c^{VWN} + a_cE_c^{LYP} \tag{2-22}$$

For which a_0=0.20, a_x=0.72, and a_c=0.81. Therefore, one mixes in 20% of the exact HF-exchange energy.

2.1.3.5 Van der Waals interactions

Van der Waals potential U^{vdW} is usually taken in the form of Lennard-Jones. It is considered to be a reasonable description of the interaction for closed-shell atoms like noble gas elements, and they are considered between all non-bonded pairs of atoms [236].

The Lennard Jones potential is a combination of attractive van der Waals forces due to dipole-dipole interactions and empirical repulsive forces due to Pauli repulsion. This Pauli repulsion is particularly strong for atoms with closed valence shells for which it dominates the interaction close to the surface. Thus there will be a balance between the short-range Pauli repulsion and the long-range van der Waals attraction leading to a physisorption minimum. In order to determine the physisorption equilibrium position for rare gases adsorbed on jellium, Zaremba and Kohn divided the total interaction into two parts: a short-range term described by Hartree–Fock theory and the longe-range van der Waals interaction. Density functional theory using the LDA or GGA for the exchange-correlation functional does not properly describe the long-range van der Waals interaction since they have a non-local character. This can be due to the fact that in the LDA and the GGA the exchange-correlation hole is still localized. Therefore, the effective electron potential outside of a metal falls off exponentially. Therefore, neither image forces nor the van der Waals interaction is appropriately reproduced. Still, there have been several attempts to properly include the van der Waals interaction in density functional theory. One of the various schemes that have been proposed to add dispersion to correct DFT approximation is based directly on the electron density and is called VdW-DF wherein the exchange-correlation energy takes the form of

$$E_{xc}[\rho(\vec{r})] = E_x^{GGA}[\rho(\vec{r})] + E_c^{LDA}[\rho(\vec{r})] + E_c^{nL}[\rho(\vec{r})] \tag{2-23}$$

the x part is taken from a GGA functional and the non-local part is added to the LDA correlation. But, still, there are DFT problems of understanding the bandgap.

2.2 Basis sets

Ab initio methods try to solve the Schrödinger equation without (or with as few as possible) fitting parameters to experimental data. Instead, they make use of experimental data in a more subtle fashion. Often, experimental data guide the selection of the computational model rather than directly entering into the computational procedure. One of the approximations is the introduction of a basis set. The motivation for developing new basis sets for use in trial wave functions follows from the need to achieve higher levels of accuracy with roughly the same size basis. A basis set is a mathematical description of the orbitals within a system, which in turn combine to approximate the total electronic wave function, used to perform the theoretical calculation. We call a basis set a “complete basis set” when an infinite number of functions are used. This is, of course, impossible in actual calculations. In an infinite coordinate system an unknown molecular orbital (MO) can be thought of as a function which will be measured by the complete basis set. In contrast, when using a finite basis set, only the components of the MO along the coordinate axes corresponding to the selected basis functions can be represented. A smaller basis set generally results in poorer representations. Larger basis sets approximate the orbitals more accurately by

imposing fewer restrictions on the locations of the electrons in space. Additionally, the type of the used basis functions also affects the accuracy.

2.2.1 Slater and Gaussian type orbitals

Two types of basis functions, also called atomic orbitals (AO), are commonly used in electronic structure calculations: Slater type orbitals (STO) and Gaussian type orbitals (GTO). STOs are mostly used for accurate calculations in atomic and diatomic systems as well as in semi-empirical methods. They can also be used with DFT methods where the exact exchange is not included. Slater orbitals have the functional form as:

$$\chi_{\zeta,n,l,m}(r,\theta,\varphi) = NY_{l,m}(\theta,\varphi)r^{n-1}e^{-\zeta r} \tag{2-24}$$

in which N and $Y_{l,m}$ represent a normalization constant and spherical harmonic functions, respectively.

Standard basis sets for electronic structure calculations use linear combinations of Gaussian functions to form the orbitals. GTOs can be written in terms of either polar or Cartesian coordinates:

$$\begin{aligned}\chi_{\zeta,n,l,m}(r,\theta,\varphi) &= NY_{l,m}(\theta,\varphi)r^{2n-2-l}e^{-\zeta r^2}\\ \chi_{\zeta,l_x,l_y,l_z}(\vec{x},\vec{y},\vec{z}) &= Nx^{l_x}y^{l_y}z^{l_z}e^{-\zeta r^2}\end{aligned} \tag{2-25}$$

the sum of l_x, l_y, l_z represents the type of orbital (p, d, f, etc.). The GTOs are inferior to the STOs in two respects, due to the r^2 dependence in the exponential term. STOs have a discontinuous derivative at the nucleus while GTOs has a zero slope. GTOs have some difficulties showing suitable behaviour close to the nucleus. It also falls off very quickly far from the nucleus compared with an STO.

In general, as a rule of thumb, three times as many GTOs as STOs are required for reaching a given level of accuracy, which is however, more than compensated for by the ease of which the required integrals can be evaluated. Therefore, according to the computational efficiency, GTOs are preferred and are used almost universally as basis functions in electronic structure calculations for a speedup when attempting to converge around multiple nearby centers.

2.2.2 Basis sets classification

After choosing the type of basis set function (STO/GTO), the most important factor is the number of functions to be used. If we choose the smallest number of functions possible, then the obtained basis set will be a minimum basis set. These basis sets use fixed-size atomic-type orbitals. Enough functions are used to contain all the electrons of the neutral atom(s). For instance, in hydrogen and helium, a single s-function is possible. The elements from the second row of the periodic table contain two s-functions

(1s and 2s) and one set of p-functions ($2p_x$, $2p_y$, and $2p_z$). In a Double Zeta (DZ) type basis set, all the basis functions are doubled. The term "zeta" refers to the fact that the exponent of STO basis functions is often denoted by the Greek letter ζ. For instance, a DZ basis set employs two s-functions as 1s and $1s'$ for hydrogen, and four s-functions as 1s, $1s'$, 2s, and $2s'$ and two sets of p-functions for the first row elements. In fact, doubling the number of basis functions allows for a much better description of different electron distributions in different directions [237]. In a Triple Zeta (TZ) type basis set, as we expect, three times as many functions as the minimum basis is used, i.e. three and six *s*-functions for hydrogen and helium, respectively.

2.2.3 Pople style basis sets

STO-nG basis sets: These are Slater type orbitals which consist of *n*-primitive GTOs (*n*-PGTOs) [238]. The exponents of this minimum type basis set are determined by fitting to the STO. It is found that using more than three PGTOs for representing the STO gives little improvement. Therefore, although basis sets with $n = 2–6$ have been derived, the STO-3G basis is a widely used minimum basis. This type of basis set has been determined for many elements of the periodic table.

k-nlmG basis sets: They were also designed by Pople and coworkers [239, 240], and are of the so-called split valence type. *k* indicates the number of used PGTOs for representing the core orbitals while the *nlm* represents the number of functions that the valence orbitals are split into, with the number of used PGTOs for their representation. More specifically, *nl* indicate a split valence, while *nlm* indicate a triple split valence. Generally, the values before the G (representing the Gaussian) indicate the *s*- and *p*-functions in the basis and the polarization functions comes after the G. Although these basis sets increase computational efficiency, they decrease the flexibility of the basis sets.

6-31G: In this basis, the core orbitals are a contraction of six PGTOs, the inner part of the valence orbitals is a contraction of three PGTOs and the outer part of the valence is represented by one PGTO.

6-311G: In this triple split valence basis, the core orbitals are a contraction of six PGTOs and the valence split into three functions, represented by three, one and one PGTOs, respectively.

To each of these basis sets, diffuse [241] and/or polarization functions can be added [242]. Diffuse functions allow orbitals to occupy a large region of space. Basis sets with diffuse functions are important for systems where electrons are relatively far from the nucleus: molecules with lone pairs, anions and other systems with a negative charge, systems in excited states, and so on. Diffuse functions are *s*- and *p*-functions, denoted by + or ++ before the G, indicating one set of diffuse *s*- and *p*-functions on heavy atoms, and adding a diffuse *s*-function to hydrogen, respectively. Polarization functions are indicated after

the G, with a separate designation for heavy atoms and hydrogen. For instance, in 6-31^{+}G(d) one set of diffuse *sp*-functions is added on heavy atoms only and a single *d*-type polarization function on heavy atoms. In 6-311^{++}G(2df,2pd) a triple split valence with additional diffuse *sp*-functions, two *d*-functions and one *f*-function on heavy atoms, and diffuse *s*- and two *p*- and one *d* functions on hydrogen. The largest standard Pople style basis set is 6-311++G(3df,3pd). In case of using just one set of polarization functions, an alternative notation * can be used, 6-31G* basis is used for 6-31G(d), or 6-31G** is identical to 6-31G(d,p).

2.2.4 Correlation consistent basis sets

Correlation consistent (cc, the convention is to use lower case letters to better distinguish it from coupled-cluster (CC)) basis sets are build by adding shells of functions to a core set of atomic HF functions. Each function in a shell contributes similar amounts of correlation energy in an atomic calculation, independent of the function type. Different sizes of cc basis sets are available in terms of the final number of contracted functions, known by their acronyms [243]: cc-pVDZ, cc-pVTZ, and cc-pVQZ (correlation consistent polarized Valence Double, Triple, Quadruple Zeta). These cc-basis sets can be augmented with diffuse functions by adding the prefix aug- to the acronym. For instance, the aug-cc-pVDZ has one extra s-, p-, and d-function.

LANL2DZ: The Los Alamos National Laboratory basis sets (LANL2DZ) is a widely used effective core potential (ECP)- type basis set, developed by Hay and Wadt [244, 245]. It has been widely used in quantum chemistry, particularly in the study of compounds or clusters containing heavy elements [244]. They are also employed in DFT calculations for atoms beyond the third row of the periodic table. ECPs are a useful means of replacing the core electrons in a calculation with an effective potential, thereby eliminating the need for the core basis functions, which usually require a large set of Gaussians to describe.

Historically, dispersion interactions have been difficult to account for in most widely used density functional. This is due to the difficulties in finding appropriate long-range correlation expressions that take proper account of good balance between exchange and correlation in a functional [246]. Recently, some improvements have been made through the use of semi-local or hybrid functional. These groups of functionals consist a large number of free parameters in the functional form. These parameters are then semi-empirically fitted using broad experimental data sets that include non-covalent interactions.

In this thesis, the M06-2X[247], a semi-local hybrid meta-GGA functional, is used. This functional is developed in the group of Prof. Donald Truhlar at the University of Minnesota [248, 249]. Minnesota functionals are a group of highly parameterized approximate exchange-correlation energy functionals. The M06 suite is a group of four

meta-hybrid GGA DFT functionals: M06-L which is fully local without HF exchange (thus it cannot be considered hybrid), M06 with 27% of the HF exchange, M06-2X with 54%, and M06-HF with 100% of the HF exchange [250, 251]. They are constructed with the empirical fitting of their parameters but constraining to the uniform electron gas. These functionals have already been widely tested for uncharged molecular systems [252, 253]. The M06-2X functional is mostly used to investigate systems that include both covalent and noncovalent interactions [254, 255]. It allows for an approximate modeling of van der Waals (VDW) interactions whenever there is a non-negligible electron density overlap. Moreover, it is a top performer within the set of 06 functionals for main group thermochemistry, kinetics, and non-covalent interactions.

Additionally, the B3LYP, WB97XD, and CBS-QB3 functionals are also used for checking the accuracy of our calculations only for the gas species. B3LYP was the first DFT exchange-correlation hybrid functional to convince computational chemists that DFT could predict molecule physicochemical properties and reaction barriers with accuracy comparable to some wave function based methods but with much improved computational efficiency. It consists of an exact Becke exchange and Lee Yang Parr correlation functional with 3 parameters to mix in the exact HF exchange-correlation. B3LYP uses the non-local correlation provided by the LYP expression and Vosko, Wilk, and Nusair (VWN) functional III for local correlation (not functional V). In other words, VWN is used to provide the excess local correlation required, since LYP contains a local term essentially equivalent to VWN.

WB97XD is known as a range-separated functional. It captures both short-range and long-range interactions. It is the latest functional from Head-Gordon which has improved the overall accuracy attainable with the long-range corrected functional groups by using a systematic optimization procedure [256]. Optimizing long-range corrected and hybrid functionals with identical numbers of parameters in their GGA exchange and correlation terms leads to noticeably better results for all properties using the long-range corrected form resulting in the WB97 functional. Re-optimizing the entire functional with one extra parameter leads to an adjustable fraction of short-range exact exchange (WB97X) that by following the Grimme's work [257] for computing the empirical dispersion corrections is denoted as the WB97X-D functional.

In Gaussian, the complete basis set-QB3 (CBS-QB3) method [258] is developed with the goal of obtaining highly accurate thermochemical values. It is used to calculate ΔH° and ΔG° values for ions and molecules.

Two different basis sets are used in this thesis, i. e., 6-31G* for first, second, and third row atoms of the periodic table and LANL2DZ from the ECP type basis set for the single transition metal atoms.

2.2.5 Basis set superstition error (BSSE)

This error is not associated with a particular method, like HF, but it rather is a basis set problem. In quantum chemistry calculations using finite basis sets are susceptible to this basis set superposition error (BSSE). As the atoms of two molecules approach one another, their basis functions overlap. Each monomer "borrows" functions from other nearby components, effectively increasing its basis set and improving the calculation of derived properties like energy. If the energy is minimized as a function of system geometry the short-range energies from the mixed basis sets must be compared with the long-range energies from the unmixed basis sets. This mismatch causes an error. Therefore, it is important to choose a "balanced" basis set, i. e., using the same basis set when comparing energies.

There are two ways to deal with BSSE. One is to say, as we implied above, that we should really compare the energy of AB with that of A with the extra basis functions provided by B, plus the energy of B with the extra basis functions provided by A. This method of correcting the energies of A and B with extra functions is called the counterpoise method [259, 260] because it balances (counterpoises) functions in A and B against functions in AB. This correction gives only an approximate value of the BSSE, and it seldom applies to anything other than weakly-bound dimers, like hydrogen-bonded and van der Waals species. Interestingly, this correction worsens calculated atomization energies, like covalent (AB → A+B), and it is not defined for species of more than two components.

The second way is to solve this error with basis functions. If each fragment A and B is endowed with a sufficiently big basis set, then extra functions from the other fragment won't change the energy considerably, because the energy will already be near the asymptotic limit. Consequently, the straightforward procedure of subtracting the energy of AB from that of A + B should give stabilization energy essentially free of BSSE.

2.2.6 Charge analysis methods

2.2.6.1 Mulliken population analysis

Mulliken charges arise from the Mulliken population analysis [261] developed by Robert S. Mulliken, after whom the method is named. Conceptually, it is very simple, with the electrons being divided up amongst the atoms according to the degree to which different atomic orbital basis functions contribute to the overall wave function. It is the oldest method for calculating the atomic charges. It is very simple, with the electrons being divided up amongst the atoms according to the degree to which different atomic orbital basis functions contribute to the overall wave function. It simply devides the canonical orbital, equally amongst the participating atoms. There is no polarization whatsoever. Although Mulliken charges can be calculated very fast, they are explicitly

sensitive to the basis set choice. In principle, a complete basis set for a molecule can be spanned by placing a large set of functions on a single atom.

2.2.6.2 Natural bond orbital analysis (NBO)

Natural bond orbital (NBO) analysis is one of many available options for 'translating' computational solutions of Schrödinger's wave equation into the familiar language of chemical bonding concepts [262]. NBO is a calculated binding orbital with maximum electron density. It is one of a sequence of natural localized orbital sets that include "natural atomic orbitals" (NAO), "natural hybrid orbitals" (NHO), "natural bonding orbitals" (NBO) and "natural (semi-) localized molecular orbitals" (NLMO). These natural localized sets are intermediate between basis atomic orbitals (AO) and molecular orbitals (MO) [263]. In computational chemistry, these natural (localized) orbitals are used to calculate the distribution of electron density in atoms and in bonds between atoms. NBO include highest percentage of the electron density, providing the most accurate possible "natural lewis structure" of the wave function. This method obviously works well for the systems that can actually be described by a lewis structure.

Chapter 3

Direct methane conversion to methanol on M and MN_4 embedded graphene (M=Ni and Si) flake: A comparative DFT study

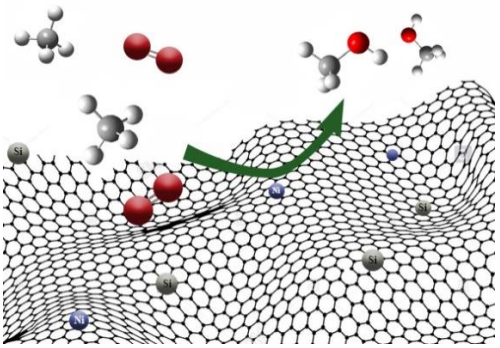

The ever-increasing global production and dispersion of methane requires novel chemistry to transform it into easily condensable energy carriers that can be integrated into the chemical infrastructure. In this context, single atom catalysts have attracted considerable interest due to their outstanding catalytic activity. We here use density functional theory (DFT) computations to compare the reaction and activation energies of M and MN_4 embedded graphene flake (M=Ni and Si) on the methane-to-methanol conversion near room temperature. Thermodynamically, conversion of methane to methanol is energetically favourable at ambient conditions. Both singlet and triplet spin state of the studied systems are considered in all of the calculations. The DFT results show that the barriers are lower when the complexes are in the triplet state than in the singlet state. In particular, Si-G with the preferred spin multiplicity of triplet seems to be viable catalysts for methane oxidation thanks to the corresponding lower energy barriers and higher energetic stability of the obtained configurations. Our results provide insight into the nature of methane conversion and may serve as guidance for fabricating cost-effective graphene-based single atom catalysts.

Publication: Parisa Nematollahi and Erik C. Neyts. Direct methane conversion to methanol on M and MN_4 embedded graphene (M=Ni and Si): A comparative DFT study. J. Applied Surface Science, 496 (2019): 143618. https://doi.org/10.1016/j.apsusc.2019.143618

3.1 Introduction

Nickel is a frequently used metal catalyst for methane conversion thanks to its availability and low cost [264, 265]. In the last decades, Ni catalysts have been studied extensively. There are different strategies for stabilizing Ni particles in catalytic reactions toward coking and sintering. Some of them include modifications of Ni particles by other metals like Co or Cu [266], incorporation of Ni into perovskites [267], or the deposition of Ni-supported catalysts [268, 269]. Many of the current investigations on CH_4 conversion via various methods employ Ni or other metals or bi-metallic surfaces. For instance, Niu et al. [270] examined the catalytic performance of pure and Pt modified Ni(111) surfaces for carbon formation from methane dehydrogenation. According to their results, CH_4 dissociation into $CH_3^* + H^*$ and CH^* decomposition into $C^* + H^*$ were the two key steps. It was found that CH^* dissociation barriers on the Ni-Pt bimetallic surfaces are higher than on pure Ni(111). Moreover, carbon formation was inhibited even with a small amount of Pt addition. They proposed that Ni-Pt(111) surface not only exhibits good resistance to carbon formation but also has a moderate cost due to the low Pt content. Ni atom is known as the most interesting non-noble metal used for methane related reactions [271-275] or CO_2 conversion [276, 277]. The usage of this metal has furthermore been studied for methane dissociation in connection with steam reforming [278]. Doping of Si, which belongs to the same group as C, and strongly prefers sp^3-like bonding, is shown to influence the electronic and structural properties of graphene [279]. Si-G can be synthesized using CVD [280] and other methods [281]. It was predicted theoretically that the large outward displacement of the Si atom and its nearest-neighbor C atoms may impose changes in the physical properties.

Graphene nano-flakes and graphene nano-ribbons are promising graphene-based materials with a size controllable energy bandgap, which might be useful for various technological applications[282, 283]. They are important because of their potential for bottom-up fabrication of molecular devices, spintronics, and quantum dot technology[284]. Similar to tight-binding calculations or solutions of the Dirac equation, ab initio calculations also show that the graphene nanoflakes have a non-zero direct bandgap. They are cheap catalysts, and being produced by a cheap method, typically contain many defects. Because of the small size of graphene flakes they can be considered as a zero-dimensional form of graphene sheet showing different properties from graphene nano-ribbons and bulk graphene. These amazing graphene-flakes are promising for a variety of applications such as electronic and magnetic devices with different molecular sizes and shapes, and in light absorption in photovoltaics due to their edge structure and wide spectrum. They have unique electronic, magnetic, and optical properties since their bandgap can be modified. And due to this property, they might be used in solar cells and light-emitting diode (LED) technology as well [285]. Moreover, the saturation of the zigzag edges of graphene flakes with different atoms (like H in our investigations) or

molecular groups leads to a spin-polarized ground state with a non-zero total magnetic moment, an electronic energy gap and spin density that strongly depends on the used atomic group to passivate the dangling bonds of the C atoms [286]. This article describes our efforts to develop a mechanism for direct conversion of methane-to-methanol on both metal-embedded graphene nanoflake (M-G) and M-embedded pyridinic N_4-graphene nanoflake (MN_4-G) (M=Ni and Si) using density functional theory (DFT) calculations. Both the singlet and triplet spin state of the studied systems are considered in all calculations. The results of this work provide a better understanding of atomic Ni or Si embedded into graphene and N-doped graphene nanoflakes and therefore lead to improved understanding of these materials for the catalytic oxidation of methane to methanol.

3.2 Computational methods

All structure optimizations and reaction pathway calculations are based on DFT using the Gaussian 16 package [287] with the M06-2X functional. The used basis sets are the 6-31G* for C, H, O, N, Si atoms, and LANL2DZ for the Ni atom. In addition, the corresponding frequency calculations were performed at the same level of theory to find whether the optimized complexes correspond to a true local minimum or not.

Our graphene model consists of a hexagonal graphene flake (4×4 graphene unit cell), containing 75 carbon atoms. For the formation of M-G (M=Ni and Si), a single C atom of the graphene flake is replaced by a single Ni or Si atom to form Ni-doped graphene nanoflake (Ni-G) or Si-doped graphene nanoflake (Si-G). Then, the MN_4 porphyrin-like co-doped graphene configuration is obtained by the removal of two adjacent C atoms and substitution of four surrounding C atoms with four N atoms and the introduction of one M atom into the pyridinic N_4-graphene flake. In order to minimize the boundary effect by dangling bonds, the edge atoms of the graphene flake are saturated by hydrogen. The triplet spin state of oxygen is considered for its adsorption configurations. The binding/adsorption energy ($E_{b/ads}$) is calculated as:

$$E_{(b/ads)} = E_{Complex} - E_{Substrate} - E_{Adsorbtae} \quad (3.1)$$

where the $E_{(Complex)}$ is the total energy of the adsorbed species over the substrate, $E_{(Substrate)}$, and $E_{(Adsorbate)}$ are the total energy of the substrate and adsorbates in the gas phase, respectively. The basis set superposition error (BSSE) is considered for calculating the adsorption energy of the gas molecules on each substrate. For all the transition state (TS) configurations the intrinsic reaction coordinate (IRC) calculations were considered [288]. IRC calculations validate the identified transition state structure of each reaction step. To better understand the interaction between the substrate and adsorbate, electron density difference (EDD, $\Delta\rho$) for the adsorbed structures are also studied to understand the interaction between the substrate and adsorbate. It is defined as:

$$\Delta\rho = \rho_{Complex} - \rho_{Adsorbate} - \rho_{Substrate} \quad (3.2)$$

where the $\rho_{Complex}$, $\rho_{Adsorbate}$, and $\rho_{Substrate}$ are the electron charge densities of the adsorbed species on the substrate system, the free adsorbate, and the pristine graphene flake, respectively. In the EDD maps, blue and red colors denoting the charge depletion and charge accumulation, respectively. Moreover, the natural bond orbital (NBO) analysis is calculated to measure the overlap population between two atoms. Additionally, the cohesive energy for the doped graphene flakes was calculated as:

$$E_{coh} = (E_{tot} - n_H E_H - n_C E_C - n_N E_N - n_M E_M)/N \quad (3.3)$$

where E_{tot} is the total energy of the doped graphene flake and E_H, E_N, E_C and E_M correspond to the energy of a single H, N, C, and metal atom in its most stable electronic configuration, respectively. The n_H, n_C, n_N, and n_M indicate the number of H, C, N, and metal atoms in the complex, respectively and N is the total number of the atoms in the doped graphene flake.

To check whether the reactions are thermodynamically possible, we calculate the change of enthalpy (ΔH) and free energy (ΔG) at 298.15 K and 1 atmosphere from the frequency calculations according to the following equations [289]:

$$\Delta H = \sum (\varepsilon_0 + H_{corr})_{\ products} - \sum (\varepsilon_0 + H_{corr})_{\ reactants} \quad (3.4)$$

$$\Delta G = \sum (\varepsilon_0 + G_{corr})_{\ products} - \sum (\varepsilon_0 + G_{corr})_{\ reactants} \quad (3.5)$$

$$H_{corr} = E_{tot} + k_B T \quad (3.6)$$

$$G_{corr} = H_{corr} - TS_{tot} \quad (3.7)$$

where ε_0 is the total electronic energy at T = 0 K. H_{corr} and G_{corr} refers to thermal corrections which should be added to ε_0 to obtain the enthalpy and Gibbs free energy, respectively. The internal thermal energy E_{tot} is obtained from translational (E_{tr}), rotational (E_{rot}), vibrational (E_{vib}), and electronic (E_{el}) energies, and S_{tot}, S_{tr}, S_{rot},S_{vib}, S_{el} are the corresponding entropies. The k_B is the Boltzmann constant. According to the NIST database[290] the methane-to-methanol conversion reaction $2CH_{4\ (g)} + O_{2\ (g)} \rightarrow 2CH_3OH_{(g)}$ is thermodynamically favourable: $\Delta G_{298.15}$ = -2.32 eV and $\Delta H_{298.15}$ = -2.63 eV. The calculated thermodynamic results for this reaction using Gaussian16 also show that it is a thermodynamically feasible reaction: $\Delta G_{298.15}$ = -1.87 eV and $\Delta H_{298.15}$ = -2.20 eV. We also investigated these thermodynamic properties of the reaction by applying various other functional and basis sets. The obtained results are provided in Table A3-3 in the Appendix section. According to our calculations, the best agreement with the NIST database data was found using the CBS-QB3 functional with 6-311G** basis set, viz. $\Delta G_{298.15}$ = -2.35 eV and $\Delta H_{298.15}$ = -2.66 eV, which is indeed very close to the database values [291, 292]. Moreover, the zero-point energy (ZPE) correction to the energy of adsorbed molecular species is calculated by:

$$ZPE = \sum_i \frac{1}{2} h\vartheta_i \quad (3.8)$$

where h and ϑ_i are Planck's constant and the frequency of the i^{th} vibrational mode, respectively.

3.3 Results and discussions

The aim of this work is to investigate the catalytic activity of Ni-G, Si-G, and SiN_4-G toward methane activation and conversion to methanol. Several theoretical and experimental studies reported the probable mechanisms for methane oxidation by metal-oxo species [293-296]. In most cases, the reaction starts with C-H bond cleavage, which is typically challenging in heterogeneous catalysis, due to its great thermodynamic stability and the strong tetrahedral C–H bonds (435 kJ mol^{-1}). Upon C-H bond cleavage, and depending on the used spin state, two different pathways with different intermediates can be identified for the H abstraction by oxygen: a non-radical and a radical process. The possibility of the reaction to proceed via the ER and LH mechanism is also considered.

3.3.1 Geometry, electronic structure, and stability of Ni-G, Si-G, and SiN_4-G

We begin with checking the stability of each substrate. To find the synthesis probability of the studied substrates without having agglomeration or clustering, we first checked the stability of each substrate against agglomeration with the dopant. To achieve this, we calculate the E_{coh} and the E_{ads} of the single dopant atom into the graphene flake. The optimized stable structures of pure and doped graphene flake along with the corresponding total/partial density of state (TDOS/PDOS) diagrams and energy gaps (E_g) have been shown in Figure 3-1. The calculated NBO charge analysis, E_{ads}, E_{coh}, and thermodynamic properties of singlet and triplet doped structures are listed in Table 3-1. In addition, various spin multiplicities have been considered for each configuration, i. e., singlet, doublet, triplet, and quadruplet. Then, the corresponding structures have been optimized. We found that as a function of progress of the reaction, the spin changes from singlet to triplet, from doublet to quadruplet or vice versa. Amongst the optimized configurations, the energetically more favourable configurations have been chosen for our calculations.

Pure graphene with C-C bond length of 1.42 Å (in agreement with the experimental value [297]), E_g = 2.66 eV, and E_{coh} = -6.79 eV is used as reference for comparing the geometry and electronic properties of doped configurations (see Table 3-1). This value is in good agreement with other theoretical and experimental studies [298-300]. The carbon atom adsorbs with an adsorption energy of -8.42 eV into the single vacancy graphene. One can see from Figure 3-1 and Table 3-1 that doping with Ni or Si atom induces drastic changes in the geometric structure and thermodynamic properties of the

graphene flake. It is clear from Table 3-1 that doping is an exothermic and thermodynamically favourable reaction leading to a more stable configuration. Ni and Si atoms form pyramidal-like configurations: they protrude outward from the surface resulting from the longer bond lengths and atomic radius compared to carbon. Subsequently, this causes displacing of the positions of the three-out-of-plane carbon neighbours as reported in previous studies [301, 302].

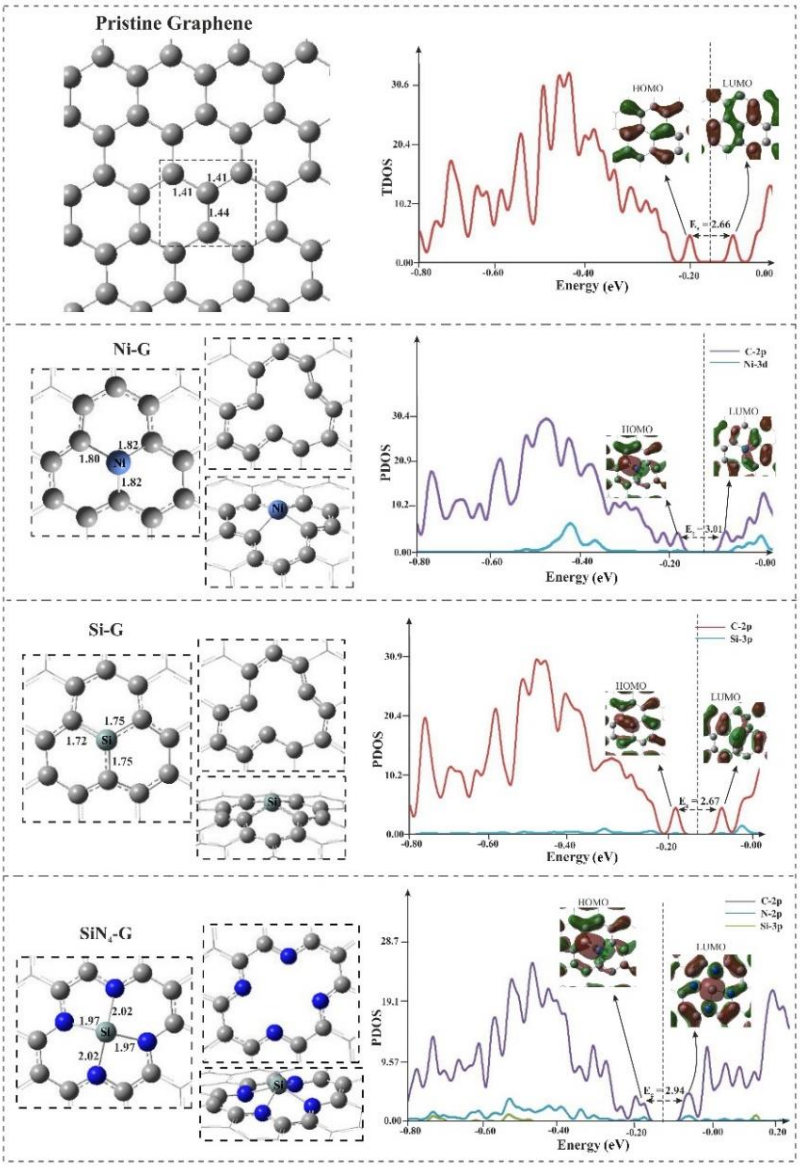

Figure 3-1. Optimized configurations of the singlet pure graphene flake, triplet Ni-G, singlet Si-G and triplet SiN_4-G along with their electronic DOS plots. All distances are in Å.

Starting with singlet Ni-G, the Ni atom adsorbs into the single vacancy of the graphene flake with an adsorption energy of E_{ads} = -6.04 eV and average bond length of

Ni-C = 1.82 Å (Table 3-1). This is much larger than that in pristine graphene, and is smaller than those found in previous studies (1.86 Å) [303, 304]. One can see from Figure 3-1 that the Ni atom protrudes 1.15 Å above the surface. According to the NBO analysis a small charge of +0.24 e is transferred from the Ni atom to the surrounding C atoms of the graphene flake, close to the value found by Xu et al. [10]. In addition, the cohesive energy of the Ni-G is E_{coh} = -6.60 eV, which is somehow lower than that of pure graphene (see Table 3-1).

In Si-G, the Si atom binds strongly with three surrounding C atoms through sp^2 hybridization leading to a slightly positively charged Si atom, ≈ 0.30 e, with a high adsorption energy E_{ads} = -10.39 eV. The Si-atom protrudes 1.04 Å above the surface. The bond length of Si-G is 1.75 Å which is in good agreement with previous studies [63, 64] but is larger than that reported by Rafique et al. [305]. The C–C bond lengths around the Si atom are slightly shortened to 1.38-1.42 Å. Moreover, the high value of the cohesive energy, E_{coh} = -6.67 eV, indicates the high energetic and configurational stability of Si-G which decrease the probability of Si diffusion or its agglomeration into a cluster after doping. It also shows that the Si atom cannot be removed thermally or by irradiation with sub-MeV electrons, like Ti-doped graphene [39]. Furthermore, the diffusion barrier (E_{diff}) of single Ni and Si atom to the surrounding carbon atoms is calculated to be E_{diff} = 4.08 eV and E_{diff} = 4.96 eV, respectively. The energy diagram of the proposed initial state (IS), TS, and final state (FS) for Si diffusion is shown in Figure A3-1 in the Appendix section. The large diffusion barriers reveal that the dopants strongly bind to the vacancy site of the graphene flake forming a stable structure.

Table 3-1.The calculated NBO analysis (+ and – signs refer to the electron donation and acceptation), adsorption energy (E_{ads}), change of enthalpy ($\Delta H_{298.15}$), change of Gibbs free energy ($\Delta G_{298.15}$), and cohesive energy (E_{coh}) of doped complexes.

Complexes	**singlet**				
	$q_{(C/Si/Ni)}$ (e)	E_{ads} (eV)	$\Delta H_{298.15}$(eV)	$\Delta G_{298.15}$(eV)	E_{coh} (eV)
Graphene flake	+0.04	-8.42	-8.54	-7.87	-6.79
Ni-G	+0.24	-6.04	-6.01	-6.01	-6.60
Si-G	+0.30	-10.39	-10.38	-10.31	-6.67
SiN_4-G	+0.77	-8.63	-8.62	-8.60	-6.09
triplet					
Graphene flake	+0.04	-6.56	-6.64	-6.10	-6.78
Ni-G	+0.36	-4.62	-4.56	-4.68	-6.61
Si-G	+0.31	-8.50	-8.47	-8.52	-6.67
SiN_4-G	+1.06	-8.17	-8.17	-8.15	-6.09

Typically, the production of vacancy defects in graphene synthesis is both unfavourable and inevitable [306]. Furthermore, stability is an important parameter that is necessary for a catalyst in practice. Nitrogen doping of the vacancy sites of graphene

reduces the number of dangling bonds and yields an energetically more favourable structure [77]. According to experimental studies, different methods applies for synthesizing different N-doping into the graphene sheet [307, 308]. Recently, MN_4-G complexes are known as efficient catalysts for ORR or CO oxidation [309, 310]. Therefore, it was quite interesting for us to study the effects of Si or Ni coordination on defective pyridinic N_4-graphene flake toward methane-to-methanol conversion. According to our results, since the Si-G showed higher energetic and configurational stability than Ni-G, we investigated the catalytic activity of Si-doping into the N_4-G (SiN_4-G) toward methane oxidation.

To model N_4-doped graphene flake, two adjacent C atoms removed from the graphene flake forming a di-vacancy graphene flake, and then replacing the C atoms of the vacancy site by four N atoms (see Figure 3-1). Next, the Si atom introduces into the vacancy site and produces the SiN_4-porphyrin-like graphene flake. In this configuration, the Si atom is surrounded by two pentagons and hexagons with average Si-N bond lengths of 1.99 Å, close to literature values [83]. NBO charge analysis shows that a charge of +0.77 e is transferred from the Si atom to the surrounding N atoms make the Si atom positively charged while surrounding N atoms are negatively charged to -3.33 e. This high charge value indicates the strong interaction between Si and N atoms of the surface, confirming the high stability of SiN_4-G against Si-clustering and its potential to be used in catalytic reactions. The single Si atom adsorbs with E_{ads} = -8.63 eV into the nitrogen vacancy site with a cohesive energy E_{coh} = -6.09 eV (Table 3-1). This can be attributed to the different degree of contribution of electron pair of nitrogen atoms to form a delocalized conjugated configuration with the Si atom.

We also compared the computed DOS plots of the pristine graphene flake with Ni-G, Si-G, and SiN_4-G in Figure 3-1. The Fermi level (E_F) is shown by the vertical dashed line at -0.15 eV. As is evident from Table 3-1 regardless of the spin state of the systems, the positive charges on the active site of the substrate increase by introducing N atoms into the surface structure. This finding shows that the incorporation of N atoms increases the donor states of the Si atom in SiN_4-G, which is due to the electron-accepting property of the N atoms. Si-3p orbitals strongly couple with 2p orbitals of neighbouring C atoms in Si-G and 2p orbitals of the surrounding N atoms in SiN_4-G above and below the Fermi level, suggesting a very strong interaction between the Si atom and C-vacancy/N-vacancy graphene flake. The energy gap between the highest occupied orbital (HOMO) and the lowest unoccupied orbital (LUMO) of Ni-G is E_g = 2.82 eV, which is larger than that of the pure graphene flake (E_g = 2.66 eV). As is also clear from the corresponding PDOS plots shown in Figure 3-1, the energy gap for Si-G, E_g = 2.67 eV, is very similar to that of pure graphene flake. The silicon creates a localized state when it bonds to a graphitic network, which would have little effect on the semi-metallic character of the graphene [63, 311, 312]. Moreover, Si is known to act as a donor when incorporated into graphene. One can see in Figure 3-1 that most states of the HOMOs

are located around the Si atom that partially explains why the Si atom in Si-G has a much energetically stable structure than Ni atom in Ni-G. In SiN_4-G, the energy gap is increased to about 0.28 eV compared to pure graphene flake indicating that the incorporation of nitrogen atoms around the single-vacancy site can effectively alter the electronic structure of the defective graphene flake as shown in Figure 3-1 and Table 3-1. The hybridization of the valence states and bonding can be seen in overlapping peaks. Generally, doping Ni and Si atom into the graphene flake and also the incorporation of nitrogen atoms in SiN_4-G result in a shift toward the Fermi level showing an increase in the electron concentration states. This makes the charge-transfer from the adsorbed species to the Ni or Si atom more facile and hence makes the interactions between adsorbent and the surface stronger.

We continue our calculations investigating the corresponding triplet configurations. In the triplet systems, the optimized configurations have not changed considerably. Therefore, the calculated data are just reported in Table 3-1. According to our results, the most energetically stable configurations are singlet graphene flake and Si-G, triplet Ni-G, and SiN_4-G. Totally, comparing the adsorption energies of a metal atom into the graphene flake vacancy site shows the following order: Si-G > Pure graphene flake > SiN_4-G > Ni-G. Therefore, we estimate that Si-G with the higher negative adsorption and cohesive energy can be considered as the more stable configuration toward methane conversion to methanol. In the present work, regardless of the stability order, all the possible mechanisms on both singlet and triplet systems are investigated and discussed in detail.

3.4 Adsorption of gas reactants

For a catalyst, the catalytic performance is (in part) determined by its ability to adsorb the adsorbates around the active sites with suitable adsorption energy. Finding the most favourable adsorption configurations of methane and O_2 on the studied substrates is therefore, the first step in unraveling the catalytic mechanism underlying methane oxidation. Therefore, we extensively investigated the individual adsorption of methane and O_2 molecules over each substrate. The O_2 molecule binds chemically to the surface by accepting electrons in its $2\pi^*$ orbitals, leading to its adsorption or dissociation over the surface and thus can be seen as a Lewis acid while Ni and Si atoms can be considered as Lewis bases. For methane adsorption, the adsorption configurations are almost the same while for oxygen adsorption, depending on the system's spin state, different initial configurations were obtained, from which the energetically more stable configuration is selected as shown in Figure 3-2. Also, the corresponding EDD map of each complex is shown in Figure 3-2. In the EDD maps, the charge depletion and accumulation sites are displayed in blue and red colors respectively. Table 3-2 reports the corresponding NBO analysis of the adsorbate/dopant, E_{ads}, and thermodynamic properties of both singlet and triplet adsorbed complexes. To

better show the adsorbed complexes of methane on substrates in the singlet and triplet systems, we named them as the X_s and X_t (X=the adsorption complex), respectively.

3.4.1 Triplet spin states

3.4.1.1 Adsorption of gas reactants on Ni-G

First, we start with triplet adsorption configurations of methane and oxygen on each substrate. Interestingly, regardless of the spin state of the complexes, there is just one stable adsorption configuration for methane in which the molecule is physisorbed over each substrate via an endergonic reaction, with very low adsorption energy. The weak adsorption energy of complex A_t, E_{ads} = -0.24 eV, and the small charge of +0.1 e transferred from the methane molecule to the surface, confirms that the methane is indeed physisorbed on Ni-G. In addition, the blue region around the Ni-C bond in the EDD map implies the weak interaction of methane with the Ni atom of the surface.

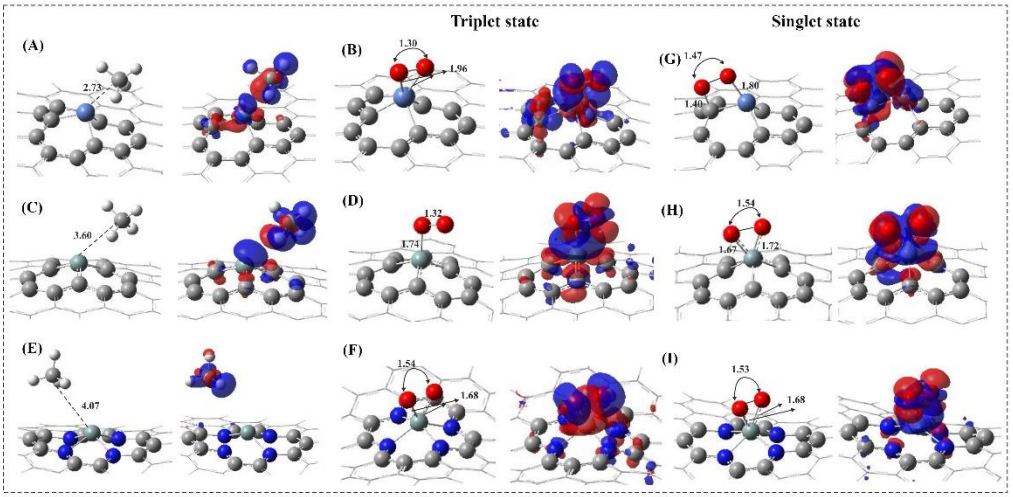

Figure 3-2. The optimized triplet adsorption configurations of methane (complexes A_t, C_t, and E_t) and oxygen (complexes B, D, and F), and singlet adsorption configurations of oxygen (complexes G, H, and I) on Ni-G, Si-G, and SiN_4-G, along with the corresponding EDD map. All distances are in Å.

In complex **B**, the oxygen molecule adsorbs on the top site of the Ni atom with the O-O bond parallel to the surface forming two Ni-O bonds with a bond length of 1.96 Å, which is a common pattern for the adsorption of O_2 on different surfaces like Mn-N_4-CNT [84], Si-doped boron carbon-nitride nanosheet [313], or Mn embedded divacancy graphene [11]. The NBO charge analysis shows that a charge of about -0.5 e is transferred from Ni-G to the O_2 molecule, occupying its $2\pi^*$ orbitals and making the Ni atom positively charged (+0.4 e) which is also clear from the corresponding EDD map in Figure 3-2. This charge transfer leads to the activation and elongation of the O-O bond length from 1.23 Å in the gas phase to 1.30 Å in the adsorbed structure. The adsorption energy of complex **B** is E_{ads} = -1.08 eV which is in good agreement with other studies

[301, 314] and is smaller than that of Mn-embedded divacancy graphene [11].

Table 3-2. The calculated NBO analysis of the adsorbate/dopant (+ and – signs refer to the electron donation and acceptation), adsorption energy (E_{ads}), change of enthalpy ($\Delta H_{298.15}$), change of Gibbs free energy ($\Delta G_{298.15}$) of CH_4 and O_2 molecule on triplet and singlet Ni-G, Si-G, and SiN_4-G. all the energy values are in eV.

Complex	triplet				Complex	singlet			
	$q_{ads/M}$ (e)	E_{ads}	$\Delta H_{298.15}$	$\Delta G_{298.15}$		$q_{ads/M}$ (e)	E_{ads}	$\Delta H_{298.15}$	$\Delta G_{298.15}$
A_t	+0.1/-0.2	-0.24	-0.22	0.03	**A_s**	0.10/0.11	-0.24	-0.22	0.06
B	-0.5/+0.4	-1.08	-1.10	-0.62	**G**	-0.69/0.46	-1.22	-1.26	-0.72
C_t	+0.0/-0.3	-0.10	-0.08	0.18	**C_s**	0.01/0.30	-0.08	-0.09	0.26
D	-0.4/+0.7	-1.76	-1.78	-1.31	**H**	-0.82/0.85	-1.07	-1.09	-0.61
E_t	-0.0/+1.1	-0.15	-0.14	0.18	**E_s**	-0.00/0.77	-0.11	-0.09	0.18
F	-0.8/+1.3	-1.89	-1.93	-1.38	**I**	-0.81/1.33	-3.06	-3.10	-2.58

3.4.1.2 Adsorption of gas reactants on Si-G

Next, we considered the adsorption of gas reactants over Si-G. Similar to Ni-G, methane (complex **C_t**) physisorbs on the active Si site of the surface, with a bond length Si-C = 3.60 Å. The very low adsorption energy, E_{ads} = -0.10 eV, confirms that there is no chemical bond formed between methane and Si-G (Table 3-2). This is further substantiated by the electron depletion region shown in the EDD map between the Si atom and methane (Figure 3-2).

The O_2 molecule adsorbs in a tilted position over Si-G forming complex **D**, which is similar to the adsorption of O_2 over other surfaces like Cu-G [254] and FeN_4-CNT [119]. It is clear from the Si-O bond (1.74 Å) that the O_2 molecule chemisorbs on the surface. The adsorption energy of complex **D** is E_{ads} = -1.76 eV which is much larger than that of Ni-G. Additionally, the accumulation of charge density around the Si-O bond is indicative for the chemical interaction of O_2 with the Si atom of the surface which is also clear by a charge of about +0.42 e transfer from the surface to $2\pi^*$ orbitals of O_2 making the Si atom positively charged (+0.7 e). This elongates the O-O bond to 1.32 Å leading to the activation of O_2 on Si-G.

3.4.1.3 Adsorption of gas reactants on SiN_4-G

We now examine the possible adsorption sites of SiN_4-G to determine the most stable configurations of adsorbates on the surface. Similar to complexes **A_t** and **C_t**, the methane molecule interacts weakly with the surface forming complex **E_t**, with negligible adsorption energy of -0.15 eV and zero charge transfer from the methane molecule to the SiN_4-G surface. It confirms by the corresponding EDD map shows in Figure 3-2.

The geometric structure of the adsorbed O_2 on SiN_4-G (complex **F**) is similar to

complex **B**. Against other complexes, oxygen adsorbs strongly on SiN_4-G forming two strong Si-O bonds with a high adsorption energy of E_{ads} = -1.89 eV. This value is slightly smaller than those of B/N-co-doped graphene [315], FeN_4-G [316], and SiN_4-G [83] and higher than that of Co–N_4 cluster [317] and Fe–N_4 cluster [76]. Oxygen chemisorbs on SiN_4-G along with high charge transferred from the surface to the $2\pi^*$ orbitals of oxygen (-0.8 e) leading to the high charge depletion on the Si atom (+1.3 e). This is also clear from the red regions around the Si-O bonds in the corresponding EDD map in Figure 3-2. The high positive value of the Si atom may correspond to the high electronegativity of the adjacent nitrogen atoms with high negative charge of -3.23 e which is in close agreement with previous experimental [318] and theoretical [319] studies performed on Fe/N/C structures. The considerable elongation of the O–O bond to 1.54 Å can mainly be attributed to the high charge transfer and the resulting decrease in a bond order of the O_2 molecule.

3.4.2 Singlet spin states

We also investigated the adsorption of gas reactants on Ni-G, Si-G, and SiN_4-G with singlet multiplicity. As discussed above, the methane adsorption configurations on the studied substrates are the same as those we shown in the triplet systems. Therefore, we just report the corresponding data of the complexes $\mathbf{A_s}$, $\mathbf{C_s}$, and $\mathbf{E_s}$ (see Table 3-2). One can see from Figure 3-2 that the optimized structure of O_2 adsorption on Ni-G and Si-G are different from those of triplet systems. In addition, to better understand and compare the adsorption energies of CH_4, O_2, O, and OH on the different substrates, we represent an individual bar chart for the reactants and intermediates (atomic oxygen and hydroxyl) in each system, in Figure A3-2. One can see from Figure A3-2 and Table 3-2 that the adsorption energy of methane on the studied substrates in the systems with triplet and singlet multiplicity decreases in the order Ni-G>SiN_4-G>Si-G. Regardless of the spin multiplicity of the adsorption configurations, the O_2 molecule adsorbs more actively on SiN_4-G, which is in good agreement with recent studies [83, 309, 316]. Totally, complexes A_t, G, C_s, D, E_t, and I are the most energetically stable adsorption configurations. Since the adsorption energy of oxygen on Ni-G (complex G) in the singlet system is lower than that on Si-G (complex D) in the triplet system and SiN_4-G (complex I) in the singlet system, we might estimate that Ni-G is not an active catalyst toward methane-to-methanol oxidation.

Comparing the spin density distribution during the methane and O_2 adsorption shows that the energetically more stable adsorption configuration of methane on Ni-G, Si-G, and SiN_4-G are the systems with a triplet, singlet, and triplet spin multiplicity, respectively. Moreover, the adsorption of O_2 on Si-G with consideration of triplet multiplicity and on Ni-G and SiN_4-G with singlet multiplicity is energetically more stable due to the lower (more negative) total energy. In case of O_2 dissociation, Si-G with triplet spin state and SiN_4-G with singlet spin state shows higher stabilities. The obtained dissociative barriers on Si-G (E_{act} = 1.24 eV) and SiN_4-G (E_{act} = 1.99 eV) indicate that

the direct dissociation of O_2 might be impossible and hardly to happen on SiN_4-G due to the large barrier of 1.99 eV.

3.5 Possible reaction mechanisms for methane oxidation over Ni-G, Si-G, and SiN_4-G

According to the above discussions, both CH_4 and O_2 tend to be adsorbed at the metal site. Since the adsorption strength of O_2 is stronger than CH_4, when the two reactants (CH_4 + O_2) are injected synchronously to the system, O_2 is more likely to occupy the active metal site of the surface. Furthermore, when the O_2 is pre-adsorbed, the co-adsorption behavior of the second molecule (CH_4) on the active center may have a noticeable impact on the subsequent reaction path. Also, the sum of adsorption energies for the individual gas precursors on Ni-G, Si-G, and SiN_4-G are mostly lower than the co-adsorption energy of the gas reactants (CH_4 + O_2) on those surfaces. Therefore, we expect that methane oxidation starts with the co-adsorbed configurations.

According to the previous investigations[205, 320], two well-established reaction mechanisms, ER and LH, have been suggested for the initiation steps in the oxidation reactions. The ER mechanism starts with the direct interaction between the free-standing CH_4 and a surface activated O_2 or remaining atomic O after the first oxygen removal. The LH mechanism consists of the co-adsorption of gas reactants interacting with each other on the surface forming intermediates adsorbed on the surface. In the following, the detailed aspects of these mechanisms for methane oxidation reaction on Ni-G, Si-G, and SiN_4-G with consideration of both singlet and triplet spin multiplicities are discussed, separately.

3.5.1 Singlet spin state

The detailed methane-to-methanol oxidation reaction in the systems with singlet multiplicity is explained in the Appendix section. Generally, methane oxidation on Ni-G, Si-G, and SiN_4-G goes through three main reactions: After chemisorption of O_2 and its activation (O^*) over the substrate, first, the methane molecule directly reacts with one of the atomic oxygen's adsorbed on metal site and forms the first methanol molecule. Then, the second methane molecule introduces to the system and dissociates to methyl ($-^*CH_3$) and hydrogen ($-H^*$) species, where the $-H^*$ moiety reacts immediately with the remained O^*, forming the hydroxyl intermediate ($-^*OH$) through a non-radical process [321]. Finally, the $-^*CH_3$ and $-^*OH$ species recombine together and thereby producing the second methanol adsorbed on the metal site. The direct formation of methanol in the first step proceeds via the ER mechanism and followed by the LH mechanism. The optimized stationary structures along with the proposed energy profile of methane oxidation on Ni-G, Si-G, and SiN_4-G are depicted in Figures A3-3, A3-4, and A3-5, respectively. For the detailed explanations of the reaction pathways please

refer to the Appendix section. Additionally, the corresponding activation barriers and thermodynamic properties of each reaction are shown in Table A3-1. The proposed reaction mechanism for methane conversion on Ni-G, Si-G, and SiN_4-G in the singlet systems are as follows:

$$O_{2\,(g)} + Si^{*} \rightarrow {}^{*}O\text{-}Si\text{-}O^{*} \quad (3.9)$$

$$CH_{4\,(g)} + {}^{*}O\text{-}Si\text{-}O^{*} \rightarrow CH_3OH_{\,(g)} + {}^{*}O\text{-}Si \quad (3.10)$$

$$CH_{4\,(g)} + {}^{*}O\text{-}Si \rightarrow {}^{*}CH_3\text{-}Si\text{-}{}^{*}OH \quad (3.11)$$

$${}^{*}CH_3\text{-}Si\text{-}{}^{*}OH \rightarrow CH_3OH_{\,(g)} + Si^{*} \quad (3.12)$$

3.5.2 Triplet spin states

For the triplet spin state, methane adsorption and activation on Si-G proceeds through four main reactions: After adsorption of O_2 on the substrate, methane oxidation starts with H abstraction by an adsorbed oxygen atom on the active Si site forming a methyl radical ($^{\cdot}CH_3$) and hydroperoxyl (-*OOH). Then, the formed $^{\cdot}CH_3$ reacts with adsorbed –*OOH and forms the first methanol on the surface. In the third step, the second C-H bond cleavage occurs, since there is one adsorbed atomic oxygen on the Si atom, forming –*OH adsorbed on the surface while the second methyl radical is located above the hydroxyl group. Finally, the $^{\cdot}CH_3$ reacts with –*OH and the second methanol is produced on top of the surface. The optimized stationary structures along with the proposed energy profile of methane oxidation on Si-G are depicted in Figure 3-3. Additionally, the corresponding activation barriers and thermodynamic properties of each reaction are shown in Table 3-3. We propose that methane oxidation on Si-G proceeds via the ER mechanism, which goes through different stepwise reaction pathways:

$$O_{2\,(g)} + Si^{*} \rightarrow Si\text{-}O^{*}{}_2 \quad (3.13)$$

$$CH_{4\,(g)} + Si\text{-}O_2{}^{*} \rightarrow {}^{\cdot}CH_3 + HOO^{*}\text{-}Si \quad (3.14)$$

$$HOO^{*}\text{-}Si + {}^{\cdot}CH_3 \rightarrow CH_3OH_{(g)} + Si\text{-}O^{*} \quad (3.15)$$

$$CH_{4\,(g)} + Si\text{-}O^{*} \rightarrow {}^{\cdot}CH_3 + HO^{*}\text{-}Si \quad (3.16)$$

$$HO^{*}\text{-}Si + {}^{\cdot}CH_3 \rightarrow CH_3OH_{(g)} + Si \quad (3.17)$$

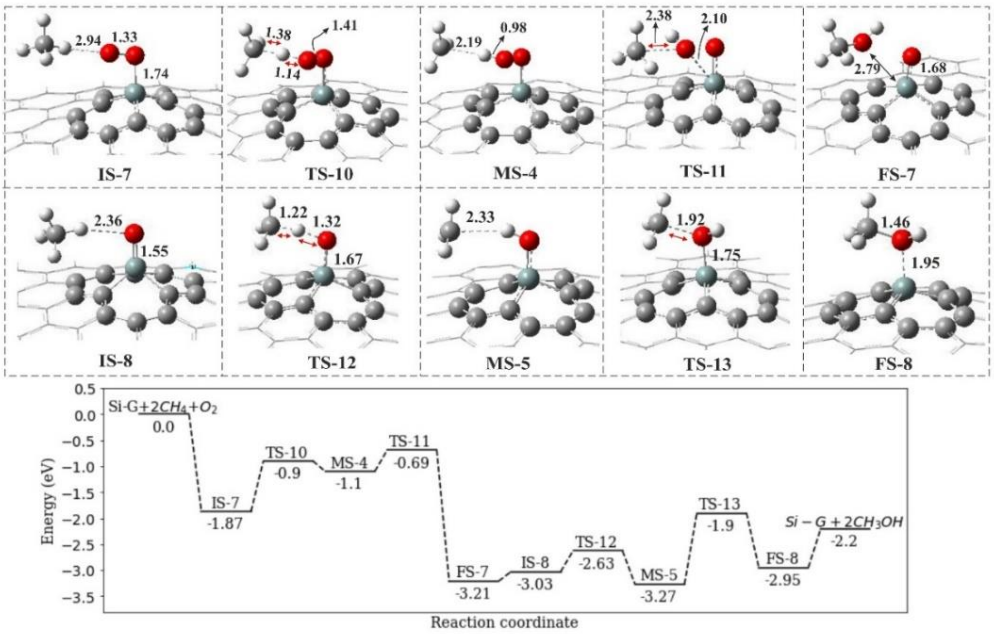

Figure 3-3. The optimized stationary structures along with the corresponding energy profile of methane conversion to methanol on Si-G with triplet spin state. All bond distances and energy values are in Å and eV, respectively

In IS-7, a linear C-H-O angle (175.40 degrees) can be seen (Figure 3-3) upon introducing the first methane to the system, with the adsorption energy of E_{ads} = -0.15 eV, and the co-adsorption energy of -2.02 eV. In this configuration, a charge of -0.42 e transferred from Si-G to the adsorbed oxygen. The charge distribution over O-O-Si is -0.13 e, -0.28 e, and +0.65 e, respectively. Then, methane approaches the adsorbed O_2 in TS-10 while the C-H bond elongates to 1.38 Å and the O-H bond decreases to 1.14 Å, leading to the formation of $^{\cdot}CH_3$ at a distance of 2.19 Å from the adsorbed hydrogen in MS-4. The energy barrier of methane activation on Si-G (IS-7→MS-4) is 0.97 eV, which is much lower than the barrier in the IS-3→ FS-3 reaction (1.89 eV), and is endothermic and endergonic (see Table 3-3). The small barrier is close to the barriers reported for different catalysts [322, 323]. According to the NBO results, in MS-4, the total negative charge accumulation on the $-^{*}OOH$ moiety is -0.36 e, and the contribution of each element is -0.38 e, -0.42 e, and +0.45 e, respectively. Methyl radical as a metastable gas can act as either a strong oxidant or reductant. Here, it acts as a reductant to reduce $-^{*}OOH$ to methanol. Passing via a thermodynamically favourable reaction (Table 3-3), methyl radical reacts with the hydroperoxide species, breaks the O-O bond, and forms the first methanol, with E_{act} = 0.41 eV, in FS-7. Upon the formation of methanol, it desorbs from the surface easily (E_{ads} = -0.33 eV). The high negative thermodynamic values of the reaction MS-4→FS-7 confirm that the reaction is exothermic $\Delta H_{298.15}$= -2.11 eV and spontaneous $\Delta G_{298.15}$= -2.05 eV at room temperature (see Table 3-3).

Upon desorption of methanol, the remained atomic oxygen on Si-G abstracts one H-atom of the introduced methane molecule forming IS-8. Similar to IS-7, the methane molecule adsorbs weakly on the surface (E_{ads} = -0.19 eV). The accumulated negative charge on the oxygen atom in IS-8 is higher (-0.62 e) than that of IS-7, so, the positive H-atom of methane molecule reacts with the negative oxygen atom and produces -*OH species adsorbed on the active Si site. Also, methyl radical is located above the adsorbed hydroxyl in a C-H distance of 2.33 Å (see MS-5 in Figure 3-3). In MS-5, the -*OH species is negatively charged to -0.25 e, while the electron accumulation on oxygen is -0.7 e. The calculated energy barrier for this exothermic and exergonic reaction ($\Delta H_{298.15}$= $\Delta G_{298.15}$= -0.24 eV) is E_{act} = 0.40 eV. Finally, by overcoming a higher energy barrier of E_{act} = 1.37 eV, the resulting intermediates recombine together and form the second methanol (E_{ads} = -0.75 eV) in an endothermic and endergonic reaction $\Delta H_{298.15}$= 0.32 eV, $\Delta G_{298.15}$= 0.43 eV. This high energy barrier may be attributed to the strong adsorption of -*OH species on Si-G which is about 0.56 eV higher than that of -O* making the Si-O bond cleavage more difficult (see Figure 3-3). Therefore, we can propose that the formation of second methanol on Si-G (reaction MS-5 → FS-8) can be the rate-limiting step.

Table 3-3. The calculated activation energy (E_{act}), change of enthalpy ($\Delta H_{298.15}$), and change of Gibbs free energy ($\Delta G_{298.15}$) for methane conversion to methanol on Si-G.

Reaction path	E_{act} (eV)	$\Delta H_{298.15}$(eV)	$\Delta G_{298.15}$(eV)
$O_{2(g)}$ + Si* → Si-O_2^*	0.00	-1.45	-1.01
IS-7 → MS-4	0.97	0.77	0.79
MS-4 → FS-7	0.41	-2.11	-2.05
IS-8 → MS-5	0.40	-0.24	-0.24
MS-5 → FS-8	1.37	0.32	0.43

The corresponding mechanisms of methane oxidation to methanol on SiN_4-G is the same as that on Si-G but here the -*OOH species will not form. Instead, the -*OH moiety forms directly on the active Si site while it is placed for about 2.40 Å farther from the second adsorbed atomic oxygen on the Si atom (see Figure 3-4, MS-6). The geometric structures of each state along with the proposed mechanisms and reaction pathways are depicted in Figures 3-4. Additionally, the corresponding activation barriers and thermodynamic properties of each reaction are shown in Table 3-4. We found that methane oxidation on SiN_4-G proceeds via the ER mechanism, which goes through the following reaction pathways:

$$O_{2\,(g)} + Si^* \rightarrow {}^*O\text{-}Si\text{-}O^* \quad (3\text{-}18)$$

$$CH_{4\,(g)} + {}^*O\text{-}Si\text{-}O^* \rightarrow {}^{\cdot}CH_3 + HO^*\text{-}Si\text{-}O^* \quad (3\text{-}19)$$

$$HO^*\text{-}Si\text{-}O^* + {}^{\cdot}CH_3 \rightarrow CH_3OH_{\,(g)} + Si\text{-}O^* \quad (3\text{-}20)$$

$$CH_{4\,(g)} + {}^*O\text{-}Si \rightarrow {}^{\cdot}CH_3 + HO^*\text{-}Si \quad (3\text{-}21)$$

$$HO^{*}\text{-}Si + {}^{\cdot}CH_3 \rightarrow CH_3OH_{(g)} + Si^{*} \quad (3\text{-}22)$$

We start from the co-adsorbed configuration of O_2 and methane with co-adsorption energy of E_{ads} = -2.25 eV, namely IS-9. One can see from Figure 3-4, that the methane molecule is located at a distance of 2.34 Å from adsorbed oxygen with an adsorption energy of E_{ads} = -0.35 eV. According to the NBO charge analysis data, a charge of -0.81 e transferred from SiN_4-G to the adsorbed oxygen making the Si atom positive (+1.4 e). Also, as mentioned in section 3.4.1.3., the O-O bond is elongated to 1.54 Å. The charge distribution of TS-14 shows that the positive H atom of methane with a charge of +0.34 e approaches the highly negative oxygen atom (-0.7 e) adsorbed on SiN_4-G. Therefore, upon activation of methane above the adsorbed oxygen on the surface in TS-14, oxygen abstracts one hydrogen atom and the -*OH species is produced on the active Si site, forming MS-6 (HO^{*}-Si-O^{*}) and ${}^{\cdot}CH_3$ is located above the adsorbed-O^{*} and -*OH species at a distance of 3.20 Å and 2.30 Å, respectively. The calculated energy barrier of this reaction is E_{act} = 0.69 eV, which is similar to other reported values for various catalysts such as Cu-ZSM-5 zeolite [324] or Fe-ZSM-5 zeolite [325]. The energy pathway in Figure 3-4 shows that the reaction IS-9 → MS-6 is endothermic $\Delta H_{298.15}$= 0.22 eV and endergonic $\Delta G_{298.15}$= 0.18 eV. In the next step, ${}^{\cdot}CH_3$ and -*OH species react together to form the first methanol. To achieve this, ${}^{\cdot}CH_3$ approaches to the -*OH moiety in TS-15. In this configuration, the C-O bond reduces to 2.00 Å and by overcoming an activation energy of E_{act} = 0.93 eV, the first methanol is produced on top of the SiN_4-G (FS-9) with adsorption energy of E_{ads} = +0.15 eV indicating the unfavourable adsorption of methanol at the presence of adsorbed atomic oxygen. Thus, it easily desorbs from the surface making the surface ready to start the second oxidation cycle. The reaction MS-6 → FS-9 is exothermic $\Delta H_{298.15}$ = -1.43 eV and spontaneous $\Delta G_{298.15}$ = -1.37 eV at room temperature.

The formation of the second methanol starts with IS-10 in which the second methane molecule is located at a distance of 2.30 Å from the O^{*} with the adsorption energy of E_{ads} = -0.53 eV. The accumulated charge on atomic oxygen is reduced to -0.51 e and the Si atom becomes less positive (+1.0 e). Upon C-H bond cleavage of methane on the surface, -*OH species adsorbs over the Si atom while the ${}^{\cdot}CH_3$ stays farther from the hydrogen atom at a distance of C-H = 2.26 Å (MS-7). The energy barrier of this step is E_{act} = 0.97 eV. This reaction proceeds endothermically, $\Delta H_{298.15}$ = 0.32 eV, and it is not spontaneous at room temperature, $\Delta G_{298.15}$ = 0.33 eV. Finally, ${}^{\cdot}CH_3$ reacts with the adsorbed -OH (E_{ads} = -2.67 eV) in an endothermic $\Delta H_{298.15}$ = 0.34 eV and endergonic $\Delta G_{298.15}$ = 0.41 eV reaction, passing via an activation energy of E_{act} = 1.07 eV. The produced methanol with Si-O bond length of 1.94 Å adsorbs strongly on active Si site of SiN_4-G, E_{ads} = -1.01 eV. However, this high adsorption energy of methanol on pure SiN_4-G is still lower than that on Fe-ZSM-5 zeolite (1.25 eV) [326, 327] and Fe-doped boron nitride nanosheet (1.17 eV) [328]. We conclude that the formation of the second methanol on SiN_4-G (reaction MS-7 → FS-10) can be the rate-limiting step.

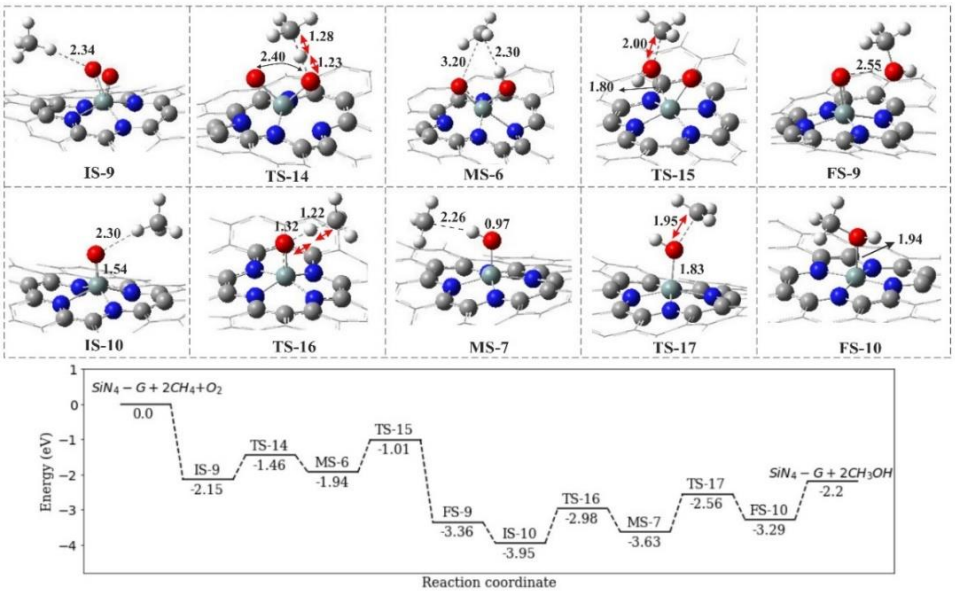

Figure 3-4. The optimized stationary structures along with the corresponding energy profile of methane conversion to methanol on SiN_4-G. All bond distances and energies are in Å and eV, respectively.

Table 3-4. The calculated activation energy (E_{act}), change of enthalpy ($\Delta H_{298.15}$), and change of Gibbs free energy ($\Delta G_{298.15}$) for methane conversion to methanol on SiN_4-G.

Reaction	E_{act} (eV)	$\Delta H_{298.15}$ (eV)	$\Delta G_{298.15}$ (eV)
$O_{2(g)} + Si^* \rightarrow {}^*O\text{-}Si\text{-}O^*$	0.00	-1.99	-1.43
IS-9 → MS-6	0.69	0.22	0.18
MS-6 → FS-9	0.93	-1.43	-1.37
IS-10 → MS-7	0.97	0.32	0.33
MS-7 → FS-10	1.07	0.34	0.41

Generally, a careful comparison of the obtained total energies of each configuration demonstrates that the most stable spin state in catalyzing methane-to-methanol oxidation on Si-G and SiN_4G is triplet and singlet, respectively, since they are energetically more stable (having the lowest total energy). In addition, although SiN_4-G may convert methane to methanol with lower activation barriers by forcing the spin to a constant value (triplet) during the reaction, the obtained configurations are not energetically stable. As mentioned before, the oxidation of methane on SiN_4-G requires very high activation barriers makes it an unfavourable catalyst for catalyzing this reaction. Moreover, in an open system, the reaction is likely to stop on SiN_4-G after the formation of the first methanol at IS-10. The probability of the second formation of methanol via the reactions IS-10 →MS-7 and MS-7→FS-10, was calculated through the Boltzmann distribution (e^{-E/k_bT}) model. Where E is the change in Gibbs free energy

The calculated equilibrium values for the distribution of products at room temperature (T=298.15 K) demonstrated that the fractions in MS-7 (3.023×10^{-6}) and FS-10 (1.26×10^{-7}) is significantly very low leading to the surface poisoning. Therefore, Si-G with the preferred spin multiplicity of triplet might be a highly active catalyst for methane-to-methanol oxidation thanks to the corresponding lower energy barriers and higher energetic stability of the obtained configurations, but surface poisoning may be an inhibiting factor for its use.

3.6 Conclusion

The catalytic conversion of methane into value-added products such as methanol is one of the major current challenges. Using DFT calculations, we explore the catalytic activity and the possible mechanisms for methane-to-methanol conversion on three different substrates: Si-G, Ni-G, and SiN_4-G. Both singlet and triplet spin states of the studied systems are considered in all of the calculations. Interestingly, depending on the spin state, methane oxidation proceeds via a non-radical or radical process. Also, it determines the reaction mechanism, ER, or LH. Generally, we propose three stepwise reactions for direct methane conversion to methanol in singlet systems. All oxidation reactions start with ER followed by the LH mechanism and the whole reaction goes through a non-radical process. In the singlet system, the obtained activation energies on Ni-G, Si-G, and SiN_4-G are rather high.

In contrast, Si-G and SiN_4-G can actively catalyze the methane conversion reaction at ambient conditions for all complexes in the triplet state, thanks to the considerably lower energy barriers. We suggest that the most probable mechanisms for methane oxidation in triplet systems is the ER mechanism going through a radical process. Our findings reveal that the most stable spin state in catalyzing methane-to-methanol oxidation on Si-G and SiN_4-G is triplet and singlet, respectively, thanks to their lowest (more negative) energies. Furthermore, catalyzing methane to methanol on SiN_4-G with singlet multiplicity requires very high activation energies. Therefore, we estimate that Si-G with the preferred spin multiplicity of triplet is both kinetically and thermodynamically preferred over Ni-G and SiN_4-G. It might be a highly active catalyst for methane-to-methanol oxidation thanks to the corresponding lower energy barriers and higher energetic stability of the obtained configurations. In addition, the formation of the second methanol on both Si-G and SiN_4-G is considered to be the rate-limiting step. To the best of our knowledge, this is the first report on the direct conversion of methane-to-methanol over these surfaces and our findings may open a new way to design such graphene-based single atom catalysts.

3.7 Appendix

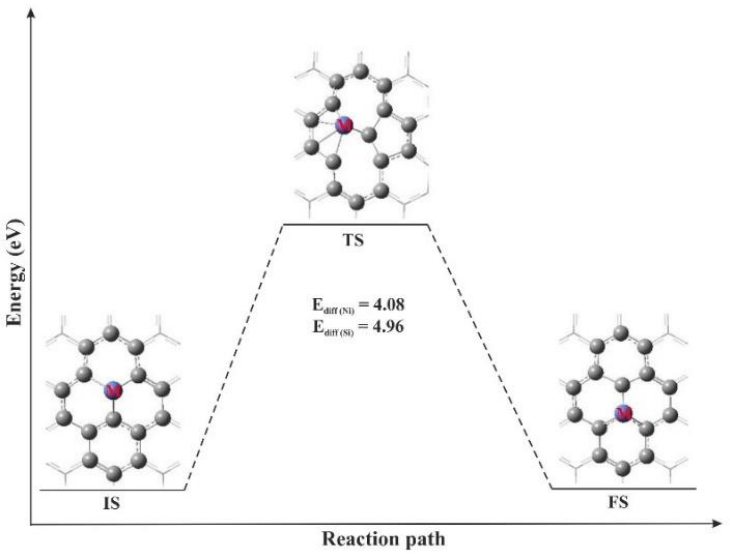

Figure A 3-1. Geometries of the IS, TS, and FS for moving a single Ni or Si atom from the single vacancy site to the nearby hollow site of graphene flake. All the energies are in eV.

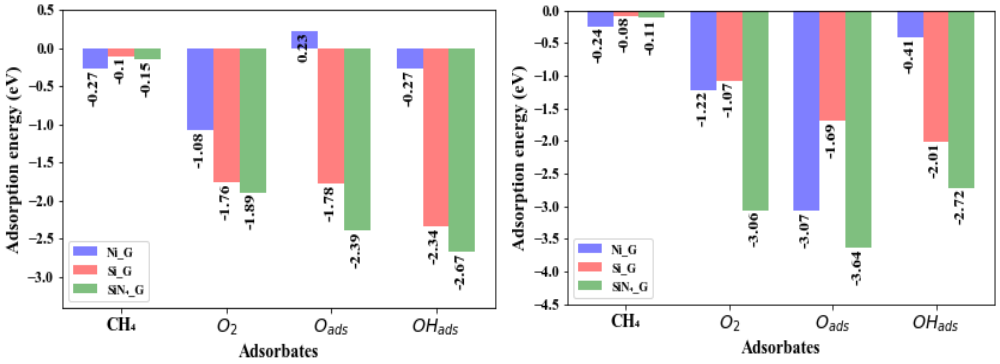

Figure A 3-2. Adsorption energies of gas molecules on triplet (left) and singlet (right) Ni-G, Si-G, and SiN_4-G

Possible reaction mechanisms for methane oxidation over Ni-G, Si-G and SiN_4-G

Singlet spin state

We start from the co-adsorbed configuration of O_2 and methane on Ni-G with the co-adsorption energy of E_{ads} = -1.38 eV, namely IS-1 (see Figure A3-3). The methane molecule adsorbs so weakly on the surface, E_{ads} = -0.17 eV, that is a direct interaction between O_2 and methane as occurs in TS-1, methane reacts with the first O_{ads} (denoted O_{Ni}) and forms the first methanol in FS-1. It is reported in Table A3-1 that the activation energy for this reaction is E_{act} = 0.91 eV and the adsorption energy of methanol is E_{ads} = -0.86 eV, with a large bond length of Ni-O_{Ni} = 2.09 Å. So, it is expected that the

methanol molecule desorbs from the surface and the remaining atomic oxygen (denoted O_C^*) is ready to react with a second methane molecule in the next step. The formation of the first methanol is found to be exothermic with a high negative value of $\Delta G_{298.15}$= -3.54 eV, indicating that the reaction is spontaneous at ambient conditions (see Table A3-1).

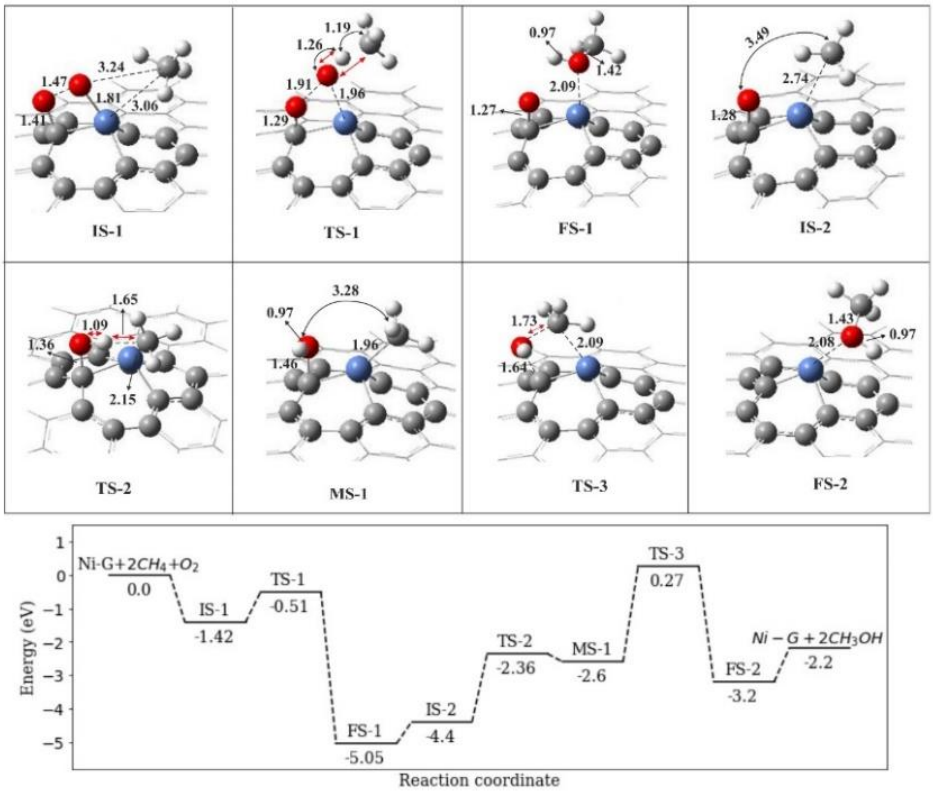

Figure A 3-3.The optimized stationary structures along with the corresponding energy profile of methane conversion to methanol on Ni-G with the singlet spin state. All bond distances and energy values are in Å and eV, respectively

In the next step, a second methane molecule is introduced to the system (E_{ads} = -0.23 eV), namely IS-2. One can see from Figure A3-3 that the second methane molecule is located at a distance of 3.49 Å from the O_C^*. According to Figure A3-3, since the O_C^* is strongly adsorbed on Ni-G (E_{ads} = -3.07 eV), a high energy barrier is needed to break the C-O_C bond. Instead, it prefers to abstract the activated H^* atom from the second methane molecule (E_{act} = 2.05 eV) and forms the MS-1 in which both -OH and -CH_3 are adsorbed on carbon and Ni atoms of the Ni-G, respectively. According to Table A3-1, the formation of these two species is endothermic with $\Delta H_{298.15}$= 1.81 eV and endergonic. In the last reaction, the -*OH molecule adsorbs so strong on the C atom that high barrier energy of E_{act} = 2.87 eV is required to cleave the C-O_C bond in order to form the second methanol in FS-2. Then, upon desorption of the second methanol with

an adsorption energy E_{ads}= -1.01 eV, another oxidation cycle can start. Generally, the reaction pathway MS-1 → FS-2 can be considered as the rate-determining step of the methanol oxidation over Ni-G in which the activation energy is so high that it inhibits the reaction through this pathway. However, the calculated thermodynamic values show that the reaction is exothermic and exergonic.

In Si-G, activation of methane starts with the co-adsorption of methane and O_2 (E_{ads} = -1.35 eV) in a position that one hydrogen atom of methane pointing toward the adsorbed oxygen atom at a distance of O-H = 2.41 Å (IS-3, Figure A3-4). The direct interaction between the weakly adsorbed methane (E_{ads} = -0.22 eV) and O_2 leads to the formation of the first methanol molecule with the activation energy of E_{act} = 1.89 eV (see Table A3-1). The formed methanol is adsorbed weakly on the Si-G surface (E_{ads} = -0.70 eV), and it can thus rather easily desorb from Si-G than Ni-G. According to Table A3-1, the negative thermodynamic values of the reaction IS-3→ FS-3 indicate that it is an exothermic and exergonic reaction.

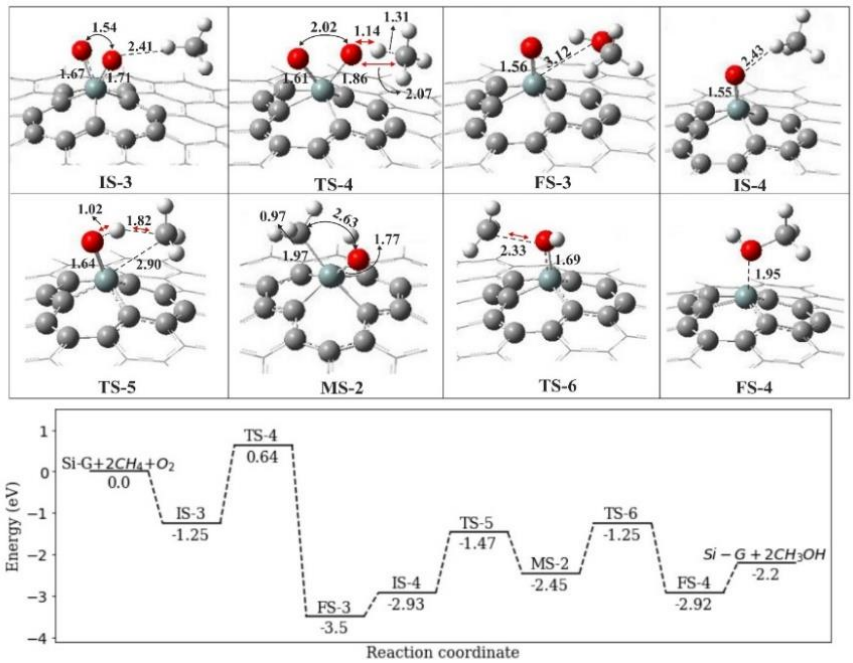

Figure A 3-4. The optimized stationary structures along with the corresponding energy profile of methane conversion to methanol on Si-G with the singlet spin state. All bond distances and energy values are in Å and eV, respectively.

In IS-4, the second methane molecule (E_{ads} = -0.18 eV) is introduced to the system positioned at a distance of O-H = 2.43 Å (see Figure A3-4). Then, the atomic oxygen abstracts one H atom from the methane molecule and forms -OH and -CH_3 moieties adsorbed on the active Si site of Si-G ($^*CH_3$-Si-*OH) (see Figure A3-4, MS-2). The methane activation barrier is E_{act} =1.49 eV and the reaction is endergonic. Our results

are in good agreement with Mayernick et al. [329, 330]. However, after cleavage of the C-H bond in methane, the formed -*OH and -*CH_3 species will recombine and produce the second methanol with an activation energy of E_{act} = 1.20 eV. Finally, the adsorbed methanol on Si-G can easily desorb from the surface with adsorption energy of E_{ads} = -0.73 eV. The formation of the second methanol is exothermic, $\Delta H_{298.15}$= -0.47 eV, and spontaneous at room temperature, $\Delta G_{298.15}$= -0.48 eV (see Table A3-1). According to the higher activation energy of the first reaction, IS-3 → FS-3, we estimate that the formation of first methanol on Si-G can be the rate-limiting step.

Methane oxidation and pathways on SiN_4-G are similar to those on Ni-G, Si-G but with higher activation barriers. Table A3-1 shows that the first and second methanol with adsorption energies of -0.86 eV and -0.82 eV are formed by overcoming a high energy barrier of about 2.65 and 2.40 eV, respectively. These high activation energies can be attributed to the high adsorption energy of the O_2 molecule over the highly positive Si atom and considerable charge transfer from the SiN_4-G to O_2 as discussed in section 3.4.1.3. Moreover, activation of the second methane on the SiN_4-G in IS-6 (E_{ads} = -0.21 eV) occurs by passing via a high energy barrier. In MS-3, the -*OH moiety adsorbs so strong on SiN_4-G (E_{ads} = -2.72 eV) that the cleavage of Si-O bond and consequently, the formation of C-O bond requires a very high energy barrier and therefore making the whole reaction IS-6 → FS-6 endothermic and endergonic (see Figure A3-5 and Table A3-1). This result is close to the results for MnN_4-G by Lu et al. [331].

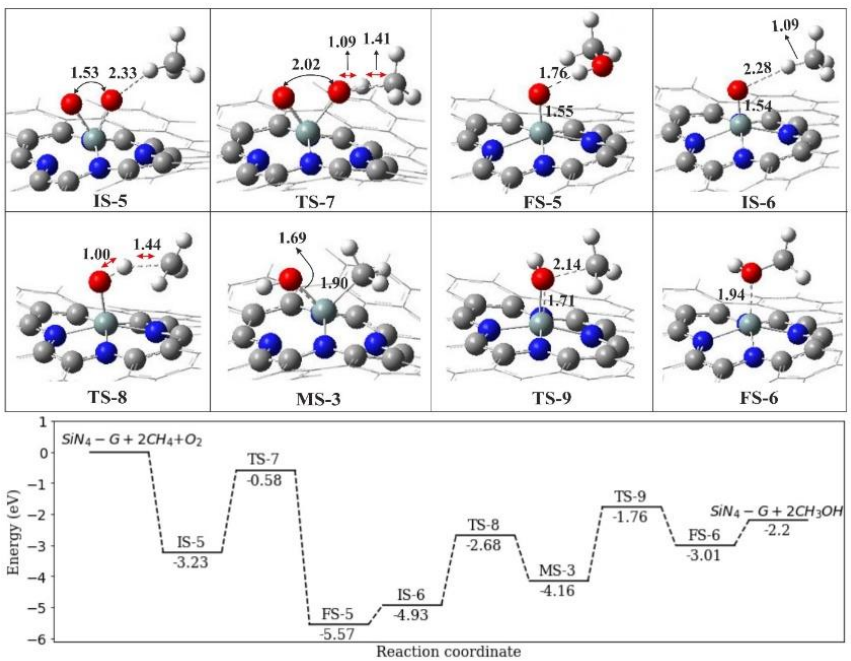

Figure A 3-5. The optimized stationary structures along with the corresponding energy profile of methane conversion to methanol on SiN_4-G with the singlet spin state. All bond distances and energy values are in Å and eV, respectively

Table A3-1. The calculated activation energy (E_{act}), change of enthalpy ($\Delta H_{298.15}$), and change of Gibbs free energy ($\Delta G_{298.15}$) for methane conversion to methanol on the singlet Ni-G, Si-G and SiN_4-G

Reaction path	E_{act} (eV)	$\Delta H_{298.15}$ (eV)	$\Delta G_{298.15}$ (eV)
Ni-G			
$O_{2(g)}$ + Ni* + C* → *O-Si+*O-C	0.00	-1.26	-0.72
IS-1 → FS-1	0.91	-3.64	-3.54
IS-2 → MS-1	2.05	1.81	1.97
MS-1 → FS-2	2.87	-0.61	-0.67
Si-G			
$O_{2(g)}$ + Si* → *O-Si-O*	0.00	-1.09	-0.61
IS-3 → FS-3	1.89	-2.25	-2.13
IS-4 → MS-2	1.49	0.48	0.61
MS-2 → FS-4	1.20	-0.47	-0.48
SiN_4-G			
$O_{2(g)}$ + Si* → *O-Si-O*	0.00	-3.10	-2.58
IS-5 → FS-5	2.65	-2.34	-2.24
IS-6 → MS-3	2.25	0.77	0.89
MS-3 → FS-6	2.40	1.15	1.10

We also studied the effect of substrate size on the adsorption behavior of gas species on Si-G. A larger graphene flake with 95 carbon atoms is considered as pure graphene flake used for the formation of Ni-G, Si-G, and SiN_4-G. The adsorption energy of the dopants into the graphene flake along with the adsorption energies of all gas species on Si-G are listed in Table A3-2. We found that the size of graphene flake has only a small effect on the adsorption energies of gas species on the studied substrates.

Table A3-2. The calculated adsorption energy (E_{ads}) of doped graphene flake and adsorbed gas reactants on Si-G in singlet and triplet systems. All the values are in eV

Complex	E_{ads}(eV)	Complex	$E_{ads\text{-}Singlet}$(eV)	$E_{ads\text{-}Triplet}$(eV)
larger graphene flake		SiG-O_2	-1.12	-2.01
Ni-G	-4.91	SiG-CH_4	-0.13	-0.11
Si-G	-9.85	SiG-O	-1.70	-1.74
SiN_4-G	-7.24	SiG-OH	-1.96	-2.02

Table A3-3. The calculated thermodynamic properties of methane-to-methanol conversion reaction in the gas phase $2CH_{4\,(g)} + O_{2\,(g)} \rightarrow 2CH_3OH_{\,(g)}$ using different functional and basis set. All values are in eV

Functional/Basis set	ΔH	ΔG
M062x/6-31G*	-2.20	-1.87
M062x/6-311G**	-2.51	-2.19
B3LYP/6-31G*	-1.79	-1.47
B3LYP/6-311+G*	-2.03	-1.72
B3LYP/6-311++G**	-2.31	-2.00
B3LYP/AUG-cc-pVQZ	-2.31	-2.01
WB97XD/6-311++G**	-2.44	-2.13
CBS-QB3/6-31G*	-2.59	-2.30
CBS-QB3/6-311G**	-2.66	-2.35

Chapter 4

Comparative DFT study on CO oxidation reaction over Si-doped BC_2N nanoflake and nanotube

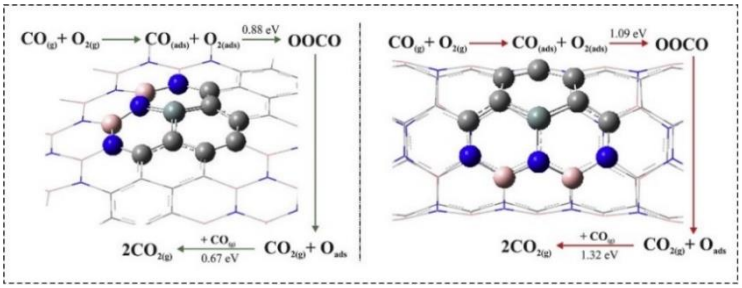

In this study, we performed DFT calculations to investigate different reaction mechanisms of CO oxidation catalyzed by Si atom embedded defective BC_2N nanostructure as well as to investigate the structural and electronic properties. The structures of all the complexes are optimized and characterized by frequency calculations at the M062X/6-31G* computational level. Also, the electronic structures and thermodynamic parameters of adsorbed CO and O_2 molecules over Si-doped BC_2N nanoflake (Si-BC_2NNS) and nanotube (Si-BC_2NNT) are examined in detail. Moreover, to investigate the curvature effect on the CO oxidation reaction, all the adsorption and CO oxidation reactions on a finite-sized armchair (6, 6) Si-BC_2NNT are also studied. Our results indicate that there can be two possible pathways for the CO oxidation with O_2 molecule: $O_{2(g)} + CO_{(g)} \rightarrow O_{2(ads)} + CO_{(ads)} \rightarrow CO_{2(g)} + O_{(ads)}$ and $O_{(ads)} + CO_{(g)} \rightarrow CO_{2(g)}$. The first reaction proceeds via the LH mechanism while the second goes through the ER mechanism. On the other hand, by increasing the tube diameter, the energy barrier increases due to the strong adsorption energy of the O_2 molecule, which is related to its dissociation over the tube surface. Our calculations indicate that the two steps energy barrier of the oxidation reaction over Si-BC_2NNS is less than that over the Si-BC_2NNT. Hence, Si-BC_2NNS may serve as an efficient and highly activated substrate to CO oxidation rather than (4, 4) Si-BC_2NNT.

Publication: Parisa Nematollahi and Erik C. Neyts. A comparative DFT study on CO oxidation reaction over Si-doped BC_2N nanosheet and nanotube, J. Applied Surface Science, 439 (2018): 934-945. https://doi.org/ 10.1016/j.apsusc.2017.12.254

In this chapter, the complete introduction is already contained in Chapter 1. Therefore, only the specifics are mentioned here. We employed DFT calculations to study oxidation of CO on a Si-BC_2N nanoflake (SiBC_2NNF) and Si-BC_2NNT. In addition, the effect of tube diameter on the oxidation of CO is also investigated in detail. Both ER and LH mechanisms are considered. To the best of our knowledge, there are no previous reports on CO oxidation over Si-BC_2NNF and Si-BC_2NNT. With our simulations, we attempt to understand and answer the following questions: Can Si doping enhance the catalytic properties of BC_2NNF and BC_2NNT? Can we consider the Si-BC_2NNF and Si-BC_2NNT as favourable catalysts for CO oxidation reaction? Does the tube diameter affect the oxidation reaction?

4.1 Computational methods

All structure optimizations and reaction pathway calculations are based on DFT using the Gaussian 16 package. The details of these calculations are mentioned in Chapter 3, except for the charge calculation method. In this chapter, the Mulliken method is used to measure the charge transfer between two atoms. A finite-size monolayer BC_2NNF was considered, consisting of 22 carbon, 22 boron, and 22 nitrogen atoms. In Si-BC_2NNF, one Si atom substitutes a carbon atom of BC_2NNF in four different sites. In addition, a finite-size armchair (4,4) BC_2NNT with 34 carbon, 18 boron, and 18 nitrogen atoms and a diameter of 5.48 Å is used as a pure nanotube. Analogous to Si-BC_2NNF, four different configurations obtained by replacing one C atom with one Si atom of the pure (4,4) BC_2NNT and then, Si-doped (4,4) BC_2NNT is formed. To investigate the curvature and diameter effect on the CO oxidation, pure armchair (6,6) BC_2NNT containing 54 carbon, 27 boron, and 27 nitrogen atoms (with a diameter of about 8.23 Å) is also considered as a pristine nanotube. In order to avoid the effect of unsaturated boundaries, hydrogen atoms were added to the edge and to both ends of the pure and Si-doped BC_2N nanoflake and nanotubes, respectively. The triplet spin state of the O_2 molecule is considered as its ground state for its adsorption over all Si-BC_2N nanostructures.

4.2 Results and discussions

4.2.1 Geometries of pristine and Si-doped BC_2NNF

Before studying the adsorption of CO and O_2 gas molecules over Si-BC_2NNF, the geometric structures and density of states (DOS) plots of optimized pristine BC_2NNF and Si-BC_2NNF are investigated in detail (see Figure 4-1). Additionally, to better understand the binding nature of the Si atom on the BC_2NNF, the Mulliken charge density was also determined. The parameters characterizing these structures such as net charge transfer (q_{CT}), adsorption energy (E_{ads}), and energy gap (E_g) are listed in Table 4-1.

As it is clear from Figure 4-1, in pristine BC_2NNF four types of chemical bonds (B-N, N–C, C–C and B–C) with different bond lengths (1.44, 1.40, 1.42 and 1.55 Å) can be identified. There are four different carbon sites in pure BC_2NNF, which can replace with one Si atom and make complexes A to D. In order to reach this aim, first of all, four different single carbon vacancy (SV) sites were optimized separately, and then, the adsorption of Si atom on these SV-BC_2NNF was studied in detail (Table 4-1). It should be noted that after doping, the Si atom protrudes somewhat out of the surface, which is due to the larger size of the Si atom compared to a C atom. Moreover, the structural optimization of Si-BC_2NNF shows that the Si dopant forms three strong covalent bonds with its nearest C and B atoms. In all these complexes, the average formed Si–C/Si–B/Si–N bond lengths increase in comparison with those of C–C/C–B/C–N in pristine BC_2NNF (see Figure 4-1).

In complex A, the Si atom doped in a C-vacancy site and binds with two C and one B atom. After the relaxation of the complex, the Si–C and Si–B bond lengths are 1.81 Å and 1.93 Å, respectively, which are significantly longer than the corresponding C–C and C–B bonds in pure BC_2NNF (1.42 Å and 1.55 Å, respectively). The adsorption energy of complex A is about -9.00 eV and a small net charge of +0.06 e is transferred from Si atom to the adjacent C and B atoms of the surface (see Table 4-1). Complex B is formed when the Si atom embedded in a SV site with one N and two other C atoms. In this case, the formed Si–N and Si–C bond length are also elongated, viz. to 1.66 Å and 1.70 Å, respectively. Corresponding to Table 4-1 results, this complex has the E_{ads} = -10.83 eV and a net charge transfer of 0.51 e from Si atom to C and N atoms of the surface. There is another active C-vacancy site in which the Si-atom binds with three C atoms, two of them connected with two B atoms while the other binds with a C atom (complex C). Here, the average Si–C bond length after relaxation is 1.72 Å, which is longer than that of pristine BC_2NNF (1.42 Å). The adsorption energy of the complex C is calculated to be -10.56 eV. Analogous with complex C, in complex D the dopant binds to two carbon atoms (which in turn bind with two N atoms) and with a carbon atom which is connected to a C atom, with E_{ads} = -9.95 eV. This value is smaller than that in complex C (see Table 4-1).

As discussed above, it is found that graphite is a semi-metallic material while h-BN is an insulator with a bandgap $\geq$ 5.8 eV [120, 332]. So, it can be anticipated that new pristine BC_2N nanosheet (BC_2NNS) has a honeycomb structure with an energy bandgap smaller than that of h-BN, thus constituting a new semiconducting material. In order to further understand the electronic properties of pure and Si-BC_2NNF, the TDOS plots of these configurations are also investigated and compared with each other. Because the electronic properties mainly depend on the electronic states around the Fermi level, we here focus on these states. As shown in Table 4-1, the bandgap of pristine BC_2NNF is about 3.58 eV while in Si-doped configurations it is found to increase and decrease in complexes C and A to 3.63 eV and 3.10 eV, respectively. This indicates that the

electronic properties of BC_2NNF are changed by Si-doping. According to all obtained results, complex B has the highest adsorption energy and also net charge transfer (and can thus be considered to be the most stable structure), such that we have chosen complex B as the basic structure in catalytic CO oxidation by O_2, rather than complex A which has a smaller bandgap and adsorption energy.

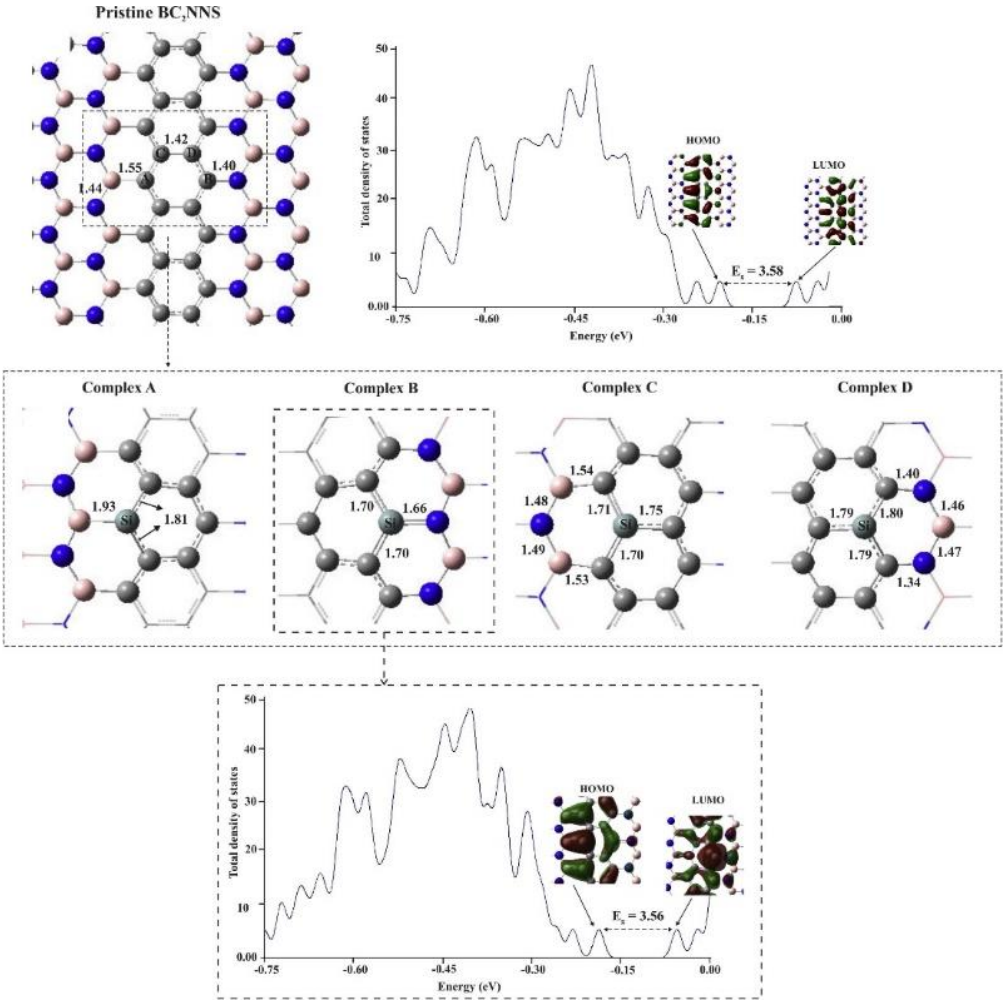

Figure 4-1. Optimized structures of pure BC_2NNF and different possible Si embedded BC_2NNF configurations (complexes A to D), along with their corresponding total density of states (TDOS) plots. Color code for each optimized structure: Blue ball: N; light gray ball: C; dark gray ball: Si, pink ball: B. All bond distances and energy gaps (E_g) between HOMO and LUMO are in Å and eV, respectively.

Table 4-1. The calculated Mulliken net charge transfer (q_{CT}) (+ and – signs refer to the electron donation and acceptation), adsorption energy (E_{ads}), and LUMO-HOMO energy gap (E_g) of pristine BC_2NNF and (4,4) BC_2NNT along with the Si-doped form of these nanostructures.

Reaction	E_{ads} (eV)	q_{CT} (e)	E_g (eV)
Pristine BC_2NNF	-	-	3.58
A	-9.00	+0.06	3.10
B	-10.83	+0.51	3.56
C	-10.56	+0.34	3.63
D	-9.95	+0.28	3.58
Pristine (4,4) BC_2NNT	-	-	3.93
Si-doped (4,4) BC_2NNT	-8.10	+0.54	3.90

4.2.2 Geometries of the pristine and Si-doped (4, 4) BC_2NNT

In order to better understand the effects of different BC_2N nanostructures on CO oxidation, a finite-sized armchair (4,4) BC_2NNT is used as a basic model for our calculations. The optimized structure of pristine (4,4) BC_2NNT and (4,4) Si-BC_2NNT along with their corresponding bond lengths are shown in Figure 4-2. Also, all the related geometric values are presented in Table 4-1. One can see from Figure 4-2 that the C–C and C–N bond lengths in pure (4,4) BC_2NNT is 1.42 and 1.39 Å, respectively, which is in good agreement with previous reports [333]. Similar to Si-BC_2NNF, in (4,4) Si-BC_2NNT, four possible doped configurations can be obtained, from which the one in which the Si atom directly binds with one N atom and two C atoms is chosen as the most stable structure (Figure 4-2). In this configuration, the Si-C and Si-N bond lengths are 1.72 and 1.69 Å, respectively, showing a considerable increase due to the larger size of Si compared to that of a C atom. Consequently, to accommodate these longer bond lengths, the Si-atom protrudes somewhat out of the surface. Moreover, according to Table 4-1, the adsorption energy of (4,4) Si-BC_2NNT is E_{ads}= -8.10 eV and a net charge of about +0.54 e is transferred from Si atom to the adjacent N and C atoms, which is slightly more than the charge transfer in complex B.

Also shown in Figure 4-2 is the comparison between the computed TDOS of (4,4) BC_2NNT and (4,4) Si-BC_2NNT. The TDOS of the pristine nanotube shows that the bandgap between HOMO and the LUMO is 3.93 eV while in the doped nanotube this value is slightly lowered to 3.90 eV. This shows that Si-doping has affected the electronic properties of pristine BC_2NNT by decreasing the energy gap.

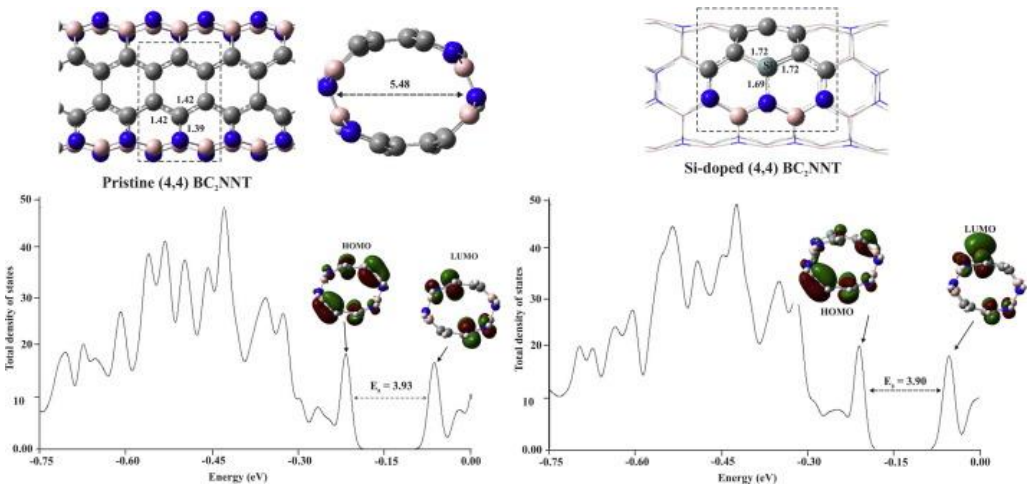

Figure 4-2. The optimized structures of pure (4,4) BC_2NNT and Si embedded (4,4) BC_2NNT, along with their total density of states (TDOS) plots. All bond distances and energy gaps (E_g) are in Å and eV, respectively.

4.2.3 Adsorption of O_2 and CO molecules over Si-BC_2NNF and (4,4) Si-BC_2NNT

Before studying the CO oxidation reaction, we extensively investigated the adsorption of CO and O_2 molecules separately over Si-BC_2NNF and Si-BC_2NNT, as adsorption of the reactants is the step prior to the actual surface reaction.

For O_2 and CO adsorption on Si-BC_2NNF various adsorbed configurations are obtained. Then, the most energetically stable configuration is chosen as the final adsorbed structure, which is depicted in Figure 4-3, along with their corresponding electron density difference (EDD) maps. Also, the related E_{ads} with other geometric quantities along with thermodynamic properties are listed in Table 4-2.

First, the O_2 and CO molecules are oriented parallel and perpendicular to the Si-BC_2NNF individually and after relaxation, various adsorbed configurations are obtained. Amongst the one in which the O_2 molecule is in a parallel position to the surface on top of the Si atom is considered as the energetically most favourable structure for the adsorption on the Si-BC_2NNF (complex E) due to its lower energy and larger adsorption energy than other complexes.

In complex E, the O_2 molecule adsorbs on Si atom of Si-BC_2NNF while it forms a V shape with two individual Si–O1 and Si–O2 bonds with binding distances of 1.73 Å and 1.66 Å, respectively (see Figure 4-3). The E_{ads} of complex E is about -1.43 eV which is in close agreement with that of Si-doped graphene (-1.58 eV) [63] and lower than that of Si-BNNS in Lin et al. [334] study. As shown in Table 4-2, a high charge of +0.84 e is transferred from Si-BC_2NNF to the $2\pi^*$ orbitals of the O_2 molecule. The electron configuration of O_2 is $(\sigma_{2s})^2\,(\sigma^*_{2s})^2\,(\sigma_{2pz})^2\,(\pi_{2px})^2\,(\pi_{2py})^2\,(\pi_{2px}{}^*)^1(\pi_{2py}{}^*)^1$, and thus the half-

filled anti-bonding orbital of O_2 is occupied with the transferred electrons. This causes the elongation and also activation of O1–O2 bond from 1.20 Å in the free O_2 molecule to 1.54 Å in the adsorbed form. This sizable charge transfer is also clear from the EDD map of complex E as depicted in Figure 4-3. The red colors show the high charge accumulation around the two Si–O1 and Si–O2 bond. It can be understood from the negative values of thermodynamic parameters for O_2 adsorption listed in Table 4-2 that the formation of complex E is an exothermic process ($\Delta H_{298.15}$ = -1.50 eV) and proceeds spontaneously at room temperature ($\Delta G_{298.15}$ = -1.02 eV).

Analogous with the O_2 molecule, the most favourable configuration for CO adsorption on Si-BC_2NNF (complex F) is the one in which CO adsorbs vertically above the Si atom with a Si-C distance of 2.28 Å (see Figure 4-3). The CO molecule in this complex with the adsorption energy E_{ads} = -0.23 eV is physically adsorbed on the Si-BC_2NNF. As is apparent from the Mulliken charge analysis listed in Table 4-2, only a small charge is transferred, 0.14 e, from the CO molecule to the Si-BC_2NNF, which further confirms the weak interaction between CO and the surface. In addition, it is clear from the EDD plot of complex F that there is not a visible binding between Si and C atom (Figure 4-3). According to Table 4-2, although the production of complex F is exothermic ($\Delta H_{298.15}$ = -0.21 eV) it does not occur spontaneously at room temperature ($\Delta G_{298.15}$ = 0.16 eV).

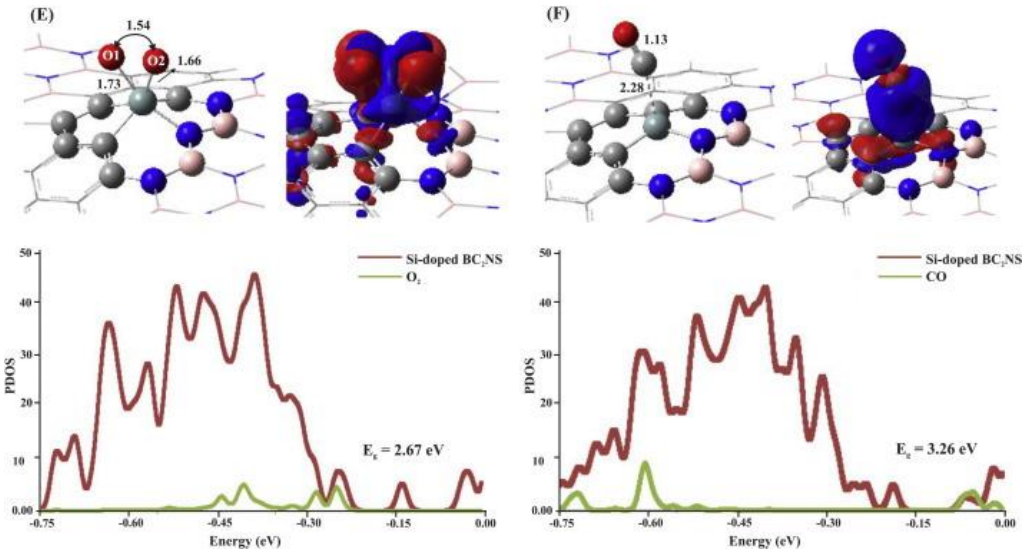

Figure 4-3. The optimized structures of adsorbed O_2 and CO molecules over Si-BC_2NNF (complexes E and F) along with their corresponding electron density difference (EDD) maps and partial density of states (PDOS) plots. In the EDD maps, the charge depletion and accumulation sites are displayed in blue and red color, respectively. All bond distances and energy gaps (E_g) are in Å and eV, respectively.

Finally, it can be understood from the projected density of states (PDOS) of complexes E and F that upon adsorption of the O_2 molecule, the calculated LUMO-

HOMO energy gaps reduce in comparison with that of complex B (E_g = 3.56 eV). This reduction is more visible in complex E (E_g = 2.67 eV) than that in complex F (E_g = 3.26 eV). This can be related to the slight shift of both conduction and valence levels to higher energies, and therefore, the E_g of complex E decreases considerably. Thus, we conclude that the electronic properties of Si-BC_2NNF are more sensitive to O_2 than to CO. Generally, these results illustrate that when there is a mixture of O_2 and CO gas molecules, the O_2 molecule will adsorb first on the Si-BC_2NNF surface. Therefore, Si-BC_2NNF can be used as a potential sensor for adsorption of O_2 molecules.

We also investigated the molecular adsorption of O_2 and CO on a tubular armchair (4,4) Si-BC_2NNT. Similar to Si-BC_2NNF there are two adsorption configurations depending on the O_2 orientation over the (4,4) Si-BC_2NNT. The corresponding O_2 and CO adsorption structures are shown in Table A4-1, along with their adsorption energies (complexes G, G1, and H). In addition, the adsorbed configurations with their exact geometric binding distances and corresponding EDD map are depicted in Figure 4-4. The geometric and thermodynamic parameters of these structures are listed in Table 4-2.

Table 4-2. The calculated bond length (R), adsorption energy (E_{ads}), Mulliken net charge transfer (q_{CT}) (+ and – signs refer to the electron donation and acceptation), energy gap (E_g), change of Gibbs free energy ($\Delta G_{298.15}$) and change of enthalpy ($\Delta H_{298.15}$) of O_2 and CO adsorption over Si-BC_2NNF and (4,4) Si-BC_2NNT[a].

Complex	$R_{(Si\text{-}O1/Si\text{-}O2/Si\text{-}C)}$ (Å)	E_{ads} (eV)	q_{CT} (e)	E_g (eV)	$\Delta G_{298.15}$ (eV)	$\Delta H_{298.15}$ (eV)
Si-BC_2NNF						
E	1.73/1.66	-1.43 (-1.33)	-0.84	2.67	-1.02	-1.50
F	2.28	-0.23 (-0.13)	+0.14	3.26	0.16	-0.21
(4,4)SiBC_2NNT						
G	1.69/1.67	-0.62 (-0.44)	-0.81	1.81	-0.17	-0.64
H	2.11	-0.39 (-0.31)	+0.18	3.77	0.02	-0.39

[a] The E_{ads} values within the parenthesis is the calculated adsorption energy performed by considering basis-set superposition error (BSSE).

Among two different adsorption configurations of O_2 molecule over the tube surface shown in Table A4-1, complex G, with adsorption energy E_{ads} = -0.62 eV is chosen as the most favourable structure on the tube surface. In this complex, the O_2 molecule is positioned horizontally above the surface forming a V shape with two Si–O1 and Si-O2 bonds with average bond lengths of 1.68 Å. The adsorption energy of this complex is about -0.81 eV less favourable than that of complex E configuration. In this case, a charge of about +0.81 e is transferred from the Si atom to the $2\pi^*$ orbitals of the O_2 molecule, which leads to the elongation of the O1–O2 bond (1.54 Å). This also corresponds to the EDD iso-surface map (as displayed in Figure 4-4), where the red colors around the Si–O bonds confirm the chemical bond. Moreover, with respect to the data of Table 4-2, it can be concluded that the adsorption of the O_2 molecule on (4,4) Si-BC_2NNT is exothermic (ΔH_{298} = -0.64 eV) and occurs spontaneously at room

temperature (ΔG_{298} = -0.17 eV).

For CO adsorption (complex H), the CO molecule physisorbs vertically on the (4,4) Si-BC_2NNT above the Si atom of the tube surface, with a bond length Si–C = 2.11 Å. The corresponding adsorption energy of this complex is calculated to be about E_{ads} = -0.39 eV, which is more than that of complex F. The low adsorption energy and also the long bond length between Si and C atom (2.11 Å) demonstrate a rather weak physical interaction between the CO molecule and the tube surface which is also obvious from its EDD map (Figure 4-4). It is clear that there is no significant binding in the blue (charge depleted) regions. Corresponding to this weak interaction, a small charge of +0.18 e is transferred from the CO molecule to the Si atom of the BC_2NNT. The reaction of CO adsorption over (4,4) Si-BC_2NNT is exothermic ($\Delta H_{298.15}$ = -0.39 eV) but the positive value of $\Delta G_{298.15}$ indicates that it is not favourable thermodynamically (Table 4-2).

The PDOS of the adsorbed gas molecules over (4,4) Si-BC_2NNT and the energy gap values confirm that by adsorption of individual O_2 and CO molecule over the tube surface, the LUMO-HOMO energy gap reduces from 3.90 eV in pristine (4,4) Si-BC_2NNT to 1.81 eV in complex G and 3.77 eV in complex H. It can be expected from adsorption energies of complexes G and H that the latter has a negligible change in its bandgap compared to that of pristine (4,4) Si-BC_2NNT and complex G. Therefore, from the results presented above we conclude that the electronic properties of pristine (4,4) Si-BC_2NNT are much more sensitive to O_2 adsorption in comparison to CO adsorption.

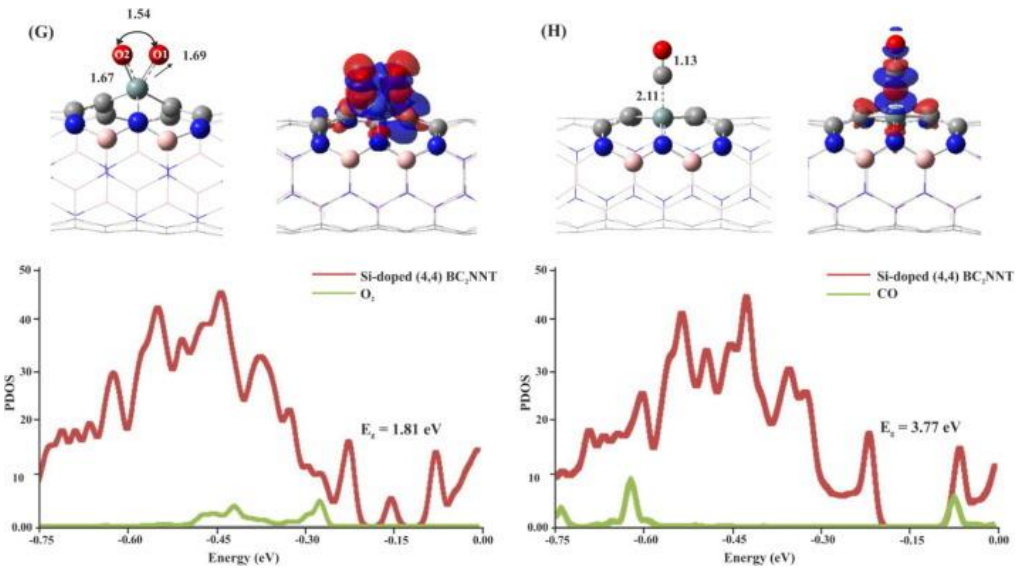

Figure 4-4. The optimized structures of adsorbed O_2 and CO molecules over (4,4) Si-doped BC_2NNT (complexes G and H) with their corresponding electron density difference (EDD) maps and partial density of states (PDOS) plots. In the EDD maps, the charge depletion and accumulation sites are displayed in blue and red colors, respectively. All bond distances and energy gap (E_g) are in Å and eV, respectively.

Along with these oxidation mechanisms, it is a priori not clear whether the adsorption of O_2 depends on the diameter size of the nanotube or not. To answer this question, we also carefully studied the curvature effect on the adsorption of O_2 molecule. For this purpose, a finite-sized armchair (6,6) BC_2NNT is chosen as the basic structure for our calculations. The geometries of the pure (6,6) BC_2NNT and (6,6) Si-BC_2NNT along with their relative TDOS plots are investigated in detail (see Figure A4-1). The Mulliken charge transfer and energy gap values of these nanotubes are also listed in Table A4-2. It should be noted that various adsorption configurations are checked for this nanotube but most of them lead to one similar adsorption configuration of the O_2 molecule over the (6,6) Si-BC_2NNT in which the O_2 molecule forms a four-membered ring (4MR) over Si and C atoms of the tube surface (Figure A4-2). In contrast to O_2, the adsorption of CO on the (6,6) Si-BC_2NNT is similar to those we had before. All geometric and thermodynamic properties of adsorbed gas molecules over (6,6) Si-BC_2NNT are listed in Table A4-3 from which the adsorption energy of complex I, E_{ads} = -1.98 eV, is higher than that of complexes E and G, which can be due to the dissociative adsorption of O_2 over the tube surface. Like other CO adsorption configurations, it physically adsorbs over (6,6) Si-BC_2NNT with low E_{ads} = -0.32 eV (see Table 4-3). In addition, as shown in the PDOS plot of complex I, the energy gap of this complex E_g = 3.77 eV which is somewhat smaller than the gap of (6,6) Si-BC_2NNT, E_g = 3.95 eV. This indicates that the adsorption of O_2 and CO molecule has less effect on electronic properties of (6,6) Si-BC_2NNT than that of Si-BC_2NNF and (4,4) Si-BC_2NNT.

4.2.4 CO oxidation over Si-BC_2NNF and (4,4) Si-BC_2NNT

Generally, CO oxidation occurs via either the ER or the LH mechanisms [335, 336]. The difference between these two mechanisms is that in the ER mechanism, the gas phase molecule (CO) directly reacts with the activated pre-adsorbed O_2 molecule over the surface while in the LH mechanism the co-adsorbed CO and O_2 react together to form the product. Generally, the ability of the gas molecule to adsorb on the active site of the surface determines the pathway on the catalyst. It is known that the reaction pathway is indeed directly determined by the catalyst. For instance, in a theoretical study performed by Lu et al. [337] the CO oxidation reaction on Cu- and Au- embedded graphene starts with LH mechanism while in another investigation by Xu et al. [205], it was proposed that different dopants on the graphene sheet can oxidize the CO molecule through different mechanisms and energy barriers. In our case, we studied both LH and ER mechanisms in detail and we found that the surface oxidation of CO first starts with the strong and weak adsorption of O_2 and CO gas molecules over the surface, respectively, eventually leading to the formation of two CO_2 gas molecules:

$$O_{2(gas)} + 2CO_{(gas)} \longrightarrow 2CO_{2(gas)} \quad (4\text{-}1)$$

After the adsorption of both species on the surface, the reaction mechanism proceeds

with the LH and followed by the ER mechanism as follows [338]:

$$O_{2(ads)} + CO_{(ads)} \longrightarrow O_{(ads)} + CO_{2(gas)} \quad (4\text{-}2)$$

$$O_{(ads)} + CO_{(gas)\ )} \longrightarrow CO_{2(gas)} \quad (4\text{-}3)$$

Since the adsorption energy of O_2 is higher than that of CO over Si-BC_2N nanostructures, it can be expected that the Si sites of Si-BC_2NNF and (4,4) Si-BC_2NNT are predominantly occupied with O_2 molecules rather than with CO. Note that in the first reaction step, a stable reaction path following the ER mechanism could not be established in the simulation and the LH mechanism is more favourable for the first CO oxidation reaction pathway on Si-BC_2NNF and (4,4) Si-BC_2NNT, followed by the ER mechanism in the second reaction step. The minimum energy pathway (MEP) along with the optimized structures for the initial state (IS), transition state (TS), and final state (FS) of CO oxidation are calculated and shown in Figure 4-5. In addition, the corresponding activation energies (E_{act}) and thermodynamic parameters of each reaction pathway are listed in Table 4-3.

The CO oxidation over Si-BC_2NNF starts with complex E due to the strong interaction of the O_2 molecule with the surface. In order to find the most favourable IS structure, all probable adsorption sites were checked carefully. As shown in Figure 4-5, we have chosen the most stable co-adsorbed O_2+CO configuration as IS-1 with higher (more negative) adsorption energy E_{ads} = -1.79 eV in comparison with the adsorption energy of the individual O_2 and CO species over Si-BC_2NNF. In IS-1, the CO molecule is positioned parallel to the surface at a distance of about 2.78 Å from the O1 atom. In TS-1 the CO molecule approaches the O1 atom in order to form the CO_2 molecule. In this structure, the C–O1 and O1–O2 distances reduce from 2.78 and 1.53 Å in IS-1 to 1.97 and 1.48 Å, respectively (see Figure 4-5). Subsequently, in FS-1, the first CO_2 molecule is formed by the cleavage of O1–O2 bond and it desorbs simply from the Si-BC_2NNF surface (E_{ads} = -0.29 eV). As it is clear from Table 4-3, the energy barrier of this exothermic reaction pathway (IS-1 → FS-1) is E_{act} = 0.88 eV. Also, the negative value of $\Delta G_{298.15}$ = -3.67 eV shows that the reaction is spontaneous at room temperature.

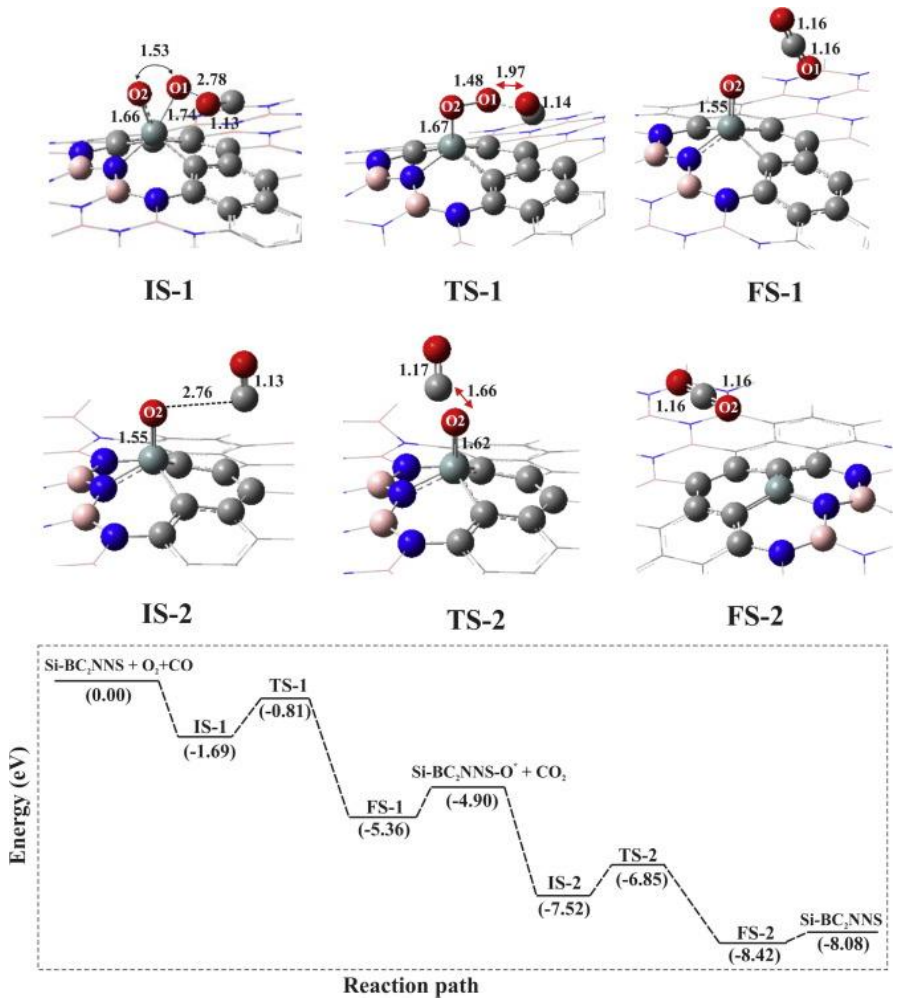

Figure 4-5. The energy profile of the minimum-energy pathway (MEP) and optimized stationary points for the CO oxidation reaction over Si-BC_2NNF. All bond distances are in Å.

Table 4-3. The calculated activation energy (E_{act}), reaction energy (ΔE), change of Gibbs free energy ($\Delta G_{298.15}$) and change of enthalpy ($\Delta H_{298.15}$) for different pathways of CO oxidation reaction over Si-BC_2NNF

Reaction	E_{ads} (eV)	ΔE (eV)	$\Delta G_{298.15}$ (eV)	$\Delta H_{298.15}$ (eV)
IS-1→ FS-1	0.88	-3.67	-3.67	-3.63
IS-2 → FS-2	0.67	-0.90	-0.90	-0.86

Upon desorption of CO_2, there is one oxygen atom (named O_2) left on the Si-BC_2NNF surface which is ready to react with another CO molecule. The most stable configuration (IS-2) is obtained when the CO molecule is positioned vertically at a distance of 2.76 Å from the adsorbed atomic oxygen on Si-BC_2NNF with a Si–O2 bond length of 1.55 Å (see Figure 4-5). The O_2 atom is pushed away from the Si atom upon

the approach of the CO molecule in TS-2, resulting in the formation of the second CO_2 molecule in FS-2. One can see from Figure 4-5 that in TS-2, the Si-O2 and C=O bond lengths are increased while the O2–C distance decreases from 2.76 to 1.66 Å. In FS-2, the physisorbed CO_2 molecule can desorb from the surface with E_{ads} = -0.01 eV. The Si-BC_2NNF is then ready to start a new CO oxidation cycle. The calculated E_{act} for IS-2 → FS-2 reaction pathway is 0.67 eV which is lower than that reported in Si-doped BNNS [334]. Also, the reaction is exothermic and spontaneous at room temperature (see Table 4-3).

On the other hand, the oxidation of CO over the (4,4) Si-BC_2NNT surface is also investigated in detail. Similar to Si-BC_2NNF, the oxidation reaction over (4,4) Si-BC_2NNT starts with the LH mechanism followed by the ER mechanism. The geometries of IS, TS, and FS along with their energy profile are presented in Figure 4-6. Also, Table 4-4 summarizes the calculated E_{act} and thermodynamic parameters of the corresponding reaction pathways. The oxidation reaction of CO over (4,4) Si-BC_2NNT starts with the co-adsorbed O_2+CO configuration as an IS-3 with E_{ads} = -0.88 eV which is higher than the adsorption energy of individual O_2 and CO over tube surface. In IS-3, the vertical CO molecule approaches the adsorbed O_2 molecule with C–O1 distance of 2.81 Å. In the transition state, named TS-3, the CO molecule approaches the O1 atom (C–O1 = 1.62 Å) to form the first CO_2 molecule. In this state, the Si-O1 and O1–O2 bond lengths are reduced from 1.67 and 1.54 Å to 1.65 and 1.50 Å, respectively. The reaction barrier is about 1.09 eV, which is higher than that on Si-BC_2NNF. Then, the first CO_2 molecule is physisorbed on the (4,4) Si-BC_2NNT surface in FS-3 and released from the tube surface (E_{ads} = -0.25 eV) while the O2 atom remains over the Si atom with a Si–O2 bond length of 1.55 Å. With respect to the calculated results listed in Table 4-4, the negative values of thermodynamic parameters indicate that this reaction pathway is exothermic and thermodynamically favourable.

In the next pathway, the second CO molecule is placed parallel to the surface and reacts with the atomic O_2 in order to form the second CO_2 molecule (Figure 4-6). In this configuration (IS-4), the C–O2 bond length is 2.98 Å and the bond length between Si and atom O2 is increased from 1.55 in FS-3 to 1.66 in IS-4. Also, it is noteworthy that the C–Si–O2 angle in IS-4 decreases from 109.79º in FS-3 to 52.13º. By the approach of the CO molecule to atom O2 (C–O2 = 1.71 Å), TS-4 forms and the CO_2 molecule produces in FS-4. In this state, the CO_2 molecule is at a distance of 2.95 Å from the Si atom and desorbs easily from the surface (E_{ads} = -0.01 eV). The pure (4,4) Si-BC_2NNT surface can then start another CO oxidation reaction. This reaction pathway has a high activation energy (E_{act} = 1.32 eV) which can be due to the breaking of the chemical bonds between Si and C atom of the surface with atom O2 in IS-4 (Figure 4-6). The IS4 → FS-4 reaction is exothermic and favourable at room temperature ($\Delta H_{298.15}$ = -0.99 eV and $\Delta G_{298.15}$ = -0.98 eV).

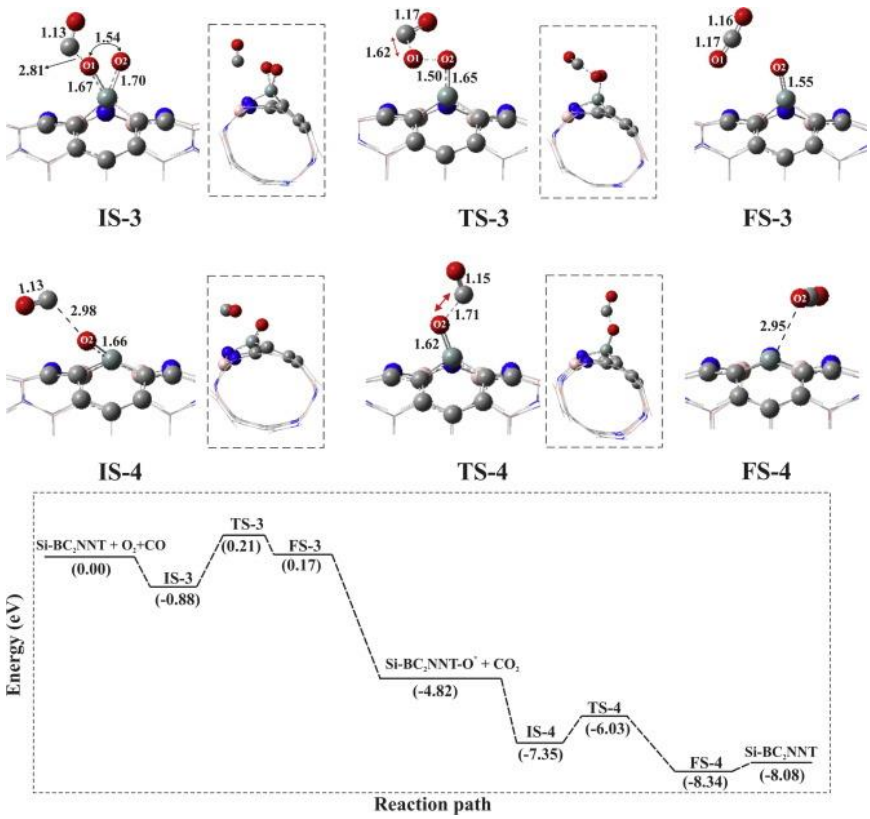

Figure 4-6. Schematic energy profile of the minimum-energy pathway (MEP) and optimized stationary points for the CO oxidation reaction over (4,4) Si-BC_2NNT (complex G). All bond distances are in Å.

Table 4-4. The calculated activation energy (E_{act}), reaction energy (ΔE), change of Gibbs free energy ($\Delta G_{298.15}$) and change of enthalpy ($\Delta H_{298.15}$) for different pathways of CO oxidation reaction over (4,4) Si-BC_2NNT

Reaction	E_{ads} (eV)	ΔE (eV)	$\Delta G_{298.15}$ (eV)	$\Delta H_{298.15}$ (eV)
IS-3→ FS-3	1.09	-3.66	-3.60	-3.66
IS-4 → FS-4	1.32	-0.99	-0.98	-0.99

Finally, also the oxidation of CO over the (6,6) Si-BC_2NNT is studied. Figure A4-3 shows the energy profile and geometric values of the CO oxidation reaction, the activation energy, and the various thermodynamic values, as listed in Table A4-4. It is clear from the obtained results that both reaction pathways (IS-5 → FS-5 and IS-6 → FS-6) are exothermic and spontaneous at ambient conditions. In this case, the larger diameter of the tube leads to higher energy barriers for CO oxidation (see Figure A4-3). This can be attributed to the dissociative adsorption configuration of O_2 over the tube surface (E_{ads} = -1.98 eV) which in contrast to (4,4) Si-BC_2NNT (E_{ads}= -0.81 eV) lead to the higher energy barriers in the CO oxidation reaction. So, the (4,4) Si-BC_2NNT properties are more close to the nanosheet rather than (6,6) Si-BC_2NNT.

4.3 Conclusion

In this work, the oxidation reaction of CO over Si-BC_2NNF and armchair (4,4) Si-BC_2NNT is systematically studied by means of DFT calculations. The structures of all complexes are optimized and characterized by frequency calculations at the M062X/6-31G* computational level. Also, the catalytic and electronic properties of the complexes such as E_{ads}, DOS plots, E_g, E_{act}, and EDD maps are carefully studied. Moreover, to investigate the curvature effect on the CO oxidation reaction, the adsorption of O_2 and CO on a finite-sized armchair (6,6) Si-BC_2NNT is also studied. The two possible reaction pathways proposed for the oxidation of CO with O_2 molecule are as follows: $O_{2(ads)} + CO_{(gas)} \rightarrow CO_{2(gas)} + O_{(ads)}$ and $O_{(ads)} + CO_{(gas)} \rightarrow CO_{2(gas)}$. It is found that the first step goes through the LH pathway, while the second proceeds through the ER mechanism. Our results indicate that the overall energy barrier for the two-step oxidation process over Si-BC_2NNF is less than that over Si-BC_2NNT. Therefore, we suggest that Si-BC_2NNF may be considered as a possible candidate for low-temperature CO oxidation reaction by O_2 with low cost and better activity rather than Si-BC_2NNT. Further, we found that by increasing the tube diameter, the energy barrier increases due to the strong adsorption energy of the O_2 molecule which is related to its dissociation over the tube surface. Thus, we can claim that Si-BC_2NNF could serve as a more efficient substrate for CO oxidation than (4,4) Si-BC_2NNT.

4.4 Appendix

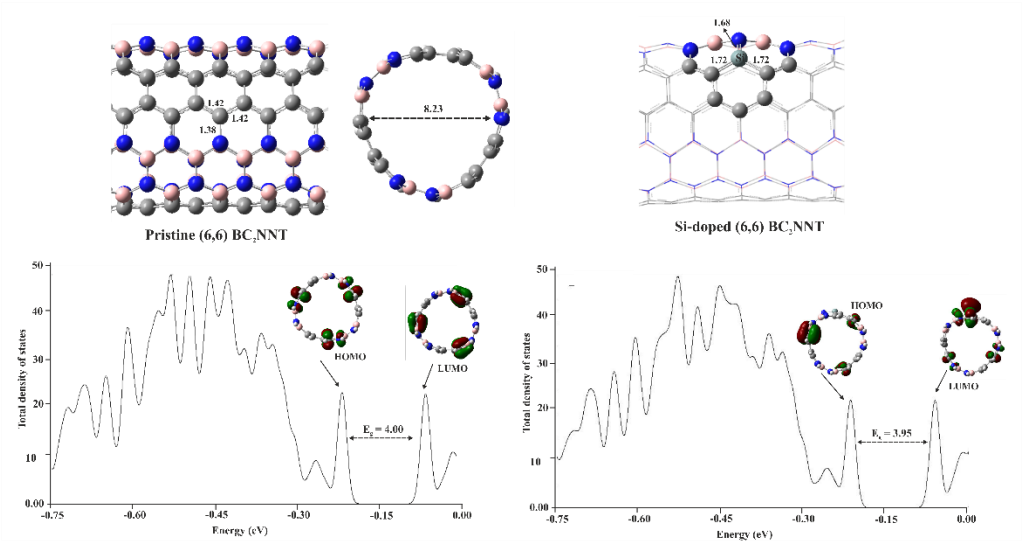

Figure A 4-1. The optimized structures of pure (6,6) BC_2NNT and Si-embedded (6,6) BC_2NNT, along with their total density of states (TDOS) plots. All distances and energy gap (E_g) are in Å and eV, respectively

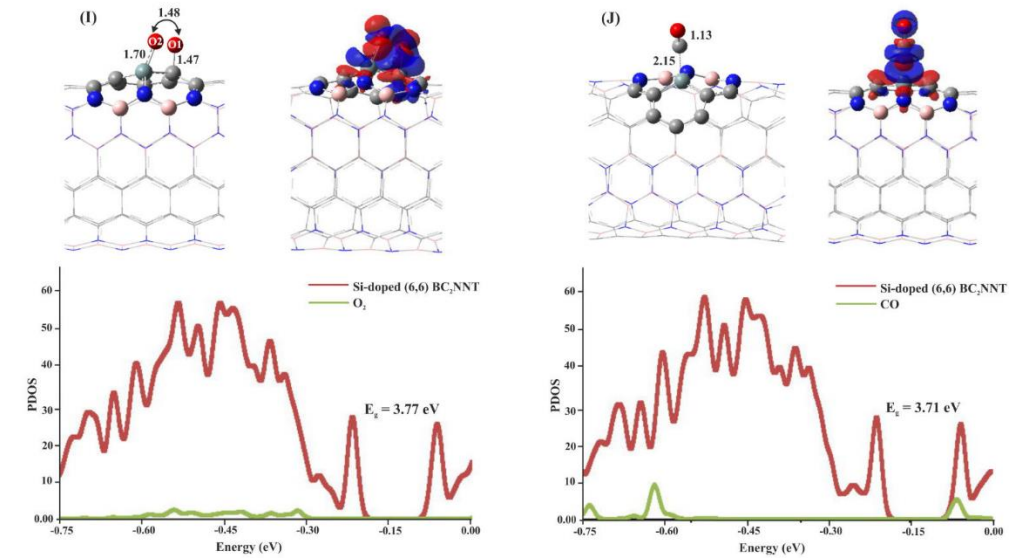

Figure A 4-2. The optimized structures of adsorbed O_2 and CO molecules over (6,6) Si-BC_2NNT (complexes I and J) along with their corresponding EDD maps and related partial density of states (PDOS) plots. In the electron density difference (EDD) maps, the charge depletion and accumulation sites are displayed in blue and red, respectively. All distances and energy gap (E_g) are in Å and eV, respectively.

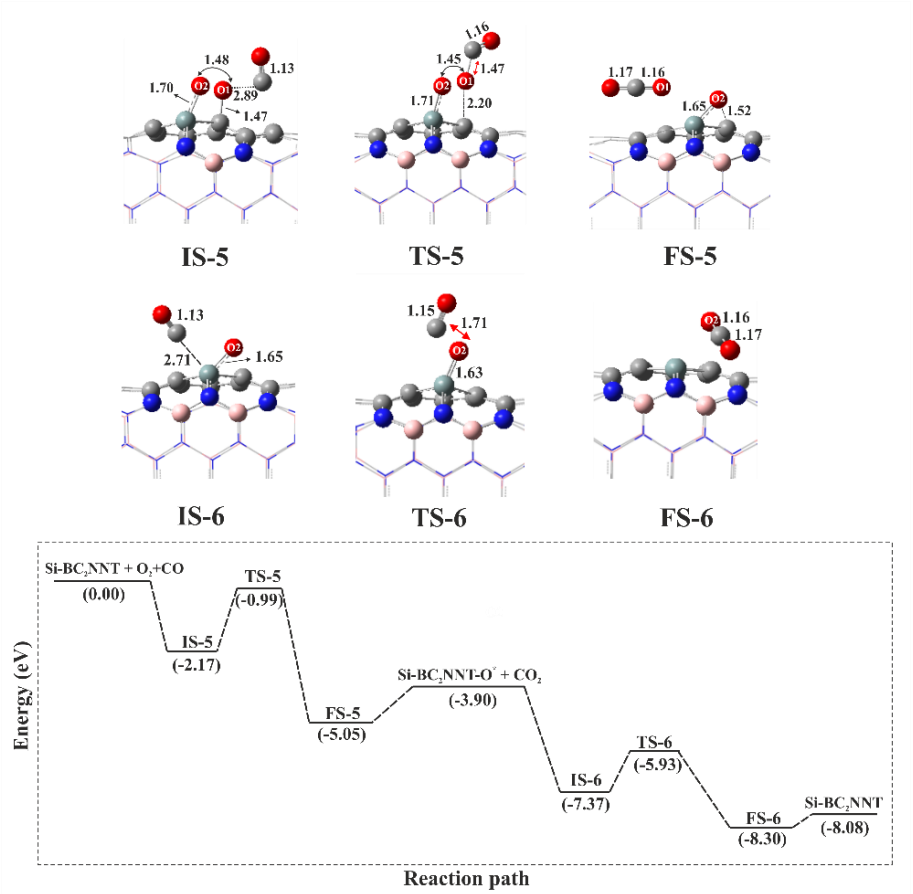

Figure A 4-3. A schematic energy profile of the minimum-energy pathway (MEP) and optimized stationary points for the CO oxidation reaction over (6,6) Si-BC_2NNT (complex I). All bond distances and energies are in Å and eV, respectively

Table A 4-1. Different O_2 and CO adsorption configurations over (4,4) Si-BC_2NNT, along with their corresponding adsorption energies (E_{ads}). Color code for each optimized structure: Blue ball: N; light gray ball: C; dark gray ball: Si, pink ball: B, red ball: O

	G	G1	H
Configurations	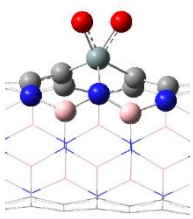	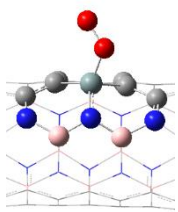	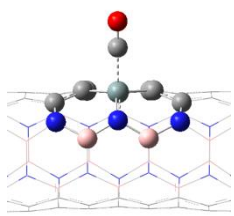
E_{ads}(eV)	-0.62	0.40	-0.39

Table A 4-2. The calculated net charge-transfer (q) and LUMO-HOMO bandgap energy (E_g) of pristine and Si-doped (6,6) BC_2NNT

Complex	E_{ads}(eV)	q_{CT} (e)	E_g (eV)
Pristine (6,6) BC_2NNT			4.00
Si-doped (6,6) BC_2NNT	-12.86	0.54	3.95

Table A 4-3. The calculated bond length (R), adsorption energy (E_{ads}), Mulliken net charge-transfer (q_{CT}), LUMO-HOMO bandgap energy (E_g), change of Gibbs free energy (ΔG_{298}) and change of enthalpy (ΔH_{298}) of O_2 and CO adsorption over Si-doped (6,6) BC_2NNT[a].

Complex	$R_{(Si\text{-}O1/Si\text{-}O2/Si\text{-}C)}$ (Å)	E_{ads} (eV)	q_{CT} (e)	E_g (eV)	ΔG_{298} (eV)	ΔH_{298} (eV)
Si-doped (6,6) BC_2NNT						
I	1.47/1.70	-1.98 (-1.87)	-0.65	3.77	-1.48	-2.02
J	2.15	-0.32 (-0.24)	+0.16	3.71	0.08	-0.33

[a] The E_{ads} values within the parenthesis is the calculated adsorption energy performed by considering basis-set superposition error (BSSE).

Table A 4-4. The calculated activation energy (E_{act}), reaction energy (ΔE), change of Gibbs free energy (ΔG_{298}) and change of enthalpy (ΔH_{298}) for different pathways of CO oxidation reaction over Si-doped (6,6) BC_2NNT

Reaction	E_{act} (eV)	ΔE (eV)	ΔG_{298} (eV)	ΔH_{298} (eV)
Si-doped (6,6) BC_2NNT				
IS-5 → FS-5	1.18	-2.88	-2.83	-2.88
IS-6 → FS-6	1.44	-0.93	-0.93	-0.93

Chapter 5

The role of healed N-vacancy defective BC_2N nanoflake and nanotube by NO molecule in the oxidation of NO and CO gas molecules

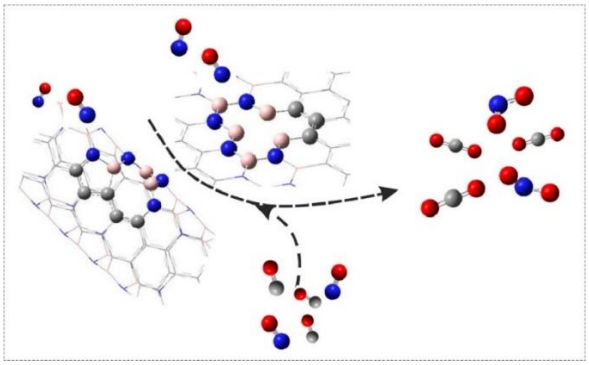

In this study, the healing of N-vacancy boron carbon nitride nanoflake (NV-BC_2NNF) and nanotube (NV- BC_2NNT) by NO is studied by means of density functional theory calculations. Two different N-vacancies are considered in each of these structures in which the vacancy site is surrounded by either three B-atoms (NB) or by two B- and one C-atom (NBC). By means of the healed BC_2NNF and BC_2NNT as a substrate, the removal of toxic NO and CO is possible. It should be noted that the obtained energy barriers of both healing and oxidation processes are significantly lower than those on graphene, carbon nanotubes or boron nitride nanostructures. Also, at the end of the oxidation process, the pure BC_2NNF or BC_2NNT is obtained without any additional defects. Therefore, by using this method, defective BC_2NNF / BC_2NNT can be purified. Moreover, the thermochemistry calculations indicate that the healing process of the NV-BC_2NNF and NV- BC_2NNT by NO are feasible at room temperature. So, we can claim that this study could be very helpful in both purifying the defective BC_2NNF / BC_2NNT while in the same effort removing toxic NO and CO gases.

Publication: Parisa Nematollahi, Mehdi D. Esrafili, and Erik C. Neyts. The role of healed N-vacancy defective BC_2N sheet and nanotube by NO molecule in oxidation of NO and CO gas molecules J. Surface Science, 672 (2018): 39-46. https://doi.org/10.1016/j.susc.2018.03.002

The corresponding introduction of this Chapter is already contained in Chapter 1, and only the specifics are mentioned here. DFT calculations were employed to investigate the healing of NV-BC_2NNF and armchair (4,4) NV-BC_2NNT by means of NO. Moreover, the removal of extra atomic O from the healed BC_2NNF and BC_2NNT by another NO or CO molecule is also investigated in detail. To the best of our knowledge, there are no previous reports on healing single vacancies in defective BC_2NNF and BC_2NNT by using NO, which is the focus of this paper. These results have practical implications for the development of novel BCN based nanodevices acting as gas sensors or metal-free catalysts.

5.1 Computational methods

All structure optimizations and reaction pathway calculations are based on DFT using the Gaussian 16 package with the detailed methods mentioned in Chapter 3, except the charge calculation method. In this chapter, the Mulliken method is considered to measure the charge transfer between two atoms. We selected a BC_2NNF consisting of 44 carbon, 11 boron,, and 11 nitrogen atoms and the armchair (4, 4) BC_2NNT containing 44 carbon, 22 boron, and 22 nitrogen atoms. To avoid the unsaturated boundary effect, hydrogen atoms are added to both ends of BC_2NNT and to the edges of the BC_2NNF.Results and discussions

5.1.1 Geometry of NV-BC_2NNF

The partial structure of the optimized pure BC_2NNF, with three types of bonds, namely N-B, N-C and B-C, with corresponding lengths of 1.44 Å, 1.40 Å, and 1.55 Å, respectively, is shown in Figure 5-1 (configuration A). In this configuration, two different kinds of N-vacancies can be considered, involving the hollow center between three B-atoms (NB) (configuration B) and between two B-atoms and one C-atom (NBC) (configuration C). In configuration B, a 12-membered ring is produced by the removal of one N atom. In this case, the B1–B2, B2–B and B1–B3, bond distances are modified, i.e., from 2.50, 2.52 and 2.50 Å in configuration B to 2.44, 2.35 and 2.51 Å in configuration A, respectively. The average bond length of the three boron atoms surrounding the vacancy increased from 1.44 Å in pure BC_2NNF to 2.43 Å in configuration B. As is apparent from Figure 5-1, in configuration C, the three nearest atoms to the vacancy site are two B-atoms and one C-atom. The B1-C1, C1-B3, and B1-B3 bond lengths are modified from 2.25, 2.25 and 2.59 Å in pure BC_2NNF to 2.47, 2.46 and 2.50 Å in configuration C. Also, according to previous studies, the average distance between the B atoms at the vacancy site in NV-BC_2NNF (≈2.43 Å) is longer than that in the NV-BN nanosheets (≈2.33 Å) [339].

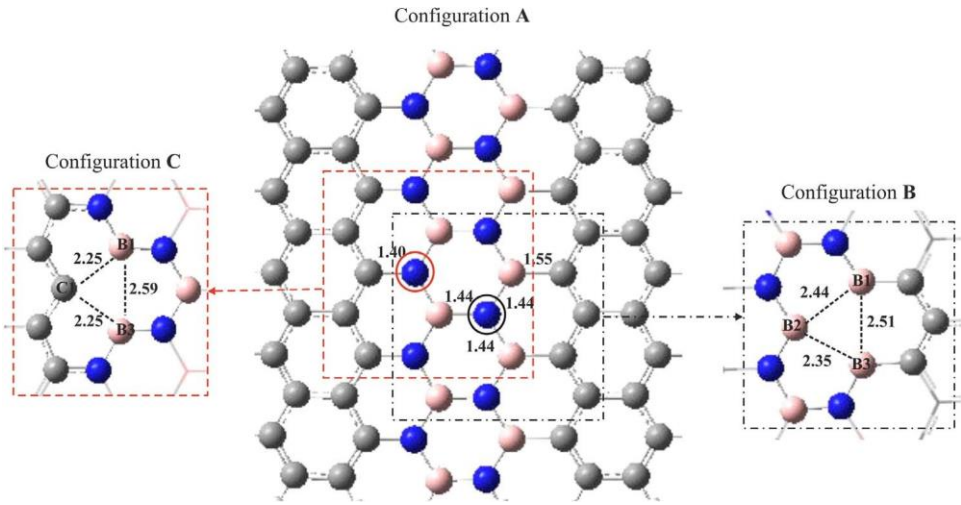

Figure 5-1. Optimized structures of BC_2NNF (configuration A) and two different NV-BC_2NNFs (configurations B (NB-vacancy) and C (NBC-vacancy). All distances are in Å.

5.1.2 Healing of NV-BC_2NNF by NO

In the healing process of configurations B and C by the NO molecule, firstly, the NO molecule either physically or chemically adsorbs at the vacancy site, and then fills the vacancy. The formed N-doped defective BC_2NNF has extra atomic oxygen (O_{ads}) (see Figure 5-2a) which by introducing the second molecule (NO or CO) to the system, can be eliminated from the surface. The corresponding structures of the healed NO molecule on configurations B and C along with their minimum energy pathway (MEP) and optimized structures for the initial state (IS), transition state (TS), and final state (FS) are depicted in Figure 5-2. Additionally, the relevant adsorption energy (E_{ads}), activation energy (E_{act}), and thermodynamic parameters for each reaction pathway are given in Table 5-1.

In configuration B, when the NO molecule adsorbs on the boron atom of the vacancy site N-B=2.84 Å with E_{ads} = –7.45 eV, IS-1 is formed (see Figure 5-2a). In TS-1, the NO molecule approaches the other B atoms of the vacancy site, causing a reduction in the N-B bond length from 2.84 Å in IS-1 to 1.69 Å in TS-1. In the next step (FS-1), the NO molecule is doped into the NB-BC_2NNF. In this structure, the N atom binds with three B-atoms while the O atom makes a three-membered ring (3MR) connecting to the nearest B-atom around the vacancy site. The obtained complex is named D in further discussion. Furthermore, it can be concluded from Table 5-1 that the energy barrier of vacancy healing in configuration B is very low, E_{act} = 0.10 eV, and it is a strongly exothermic process with $\Delta H_{298.15} = -5.23$ eV. Also, this reaction proceeds spontaneously at room temperature ($\Delta G_{298.15} = -4.96$ eV).

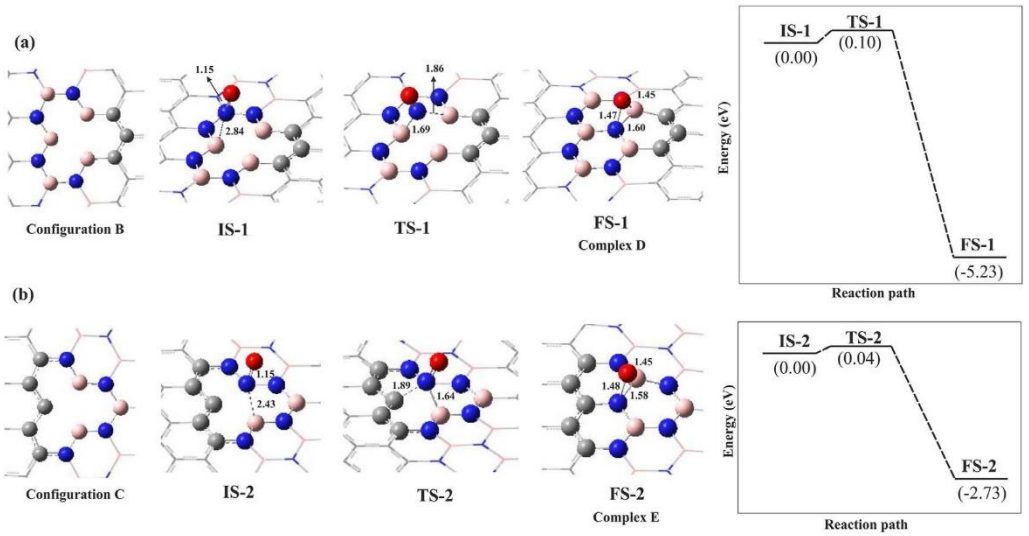

Figure 5-2. The optimized geometry and energy profile of healing the N-vacancy BC_2NNF by NO molecule into the configurations B (a) and C (b). All energy values and distances are in eV and Å, respectively. Color code for each optimized structure: Blue ball: N; red bull: O, pink ball: B and gray ball: C.

By introducing the NO molecule to the configuration C, the vertically oriented NO molecule is positioned above the B atom of the vacancy with the B-N=2.43 Å bond length (see Figure 5-2b) and the adsorption energy of $E_{ads} = -7.35$ eV, which shows the strong binding of the NO molecule to the vacancy site. In TS-2, the NO molecule approaches to C atom of the vacancy site, with N–C bond length of 1.89 Å, while the B-N bond length is reduced to 1.64 Å. The activation energy of this step is almost negligible ($E_{act} \approx 0.04$ eV). In the next step, the NO molecule is doped into the vacancy site and forms FS-2, namely complex E in the further discussion. Analogous with complex D, a 3MR is formed with three B–O, N–O, and B–N bond lengths of 1.45, 1.48, and 1.58 Å, respectively. It can be seen from Table 5-1 that the reaction pathway IS2→FS-2 is an exothermic process with $\Delta H_{298.15} = -2.72$ eV. Also, this reaction is spontaneous at room temperature ($\Delta G_{298.15} = -2.07$ eV). According to our results, the healing energy barriers of configurations B and C are lower than those in previous studies. For instance, Feng et al. [340] reported the energy barrier of 0.25 eV for the healing of N vacancy by NO_2.

Table 5-1. The calculated adsorption energy (E_{ads}) of adsorbed NO molecule over NV-BC_2NNF, along with their corresponding activation energy (E_{act}), reaction energy (ΔE), change of Gibbs free energy ($\Delta G_{298.15}$) and change of enthalpy ($\Delta H_{298.15}$) for the healing process of NV-BC_2NNF by NO molecule.

Reaction	E_{ads} (eV)	E_{act} (eV)	ΔE (eV)	$\Delta G_{298.15}$ (eV)	$\Delta H_{298.15}$ (eV)
IS-1 → FS-1	-7.45	0.10	-5.23	-4.96	-5.23
IS-2 → FS-2	-7.35	0.04	-2.73	-2.07	-2.73

5.1.3 Oxygen removal of the healed BC_2NNF by NO

It was previously found that the adsorbed atomic oxygen over CNTs or SiCNTs can be eliminated from the surface by introducing a second CO [334, 341], N_2O [203, 342] or second NO molecule [342]. Therefore, here, the removal of extra atomic O by introducing the second NO molecule to the system is investigated in detail. In order to better understand this process, all the IS, TS, and FS configurations along with their MEP diagrams, are depicted in Figure 5-3. In addition, the corresponding activation energy and thermodynamic properties ($\Delta G_{298.15}$, $\Delta H_{298.15}$, ΔE) are listed in Table 5-2. By introducing the NO molecule to complex D, IS-3 is formed in which the NO molecule is placed in a tilted position above the 3MR with bond length N-O_{ads} = 2.94 Å (see Figure 5-3a). Then, by passing via TS-3 with the energy barrier of 0.8 eV the NO_2 molecule can be formed. In this structure, the NO molecule approaches to O_{ads}, with bond length O–N = 1.89 Å. In FS-3, the physically adsorbed NO_2 molecule over the BC_2NNF is placed in a parallel position, at a distance of 3.05 Å from the surface. Finally, the NO_2 molecule can easily desorb from the BC_2NNF due to the small adsorption energy E_{ads} = -0.25 eV. In addition, according to Table 5-2, the formation of NO_2 molecule is exothermic with $\Delta H_{298.15}$ = -1.47 eV and is thermodynamically favourable at room temperature ($\Delta G_{298.15}$ = -1.50 eV).

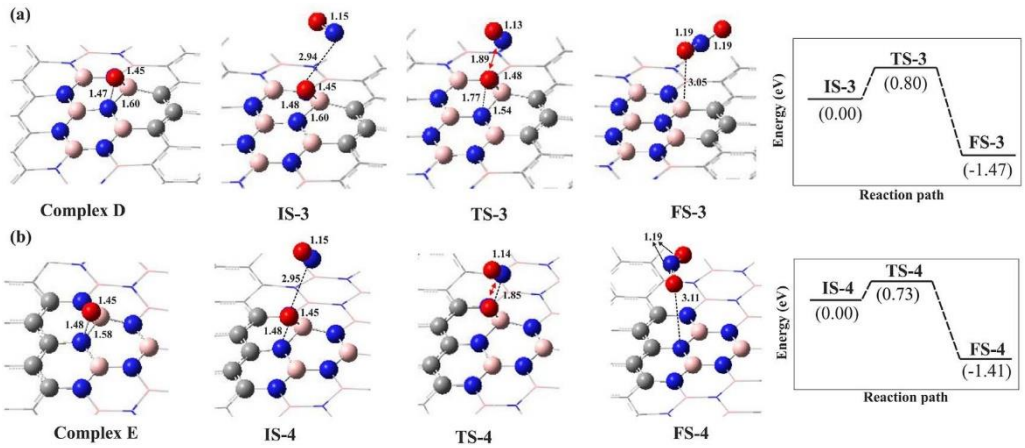

Figure 5-3. The optimized geometry and reaction profiles of NO oxidation reaction over the healed BC_2NNF surface by NO molecule. All distances are in Å

Similarly, when the NO molecule is added to complex E, the same reaction occurs: in IS-4, the NO molecule approaches the attached O_{ads} atom with bond length N-O_{ads} = 2.95 Å (see Figure 5-3b). TS-4 is characterized by an activation energy E_{act}=0.73 eV, indicating that the B-O and N-O bonds can easily break, which facilitates the interaction of the O_{ads} with the second NO molecule. In this configuration, the N atom of the NO molecule approaches the O_{ads} in order to form the NO_2 molecule. The formed NO_2 molecule lies almost parallel to the surface, at a distance of N-O = 3.11 Å. In FS-4, the N-O bond length of the physisorbed NO_2 molecule increases

from 1.15 Å in IS-4 to 1.19 Å in the NO_2 gas form. This gas molecule can then be easily released from the BC_2NNF surface due to its low adsorption energy, E_{ads}= -0.30 eV. Also, upon desorption of NO_2, the pure defect-free BC_2NNF is obtained.

Table 5-2. The calculated activation energy (E_{act}), reaction energy (ΔE), change of Gibbs free energy ($\Delta G_{298.15}$) and change of enthalpy ($\Delta H_{298.15}$) for the NO oxidation over the healed BC_2NNF by NO molecule

Reaction	E_{act} (eV)	ΔE (eV)	$\Delta G_{298.15}$ (eV)	$\Delta H_{298.15}$ (eV)
IS-3 → FS-3	0.80	-1.47	-1.50	-1.47
IS-4 → FS-4	0.73	-1.41	-1.51	-1.41

The reaction pathway IS-4 → FS-4 is also exothermic, with $\Delta H_{298.15}$ = -1.41 eV, and is thermodynamically spontaneous at ambient conditions ($\Delta G_{298.15}$= -1.51 eV). The obtained energy barrier values are lower than those reported by Wang et al. [343].

5.1.4 Geometry of NV-BC_2NNT

We also studied the healing of the N-vacancy by an NO molecule over the armchair (4, 4) BC_2NNT. In order to achieve this, a tubular armchair (4, 4) BC_2NNT is used as shown in Figure 5-4 (configuration F). There are three different bonds: C–N, C–B, and B–N with bond lengths of 1.38, 1.53, and 1.45 Å, respectively. Analogous with BC_2NNF, removing one N atom from two different positions in the middle of BC_2NNT, two ideal single N-vacancy defects are produced: NB and NBC. These two possible defect sites for the N-vacancy BC_2NNT are depicted as configurations G and H (see Figure 5-4).

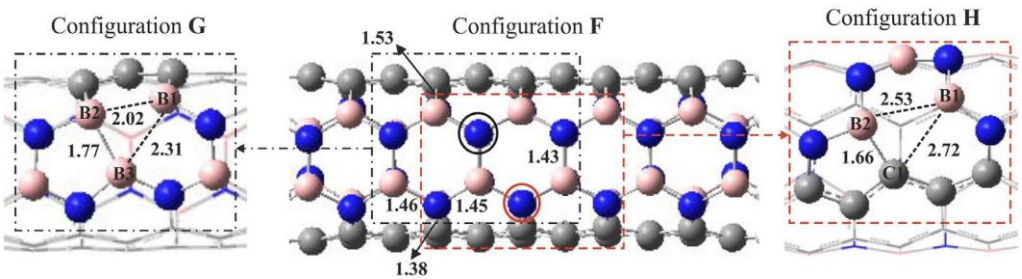

Figure 5-4. Optimized structures of BC_2NNT (configuration F) and two different NV-BC_2NNTs (configurations G (NB-vacancy) and H (NBC-vacancy). All distances are in Å.

In complex G, the N-vacancy defective BC_2NNT is produced by removing one N atom which is surrounded by three closest B atoms (B1, B2, and B3): NB. Upon the removal of the N atom, the two B atoms near the vacancy site (B2 and B3) move so close to each other that their binding distance (≈1.77 Å) becomes smaller than that in pristine BC_2NNT (2.49 Å), thereby forming a 5-membered ring (5MR). In this configuration, the binding distances of the B atoms (B1–B3 and B2–B3) in the remaining 9-membered ring decrease from 2.38 Å in pristine BC_2NNT to 2.02 and 2.31 Å in the defected tube, respectively (see Figure 5-4). These data are also close to other related BN structures [344]. For instance, Xiao et al. [345] reported theoretically that the B2-

B3 bond length in the N vacancy BNNT is about 1.78 Å and these two-coordinated B atoms in the defect protrude from the circumference of the tube.

Configuration H is the same structural configuration as complex G, but in this case, the vacancy is surrounded by two B-atoms (B1, B3) and one C-atom (C1): NBC. Analogous to configuration G, the two nearest B1 and C1 atoms at the vacancy site approach each other and form a 5MR upon removal of the N atom. Again the two B2 and C1 atoms bind together with a bond distance B2–C1 = 1.66 Å, which is smaller than that in complex G (1.77 Å) and in pristine BC_2NNT (2.42 Å). Also, the other binding distances of B1–B2 and B1–C1 in the remaining 9- membered ring increase from 2.49 and 2.42 Å in pure BC_2NNT to 2.53 and 2.72 Å in the defected tube, respectively (see Figure 5-4).

5.1.5 Healing of NV-BC_2NNT by NO

In the case of BC_2NNT, the healing process of NV-BC_2NNT by an NO molecule proceeds similar to NV-BC_2NNF via two main steps: (1) the physical or chemical adsorption of the NO molecule at the vacancy site and (2) removing the O_{ads} by another NO molecule. The optimized structures of the NO molecule over configurations G and H along with their MEP diagram and their corresponding stationary points (IS, TS and FS) are shown in Figure 5-5. Moreover, the geometric and thermodynamic properties of these reaction pathways are listed in Table 5-3. By adding a NO molecule to the complex G, IS-5 is obtained. In this structure, the NO molecule is chemically attached to the B atom of the vacancy site. As a result, the B atom protrudes somewhat out of the tube surface with bond lengths B–O = 1.52 Å and N = O = 1.12 Å. The distance between the N atom and the other two B atoms of the vacancy is 3.28 and 2.60 Å, respectively. In addition, the high adsorption energy E_{ads} = −8.17 eV indicates that there is a great tendency for NO molecule to react with the NB vacancy site of BC_2NNT. In TS-5 the NO molecule approaches both B atoms of the vacancy site via its N and O atoms. In this structure, the N-B and O-B bond lengths are 2.55 and 2.10 Å, respectively, which causes the elongation and also activation of the N-O bond from 1.22 Å in IS-5 to 1.25 Å in this state. By overcoming a low energy barrier of 0.65 eV, the NO molecule heals the N-vacancy site of BC_2NNT, yielding the FS-5 configuration in which the NO molecule forms a three-membered ring with B-O, N-O and B-N bond lengths of 1.40, 1.44 and 2.08 Å, respectively. It can be concluded from the high values for the thermodynamic properties that the healing of the N-vacancy in BC_2NNT by NO is exothermic ($\Delta H_{298.15}$ = −5.95 eV) and occurs at room temperature ($\Delta G_{298.15}$ = −5.82 eV).

As shown in Figure 5-5b, upon introducing the second NO molecule to configuration H, IS-6 is formed. The NO molecule is positioned right in the middle of the vacancy site and binds with two B-atoms with average bond lengths of 1.57 Å and an adsorption energy E_{ads} = −5.75 eV, while it is somewhat far from the C atom, N-C = 2.40 Å. In TS-6, the N atom approaches the C atom to make a chemical bond. In FS-6, a stable three-

membered ring is formed in which the O atom is placed between two B-atoms and a N-atom with BO, N-O and B-N bond lengths of 1.46, 1.47 and 1.57 Å, respectively (see Figure 5-5b). In this structure, the formed N-C bond is 1.48 Å and the N-O bond is elongated from 1.20 Å in IS-6 to 1.29 Å. The activation energy of this path IS-6 → FS-6, is calculated as E_{act} = 1.37 eV, which is higher than that in IS-5 → FS-5. The reaction is exothermic and spontaneous at room temperature (see Table 5-3). The healing process of N-vacancy BC_2NNT by No molecule has a lower energy barrier than that in BNNT studied by Xiao et al. [345]. The healing energy barrier of the N-vacancy in BNNT by NO will be within the range from 0.41 to 0.54 eV in the real cases. This is almost near to the obtained theoretical value of the healing of N-vacancy BC_2NNT by NO molecule (see Figure 5-5, configuration G).

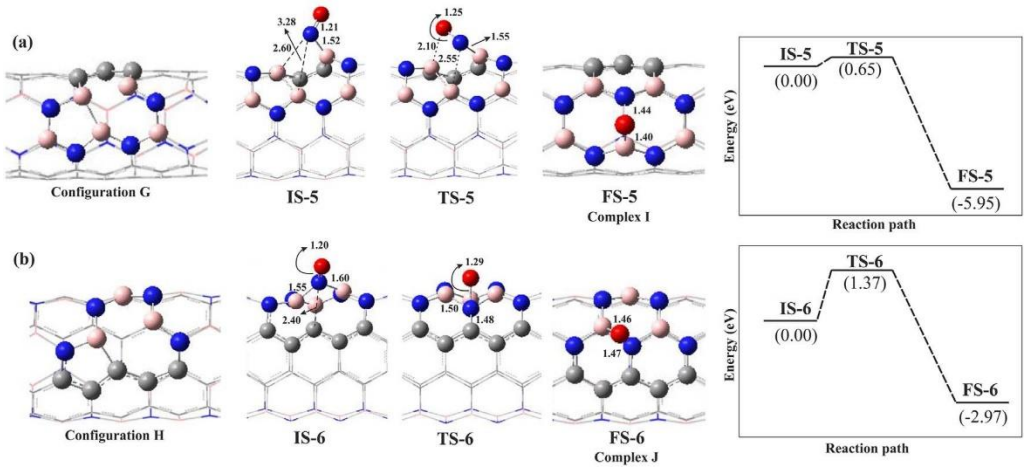

Figure 5-5. The optimized geometry and energy profile of the N-vacancy BC_2NNT recombination process by NO molecule adsorption onto configurations G (a) and H (b) along with their relative energy profile. All energy values and distances are in eV and Å, respectively. Color code for each optimized structure: Blue ball: N; red bull: O, pink ball: B and gray ball: C

Table 5-3. The calculated adsorption energy (E_{ads}) of adsorbed NO molecule over NV-BC_2NNT, along with their corresponding activation energy (E_{act}), reaction energy (ΔE), change of Gibbs free energy ($\Delta G_{298.15}$) and change of enthalpy ($\Delta H_{298.15}$) for the healing of process of NV-BC_2NNT by NO molecule

Reaction	E_{ads} (eV)	E_{act} (eV)	ΔE (eV)	$\Delta G_{298.15}$ (eV)	$\Delta H_{298.15}$ (eV)
IS-5 → FS-5	-8.17	0.65	-5.95	-5.82	-5.95
IS-6 → FS-6	-5.75	1.37	-2.65	-2.56	-2.65

5.1.6 Oxygen removal of the healed BC_2NNT by NO

Finally, we studied the removal of O_{ads} from the healed BC_2NNT using the second NO molecule. The geometries of the related IS, TS and FS configurations are shown in Figure 5-6. Also, the related activation energy and thermodynamic properties are listed in Table 5-4. The oxidation reaction starts by introducing the NO molecule to complex I, named IS-7. After relaxation, the NO molecule is placed horizontally on top of the

tube surface in a distance of N-O_{ads}=2.89 Å from the adsorbed oxygen atom. Then, it approaches the O_{ads} in order to make a chemical bond with it (TS-7). In this state, the N-O_{ads} bond length decreases to 1.83 Å while the N-O bond length decreases from 1.15 Å in IS-7 to 1.13 Å. The energy barrier of this step is 1.61 eV which eventually results in the formation of an NO_2 molecule in FS-7. In this stage, the NO_2 molecule is physically adsorbed over the BC_2NNT (O-B =2.85 Å), and can be easily desorbed from the surface (E_{ads} = -0.18 eV). The formed NO_2 molecule has N-O bond lengths of 1.19 Å which is the same as that in the gas phase. In contrast to all previous pathways, this reaction IS-7→FS-7 is slightly endothermic with the reaction enthalpy of $\Delta H_{298.15}$=0.64 eV (Table 5-4) and the positive value of $\Delta G_{298.15}$ indicates that it is not favourable thermodynamically.

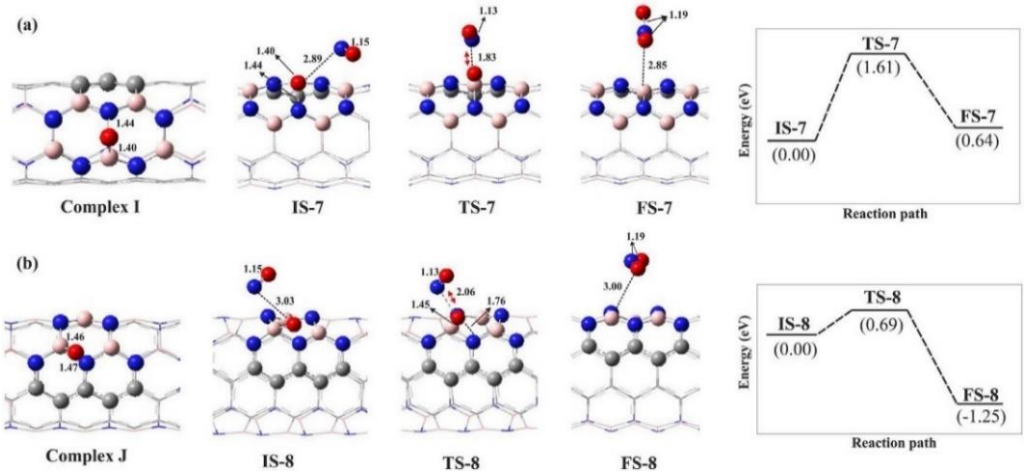

Figure 5-6. The optimized geometry and reaction profiles of NO oxidation reaction over the healed BC_2NNT surface by NO molecule. All distances are in Å

Next, we investigate the same reaction starting with complex J. Introduction of the second NO molecule results in IS-8. After optimization, the NO molecule is positioned on top of the O_{ads}, with distance N-O_{ads} = 3.03 Å (see Figure 5-6b). When the NO molecule approaches the O_{ads} to a distance of 2.06 Å in TS-8, the NO_2 molecule can produce. The activation energy of this step is 0.69 eV which is in close agreement with Liu et al. [339] study. Finally, the NO_2 molecule is formed in FS-8 and released from the BC_2NNT surface because of the low adsorption energy, E_{ads}= -0.29 eV. According to the obtained results listed in Table 5-4, the pathway is exothermic and the reaction proceeds spontaneously at room temperature ($\Delta G_{298.15}$=-1.28 eV). The obtained energy barriers of O-removal by NO molecule over BC_2NNT are lower than those in BNNT [345].

Table 5-4. The calculated activation energy (E_{act}), reaction energy (ΔE), change of Gibbs free energy ($\Delta G_{298.15}$) and change of enthalpy ($\Delta H_{298.15}$) for the NO oxidation over the healed BC_2NNT by NO molecule

Reaction	E_{act} (eV)	ΔE (eV)	$\Delta G_{298.15}$ (eV)	$\Delta H_{298.15}$ (eV)
IS-7 → FS-7	1.61	0.64	0.51	0.64
IS-8 → FS-8	0.69	-1.25	-1.28	-1.25

5.1.7 Oxygen removal of the healed BC_2NNF and BC_2NNT by CO

We also studied the removal of the adsorbed atomic oxygen over the BC_2NNF and BC_2NNT by introducing a CO molecule as another toxic gas present in the air in order to form the CO_2 molecule. All the geometric structures of IS, TS, and FS along with their MEP diagram, are depicted in Figures A5-1 and A5-2 in the Appendix section. Additionally, the corresponding energy barrier and thermodynamic parameters ($\Delta G_{298.15}$, $\Delta H_{298.15}$, and ΔE) are listed in Tables A5-1 and A5-2. All the detailed steps are the same as those found for NO oxidation. Starting with configuration D, the CO molecule is positioned over the O_{ads} with C-O_{ads} = 3.02 Å yielding IS-9. As is apparent from Figure A5-1a, in FS-9 the CO_2 gas molecule can be released from the surface due to the small adsorption energy, E_{ads}= -0.23 eV. The E_{act} of pathway IS-9 → FS-9 is 1.03 eV and it is an exothermic reaction with $\Delta H_{298.15}$=-3.98 eV. Moreover, it is thermodynamically favourable at ambient conditions (see Table A5-1).

The addition of CO molecule to configuration E forms IS-10 in which the CO molecule is located at a distance of 2.52 Å from O_{ads} (see Figure A5-1b). In approaching the adsorbed O atom in order to produce the CO_2 gas molecule, only a small activation barrier E_{act} = 0.07 eV is encountered. Overall, the reaction pathway IS-10 → FS-10 is exothermic with $\Delta H_{298.15}$ = -4.38 eV and is thermodynamically feasible ($\Delta G_{298.15}$ = -4.27 eV) at room temperature. Similar to NO_2, the CO_2 molecule easily desorbs from the BC_2NNF surface (E_{ads} = -0.25 eV).

CO oxidation on the healed BC_2NNT surface starts with configurations I and J (FigureA5-2). It is noteworthy that because of the strong interaction between the O_{ads} and the BC_2NNT, high energy barriers required for the direct removal of O_{ads} in both configurations. Introducing a CO molecule to configuration I lead to the formation of IS-11. Passing via TS-11 with an energy barrier of 1.85 eV, FS-11 will obtain in which the CO_2 molecule physisorbed over the BC_2NNT (E_{ads}= -0.16 eV). The reaction pathway IS-11 → FS-11 is exothermic with $\Delta H_{298.15}$= -1.99 eV (Table A5-2).

When the CO molecule is introduced to configuration J at a distance of 3.00 Å from O_{ads}, IS-12 is formed (Figure A5-2b). The CO_2 molecule is then produced passing via TS-12 with a significant energy barrier of 2.74 eV. In FS-12, the CO_2 molecule with a weak adsorption energy E_{ads}= -0.29 eV is produced and desorbed from the BC_2NNT surface. This reaction is also exothermic and favourable at room temperature ($\Delta H_{298.15}$= -2.05 eV and $\Delta G_{298.15}$ = -1.99 eV.

According to the experimental investigations, single X-vacancy nano-structures can be easily introduced through electron or ion-irradiation [40, 346]. They contain unsaturated atoms and therefore, they are highly reactive. Accordingly, healing of these single X-vacancy nanostructures by certain foreign molecules, especially gas molecules containing an X atom (here the NO molecule) or atoms with a similar size and reactivity as X, are favored, typically making the reaction pathway exothermic and spontaneous at room temperature. In this study, the NBC vacancy in both BC_2NNF and BC_2NNT shows lower activation energy toward the NO healing. Also, removal of the adsorbed oxygen atom by introducing the second NO or CO molecule in NBC vacancy proceeds via lower activation energy than that in NB vacancy. Generally, it is found that reactions with a barrier of less than 0.5 eV are expected to occur at room temperature. Correspondingly, we found that the required energy barrier for O-removal by NO molecule is lower on NBC-BC_2NNF and BC_2NNT than that on NB-BC_2N nanostructures and these reactions can easily occur at room temperature.

5.2 Conclusion

We have investigated the healing of the NV-BC_2NNF and NV-BC_2NNT by NO molecule using DFT calculations. Two different vacancies are chosen for each nanostructure: NB and NBC. For both NV-nanostructures, the defect site is the most active area for the healing process by NO molecule. Thus, the addition of a second NO molecule to the N-vacancy site can be expected to be a favourable reaction and can be viewed as the first step of the healing of NV-BC_2NNF and NV-BC_2NNT surfaces. The adsorption energy of NO molecule over NB and NBC vacancies of BC_2NNF is calculated as -7.45 eV and -7.35 eV while it is -8.17 eV and -5.75 eV in BC_2NNT, respectively. This indicates the strong interaction between NO and NB-BC_2NNF and NB-BC_2NNT. But, in comparison to NV-BC_2NNT, the healing of both N-vacancies (NB and NBC) of BC_2NNF proceeds via lower activation energy.

Subsequently, the introduction of a second NO or CO molecule to the system can help to the removal of the O_{ads} on the BC_2NNF and BC_2NNT surface. In O-removal by a second NO molecule, the NBC-BC_2NNF and NBC-BC_2NNT showed moderate activation energies (0.73 eV and 0.69 eV), which are lower than those of NB-vacancies. In the O-removal by a CO molecule, the NBC-BC_2NNF demonstrated the lowest barrier energy (0.07 eV) than other configurations. Thus, we can conclude that the NO molecule could be a promising candidate to heal the N-vacancy defects in both BC_2N nanostructures. Moreover, both the NBC-BC_2NNF showed better activity toward the removal of O_{ads} with NO and CO molecule. According to these results, we can claim that this study could be very helpful in both purifying the defective BC_2NNF / BC_2NNT and in the same effort removing toxic NO and CO gases.

5.3 Appendix

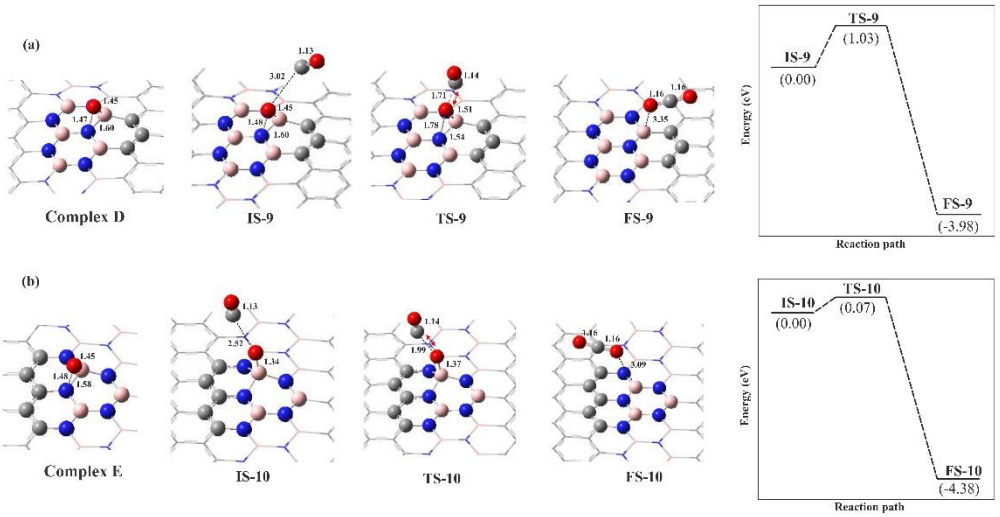

Figure A 5-1. The optimized geometry and reaction profiles of CO oxidation reaction over the healed BC_2NNF surface by NO molecule. All distances are in Å

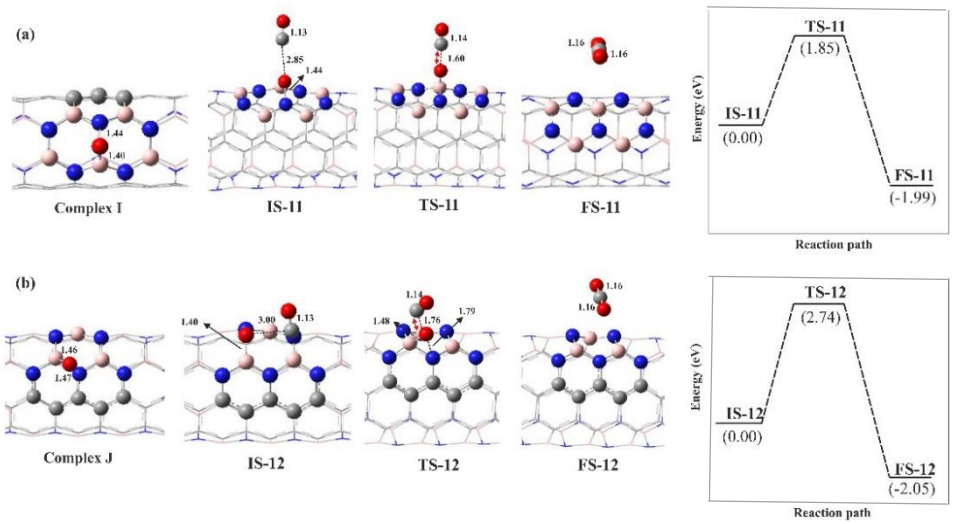

Figure A 5-2. The optimized geometry and reaction profiles of CO oxidation reaction over the healed BC_2NNT surface by NO molecule. All distances are in Å

Table A 5-1. The calculated activation energy (E_{act}), reaction energy (ΔE), change of Gibbs free energy ($\Delta G_{298.15}$) and change of enthalpy ($\Delta H_{298.15}$) for the CO oxidation over the healed BC_2NNF by NO molecule

Pathways	E_{act} (eV)	ΔE (eV)	$\Delta G_{298.15}$ (eV)	$\Delta H_{298.15}$ (eV)
IS-9 → FS-9	1.03	-3.98	-3.97	-3.98
IS-10 → FS-10	0.07	-4.38	-4.27	-4.38

Table A 5-2. The calculated activation energy (E_{act}), reaction energy (ΔE), change of Gibbs free energy ($\Delta G_{298.15}$) and change of enthalpy ($\Delta H_{298.15}$) for the CO oxidation over the healed BC_2NNT by NO molecule

Pathways	E_{act} (eV)	ΔE (eV)	$\Delta G_{298.15}$ (eV)	$\Delta H_{298.15}$ (eV)
IS-11 → FS-11	1.85	-1.99	-1.95	-1.99
IS-12 → FS-12	2.74	-2.05	-1.99	-2.05

Chapter 6

Direct oxidation of methane to methanol on Co embedded N-doped graphene flake: comparing the role of N_2O and O_2 as oxidants

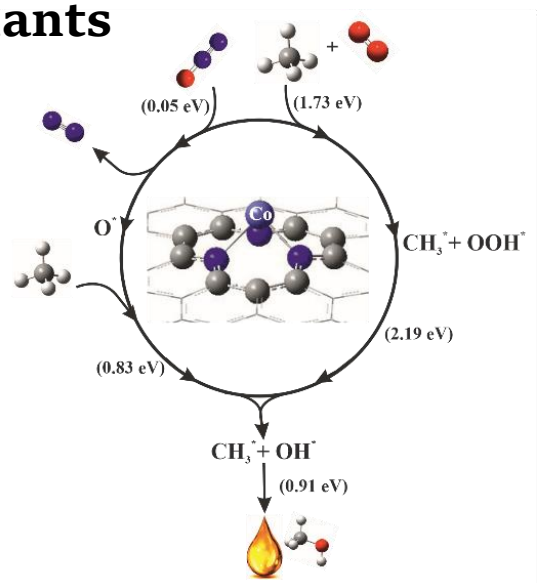

In this work, the effects of nitrogen doping into the Co atom embedded single vacancy (Co-SV-G) and di-vacancy graphene flake (Co-dV-G) are investigated and compared toward direct oxidation of methane to methanol (DOMM) by means of two different oxidants (N_2O and O_2) using DFT calculation. We found that CoN_3–G shows better catalytic activity toward adsorption of gas reactants and consequently methane oxidation thanks to the lower activation energies. A two-step method is proposed for DOMM on CoN_3-G using N_2O as an oxygen-donor. N_2O molecule adsorbs dissociatively on CoN_3-G providing atomic oxygen for catalyzing the DOMM. Moreover, the adsorption behaviors of CH_x (x=0-4) species and dehydrogenation of CH_x (x=1-4) species on CoN_3-G are investigated. We concluded that CoN_3-G can be used as an efficient catalyst for DOMM and N_2O reduction at ambient conditions which may serve as a guide for fabricating effective C/N catalysts in energy-related devices.

Publication: Parisa Nematollahi and Erik C. Neyts. Direct oxidation of methane to methanol on Co embedded N-doped graphene: comparing the role of N_2O and O_2 as oxidants. J. Applied catalysis A, (In press)

6.1 Introduction

In the last few decades, researchers have been dedicated to the synthesis of cost-effective electrocatalysts using cheaper transition metals [347] in which, cobalt-based electrocatalysts show the most promising results [348]. As of any first-row transition metal (Ni, Fe, and Cu), cobalt is a cheap, environmentally friendly, and accessible metal in comparison with noble metals [349] and it can be introduced into the graphene lattice with no difficulties [184]. Recently, Fei et al. [350] worked on the synthesis of nitrogen-enriched core-shell structured cobalt−carbon nanoparticles dispersed on graphene sheets, which can be used for hydrogen evolution reaction in both acidic and basic media. Wang et al. [351] found that the Co embedded into N-doped carbon nanotubes has a better activity toward ORR and the oxygen evolution reaction (OER) in both alkaline and neutral media due to their low cost and appropriate features to act as bi-functional catalysts for both the ORR and OER. Moreover, it is found that Co nanoparticles doped into carbon nanotube structures can decrease the local work function of the carbon surface because electrons transfer from cobalt to the surrounding carbon atoms, very easily [352]. Kattel et al. [353] investigated the ORR reaction pathway on M–N (M = Fe, Co, or Ni) catalytic clusters formed between pores in graphene supports. They found that O_2 molecule chemisorbs on CoN_4-graphene (CoN_4-G) and FeN_4-graphene (Fe-N_4) clusters but not on NiN_4-graphene (Ni-N_4) clusters. Therefore, the first two clusters were regarded as more active substrates toward ORR. The high stability is mainly attributed to the high conductivity of N-doped graphene and the embedded Co nanoparticles. N-doping increases the electron donor–acceptor properties of graphene and leads to the improvement of the conductance and interfacial electron transfer by doped Co nanoparticles [354]. Zhang et al. [72] calculated the activation barriers and thermodynamic properties of ORR on CoN_4-G. They demonstrated that CoN_4-G can enhance the ORR and resulted in the formation of two H_2O molecules. Kiefer et al. [93] reported that graphitic CoN_4 defects are stable at all potentials (U = 0–1.23 V) while CoN_2 defects are predicted to be unstable at high potentials. In addition, they predicted that the CoN_4 defect is the dominant in-plane graphitic defect in CoN_x/C electrocatalysts.

This article describes our efforts to develop a mechanism for methane conversion to methanol on a modified graphene flake. The modification of the graphene flake has been done through three ways, i. e., introducing a single vacancy (SV) and di-vacancy (dV) defect, doping the defective flake with nitrogen heteroatoms making pyridinic N-doping graphene flake (N_3- and N_4-G), and finally by introducing a single Co atom into the defective graphene flake lattice. Then, we investigated and compared the effect of nitrogen doping on the catalytic activity of the designed catalysts toward direct oxidation of CH_4 to CH_3OH using O_2 and N_2O as an oxidant. N_2O acts as an O-donor compound and gives us the ability to convert two pollutant gas simultaneously[355]. DFT calculations are utilized in order to find the most energetically favourable substrate for

the direct oxidation of methane to methanol. All the reactions take place at room temperature and then the catalytic performances of these carbon material catalysts were investigated. Moreover, the detailed surface interactions and reaction pathways that occurred on the interface of the substrate were also discussed.

6.2 Computational methods

All structure optimizations and reaction pathway calculations are based on DFT using the Gaussian 16 package with the detailed methods mentioned in Chapter 3. No significant spin contamination was found. To model the pristine graphene as a finite-size monolayer flake, a total of 85 carbon atoms were considered for all calculations. Moreover, the triplet state oxygen is considered for the adsorption configurations. The formation energies (E_f) of Co-doped N embedded substrates are calculated by:

$$\Delta E_f = E_{substrate} + a\mu_C - (E_{pureG} + b\mu_N + \mu_{Co}) \quad (6\text{-}1)$$

the $E_{substrate}$ represents the total energy of the doped graphene flake, μ_C and μ_N are the chemical potentials of the carbon and nitrogen atom, defined as the total energy per carbon atom in a pure graphene flake and the one-half of gaseous N_2 molecule, respectively. a (b) coefficients for CoN_3-G and CoN_4-G are 4(3) and 6(4), respectively. Finally, μ_{Co} is the energy for isolated Co atom. Frontier Molecular Orbitals consist of the HOMO and LUMO, which play an important role in the chemical reactivity of the molecule. The location of the HOMO determines the ability of electron donation while the LUMO dictates the ability to accept an electron. The molecular orbital calculations were also performed for all adsorbents at the same level of theory. The electronic properties of the substrates were calculated using Multiwfn 3.3.9 [356]. Reaction paths were followed for the ground state spin of the states for each reaction.

According to the NIST database, the oxidation of methane to methanol $2CH_{4\,(g)} + O_{2\,(g)} \rightarrow 2CH_3OH_{(g)}$ is a thermodynamically favourable reaction, $\Delta G^{\circ}_{298.15}$ = -2.32 eV and $\Delta H^{\circ}_{298.15}$ = -2.63 eV. The calculated thermodynamic results for this reaction using Gaussian16 also declare that it is a thermodynamically feasible reaction. $\Delta G_{298.15}$ = -1.87 eV and $\Delta H_{298.15}$ = -2.20 eV, in order to diminish or reduce the existed difference between the calculated thermodynamic values by Gaussian and those we obtained from the NIST database, we investigated the thermodynamic properties of the reaction by applying various functional and basis sets. The obtained results are provided in Table A3-3. The best agreement with the NIST database data was found using the CBS-QB3 functional [292] with 6-311G** basis set, viz. ΔG = -2.35 eV and ΔH = -2.66 eV, which is indeed very close to the database values.

6.3 Results and discussions

The aim of this work is to investigate the catalytic activity of Co-SV-G, Co-dV-G, CoN_3-G, and CoN_4-G toward methane activation and conversion to methanol using N_2O

and O_2 as an oxidant. As we mentioned in Chapter 3, the C-H bond cleavage of the methane molecule, is a challenge in heterogeneous catalysis, because of its great thermodynamic stability and strong tetrahedral bonds. Therefore, upon C-H bond cleavage, two different pathways with different intermediates can be identified for the H abstraction by oxygen: a radical and a non-radical process [357].

6.3.1 Geometric and electric properties of the substrates

Since the stability of doped graphene determines its usage in catalysis applications, an evaluation of the surface stability is required. The studied substrates are produced in three steps: (I) the creation of single vacancy graphene flake (SV-G) by removing one carbon atom (see Figure 6-1, labelled X)), and divacancy graphene flake (dV-G) by removing two carbon atoms, (labelled C3 and X)); (II) the replacement of three and four undercoordinated C atoms with N atoms to form the defective N_3-G and N_4-G, respectively; (III) incorporation of Co atom in the center of the SV-G, dV-G, N_3-G and N_4-G making Co-SV-G, Co-dV-G, CoN_3-G and CoN_4-G, respectively. These substitutions were employed in similar theoretical studies [94, 358, 359]. Figure 6-1 shows the optimized configurations of each substrate. NBO charge analysis (q) of each substrate along with the calculated binding energy of Co atom into the vacancy sites, the formation energy, energy gap (E_g), and the corresponding thermodynamic properties are listed in Table 6-1.

For pure graphene, we find a C-C bond length of 1.42 Å that is similar to the experimental value [297]. Working with a graphene flake, a bandgap is expected. We calculate an energy gap of E_g = 2.66 eV, which is used as a reference for comparing the geometry and electronic properties of doped configurations (see Table 6-1). These values are in good agreement with other theoretical and experimental studies [298-300]. In the graphene flake, a single carbon atom adsorbs with an adsorption energy of -7.23 eV into the single vacancy of graphene. One can see that in the SV-G, a five and nine-member ring (5-MR and 9-MR) are produced with C1-C2, C1-C3, and C2-C3 bond lengths of 1.76, 2.77, and 2.81 Å, respectively. By introducing a single Co atom into the SV-G configuration, the Co atom covalently binds to three surrounding carbon atoms of the vacancy site with equal Co-C bond lengths of 1.78 Å. These values are also in good agreement with previous studies (Co-C=1.79-1.90 Å) [360, 361]. Due to the larger atomic radius, the Co atom is pushed outward from the graphene plane in a tetrahedral-like configuration with respect to the neighbouring C atoms (see Figure 6-1), at a height of 1.29 Å above the graphene flake. This result is also in good agreement with other doped metal atoms into the graphene sheet [205, 362]. The calculated binding energy of the single Co atom into the SV-G is E_{bind}= -4.52 eV. To compare charge distributions in the Co-G structures, NBO charges are calculated for all obtained structures. In Co-G, a small charge of +0.25 e is transferred from the Co atom to the surrounding carbon atoms of the vacancy site making the neighbouring carbon atoms negatively charged (-0.30 e)

with Co-C bonds of 1.78 Å.

In the dV-G, first, a 5-8-5 defect [39] is produced and then by introducing the Co atom into the vacancy site, Co-dV-G forms (see Figure 6-1) with low binding energy of E_{bind}= -1.90 eV. According to the NBO charge analysis, a charge of +0.65 e is transferred from the Co atom to the surrounding C atoms of the vacancy site leading to negatively charged C atoms (-0.85 e) with Co-C bond lengths of Co-C = 1.96 Å. If three or four surrounding C atoms of the SV-G or dV-G are substituted by three or four nitrogen atoms, a defective pyridinic N_3-G or N_4-G is created, respectively. According to the previous studies, the presence of pyridinic-N atoms around any defect sites might affect the electronic structure of graphene [205, 363]. The substitution of the vacancy C atoms by N atoms can considerably reduce the formation energy of the mono- or di-vacancy graphene sheet. The reason may refer to the vanishing of the existed dangling bonds in these systems. So, it is clear that the N embedded graphene structures are the dominant configurations. According to the NBO charge analysis, each nitrogen atoms in N_3-G and N_4-G is negatively charged to -0.5 e showing that these negative sites are active enough to trap the Co atom making the CoN_3-G and CoN_4-G.

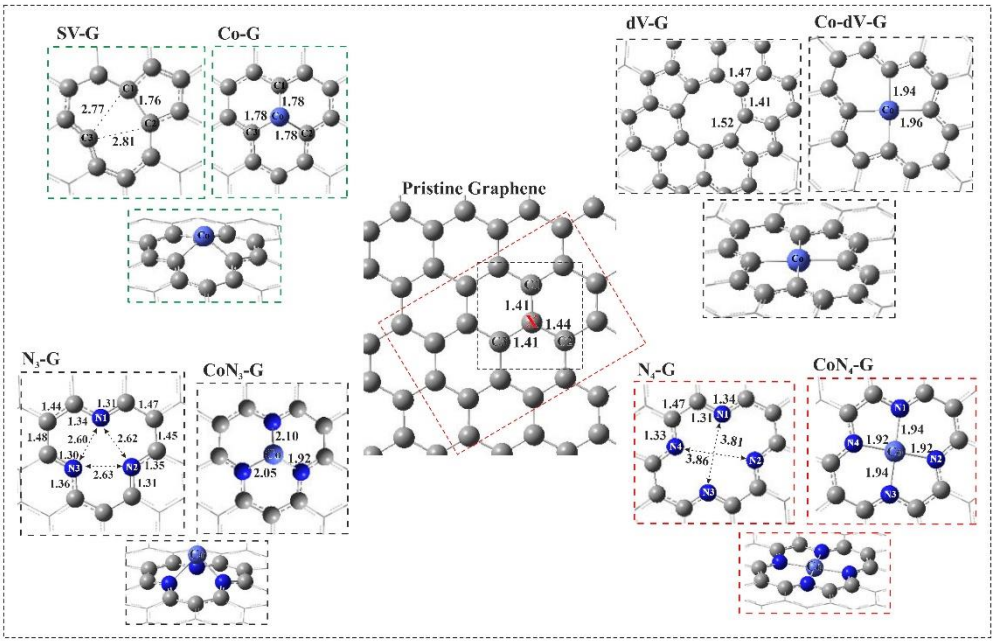

Figure 6-1. The geometric structure of pristine graphene flake, Co-SV-G, Co-dV-G, CoN_3-G and CoN_4-G. All bond lengths are in Å.

In CoN_3-G, the Co atom and the surrounding three nitrogen atoms of the vacancy site are positively (0.46 e) and negatively (-1.86 e) charged, respectively. Therefore, the CoN_3 moiety is negatively charged by -1.4 e with the formation energy of E_f = -0.95 eV. Upon adsorption of a single Co atom into the defective N_3-G, the average bond

length of Co-N is increased considerably to 2.02 Å, pushing the Co atom of the basal plane by 1.36 Å from the graphene flake surface. The calculated binding energy of Co on the N_3-G is E_{bind} = -4.58 eV, which is higher than that of PdN_3-G (E_{bind} = -3.19 eV) [364] and is quite close to that reported by Zhang et al. (E_{bind} = -4.84 eV) [365].

Table 6-1. The calculated NBO analysis (+ and – signs refer to the electron donation and acceptation), binding energy (E_{bind}), formation energy (E_f), energy gap (E_g), change of enthalpy (ΔH_{298}), and change of Gibbs free energy (ΔG_{298}) of pure graphene flake, Co-SV-G, Co-dV-G, CoN_3-G and CoN_4-G.

Complex	$q_{(Co/C\ or\ N)}$(e)	E_{bind} (eV)	E_f (eV)	E_g (eV)	$\Delta H_{298.15}$(eV)	$\Delta G_{298.15}$(eV)
graphene	+0.04	-7.23	-	2.66	-7.19	-7.23
Co-SV-G	+0.25 (-0.30)	-4.52	2.71	3.06	-4.47	-4.18
Co-dV-G	+0.65 (-0.85)	-1.90	3.31	1.78	-1.91	-1.65
CoN_3-G	+0.46 (-1.86)	-4.58	-0.95	2.48	-4.53	-4.21
CoN_4-G	+0.74 (-2.80)	-7.81	-3.47	3.20	-7.67	-7.28

In the defective N_4-G, Co-N2/N4 and Co-N1/N3 bond lengths are equal to 1.92 Å and 1.94 Å, respectively, in agreement with Orellana et al. study (Co-N =1.90 Å) [94]. In contrast to CoN_3-G, the Co adatom adsorbs in the pyridinic N_4-G and lies in the plane format by nitrogen atoms with the formation energy of E_f = -3.47 eV. The higher formation energy of CoN_4-G than CoN_3-G indicates that the Co atom can be more easily interact with the nitrogen atoms of the di-vacancy site than those in the single vacancy site. It adsorbs strongly into the N_4-G site with E_{bind} = -7.81 eV. The high adsorption energy can be related to the additional valence electrons available from the substitutional N atoms that stabilize the unpaired electron of the coordinated C atom of the graphene flake. This results in a higher charge transfer (≈ 0.74 e) from the Co atom to the four nearest N atoms of the surface, which are all negatively charged by ≈ -2.8 e. Also, it is consistent with the high electronegativity of nitrogen atoms compared with that of carbon and Co atoms, such that the Co atom binds stronger with its neighbouring N and C atoms than those in CoN_3-G and Co-G, respectively.

The EDD of three stable substrates is shown in Figure A6-1 in the Appendix section. In Co-G, the charge is mostly accumulating on the surrounding C atoms while we found that the transferred electrons from Co atom and three neighbouring N atoms induce the charge redistribution at their interfaces. Also, as shown in Figure A6-1, the charges mainly accumulate on the N atoms illustrating that more electrons (>1.0 e) are transferred from Co dopant to the neighbouring N atoms leading to the enhancement of their interaction. Similar to CoN_3-G, in CoN_4-G the transferred charge from the Co atom to the four adjacent N atoms is high, and electrons dominantly accumulate on N atoms and around the Co-N bonds. These results indicate that the N_4-G could efficiently stabilize the embedded Co atom, which is stable enough to be used in the catalytic reactions.

Furthermore, by inspecting the electronic states of CoN_3-G and CoN_4-G near the

Fermi level we can better understand the reason for having such large adsorption energies. One can see from Figure A6-2 that there are strong electron coupling between the 3d orbitals of Co atom and the 2p orbitals of N atoms around the Fermi level confirming the existence of covalent Co-N bond in the studied substrates. By doping Co atom into the vacancy site, Co atom pulls down the unoccupied localized anti-bonding states of N atoms to near the Fermi level indicating that when Co atom adsorbs over the vacancy sites, those states are partially occupied. In addition, the incorporation of N atoms shifts the bandgap above the Fermi level gradually confirming the enhancement of electron (donor) concentration states. Similar electronic results are given by Li et al. [366] reporting that the pyridinic nitrogen act as an active catalyst toward ORR [367].

Finally, we evaluate the diffusion of Co atom to its nearest vacancy site in CoN_3-G and CoN_4-G. The stable configurations of CoN_3-G and CoN_4-G are chosen as the initial state (IS). The energy profile and the related stationary structures are depicted in Figure A6-3. Very high diffusion barriers required to diffuse the Co atom to the nearest hollow sites of the surface in both substrates. This confirms the Co atom is stable enough at the defective N_3-G and N_4-G sites that prevent the metal clustering problem. These results are in agreement with the experimental investigations indicating that the bonded Co atom cannot be easily migrated to other hollow sites of the nitrogen-doped graphene surface through the leaching process [368].

6.3.2 Adsorption of gas reactants on CoN_3-G and CoN_4-G

The accumulated charge on the active Co site increases the interaction of the substrate with the gas species by increasing the polarization of the gas molecule. This was also considered in recent studies for hydrogen storage purposes [369]. There are three different active sites on each substrate, Co, N and, C. Depending on which active site the gas reactant (CH_4, O_2, N_2O) adsorbs on, different adsorption configurations will be obtained. It should be noted that for each adsorbate various adsorption sites and different adsorption patterns (including side-on and end-on) are considered. Similar to earlier reports we found that each species tends to directly interact with the metal atom at the center of the vacancy site [76, 94, 370]. The corresponding geometric structures of adsorbed gas reactants on CoN_3-G, and CoN_4-G along with their EDD maps are shown in Figure 6-2. Additionally, the calculated E_{ads}, NBO charge analysis, and thermodynamic properties of the species are reported in Table 6-2.

One can see from Figure 6-2 that in complexes A and D, methane molecule adsorbs physically over the Co atom, at a distance of 2.46 Å and 3.00 Å and with an adsorption energy of E_{ads} = -0.38 eV and E_{ads} = -0.21 eV, respectively. The corresponding calculated charge transfer from methane to the surface in complexes A and D is 0.14 e and 0.07 e, respectively. These weak interactions are also apparent from their EDD map, showing almost no charge accumulation around the Co-C bond in the two complexes. Interestingly, adsorption of methane on CoN_3-G is exothermic while its adsorption on

CoN_4-G is not spontaneous at room temperature (see Table 6-2).

In contrast to methane, the adsorption of O_2 on CoN_3-G is quite strong. In both complexes, the O_2 molecule tends to adopt a parallel position with the surface on the Co atom. In complex B, O_2 adsorbs on the Co atom makes a V shape with two Co-O bond length of 1.80 Å and large adsorption energy of E_{ads} = -1.24 eV, which is lower than that on PtN_3-G (-1.89 eV) [85]. A charge of +0.46 e is transferred from the CoN_3-G to the adsorbed O_2 molecule which makes the Co atom more positive (0.71 e), leading to the stronger adsorption of O_2 on the CoN_3-G surface and significant elongation of the O-O bond (1.40 Å). The EDD map of complex B correspondingly illustrates that the charge accumulation regions are mostly localized between the Co-O and O-O bonds. Furthermore, the higher reaction enthalpy for the formation of complex B shows that this substrate is more activated toward adsorption of O_2 molecule, $\Delta H_{298.15}$ = -1.22 eV and $\Delta G_{298.15}$ = -0.72 eV.

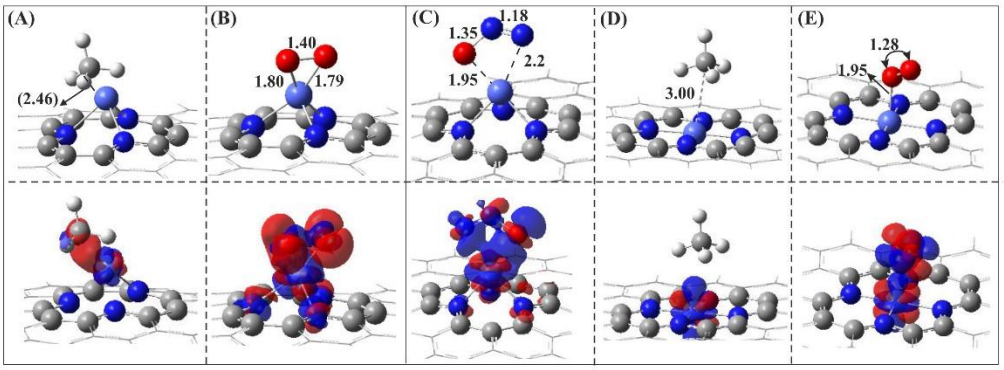

Figure 6-2. The most plausible geometric structures of the gas reactants on CoN_3-G and CoN_4-G along with the corresponding EDD map. All distances are in Å.

Table 6-2. The calculated adsorption energy (E_{ads}), NBO charge analysis (q) (+ and – signs refer to the electron donation and acceptation), change of enthalpy ($\Delta H_{298.15}$), and change of Gibbs free energy ($\Delta G_{298.15}$), of the adsorption configurations. All energies are in eV.

Complex	E_{ads} (eV)	$q_{Co/ads}$(e)	$\Delta H_{298.15}$ (eV)	$\Delta G_{298.15}$ (eV)
CoN_3-G	-	+0.46	-	-
A	-0.38	+0.33/+0.14	-0.34	-0.02
B	-1.24	+0.71/-0.46	-1.22	-0.72
C	-0.02	+0.72/-0.51	0.01	0.36
O-CoN_3-G	-2.93	+0.80/-0.52	-2.86	-2.48
CoN_4-G	-	+0.74	-	-
D	-0.21	+0.68/+0.07	-0.16	0.11
E	-0.24	+0.72/+0.04	-0.20	0.16

The O_2 molecule adopts an end-on configuration on CoN_4-G at a distance of O-Co = 1.95 Å. it adsorbs weakly on the CoN_4-G surface with a low adsorption energy E_{ads} = -0.24 eV, which can be due to the stronger binding energy of Co-N (-7.81 eV) (see Table 6-1). The obtained adsorption energy value is somewhat lower than the value reported

by Feng et al. (E_{ads} = -0.85 eV) [92], FeN_4-G (E_{ads} = -0.98 eV) and MnN_4-G (E_{ads} = -0.35 eV) [331, 371]. Consistent with the weak interaction, a negligible charge of +0.04 e is transferred from the surface to the adsorbed O_2 molecule. In the EDD map, the blue color areas around the Co-O bond confirm the weak interaction of O_2 with the surface. However, the formation of complex E is exothermic $\Delta H_{298.15}$ = -0.20 eV and endergonic $\Delta G_{298.15}$ = 0.16 eV.

Since the interaction of O_2 with CoN_3-G is stronger than that on CoN_4-G, we also evaluated the dissociation of O_2 on CoN_3-G to confirm the stability of the adsorbed structure toward oxygen dissociation. To find the energy profile of the O_2 decomposition, we started with the most stable adsorption configuration of O_2 on CoN_3-G (complex B) as IS and shown in Figure A6-4. Passing via the TS structure, the FS is obtained in which two individual O atoms are dissociatively adsorbed on Co and C atom of the surface. The formed O-Co and O-C bond lengths are 1.62 Å and 1.37 Å, respectively. The calculated activation barrier for the O_2 dissociation on CoN_3-G is calculated to be E_{act} = 2.76 eV and the reaction is endothermic, $\Delta H_{298.15}$ = 1.23 eV, and endergonic $\Delta G_{298.15}$ = 1.20 eV. The large decomposition barrier of O_2 on CoN_3-G confirms the stability of the adsorbed O_2 molecule over the surface and its low tendency to dissociate over the CoN_3-G surface.

Various spin multiplicities were considered for each configuration, i. e., singlet, doublet, triplet, and quadruplet. Our results reveal that as a function of progress of the reaction, the spin multiplicity changes eider from singlet to triplet or from doublet to quadruplet, and vice versa. The dominant spin multiplicity of some species like OH, CH_3, CH_2, CH, O, O_2, and CH_4 on Co-N_3G and CoN_4-G is different. Therefore, the energetically more stable configurations are chosen for our calculations. In addition, the adsorption behaviour of CoN_3-G and CoN_4-G toward adsorption of the gas reactants and intermediates in different spin multiplicities were also been tested. For instance investigating the O_2 dissociation on CoN_3-G considering singlet and triplet states, we chose the triplet multiplicity for the dissociation pathway not only because the configurations are energetically more stable but also because the calculated activation barrier is lower in the triplet state (2.76 eV) than in the singlet state (3.02 eV). A similar comparison was made for other configurations. Here, the energetically more favourable structures are reported.

According to above discussions and previous investigations [85, 372], we conclude that amongst the studied substrates, CoN_3-G is more active toward adsorption of gas reactants, especially O_2 molecule, and therefore is more favourable for methane conversion reaction which is in good agreement with Kattel et al. work [31]. The higher adsorption energy of O_2 molecule than methane reveals that the reactive Co sites will be dominantly covered by the O_2 when exposed to a CH_4/O_2 mixture as the reaction gas. However, the co-adsorption of CH_4 and O_2 on CoN_3-G (E_{ads} = -1.66 eV) is stronger than

the sum of the individual adsorption of CH_4 or O_2 on CoN_3-G (see Table 6-2). Therefore, we propose that all the reaction pathways start with the co-adsorption configuration of CH_4 and O_2 on the surface.

Recent theoretical studies [373-375] reported that the N_2O molecule attaches to metal-embedded nanostructures via different configurations. It may adsorb via a linear parallel position with the surface, a [3+2]- or [2+2]-cycloaddition configuration. Here, on CoN_3-G, the N_2O molecule adsorbs weakly, E_{ads} = -0.02 eV, via its O and N atoms with the Co atom of the surface while the N–N–O angle decreases from 180° in the gas phase to 123.37° in the adsorbed form (configuration C, Figure 6-2). Interestingly, upon the adsorption of N_2O on the surface, it immediately dissociates to $N_{2(g)}$ and atomic O^* molecule above active Co site (see Figure A6-5). The reaction is barrierless and thermodynamically favourable at room temperature ($\Delta H_{298.15}$ = -2.35 eV, $\Delta G_{298.15}$ = -2.43 eV). It is shown that in the final state the atomic O^* adsorbs chemically on Co atom with Co-O bond length of 1.81 Å and E_{ads} = -1.49 eV.

6.3.3 Conversion of methane to methanol on monolayer CoN_3-G

The energy landscapes for CH_x (x=0-4) adsorption and CHx (x=1-4) dehydrogenation over CoN_3-G along with the most probable C-C coupling reaction are explained and shown in the Appendix section. There are two different mechanisms for C-H bond cleavage, a surface-stabilized or a radical-like mechanism [357, 376]. In the first mechanism, the carbon atom of methane molecule partially interacts with the catalyst, while in the radical-like mechanism there is no binding or interaction with the catalyst. It is known that the radical-like pathway is the more probable route for single atom catalysts [377] due to the lower concentrations of the active sites on these substrates making them promising candidates for the direct methane to methanol oxidation [378]. We propose two different pathways for direct conversion of CH_4 to CH_3OH on CoN_3-G using N_2O and O_2 as an oxidant. N_2O acts as an O-donor compound that provides atomic oxygen to oxidize methane to methanol. Depending on the oxidation agent, the formed intermediates, and subsequently, the reaction pathways are different. The formed intermediates are a combination of $^*OH$, CH_3^*, $^*OOH$, and CH_3O^*. The schematic reaction mechanisms of oxidation routes are shown in Scheme 6-1. Most of the reactions proceed via the LH mechanism.

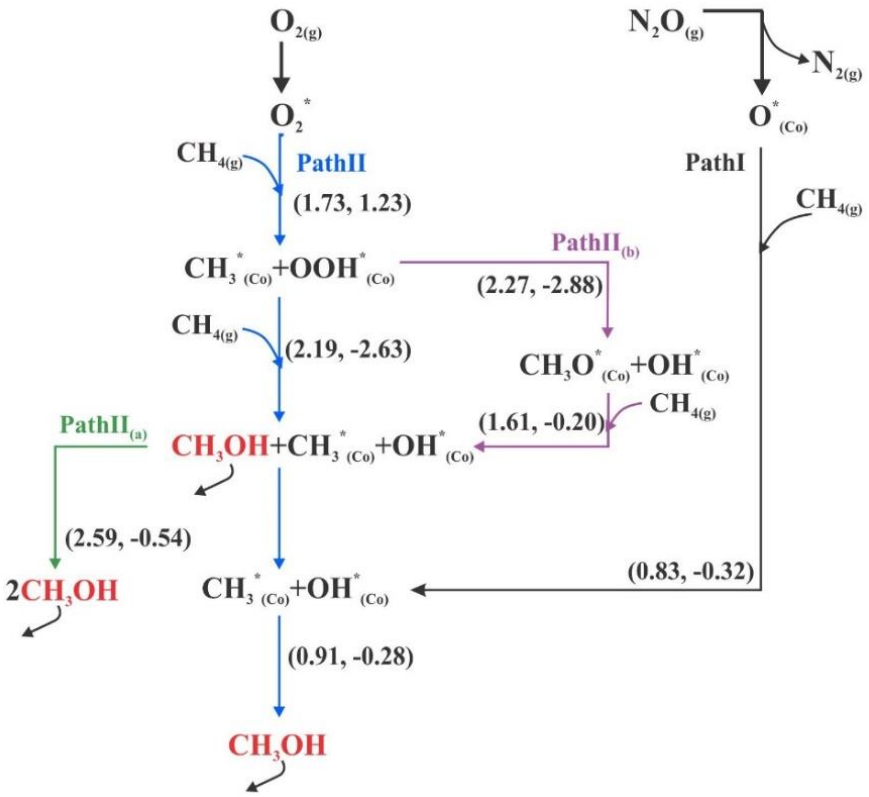

Scheme 6-1. Proposed reaction pathways on CoN_3-G. The values in parentheses refer to the energy barriers and enthalpy of the reaction in eV

6.3.3.1 Methane to methanol oxidation by N_2O

Upon desorption of N_2, the remained atomic oxygen reacts with methane to form methanol. This pathway goes through the formation of CH_3^* and OH^* intermediate species. The related stationary structures along with the preferential potential energy pathways are shown in Figure 6-3. The calculated reaction heats and the corresponding barriers are summarized in Table 6-3.

In pathway I, the oxidation reaction starts with co-adsorption of O^* and CH_4 named as IS-1. Hydrogen abstraction with oxygen occurs passing via a low energy barrier of E_{act} = 0.83 eV results in the formation of CH_3^* and $^*OH$ intermediate species on top of the Co site (MS-1) that is in good agreement with Yuan et al. work (E_{act} = 0.7 eV) [374]. Then, the combination of CH_3^* and $^*OH$ species produces the methanol molecule on CoN_3-G surface. The required energy barrier of this reaction is E_{act} = 0.91 eV. The obtained activation energies are in good agreement with that of O@Pd-BN reported by Latimer et al. [379]. According to the thermodynamic results, all the reactions are exothermic and exergonic (see Table 6-3). Due to the higher activation energy of the reaction MS-1⟶ P-1, we propose it to be the rate-limiting step.

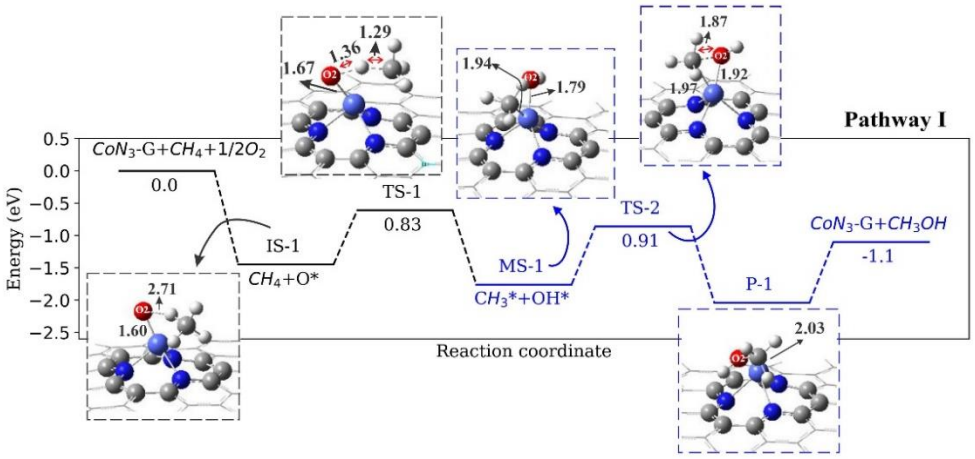

Figure 6-3. The optimized stationary points for the methane oxidation on CoN_3-G along with the corresponding energy profile of methane conversion by N_2O. All distances are in Å

Table 6-3. The calculated energy barrier (E_{act}), change of enthalpy ($\Delta H_{298.15}$) and change of Gibbs free energy ($\Delta G_{298.15}$) for different methane oxidation reactions on CoN_3-G

Reaction	$E_{act\text{-}f}$ (eV)	$E_{act\text{-}b}$ (eV)	$\Delta H_{298.15}$ (eV)	$\Delta G_{298.15}$ (eV)
Pathway I				
$N_2O_{(g)} \longrightarrow N_{2(g)} + O^*$	0.00	2.27	-2.35	-2.43
$CH_{4(g)} + O^* \longrightarrow CH_3^* + OH^*$	0.83	1.15	-0.32	-0.30
$CH_3^* + OH^* \longrightarrow CH_3OH_{(g)} + *$	0.91	1.19	-0.28	-0.28

6.3.3.2 Methane to methanol oxidation by O_2

The proposed pathway II starts with the coadsorption of O_2 and CH_4 at a distance of H-O2 = 2.40 Å above the surface (Figure 6-4, IS-2). Interestingly, we found that the C-H and Co-O cleavage of methane and adsorbed atomic O^* has the highest barrier energies of E_{act} = 1.73 eV and E_{act} = 2.19 eV, respectively, which inhibited the formation of methanol. In both first and second reaction of methane with oxygen, breaking of the C−H bond occurs concurrently with the formation of an O−H bond and Co−C bond on CoN_3-G, and a further elongation of the O−O bond to 1.97 Å. Formation of the first CH_3OH occurs with the introduction of second methane to the system IS-3⟶P-2. Although the activation of second CH_4 requires ∼0.46 eV more energy it is more exergonic (see Table 6-4). The second CH_3OH is formed upon the association of the CH_3^* and $^*OH$ species with a reasonable energy barrier of 0.91 eV. Finally, upon the desorption of the second CH_3OH, E_{des}= 0.57 eV, the catalytic cycle is closed. As CH_4 is only physisorbed at Co active site and then reacts with preadsorbed O_2, the methane conversion mechanism in all the reactions can be described as an ER mechanism, except the reaction MS-1⟶P-1 that proceeds via the LH mechanism. The rate-limiting step is the formation of P-2 (second C−H and Co-O cleavage).

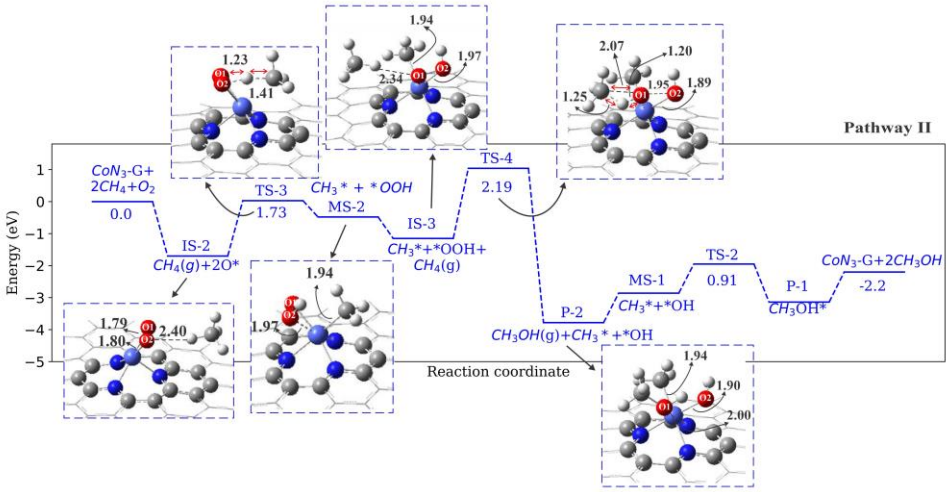

Figure 6-4. The optimized stationary points for methane oxidation on CoN_3-G along with the corresponding potential energy profile of pathway II. All distances are in Å

We also investigated the other possibilities of methanol formation on CoN_3-G by formation of other intermediates. We found two other possible pathways (labeled as pathways $II_{(a)}$ and $II_{(b)}$) that goes via the formation and recombination of CH_3^*, O^*, OH^*, and CH_3O^* species on CoN_3-G. The related potential energy profile is shown in Figure A6-8. The calculated activation energies and thermodynamic values are listed in Table 6-4. One can see from Figure A6-8 that in Pathway $II_{(a)}$ and $II_{(b)}$ the reaction MS-2 ⟶ MS-3 (formation of CH_3O^* and $^*OH$) and P-2 ⟶ P-3 requires is the rate limiting step, respectively. Therefore, we estimate that the possibility of methane conversion to methanol via pathways $II_{(a)}$ and $II_{(b)}$ is very low.

Table 6-4. The calculated energy barrier (E_{act}), change of enthalpy ($\Delta H_{298.15}$) and change of Gibbs free energy ($\Delta G_{298.15}$) for different methane oxidation reactions on CoN_3-G.

Reaction	E_{act} (eV)	$\Delta H_{298.15}$ (eV)	$\Delta G_{298.15}$ (eV)
Pathway II			
$O_{2(g)}+2^* \rightarrow 2O^*$	0.00	-1.22	-0.72
$CH_{4(g)} + 2O^* \longrightarrow CH_3^* + {}^*OOH$	1.73	1.23	1.38
$CH_{4(g)} + CH_3^* + {}^*OOH \longrightarrow CH_3OH_{(g)} + CH_3^* + {}^*OH$	2.19	-2.63	-2.52
$CH_3^* + {}^*OH \longrightarrow CH_3OH_{(g)} + 2^*$	0.91	-0.28	-0.28
Pathways $II_{(a)}$ and $II_{(b)}$			
$CH_3^* + {}^*OOH \longrightarrow CH_3O^* + {}^*OH$	2.27	-2.88	-2.97
$CH_{4(g)} + CH_3O^* + {}^*OH \longrightarrow CH_3OH_{(g)} + CH_3^* + {}^*OH$	1.61	-0.20	-0.20
$CH_3OH_{(g)} + CH_3^* + {}^*OH \longrightarrow 2CH_3OH_{(g)} + 2^*$	2.59	-0.54	-0.47

In fact, to produce methanol, the most favourable pathway is pathway I in which methane catalysed by atomic oxygen, which is donated to the system by dissociative adsorption of N_2O over CoN_3-G. It proceeds via the LH mechanism and all the reactions are thermodynamically favourable. Therefore, we propose that CoN_3-G can actively

convert methane to methanol using N_2O as an oxidant agent thanks to the lower activation barriers.

6.4 Conclusions

In summary, the geometric stability and catalytic activity of Co-SV-G, Co-dV-G, CoN_3-G and CoN_4-G toward adsorption of gas reactants are studied in detail by means of DFT calculations. Studying the geometric, electronic and thermodynamic properties of all optimized structures showed that amongst other modified graphene flakes, CoN_3-G and CoN_4-G are energetically more stable than other substrates. Investigating the adsorption behavior of CoN_3-G and CoN_4-G toward the gas reactants indicated that CoN_3-G has a higher tendency for the adsorption of methane and oxygen. Therefore, we chose CoN_3-G as for methane-to-methanol oxidation. Two powerful oxidants are used for catalyzing methane oxidation, viz. O_2 and N_2O. N_2O adsorbs dissociatively on CoN_3-G providing atomic oxygen for methane oxidation. Oxidation of methane by means of N_2O proceeds via two steps on CoN_3-G with considerably lower energy barriers while using O_2 as oxidant proceeds through a pathway with higher activation barriers. All the C-H bond cleavage reactions proceed via the ER mechanism and followed by the LH mechanism.

Investigating the adsorption (CH_x, x=0-4) and dehydrogenation (CH_x, x=1-4) process of methane on CoN_3-G indicated that the adsorption energy of CH_4, CH_3, CH_2, CH, and C on CoN_3-G increases by reducing the number of hydrogen atoms. In the dehydrogenation process, all pathways start from the C-H scission ($CH_x \longrightarrow CH_{x-1} + H$) and dehydrogenation of methane to methyl showed the lower energy barrier of 1.10 eV. This makes the C-C coupling of the two-methyl group to ethane easier passing via an energy barrier of 0.45 eV. Our results suggest a two-step method for methanol formation on CoN_3-G using N_2O as an oxygen-donor. To the best of our knowledge, this is the first report on the direct oxidation of methane-to-methanol on CoN_3-G using different oxidants. We believe our findings may open a new way to design such heteroatom doped graphene-based single atom catalysts to eliminate toxic molecules, which are harmful to the environment.

6.5 Appendix

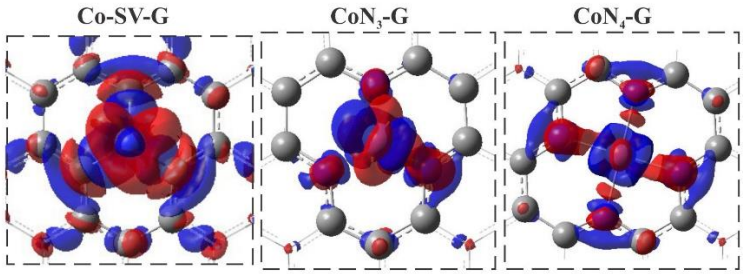

Figure A 6-1. The electron charge distribution (EDD) plots of Co-SV-G, CoN_3-G, and CoN_4-G

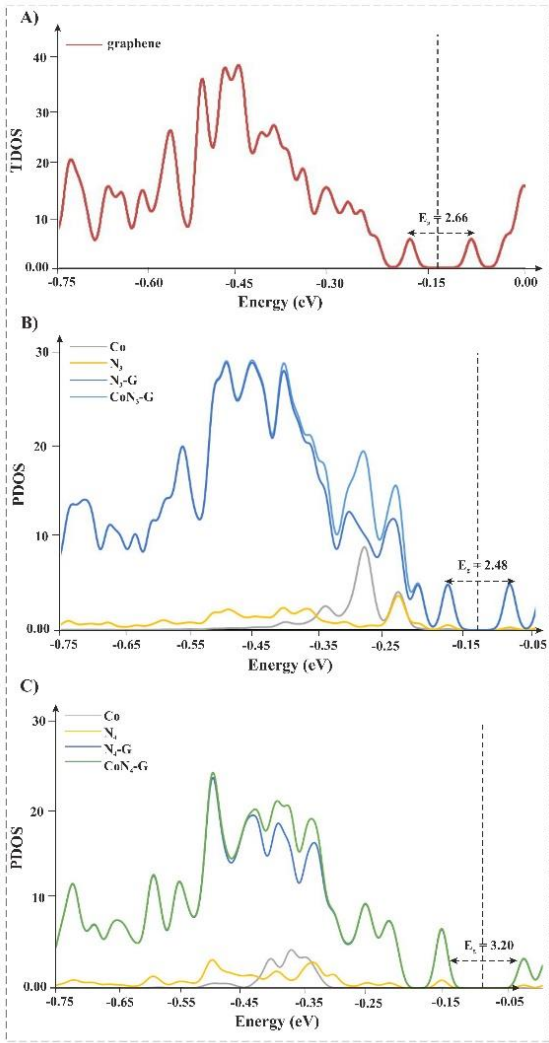

Figure A 6-2. Total density of state (TDOS) diagram for pure graphene flake (A) and Partial density of state (PDOS) diagram for CoN_3-G (B) and CoN_4-G (C) systems.

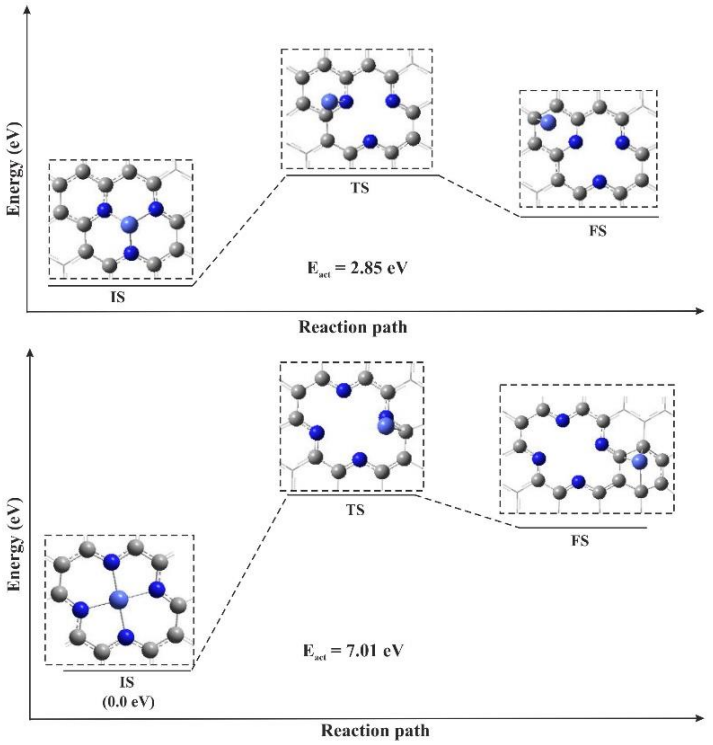

Figure A 6-3. The free energy diagram of the most probable diffusion of single Co atom on the CoN_3-G and CoN_4-G along with their corresponding optimized structures of initial state (IS), transition state (TS) and final state (FS). All distances and free energy values are in Å and eV, respectively.

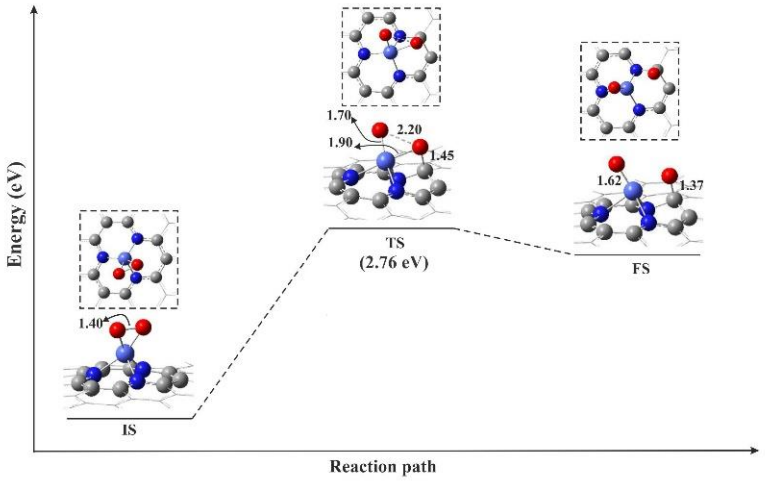

Figure A 6-4. The energy profile of the O_2 dissociation on CoN_3-G along with the related optimized structures of the stationary states. All distances are in Å

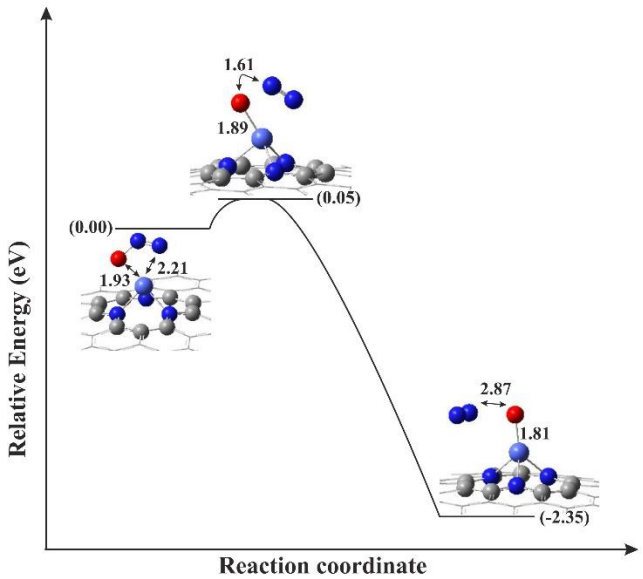

Figure A 6-5. Potential energy profile for dissociation reaction of $N_2O_{(g)} \rightarrow N_{2(g)} + O^*$ on CoN_3-G surface

Adsorption of CH_x (x=0-4) on CoN_3-G

To understand the catalytic activity of the CoN_3-G toward activation of methane, we investigated the adsorption and dehydrogenation of CH_x (x = 0-4) on the surface. The more energetically favourable configurations of the adsorbed species are shown in Figure A6-6. The calculated adsorption energies, bond lengths and adsorption thermodynamics are listed in Table A6-1. Our results show that the Co-C bond lengths almost decrease with a decrease in the number of H atoms. This can be due to the increase in free valence electrons by decreasing the H atoms, which results in the stronger interactions (shorter Co-C bond length) between CH_x and the CoN_3-G surface. Interestingly, the C-H bond lengths in most of the case are a fixed number of about 1.10 Å showing that the geometry of the adsorbed CH_x does not change after the adsorption. These values are in close agreement with those of Au- and Al-graphene [182] and Pt-graphene [380].

The non-planar methyl adsorbs on the top of Co atom with H-C-H angles (107.3°) indicating the sp^3 hybridization of C atom while the C atom in the radical methyl has sp^2 hybridization. In contrast to CH_3, the CH_2 fragment binds more strongly to the Co atom resulting in the shorter Co-C bond length. The H-C-H angle is 108.4° indicative of sp^2 hybridization. CH forms a bridge between C and N atoms with Co-C and N-C bond lengths of 1.90 Å and 1.46 Å indicating that it tends to interact with N atom rather than C atom.

Table A 6-1. Adsorption energies, Co–C bond lengths, changes of enthalpy ($\Delta H_{298.15}$), and changes of Gibbs free energy ($\Delta G_{298.15}$) of CH_x (x = 0–4) on CoN_3-G.

Species	E_{ads} (eV)	Co-C (Å)	$\Delta H_{298.15}$ (eV)	$\Delta G_{298.15}$ (eV)
CH_4	-0.38	2.46	-0.34	-0.02
CH_3	-1.77	2.00	-1.63	-1.17
CH_2	-2.95	1.80	-2.80	-2.33
CH	-3.07	1.90	-2.98	-2.45
C	-4.71	1.81	-4.73	-4.27

Upon adsorption of CH_4, it may dissociate to CH_3, CH_2, CH, and C surface fragments. Therefore, to find the relative stability of the intermediates we calculate the dehydrogenation reactions of CH_4 on the CoN_3-G surface. The optimized stationary structures of each reaction are shown in Figure A6-6. In the dehydrogenation processes, a hydrogen atom transfers from CH_x (x=1-4) to either the surrounding N atoms or Co atom and then desorbs from the surface. In the next step, the remaining specie is considered as the initial state and undergoes the next hydrogenation reaction. The forward and backward barrier energies and thermodynamic properties are reported in Table A6-2. In contrast to methane, the dehydrogenation of CH_3, CH_2, and CH are more difficult regarding to the high activation energies (> 2.00 eV) indicating that hydrogen atom tends to reacts with CH_3, CH_2, and CH species to form the more stable configuration of CH_4, CH_3, and CH_2 and CH, respectively (Table A6-2).

Table A 6-2. Forward and backward barrier energies, changes of enthalpy ($\Delta H_{298.15}$), and changes of Gibbs free energy ($\Delta G_{298.15}$) for dehydrogenation reactions on CoN_3-G

Reaction	E_{act-f} (eV)	E_{act-b} (eV)	$\Delta H_{298.15}$ (eV)	$\Delta G_{298.15}$ (eV)
$CH_4 \rightarrow CH_3+H$	1.10	0.00	1.09	1.14
$CH_3 \rightarrow CH_2+H$	2.90	0.39	2.49	2.56
$CH_2 \rightarrow CH+H$	2.05	0.47	1.58	1.57
$CH \rightarrow C+H$	2.72	0.08	2.66	2.58

C-C coupling reactions on the CoN_3-G surface

C-C coupling depends on the binding energies of the adsorbed CH_x species. Amongst all CH_x species adsorbed on CoN_3-G, methyl group adsorbs on the surface with lower adsorption energy. In addition, since the dehydrogenation of CH_4 to CH_3^* requires lower activation energy, then we can estimate that there might be a possibility of ethane formation in a C-C coupling process during the oxidation reaction. The related initial, transition, and final structures of this coupling reaction are demonstrated in Figure A6-7. The low barrier energy and exergonicity of the reaction confirm that this reaction is likely to occur. The obtained activation energy is almost 2.45 eV lower than that of IrO_2(110) surface [381]. Therefore, our results indicate that the self-coupling reaction of CH_3 is more energetically and thermodynamically favourable than other C-C couplings.

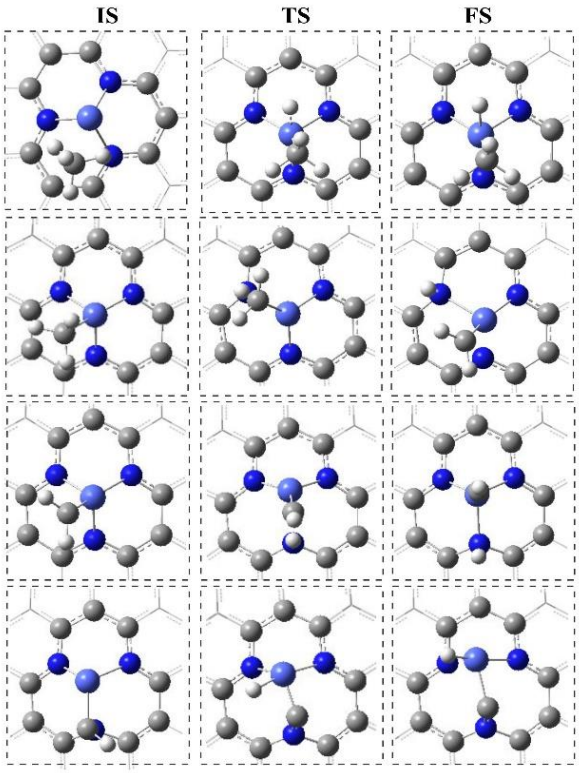

Figure A 6-6. Initial state, transition state and final state for dehydrogenation reaction of CH_x (x=1-4) on the CoN_3-G surface

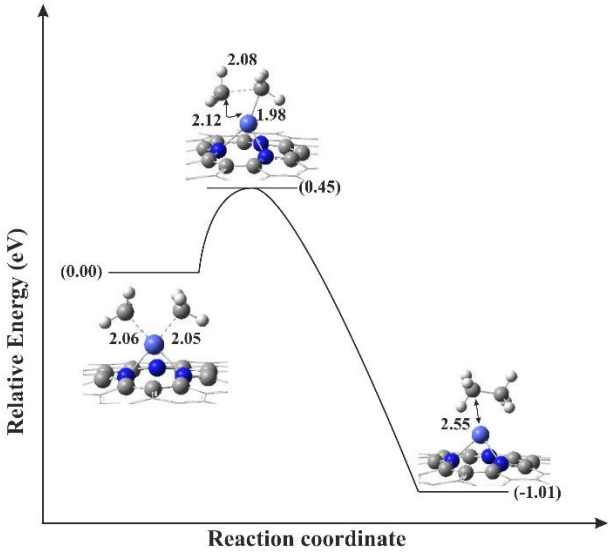

Figure A 6-7. Potential energy diagram for C_2H_6 formation on the CoN_3-G surface

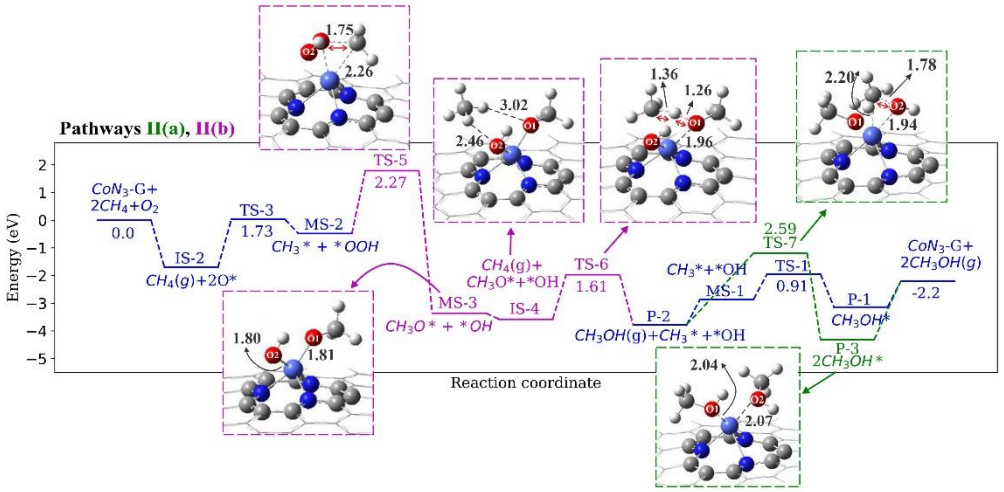

Figure A 6-8. The optimized stationary points for methane oxidation on CoN_3-G along with the corresponding potential energy profile of pathways II(a) (showed in blue-purple-green colors) and II(b) (showed in blue-purple-blue colors). All distances are in Å.

Conclusions and outlook

The detailed mechanisms of catalytic gas conversion reactions on nanostructured surfaces are still not entirely known. In this thesis, I employed DFT calculations to study the catalytic activity of tailored nanocatalysts toward gas conversion reactions. The selected nanocatalysts are graphene, carbon nanotubes, boron carbon nitride nanosheets, and boron carbon nitride nanotubes. To further increase their catalytic activity, the surfaces of these nanocatalysts are modified by introducing different defects and single metal atoms or heteroatoms into their structure. Such modified nanocatalysts hold great promise for gas conversion applications. To better understand the fundamental catalytic properties of each nanocatalyst, their structural and thermodynamic properties must be controlled. To gain a fundamental insight in the catalytic reactions, the interaction of the gas species on and with the surface, and the corresponding reaction mechanisms are also investigated.

7.1 Modified graphene

It is known that modification of nanostructured carbon by doping heteroatoms, like N, into the graphene lattice, and especially metal atom embedded pyridinic-N graphene (MN_4-G), considerably increases their electronic and catalytic properties for the Oxygen Reduction Reaction (ORR) in fuel cells. However, in our study as outlined in Chapter 3, we found that this is not generally true, at least in methane conversion to methanol. I used M- and M-doped pyridinic-N_4 graphene flake (M=Ni and Si) to fundamentally investigate the activity of those modified surfaces toward activation of methane and consequently its oxidation to methanol. I considered two spin multiplicities, singlet and triplet, for all the optimized structures to better understand the effect of the spin multiplicity on the adsorption behavior and catalytic activity of the used substrates. Depending on the used multiplicity, the adsorption of the gas reactants and correspondingly, the oxidation pathway, and the dominant reaction mechanism change. According to our results, the energetically most stable configurations for graphene flake and Si-G were obtained by considering the singlet multiplicity, while Ni-G and SiN_4-G had lower energy and higher energetic stability with triplet multiplicity. Comparing the calculated adsorption energies of a metal atom into the graphene flake vacancy site showed the following order: Si-G > pure graphene flake> SiN_4-G > Ni-G. Therefore, these calculations indicate that Si-G is the most stable configuration of the investigated structures. Studying the adsorption behavior of each substrate toward the adsorption of gas reactants showed that the energetically more stable adsorption configuration of methane on Ni-G, Si-G, and SiN_4-G are the systems with triplet, singlet, and triplet spin multiplicity, respectively. Moreover, the adsorption of O_2 on Si-G with triplet multiplicity and on Ni-G and SiN_4-G with singlet multiplicity is energetically more stable due to the lower (more negative) total energy.

In the next step I investigated the oxidation of methane to methanol considering both singlet and triplet spin multiplicities. Interestingly, depending on the spin state, methane oxidation proceeds via a non-radical or radical process. Also, it determines the reaction mechanism, viz. Eley-Rideal or Langmuir-Hinshelwood. Methane oxidation on Ni-G, Si-G and SiN_4-G considering singlet state, goes through three main reactions in which the direct formation of methanol in the first step, subsequently proceeds via the ER mechanism and finally an LH process closes the catalytic cycle. The obtained activation energies on Ni-G and SiN_4-G were rather high (> 2.00 eV) while in Si-G the activation energies were in the range of 1.20-1.89 eV. For the triplet spin state, methane adsorption and activation on Si-G and SiN_4-G proceeds through four main reactions and via a radical process. We proposed that methane oxidation on Si-G proceed via the ER mechanism, which goes through different stepwise reaction pathways.

A careful comparison of the energies of each configuration demonstrates that Si-G and SiN_4G adopt the triplet and singlet spin state, respectively, in catalyzing methane to methanol. However, when using SiN_4-G, the obtained configurations appear not to be stable. Therefore, we propose that Si-G might be a suitable catalyst for methane-to-methanol oxidation, thanks to the low energy barriers (<1.37 eV) and higher energetic stability of the obtained configurations.

In Chapter 6, the effects of pyridinic-N_3- and N_4-doping into the Co atom embedded single vacancy (Co-SV-G) and di-vacancy graphene flake (Co-dV-G) is investigated and compared toward direct oxidation of methane to methanol by means of two different oxidants (N_2O and O_2). Analysis of the surface properties showed that amongst the four studied substrates, Co atom is more stable at the defective N_3-G and N_4-G sites thanks to the higher binding energy of Co atom into the graphene flake lattice, lower formation and total energy which make these surfaces stable toward metal clustering. Our calculations further revealed that CoN_3-G is more active toward the adsorption of gas reactants, especially O_2, than CoN_4-G. Moreover, the higher adsorption energy of O_2 than methane results in the Co sites to be dominantly covered by O_2 when exposed to a CH_4/O_2 mixture as the reaction gas.

A two-step method for methanol formation on CoN_3-G using N_2O as an oxygen-donor is suggested. Upon dissociative adsorption of N_2O on the surface, it produces the N_2(g) and atomic O^* at the active Co site at room temperature. Then, the oxidation reaction starts with the co-adsorption of O^* and CH_4. C-H bond cleavage of methane results in the formation of CH_3^* and $^*OH$ intermediate species on top of the Co site. Then, the combination of CH_3^* and $^*OH$ species produces the methanol molecule. Further, our calculations indicate that oxidation of methane on CoN_3-G using N_2O as an oxidant is kinetically and thermodynamically more favorable. The calculated activation barriers are 0.83 eV and 0.91 eV.

7.2 Modified BC_2NNF and BC_2NNT

CO oxidation over metallic surfaces as well as carbon-based nanocatalysts has been studied quite extensively. In Chapters 4 and 5 of this thesis, we studied this well-known reaction on modified BC_2NNF and BC_2NNT substrates. The pure BC_2NNF and BC_2NNT substrates are modified in two different ways; (i) by doping a single Si atom into the four different C-vacancy sites, and (ii) by introducing two types of N-vacancy defects (NB- and NBC-) to their surfaces.

In Chapter 4, we first investigated the energetic stability of the different structures. We found that the most stable configuration of Si-BC_2NNF and Si-BC_2NNT is the one where a Si atom is embedded in a single vacancy site with one N and two other C atoms. Starting from the co-adsorption configurations of CO and O_2, the CO oxidation proceeds via two main reactions, (i) $O_{2(g)} + CO_{(g)} \rightarrow CO_{2(g)} + O_{(ads)}$ and (ii) $O_{(ads)} + CO_{(g)} \rightarrow CO_{2(g)}$. The first reaction proceeds on both Si-BC_2NNF and Si-BC_2NNT via the LH mechanism while the second goes through the ER mechanism. According to our computations, Si-BC_2NNF could be considered as a possible candidate for low-temperature CO oxidation with better activity than Si-BC_2NNT.

In Chapter 5, two different N-vacancies are considered in each of these structures in which the vacancy site is surrounded by either three B-atoms (NB) or by two B- and one C-atom (NBC). By means of the healed BC_2NNF and BC_2NNT as a catalyst, the removal of toxic NO and CO is possible. Therefore, by using this method, defective BC_2NNF / BC_2NNT can be purified. According to our results, in O-removal by a second NO molecule, the NBC-BC_2NNF and NBC-BC_2NNT show moderate activation energies (0.73 eV and 0.69 eV), which are lower than those in the case of NB-vacancies. In the O-removal by a CO molecule, the NBC-BC_2NNF shows the lowest barrier energy (0.07 eV) of all configurations. Thus, we can conclude that the NO molecule could be a promising candidate to heal the N-vacancy defects in both BC_2N nanostructures. Moreover, both the NBC-BC_2NNF showed better activity toward the removal of O_{ads} with NO and CO molecules. This study could be very helpful in both purifying the defective BC_2NNF / BC_2NNT and in the same effort removing toxic NO and CO gases.

7.3 Outlook

Recently, the use of non-metal catalysts received considerable experimental attention. Although there are various investigations indicating that so-called single metal atom embedded graphene-based nanocatalysts (SANCs) are promising catalysts for different catalytic reactions, however, so far very few computational models have been developed on the detailed atomic and kinetic properties of the gas conversion reactions on SANCs to support the experiments. In this thesis, I have partially filled this knowledge gap.

In Chapters 3 and 6 we demonstrated that the spin multiplicity has an important effect on the adsorption of gas reactants and correspondingly, on the reaction mechanisms and also the oxidation pathways. Nevertheless, the effects of other parameters like the addition of extra charge, or external electric fields on the conversion process are not known. We found that introducing pyridinic-N atoms into the lattice of graphene might or might not increase the activity of the substrate for catalytic reactions, especially the methane oxidation reaction. SiN_4-G and CoN_4-G were not so active for methane conversion while CoN_3-G confirmed the claim that heteroatom doped graphene can play a significant role in tuning the electric and catalytic properties of the graphene flake. Doping or bi-doping with other heteroatoms, such as B, P, O, and S, into different defective graphene surface sites could also be explored further: which defects are more active for methane oxidation, what ratio of doping would be the best, etc. Also, we may be interested to know other ways of graphene modification. Doping bi-metals or small metal clusters into different defective graphene flakes would be an interesting way to tune the surface and can be investigated more carefully.

In Chapters 4 and 5, we worked on tuning and healing of defective graphene-like nanostructures, i.e., BC_2N nanostructures. Further investigations can be done on using either decorating single metal- or small metal clusters-doping into the defective BC_2N nanostructures. Increasing the number of metal atoms, making a small cluster, might indeed have a considerable effect on catalyzing the oxidation reactions due to the high density of available active sites. Modification of different graphene-like nanocatalysts i.e. BN-, SiC-, or CN-nanostructures is another option to expand our knowledge about these interesting green nanocatalysts. With respect to the different atoms, B, N, Si, C, etc., used in such kind of catalysts, various defect configurations are obtained during the synthesis process. How we can increase the electronic and catalytic properties of these defective nanostructures and make them ready to be used in applications?

Although many efforts have been done to find the most promising nanocatalyst for industrial usage, both computational, and experimental work is needed to eventually achieve real applications with these carbon-based nanomaterials. In order to bring the theoretical calculations closer to the experimental observations, supplementary kinetic calculations can be a good option. In this way, we can study the reaction rates to estimate the surface coverages, rates and rate-determining steps. In this spirit, we have recently developed a microkinetic model parameterized with DFT results in order to derive the kinetics of the studied reactions. Further investigations are necessary to improve the performance of SANCs for application in gas conversion and energy storage.

Academic CV

Parisa Nematollahi

Contact
University of Antwerp (CDE, D.B.230)
Department of Chemistry, PLASMANT group,
2610 Antwerpen, Belgium
Mobile: (+32) 484 835 459
Email: pn.comchem@gmail.com; Nematollahi.par@gmail.com
Skype: parisa.nematollahi@outlook.com

Education

Ph.D in Chemistry, University of Antwerp, Belgium Jul 2017-present

Thesis: "Density functional theory calculations for understanding gas conversion reactions on single metal atom embedded carbon-based nanocatalysts" under the supervision of Prof. Dr. Erik Neyts.

M.Sc. in NanoChemistry, University of Maragheh, Iran *Aug 2013-Feb 2016*

Thesis: "Theoretical investigation of gas conversion (CO, NO_x, SO_x) using DFT calculations" under the supervision of Prof. Mehdi Esrafili

M.Sc. in Inorganic Chemistry, Islamic Azad University, Iran *Aug 2008-Feb 2011*

Thesis: "Experimental investigation of wastewater treatments using modified waste plants with the synthesized nanoparticles" under the supervision of Prof. Hamid Aghabozorg

B.Sc. in Pure Chemistry, Islamic Azad University, Iran *Aug 2001-Feb 2005*

Professional skills

Nanochemistry, Heterogeneous catalysis, Surface interactions:

2D materials, Graphene, Carbon nanotubes, Boron nitride, Silicon carbide, Boron carbon nitride

Programming:

Python, Familiar with Matlab, Kinetic modeling

DFT Simulations:

VASP, Gaussian, $DMol^3$

General computer skills:

MS Office, Endnote, InDesign, Photoshop, CorelDraw, Familiar with Latex, Linux

Collaborations

University of Notre Dame, Notre Dame, Indiana, US March 2019-April 2019

This research project in collaboration with Prof. W. Schneider is done on finding the kinetic model of Ru embedded N-doped graphene and carbon nanotube for formic acid decomposition and formation. This project is going to be published soon (2020).

Conference contributions

1. P. Nematollahi, E. C. Neyts, DFT and microkinetic modeling of catalytic formic acid decomposition and formation on Ru-doped N embedded graphene and Nanotube, 2019, the second symposium of Chemical Research in Flanders - "CRF-2"; Blankenberge, Floreal club, Belgium, October 14-16, **Oral presentation**.
2. P. Nematollahi, E. C. Neyts, DFT and microkinetic modeling of catalytic formic acid decomposition and formation on Ru-doped N embedded graphene and Nanotube, 2019, the 30th International Conference on Diamond and Carbon Materials, Seville, Spain, September 8-12, **Oral presentation**.
3. P. Nematollahi, E. C. Neyts, Direct methane conversion to methanol on M and MN_4 embedded graphene (M=Ni and Si): A comparative DFT study, 2019, ICAMM Conference – International Conference on Advanced Materials Modelling; Rennes, France, July 1-3, **Oral presentation**.
4. P. Nematollahi, E. C. Neyts, Direct methane conversion to methanol on M and MN_4 embedded graphene (M=Ni and Si): A comparative DFT study, 2018, Game of materials, Dubrovnic, Croatia, October 30 – November 2, **Poster presentation**.
5. P. Nematollahi, E. C. Neyts, The role of healed N-vacancy defective BC_2N sheet and nanotube by NO molecule in oxidation of NO and CO gas molecules, 2017, Hands-on conference; Density-Functional Theory and Beyond: Accuracy, Efficiency, and Reproducibility in Computational Materials Science; Humboldt University, Berlin, Germany, July 31 to August 11, **Poster presentation**.
6. P. Nematollahi, H. Aghabozorg, 1st International conference on the environmental crisis and its solutions, 2013, Kish Island, Iran, **Poster presentation**.
7. P. Nematollahi, H. Aghabozorg, 1st National Conference on Nano Science and Nano Technology, 2011, YAZD, Iran, **Poster presentation**.

Workshop contributions

1. P. Nematollahi, E. C. Neyts, 2019, ICAMM Conference – International Conference on Advanced Materials Modelling; Rennes, France, June 26-30, VASP workshop.
2. P. Nematollahi, E. C. Neyts, The role of healed N-vacancy defective BC_2N sheet and nanotube by NO molecule in oxidation of NO and CO gas molecules, 2017, Density-Functional Theory and Beyond: Accuracy, Efficiency, and Reproducibility in Computational Materials Science; Humboldt University, Berlin, Germany, July 31 to August 11, Hands-on Workshop and conference.

Awards

Elsevier Young Scholarship Award, the 30th International Conference on Diamond and Carbon Materials, Seville, Spain, September 8-12.

Other relevant information

Languages: Persian (native), English (fluent, IELTS=6.5), Nederland (level A2-B1)
Journal Reviewer: ACS Applied materials and interface, Journal of Inorganic and Organometallic Polymers and Materials, Journal of Applied surface science, Vaccume

List of publications

In Preparation

1. P. Nematollahi, E. C. Neyts, Single Co atom supported on defective N-doped graphene for direct methane-to-methanol oxidation Journal of Applied Catalysis A: General, *submitted.*

2. P. Nematollahi, H. Ma, W. Schneider, E. C. Neyts, DFT and microkinetic modeling of catalytic formic acid decomposition and formation on Ru-doped N embedded graphene and Nanotube, *to be submitted.*

Journal Papers

3. P. Nematollahi, E. C. Neyts, Direct methane conversion to methanol on M and MN_4 embedded graphene (M=Ni and Si): A comparative DFT study, Applied Surface Science, (2019) 496, 143618.

4. P. Nematollahi, M.D. Esrafili, E. C Neyts, The role of healed N-vacancy defective BC_2N sheet and nanotube by NO molecule in oxidation of NO and CO gas molecules, *Surface Science,* (2018) 672, 39-46.

5. P. Nematollahi, E. C. Neyts, A comparative DFT study on CO oxidation reaction over Si-doped BC_2N nanosheet and nanotube, *Applied Surface Science,* (2018) 439, 934-945.

6. M.D. Esrafili, P. Nematollahi, Potential of Si-doped boron nitride nanotubes as a highly active and metal-free electrocatalyst for oxygen reduction reaction: A DFT study, *Synthetic Metals;* 226 (2017) 129-138.

Related to master thesis

7. M.D. Esrafili, R. Nurazar, E Vessally, P. Nematollahi, A. Bekhradnia, A DFT study on electronic and optical properties of aspirin-functionalized $B_{12}N_{12}$ fullerene-like nanocluster; *Structural Chemistry,* 28.3 (2017) 735-748.

8. P. Nematollahi, M.D. Esrafili, Catalytic activity of silicon carbide nanotubes and nanosheets for oxidation of CO: a DFT study, *New Journal of Chemistry,* 40 (2016) 2775-278.

9. M.D. Esrafili, P. Nematollahi, R. Nurazar, A comparative study of CO oxidation reaction over pristine and C-doped boron nitride fullerene, *RSC Advances,* 6 (2016) 17172-17178.

10. M.D. Esrafili, N. saeidi, P. Nematollahi, Si-doped graphene: A promising metal-free catalyst for oxidation of SO_2, Parisa Nematollahi, *Chemical Physics Letters,* 649

(2016) 3743.

11. M.D. Esrafili, P. Nematollahi, R. Nurazar, Pd-embedded graphene: An efficient and highly active catalyst for oxidation of CO, *Superlattices and Microstructures,* 92 (2016) 60-67.

12. M.D. Esrafili, P. Nematollahi, H. Abdollahpour, A comparative DFT study on the CO oxidation reaction over Al- and Ge-embedded graphene as efficient metal-free catalyst, *Applied Surface Science,* 378 (2016) 418-425.

13. P. Nematollahi, M.D. Esrafili, A. Bagheri, Functionalization of single-walled (n,0) carbon and boron nitride nanotubes by carbonyl derivatives (n=5,6): A DFT study, *Canadian Journal of Chemistry,* 94 (2016) 1-7.

14. M.D. Esrafili, P. Nematollahi, R. Nurazar, A density functional theory study on adsorption and decomposition mechanisms of acetic acid over silicon carbide nanotubes, *Syntheitc Metals*, 215 (2016) 164-169

15. M.D. Esrafili, N. saeidi, P. Nematollahi, The healing of B-/N-vacancy in boron nitride nanotube by using CO molecule: A density functional study, *New Journal of Chemistry*, 40:9 (2016) 8024-8031.

16. P. Nematollahi, M.D. Esrafili, A DFT study on the N_2O reduction by CO molecule over silicon carbide nanotubes and nanosheets, *RSC Advances*, 6:64 (2016) 59091-59099.

17. M.D. Esrafili, F. Mohammadian Sabet, P. Nematollahi, Oxidation of CO by N_2O over Al-and Ti-doped graphene: a comparative study, *RSC Advances*, 6:69 (2016) 64832-64840.

18. M.D. Esrafili, F. Mohammadian Sabet, P. Nematollahi, Catalytic decomposition of hydrazine borane over pristine and Al-embedded boron nitride nanotubes: A DFT study, *International Journal of Hydrogen Energy*, 41:44 (2016) 20172-20184.

19. M.D. Esrafili, F. Sharifi, and P. Nematollahi, A comparative theoretical study of CO oxidation reaction by O_2 molecule over Al- or Si-decorated graphene oxide, *Journal of Molecular Graphics and Modelling*, 69 (2016) 8-16.

20. M.D. Esrafili, F. Sharifi, and P. Nematollahi, Al- or Si-decorated graphene oxide: A favourable metal-free catalyst for the N_2O reduction, *Applied Surface Science*, 387 (2016) 454-460.

21. M.D. Esrafili, R. Nurazar, P. Nematollahi, Ambient carbon dioxide capture by different dimensional AlN nanostructures: A comparative DFT study, *Superlattices*

and Microstructures, 96 (2016) 164-173.

22. M.D. Esrafili, N. saeidi, P. Nematollahi, A DFT study on SO_3 capture and activation on Si-or Al-doped graphene, *Chemical Physics Letters*, 658 (2016) 146-151.

23. Gh. Mahmoudi, F. A. Afkhami, H. Sekhar Jena, P. Nematollahi, M.D Esrafili, P. Garczarek, K. Van Hecke, M. Servati Gargari, A.M. Kirillov, Halide ion-driven self-assembly of Zn (ii) compounds derived from an asymmetrical hydrazone building block: a combined experimental and theoretical study, *New Journal of Chemistry*, 40.12 (2016): 10116-10126.

24. M.D. Esrafili, N. saeidi, P. Nematollahi, Can Si-embedded boron nitride nanotubes act as a favourable metal-free catalyst for CO oxidation by N_2O? *RSC Advances,* 5 (2015) 100290-100298.

25. M.D. Esrafili, R. Mohammad-Valipour, S.M. Mousavi-Khoshdel, and P. Nematollahi, A comparative study of CO oxidation on nitrogen- and phosphorus-doped graphene, *ChemPhysChem,* 16 (2015) 3719-3727.

26. M.D. Esrafili, M. Ghanbari, R. Nurazar, P. Nematollahi, Theoretical study of formamide decomposition pathways over (6, 0) silicon-carbide nanotube, *J. Molecular Modeling*, 21 (2015) 79.

27. M.D. Esrafili, P. Nematollahi, A computational investigation of oxygen reduction reaction mechanisms on Si- and Al-doped graphene: A comparative study, *Advanced Materials Letters*, 6 (2015) 527-530.

28. M.R. Sazegar, A. Banakar, N. Bahrami, A. Bahrami, M. Baghbani, P. Nematollahi and M. Mottaghi, The antioxidant activity of chamomile (Matricaria Chamomilla L.) extract in sunflower oil, *World Applied Sciences Journal*, 9 (2010) 873.

Book Chapter

K. Kakaei, M. Esrafili, A. Ehsani, Graphene surfaces: particles and catalysis, ISBN: 9780128145234.

Bibliography

1. A. Hellman, A. Resta, N. Martin, J. Gustafson, A. Trinchero, P.-A. Carlsson, O. Balmes, R. Felici, R. van Rijn and J. Frenken, *J. Phys. Chem. Lett.*, 2012, **3**, 678-682.
2. B. Obama, *Science*, 2017, **355**, 126-129.
3. K. Jiang, S. Back, A. J. Akey, C. Xia, Y. Hu, W. Liang, D. Schaak, E. Stavitski, J. K. Nørskov and S. Siahrostami, *Nat. Commun.*, 2019, **10**, 1-11.
4. S. Yang, J. Kim, Y. J. Tak, A. Soon and H. Lee, *Angew. Chem.*, 2016, **55**, 2058-2062.
5. J. Lin, A. Wang, B. Qiao, X. Liu, X. Yang, X. Wang, J. Liang, J. Li, J. Liu and T. Zhang, *J. Am. Chem. Soc.*, 2013, **135**, 15314-15317.
6. X.-F. Yang, A. Wang, B. Qiao, J. Li, J. Liu and T. Zhang, *Acc. Chem. Res.*, 2013, **46**, 1740-1748.
7. T. E. James, S. L. Hemmingson and C. T. Campbell, *ACS Catal.*, 2015, **5**, 5673-5678.
8. X.-Y. Liang, N. Ding, S.-P. Ng and C.-M. L. Wu, *Appl. Surf. Sci.*, 2017, **411**, 11-17.
9. O. Faye, U. Eduok, J. Szpunar, B. Szpunar, A. Samoura and A. Beye, *Int. J. Hydrogen Energ.*, 2017, **42**, 4233-4243.
10. X.-Y. Xu, J. Li, H. Xu, X. Xu and C. Zhao, *New J. Chem.*, 2016, **40**, 9361-9369.
11. Q. Jiang, J. Zhang, Z. Ao, H. Huang, H. He and Y. Wu, *Frontiers in chemistry*, 2018, **6**.
12. A. K. Geim and K. S. Novoselov, in *Nanoscience and Technology: A Collection of Reviews from Nature Journals*, World Scientific, 2010, pp. 11-19.
13. A. A. Balandin, S. Ghosh, W. Bao, I. Calizo, D. Teweldebrhan, F. Miao and C. N. Lau, *Nano Lett.*, 2008, **8**, 902-907.
14. C.-S. Chen, W.-H. Cheng and S.-S. Lin, *Appl. Catal. A: Gen.*, 2004, **257**, 97-106.
15. P. Su, K. Iwase, S. Nakanishi, K. Hashimoto and K. Kamiya, *Small*, 2016, **12**, 6083-6089.
16. W. Choi, I. Lahiri, R. Seelaboyina and Y. S. Kang, *Crit. Rev. Solid State*, 2010, **35**, 52-71.
17. J. Liu, Z. Lin, T. Liu, Z. Yin, X. Zhou, S. Chen, L. Xie, F. Boey, H. Zhang and W. Huang, *Small*, 2010, **6**, 1536-1542.
18. J. Y. Son, Y.-H. Shin, H. Kim and H. M. Jang, *ACS Nano*, 2010, **4**, 2655-2658.
19. K. M. Shahil and A. A. Balandin, *Solid State Commun.*, 2012, **152**, 1331-1340.
20. A. K. Mishra and S. Ramaprabhu, *J. Phys. Chem. C.*, 2011, **115**, 14006-14013.
21. Z. Liu, D. He, Y. Wang, H. Wu and J. Wang, *Solar Energy Materials and Solar Cells*, 2010, **94**, 1196-1200.
22. H. Chang, X. Lv, H. Zhang and J. Li, *Electrochemistry Communications*, 2010, **12**, 483-487.
23. Z. Wang, J. Zhang, P. Chen, X. Zhou, Y. Yang, S. Wu, L. Niu, Y. Han, L. Wang and F. Boey, *Biosensors and Bioelectronics*, 2011, **26**, 3881-3886.
24. F. Schedin, A. Geim, S. Morozov, E. Hill, P. Blake, M. Katsnelson and K. Novoselov, *Nat. Mater.*, 2007, **6**, 652-655.
25. C. Lee, X. Wei, J. W. Kysar and J. Hone, *Science*, 2008, **321**, 385-388.
26. A. K. Geim and K. S. Novoselov, *Nat. Mater.*, 2007, **6**, 183-191.
27. C. Berger, Z. Song, X. Li, X. Wu, N. Brown, C. Naud, D. Mayou, T. Li, J. Hass and A. N. Marchenkov, *Science*, 2006, **312**, 1191-1196.
28. Y. Yang, X. Yang, Y. Yang and Q. Yuan, *Carbon*, 2018, **129**, 380-395.
29. Y. Tang, Z. Yang and X. Dai, *J. Chem. Phys.*, 2011, **135**, 224704.

30. X. Qin, Q. Meng and W. Zhao, *Surf. Sci.*, 2011, **605**, 930-933.
31. S. Kattel, P. Atanassov and B. Kiefer, *J. Phys. Chem. C.*, 2012, **116**, 8161-8166.
32. Z. He, K. He, A. W. Robertson, A. I. Kirkland, D. Kim, J. Ihm, E. Yoon, G.-D. Lee and J. H. Warner, *Nano Lett.*, 2014, **14**, 3766-3772.
33. S. Kattel, P. Atanassov and B. Kiefer, *J. Mater. Chem. A*, 2014, **2**, 10273-10279.
34. D. Wei, Y. Liu, Y. Wang, H. Zhang, L. Huang and G. Yu, *Nano Lett.*, 2009, **9**, 1752-1758.
35. Y.-C. Lin, C.-Y. Lin and P.-W. Chiu, *Appl. Phys. Lett.*, 2010, **96**.
36. D. Usachov, O. Vilkov, A. Gruneis, D. Haberer, A. Fedorov, V. K. Adamchuk, A. B. Preobrajenski, P. Dudin, A. Barinov, M. Oehzelt, C. Laubschat and D. V. Vyalikh, *Nano Lett.*, 2011, **11**, 5401-5407.
37. Y. J. Cho, H. S. Kim, S. Y. Baik, Y. Myung, C. S. Jung, C. H. Kim, J. Park and H. S. Kang, *J. Phys. Chem. C.*, 2011, **115**, 3737-3744.
38. A. Hashimoto, K. Suenaga, A. Gloter, K. Urita and S. Iijima, *Nature*, 2004, **430**, 870-873.
39. F. Banhart, J. Kotakoski and A. V. Krasheninnikov, *ACS Nano*, 2010, **5**, 26-41.
40. J. Kotakoski, A. Krasheninnikov, U. Kaiser and J. Meyer, *Phys. Rev. Lett.*, 2011, **106**, 105505.
41. Y. Jia, L. Zhang, A. Du, G. Gao, J. Chen, X. Yan, C. L. Brown and X. Yao, *Adv. Mater.*, 2016, **28**, 9532-9538.
42. D.-W. Wang and D. Su, *Energy Environ. Sci.*, 2014, **7**, 576-591.
43. B. Guo, L. Fang, B. Zhang and J. R. Gong, *Insciences J.*, 2011, DOI: 10.5640/insc.010280, 80-89.
44. Y. Fujimoto and S. Saito, *Phys. Rev. B*, 2011, **84**, 245446.
45. I. Maciel, J. Campos-Delgado, E. Cruz-Silva, M. Pimenta, B. Sumpter, V. Meunier, F. Lopez-Urias, E. Munoz-Sandoval, H. Terrones and M. Terrones, *Nano Lett.*, 2009, **9**, 2267-2272.
46. Z. Yang, Z. Yao, G. Li, G. Fang, H. Nie, Z. Liu, X. Zhou, X. a. Chen and S. Huang, *ACS Nano*, 2011, **6**, 205-211.
47. X. Zhang, Z. Lu, G. Xu, T. Wang, D. Ma, Z. Yang and L. Yang, *Phys. Chem. Chem. Phys.*, 2015, **17**, 20006-20013.
48. F. Li, J. Zhao and Z. Chen, *J. Phys. Chem. C.*, 2012, **116**, 2507-2514.
49. C. Attaccalite, L. Wirtz, M. Lazzeri, F. Mauri and A. Rubio, *Nano Lett.*, 2010, **10**, 1172-1176.
50. D. Usachov, O. Vilkov, A. Gruneis, D. Haberer, A. Fedorov, V. Adamchuk, A. Preobrajenski, P. Dudin, A. Barinov and M. Oehzelt, *Nano Lett.*, 2011, **11**, 5401-5407.
51. Y. Liu, J. Zhao and Q. Cai, *Phys. Chem. Chem. Phys.*, 2016, **18**, 5491-5498.
52. Y.-X. Yu, *Phys. Chem. Chem. Phys.*, 2013, **15**, 16819-16827.
53. M. Inagaki, M. Toyoda, Y. Soneda and T. Morishita, *Carbon*, 2018, **132**, 104-140.
54. G. Frenking and N. Froehlich, *Chem. Rev.*, 2000, **100**, 717-774.
55. Y. Li, Z. Zhou, G. Yu, W. Chen and Z. Chen, *J. Phys. Chem. C.*, 2010, **114**, 6250-6254.
56. D. Cortés-Arriagada and N. Villegas-Escobar, *Appl. Surf. Sci.*, 2017, **420**, 446-455.
57. E. J. Santos, A. Ayuela, S. Fagan, J. Mendes Filho, D. Azevedo, A. Souza Filho and D. Sánchez-Portal, *Phys. Rev. B*, 2008, **78**, 195420.
58. Y.-g. Wu, M. Wen, Q.-s. Wu and H. Fang, *J. Phys. Chem. C.*, 2014, **118**, 6307-6313.
59. Y. Tong, Y. Wang and Q. Wang, *Struct. Chem.*, 2017, DOI: 10.1007/s11224-017-0934-y.
60. S. Sun, G. Zhang, N. Gauquelin, N. Chen, J. Zhou, S. Yang, W. Chen, X. Meng, D. Geng and M. N. Banis, *Sci. Rep.*, 2013, **3**, 1775.
61. L. Ma, J.-M. Zhang, K.-W. Xu and V. Ji, *Appl. Surf. Sci.*, 2015, **343**, 121-127.

62. T.-T. Jia, C.-H. Lu, Y.-F. Zhang and W.-k. Chen, *J. Nanopart. Res.*, 2014, **16**, 1-11.
63. Y. Tang, Z. Liu, X. Dai, Z. Yang, W. Chen, D. Ma and Z. Lu, *Appl. Surf. Sci.*, 2014, **308**, 402-407.
64. Y. Chen, X.-c. Yang, Y.-j. Liu, J.-x. Zhao, Q.-h. Cai and X.-z. Wang, *J. Mol. Graph. Model.*, 2013, **39**, 126-132.
65. J. H. Cho, S. J. Yang, K. Lee and C. R. Park, *Int. J. Hydrogen Energ.*, 2011, **36**, 12286-12295.
66. M. D. Esrafili, N. Saeidi and P. Nematollahi, *Chem. Phys. Lett.*, 2016, **649**, 37-43.
67. V. Tripkovic, M. Vanin, M. Karamad, M. r. E. Björketun, K. W. Jacobsen, K. S. Thygesen and J. Rossmeisl, *J. Phys. Chem. C.*, 2013, **117**, 9187-9195.
68. J. Dai and J. Yuan, *Phys. Rev. B*, 2010, **81**, 165414.
69. Y.-a. Lv, G.-l. Zhuang, J.-g. Wang, Y.-b. Jia and Q. Xie, *Phys. Chem. Chem. Phys.*, 2011, **13**, 12472-12477.
70. A. Krasheninnikov, P. Lehtinen, A. S. Foster, P. Pyykkö and R. M. Nieminen, *Phys. Rev. Lett.*, 2009, **102**, 126807.
71. J. A. Rodríguez-Manzo, O. Cretu and F. Banhart, *ACS Nano*, 2010, **4**, 3422-3428.
72. X. Zhang, Z. Lu and Z. Yang, *Int. J. Hydrogen Energ.*, 2016, **41**, 21212-21220.
73. X. Sun, K. Li, C. Yin, Y. Wang, M. Jiao, F. He, X. Bai, H. Tang and Z. Wu, *Carbon*, 2016, **108**, 541-550.
74. C. Zhang, L. Fu, N. Liu, M. Liu, Y. Wang and Z. Liu, *Adv. Mater.*, 2011, **23**, 1020-1024.
75. Z. Luo, S. Lim, Z. Tian, J. Shang, L. Lai, B. MacDonald, C. Fu, Z. Shen, T. Yu and J. Lin, *J. Mater. Chem.*, 2011, **21**, 8038-8044.
76. D. H. Lee, W. J. Lee, W. J. Lee, S. O. Kim and Y.-H. Kim, *Phys. Rev. Lett.*, 2011, **106**, 175502.
77. R. Lv, Q. Li, A. R. Botello-Méndez, T. Hayashi, B. Wang, A. Berkdemir, Q. Hao, A. L. Elías, R. Cruz-Silva and H. R. Gutiérrez, *Sci. Rep.*, 2012, **2**, 586.
78. V. D. Pham, J. r. m. Lagoute, O. Mouhoub, F. d. r. Joucken, V. Repain, C. Chacon, A. Bellec, Y. Girard and S. Rousset, *ACS Nano*, 2014, **8**, 9403-9409.
79. Y. Wang, Y. Shao, D. W. Matson, J. Li and Y. Lin, *ACS Nano*, 2010, **4**, 1790-1798.
80. H. Wang, T. Maiyalagan and X. Wang, *ACS Catal.*, 2012, **2**, 781-794.
81. H. Fei, R. Ye, G. Ye, Y. Gong, Z. Peng, X. Fan, E. L. Samuel, P. M. Ajayan and J. M. Tour, *ACS Nano*, 2014, **8**, 10837-10843.
82. M. D. Esrafili, R. Mohammad-Valipour, S. M. Mousavi-Khoshdel and P. Nematollahi, *ChemPhysChem*, 2015, **16**, 3719-3727.
83. Y. Tang, W. Chen, Z. Shen, S. Chang, M. Zhao and X. Dai, *Carbon*, 2017, **111**, 448-458.
84. Z. Lu, M. Yang, D. Ma, P. Lv, S. Li and Z. Yang, *Appl. Surf. Sci.*, 2017, **426**, 1232-1240.
85. X. Liu, Y. Sui, T. Duan, C. Meng and Y. Han, *Catal. Sci. Technol*, 2015, **5**, 1658-1667.
86. X. Zhou, L. J. Wan and Y. G. Guo, *Adv. Mater.*, 2013, **25**, 2152-2157.
87. Y. Zheng, Y. Jiao, Y. Zhu, L. H. Li, Y. Han, Y. Chen, A. Du, M. Jaroniec and S. Z. Qiao, *Nat. Commun.*, 2014, **5**, 3783.
88. A. L. M. Reddy, A. Srivastava, S. R. Gowda, H. Gullapalli, M. Dubey and P. M. Ajayan, *ACS Nano*, 2010, **4**, 6337-6342.
89. C. W. Bezerra, L. Zhang, K. Lee, H. Liu, A. L. Marques, E. P. Marques, H. Wang and J. Zhang, *Electrochim. Acta*, 2008, **53**, 4937-4951.
90. J. Luque-Centeno, M. Martínez-Huerta, D. Sebastián, G. Lemes, E. Pastor and M. Lázaro, *Renewable Energy*, 2018, **125**, 182-192.

91. A. T. Lee, J. Kang, S.-H. Wei, K. Chang and Y.-H. Kim, *Phys. Rev. B*, 2012, **86**, 165403.
92. Y. Feng, F. Li, Z. Hu, X. Luo, L. Zhang, X.-F. Zhou, H.-T. Wang, J.-J. Xu and E. Wang, *Phys. Rev. B*, 2012, **85**, 155454.
93. S. Kattel, P. Atanassov and B. Kiefer, *Phys. Chem. Chem. Phys.*, 2013, **15**, 148-153.
94. W. Orellana, *J. Phys. Chem. C.*, 2013, **117**, 9812-9818.
95. S. Gupta, D. Tryk, I. Bae, W. Aldred and E. Yeager, *J. Appl. Electrochem.*, 1989, **19**, 19-27.
96. W. Ju, A. Bagger, G. P. Hao, A. S. Varela, I. Sinev, V. Bon, B. Roldan Cuenya, S. Kaskel, J. Rossmeisl and P. Strasser, *Nat. Commun.*, 2017, **8**, 944.
97. N. Hamada, S.-i. Sawada and A. Oshiyama, *Phys. Rev. Lett.*, 1992, **68**, 1579.
98. R. Saito, M. Fujita, G. Dresselhaus and u. M. Dresselhaus, *Appl. Phys. Lett.*, 1992, **60**, 2204-2206.
99. Y.-Y. Fan, A. Kaufmann, A. Mukasyan and A. Varma, *Carbon*, 2006, **44**, 2160-2170.
100. T. Dinadayalane, J. S. Murray, M. C. Concha, P. Politzer and J. Leszczynski, *J. Chem. Theory Comput.*, 2010, **6**, 1351-1357.
101. H. Chu, L. Wei, R. Cui, J. Wang and Y. Li, *Coord. Chem. Rev.*, 2010, **254**, 1117-1134.
102. R. Q. Long and R. T. Yang, *J. Am. Chem. Soc.*, 2001, **123**, 2058-2059.
103. H. Dai, *Acc. Chem. Res.*, 2002, **35**, 1035-1044.
104. P. Ajayan, V. Ravikumar and J.-C. Charlier, *Phys. Rev. Lett.*, 1998, **81**, 1437.
105. S. Zhang, S. L. Mielke, R. Khare, D. Troya, R. S. Ruoff, G. C. Schatz and T. Belytschko, *Phys. Rev. B*, 2005, **71**, 115403.
106. Y. Tang, B. L. Allen, D. R. Kauffman and A. Star, *J. Am. Chem. Soc.*, 2009, **131**, 13200-13201.
107. M. Glerup, J. Steinmetz, D. Samaille, O. Stephan, S. Enouz, A. Loiseau, S. Roth and P. Bernier, *Chem. Phys. Lett.*, 2004, **387**, 193-197.
108. C. J. Lee, S. C. Lyu, H.-W. Kim, J. H. Lee and K. I. Cho, *Chem. Phys. Lett.*, 2002, **359**, 115-120.
109. M. S. Saha and A. Kundu, *J. Power Sources*, 2010, **195**, 6255-6261.
110. S. Sun, G. Zhang, Y. Zhong, H. Liu, R. Li, X. Zhou and X. Sun, *ChemComm*, 2009, 7048-7050.
111. K. Gong, F. Du, Z. Xia, M. Durstock and L. Dai, *Science*, 2009, **323**, 760-764.
112. S. Maldonado and K. J. Stevenson, *J. Phys. Chem. B.*, 2005, **109**, 4707-4716.
113. K. Jiang, L. S. Schadler, R. W. Siegel, X. Zhang, H. Zhang and M. Terrones, *J. Mater. Chem.*, 2004, **14**, 37-39.
114. Y. Chen, J. Wang, H. Liu, R. Li, X. Sun, S. Ye and S. Knights, *Electrochemistry communications*, 2009, **11**, 2071-2076.
115. P. Yin, T. Yao, Y. Wu, L. Zheng, Y. Lin, W. Liu, H. Ju, J. Zhu, X. Hong and Z. Deng, *Angew. Chem.*, 2016, **55**, 10800-10805.
116. L. Zhang, J. M. T. A. Fischer, Y. Jia, X. Yan, W. Xu, X. Wang, J. Chen, D. Yang, H. Liu and L. Zhuang, *J. Am. Chem. Soc.*, 2018, **140**, 10757-10763.
117. P. Ayala, R. Arenal, M. Rümmeli, A. Rubio and T. Pichler, *Carbon*, 2010, **48**, 575-586.
118. M. S. Saha, R. Li, X. Sun and S. Ye, *Electrochemistry Communications*, 2009, **11**, 438-441.
119. F. Gao, G.-L. Zhao, Z. Wang, D. Bagayoko and D.-J. Liu, *Catal. Commun.*, 2015, **62**, 79-82.
120. Y. Kubota, K. Watanabe, O. Tsuda and T. Taniguchi, *Science*, 2007, **317**, 932-934.
121. A. Y. Liu, R. M. Wentzcovitch and M. L. Cohen, *Phys. Rev. B*, 1989, **39**, 1760.

122. E.-J. Kan, X. Wu, Z. Li, X. C. Zeng, J. Yang and J. Hou, *J. Chem. Phys.*, 2008, **129**, 084712.

123. A. Du, Y. Chen, Z. Zhu, G. Lu and S. C. Smith, *J. Am. Chem. Soc.*, 2009, **131**, 1682-1683.

124. S. Y. Kim, J. Park, H. C. Choi, J. P. Ahn, J. Q. Hou and H. S. Kang, *J. Am. Chem. Soc.*, 2007, **129**, 1705-1716.

125. O. Stephan, P. Ajayan, C. Colliex and P. Redlich, *Science*, 1994, **266**, 1683.

126. P. Redlich, J. Loeffler, P. Ajayan, J. Bill, F. Aldinger and M. Rühle, *Chem. Phys. Lett.*, 1996, **260**, 465-470.

127. Y. Zhang, H. Gu, K. Suenaga and S. Iijima, *Chem. Phys. Lett.*, 1997, **279**, 264-269.

128. S. Enouz, O. Stéphan, J.-L. Cochon, C. Colliex and A. Loiseau, *Nano Lett.*, 2007, **7**, 1856-1862.

129. K. Raidongia, D. Jagadeesan, M. Upadhyay-Kahaly, U. Waghmare, S. K. Pati, M. Eswaramoorthy and C. Rao, *J. Mater. Chem.*, 2008, **18**, 83-90.

130. R. Majidi, *Physica E.*, 2015, **74**, 371-376.

131. J. P. Nicolich, F. Hofer, G. Brey and R. Riedel, *J. Am. Ceram. Soc.*, 2001, **84**, 279-282.

132. A. Y. Liu, R. M. Wentzcovitch and M. L. Cohen, *Phys. Rev. B*, 1989, **39**, 1760-1765.

133. M. Watanabe, S. Itoh, T. Sasaki and K. Mizushima, *Phys. Rev. Lett.*, 1996, **77**, 187.

134. K. Suenaga, C. Colliex, N. Demoncy, A. Loiseau, H. Pascard and F. Willaime, *Science*, 1997, **278**, 653-655.

135. S. Sen, K. Moses, A. J. Bhattacharyya and C. Rao, *Chemistry–An Asian Journal*, 2014, **9**, 100-103.

136. Z. Weng-Sieh, K. Cherrey, N. G. Chopra, X. Blase, Y. Miyamoto, A. Rubio, M. L. Cohen, S. G. Louie, A. Zettl and R. Gronsky, *Phys. Rev. B*, 1995, **51**, 11229.

137. M. Terrones, D. Golberg, N. Grobert, T. Seeger, M. Reyes-Reyes, M. Mayne, R. Kamalakaran, P. Dorozhkin, Z. C. Dong and H. Terrones, *Adv. Mater.*, 2003, **15**, 1899-1903.

138. T. Pankewitz and W. Klopper, *J. Phys. Chem. C.*, 2007, **111**, 18917-18926.

139. H. Pan, Y. P. Feng and J. Lin, *Phys. Rev. B*, 2006, **74**, 045409.

140. Y. Wang, B. Zhou, X. Yao, G. Huang, J. Zhang and Q. Shao, *Chem. Phys. Lett.*, 2014, **616**, 61-66.

141. R. Ghafouri, M. Anafcheh and M. Zahedi, *Physica E.*, 2014, **58**, 94-100.

142. A. A. Peyghan and M. Noei, *Comput. Mater. Sci.*, 2014, **82**, 197-201.

143. N. Song, Y. Wang, Q. Sun and Y. Jia, *Appl. Surf. Sci.*, 2012, **263**, 182-186.

144. A. Ahmadi Peyghan, N. L. Hadipour and Z. Bagheri, *J. Phys. Chem. C.*, 2013, **117**, 2427-2432.

145. N.-x. Qiu, Z.-y. Tian, Y. Guo, C.-h. Zhang, Y.-p. Luo and Y. Xue, *Int. J. Hydrogen Energ.*, 2014, **39**, 9307-9320.

146. M. Noei and A. A. Peyghan, *J. Mol. Model.*, 2013, **19**, 3843-3850.

147. C. Rupp, J. Rossato and R. Baierle, *J. Chem. Phys.*, 2009, **130**, 114710.

148. Y. S. Wang, P. F. Yuan, M. Li, W. F. Jiang, Q. Sun and Y. Jia, *Comput. Mater. Sci.*, 2012, **60**, 181-185.

149. N.-x. Qiu, Z.-y. Tian, Y. Guo, C.-h. Zhang, Y.-p. Luo and Y. Xue, *Int. J. Hydrogen Energ.*, 2014, **39**, 9307-9320.

150. H. M. Leicester and H. S. Klickstein, *A Source Book in Chemistry, 1400-1900*, Harvard University Press, 1952.

151. J. Hagen, *Industrial catalysis: a practical approach*, John Wiley & Sons, 2015.

152. P. W. Van Leeuwen, *Homogeneous catalysis: understanding the art*, Springer Science & Business Media, 2006.

153. I. Chorkendorff and J. W. Niemantsverdriet, *Concepts of modern catalysis and kinetics*, John Wiley & Sons, 2017.

154. A. Gross, *A Microscopic Perspective. Originally published in the series: Advanced Texts in Physics*, 2003, **132**.

155. I. Langmuir, *Transactions of the Faraday Society*, 1922, **17**, 621-654.

156. C. Hinshelwood, *Journal*, 1940.

157. D. Eley, *Advances in catalysis*, 1948, **1**.

158. E. Rideal, 1939.

159. D. Eley and E. Rideal, *Nature*, 1940, **146**, 401-402.

160. P. Klaus, M. Schmies and M. Wilch, 2019.

161. M. P. Allen and D. J. Tildesley, *Computer simulation of liquids*, Oxford university press, 2017.

162. R. Pathria, *Statistical Mechanics*, 1996, 43-89.

163. T. R. Karl and K. E. Trenberth, *Science*, 2003, **302**, 1719-1723.

164. M. Bradford and M. Vannice, *Catalysis Reviews*, 1999, **41**, 1-42.

165. V. L. Sushkevich, D. Palagin, M. Ranocchiari and J. A. van Bokhoven, *Science*, 2017, **356**, 523-527.

166. B. Wang, S. Albarracín-Suazo, Y. Pagán-Torres and E. Nikolla, *Catal. Today*, 2017, **285**, 147-158.

167. F.-W. Chang, M.-S. Kuo, M.-T. Tsay and M.-C. Hsieh, *Appl. Catal. A: Gen.*, 2003, **247**, 309-320.

168. D. Pakhare and J. Spivey, *Chem. Soc. Rev.*, 2014, **43**, 7813-7837.

169. J. Bitter, K. Seshan and J. Lercher, *J. Catal.*, 1998, **176**, 93-101.

170. Y.-Z. Lin, J. Sun, J. Yi, J.-D. Lin, H.-B. Chen and D.-W. Liao, *Journal of Molecular Structure: THEOCHEM*, 2002, **587**, 63-71.

171. C. Carrara, J. Munera, E. Lombardo and L. Cornaglia, *Topics in Catalysis*, 2008, **51**, 98-106.

172. K. Sutthiumporn and S. Kawi, *Int. J. Hydrogen Energ.*, 2011, **36**, 14435-14446.

173. Z. Bian, S. Das, M. H. Wai, P. Hongmanorom and S. Kawi, *ChemPhysChem*, 2017, **18**, 3117-3134.

174. Z. Kowalczyk, K. Stołecki, W. Rarog-Pilecka, E. Miśkiewicz, E. Wilczkowska and Z. Karpiński, *Appl. Catal. A: Gen.*, 2008, **342**, 35-39.

175. S. Wang and G. Lu, *Appl. Catal. A: Gen.*, 1998, **169**, 271-280.

176. C. j. Liu, J. Ye, J. Jiang and Y. Pan, *ChemCatChem*, 2011, **3**, 529-541.

177. R. Benrabaa, A. Löfberg, A. Rubbens, E. Bordes-Richard, R. Vannier and A. Barama, *Catal. Today*, 2013, **203**, 188-195.

178. S. Lögdberg, J. Yang, M. Lualdi, J. C. Walmsley, S. Järås, M. Boutonnet, E. A. Blekkan, E. Rytter and A. Holmen, *J. Catal.*, 2017, **352**, 515-531.

179. G. G. Jeba, M. T. Conato, J. D. Rimer and M. P. Harold, *Chem. Eng. J.*, 2017.

180. R. Alizadeh, E. Jamshidi and G. Zhang, *Journal of Natural Gas Chemistry*, 2009, **18**, 124-130.

181. M. Beckner and A. Dailly, *Applied Energy*, 2016, **162**, 506-514.

182. Y. Tang, Z. Shen, W. Chen, L. Pan, X. Wang and X. Dai, *Appl. Surf. Sci.*, 2016, **390**, 461-471.

183. J. Liu, B. R. Bunes, L. Zang and C. Wang, *Environmental Chemistry Letters*, 2018, **16**, 477-505.

184. H. Wang, Q. Wang, Y. Cheng, K. Li, Y. Yao, Q. Zhang, C. Dong, P. Wang, U. Schwingenschlögl and W. Yang, *Nano Lett.*, 2011, **12**, 141-144.

185. T. Quinn and P. Choudhury, *Molecular Catalysis*, 2017, **431**, 9-14.

186. S. Pornsatitworakul, S. Phikulthai, S. Namuangruk and B. Boekfa, 2015.

187. F. W. Maurer, *Am. J. Physiol.*, 1941, **133**, 180-188.

188. E. M. Killick, *Physiol. Rev.*, 1940, **20**, 313-344.

189. N. Lopez and J. K. Nørskov, *J. Am. Chem. Soc.*, 2002, **124**, 11262-11263.

190. H.-Y. Su, M.-M. Yang, X.-H. Bao and W.-X. Li, *J. Phys. Chem. C.*, 2008, **112**, 17303-17310.

191. H. Gao, *Appl. Surf. Sci.*, 2016, **379**, 347-357.

192. S. Piccinin and M. Stamatakis, *ACS Catal.*, 2014, **4**, 2143-2152.

193. D.-J. Liu, *J. Phys. Chem. C.*, 2007, **111**, 14698-14706.

194. F. C. H. Lim, J. Zhang, H. Jin, M. B. Sullivan and P. Wu, *Appl. Catal. A: Gen.*, 2013, **451**, 79-85.

195. R. S. Johnson, A. DeLaRiva, V. Ashbacher, B. Halevi, C. J. Villanueva, G. K. Smith, S. Lin, A. K. Datye and H. Guo, *Phys. Chem. Chem. Phys.*, 2013, **15**, 7768-7776.

196. T. Bunluesin, H. Cordatos and R. Gorte, *J. Catal.*, 1995, **157**, 222-226.

197. L. Liu, F. Zhou, L. Wang, X. Qi, F. Shi and Y. Deng, *J. Catal.*, 2010, **274**, 1-10.

198. X. L. Xu, E. Yang, J. Q. Li, Y. Li and W. K. Chen, *ChemCatChem*, 2009, **1**, 384-392.

199. B. Qiao, A. Wang, X. Yang, L. F. Allard, Z. Jiang, Y. Cui, J. Liu, J. Li and T. Zhang, *Nat. Chem.*, 2011, **3**, 634-641.

200. S. Dey Baruah, N. K. Gour, P. J. Sarma and R. C. Deka, *Comput. Theor. Chem.*, 2017, **1114**, 1-7.

201. I. Fampiou and A. Ramasubramaniam, *J. Phys. Chem. C.*, 2015, **119**, 8703-8710.

202. S. Lin, X. Ye, R. S. Johnson and H. Guo, *J. Phys. Chem. C.*, 2013, **117**, 17319-17326.

203. S. Wannakao, T. Nongnual, P. Khongpracha, T. Maihom and J. Limtrakul, *J. Phys. Chem. C.*, 2012, **116**, 16992-16998.

204. K. Kim, J.-Y. Choi, T. Kim, S.-H. Cho and H.-J. Chung, *Nature*, 2011, **479**, 338-344.

205. G. Xu, R. Wang, F. Yang, D. Ma, Z. Yang and Z. Lu, *Carbon*, 2017, **118**, 35-42.

206. L.-y. Feng, Y.-j. Liu and J.-x. Zhao, *J. Power Sources*, 2015, **287**, 431-438.

207. Q. Jiang, Z. Ao, S. Li and Z. Wen, *RSC Adv.*, 2014, **4**, 20290-20296.

208. Y. Tang, Z. Yang and X. Dai, *Phys. Chem. Chem. Phys.*, 2012, **14**, 16566-16572.

209. Y. Li, Y. Yu, J.-G. Wang, J. Song, Q. Li, M. Dong and C.-J. Liu, *Appl. Catal. B-Environ.*, 2012, **125**, 189-196.

210. B. Schumacher, V. Plzak, M. Kinne and R. Behm, *Catalysis letters*, 2003, **89**, 109-114.

211. J.-H. Guo and H. Zhang, *Struct. Chem.*, 2011, **22**, 1039.

212. N. Kumar, K. Subrahmanyam, P. Chaturbedy, K. Raidongia, A. Govindaraj, K. P. Hembram, A. K. Mishra, U. V. Waghmare and C. Rao, *ChemSusChem*, 2011, **4**, 1662-1670.

213. P. Hohenberg and W. Kohn, *Phys. Rev*, 1964, **136**, B864.

214. R. M. Martin and R. M. Martin, *Electronic structure: basic theory and practical methods*, Cambridge university press, 2004.

215. E. Schrödinger, *Ann Physik*, 1926, **79**, 361-377.

216. M. Born and R. Oppenheimer, *Annalen der physik*, 1927, **389**, 457-484.

217. E. Fermi, *Rend. Accad. Naz. Lincei*, 1927, **6**, 5.

218. L. H. Thomas, 1927.

219. P. Hohenberg, *Phys. Rev*, 1965, **140**, A1133-A1138.

220. P. Geerlings, F. De Proft and W. Langenaeker, in *Advances in Quantum Chemistry*, Elsevier, 1998, vol. 33, pp. 303-328.

221. E. Lewars, *Introduction to the theory and applications of molecular and quantum mechanics*, 2003, 318.

222. W. Kohn and L. Sham, *Phys. Rev. A*, 1965, **140**, 113.

223. D. Sholl and J. A. Steckel, *Density functional theory: a practical introduction*, John Wiley & Sons, 2011.

224. D. M. Ceperley and B. J. Alder, *Phys. Rev. Lett.*, 1980, **45**, 566.

225. J. P. Perdew and W. Yue, *Phys. Rev. B*, 1986, **33**, 8800.

226. J. P. Perdew, K. Burke and M. Ernzerhof, *Phys. Rev. Lett.*, 1996, **77**, 3865.

227. C. Lee, W. Yang and R. Parr, *Phys. Rev. A*, 1988, **38**, 3098.

228. A. D. Becke, *J. Chem. Phys.*, 1998, **109**, 2092-2098.

229. C. Lee, W. Yang and R. G. Parr, *Phys. Rev. B*, 1988, **37**, 785.

230. M. Ernzerhof and G. E. Scuseria, *J. Chem. Phys.*, 1999, **111**, 911-915.

231. E. Proynov, E. Ruiz, A. Vela and D. Salahub, *International Journal of Quantum Chemistry*, 1995, **56**, 61-78.

232. S. Kurth, J. P. Perdew and P. Blaha, *International journal of quantum chemistry*, 1999, **75**, 889-909.

233. F. Tran, P. Blaha and K. Schwarz, *J. Phys. Condens. Matter*, 2007, **19**, 196208.

234. J. C. Slater, *Physical review*, 1951, **81**, 385.

235. A. Becke, *The role of exact*, 1993.

236. J. E. Jones, *Proceedings of the Royal Society of London. Series A, Containing Papers of a Mathematical and Physical Character*, 1924, **106**, 463-477.

237. F. Jensen, *Introduction to computational chemistry*, John wiley & sons, 2017.

238. W. J. Hehre, R. F. Stewart and J. A. Pople, *J. Chem. Phys.*, 1969, **51**, 2657-2664.

239. J. S. Binkley and J. A. Pople, *J. Chem. Phys.*, 1977, **66**, 879-880.

240. H. Kjær and S. P. Sauer, *J. Chem. Theory Comput.*, 2011, **7**, 4070-4076.

241. M. J. Frisch, J. A. Pople and J. S. Binkley, *J. Chem. Phys.*, 1984, **80**, 3265-3269.

242. M. M. Francl, W. J. Pietro, W. J. Hehre, J. S. Binkley, M. S. Gordon, D. J. DeFrees and J. A. Pople, *J. Chem. Phys.*, 1982, **77**, 3654-3665.

243. R. Kendall, *J. chem. Phys*, 1992, **96**, 6796-6806.

244. P. J. Hay and W. R. Wadt, *J. Chem. Phys.*, 1985, **82**, 270-283.

245. L. Fernandez Pacios and P. Christiansen, *J. Chem. Phys.*, 1985, **82**, 2664-2671.

246. L. Goerigk and S. Grimme, *J. Chem. Theory Comput.*, 2011, **7**, 291-309.

247. M. Frisch, G. Trucks, H. Schlegel, G. Scuseria, M. Robb, J. Cheeseman, G. Scalmani, V. Barone, B. Mennucci and G. Petersson, *There is no corresponding record for this reference.[Google Scholar]*.

248. Y. Zhao and D. G. Truhlar, *Chem. Phys. Lett.*, 2011, **502**, 1-13.

249. R. Peverati and D. G. Truhlar, *J. Phys. Chem. Lett.*, 2011, **2**, 2810-2817.

250. Y. Zhao and D. G. Truhlar, *Theor. Chem. Acc.*, 2008, **120**, 215-241.

251. Y. Zhao and D. G. Truhlar, *J. Chem. Phys.*, 2006, **125**, 194101.

252. C. A. Morgado, P. Jurečka, D. Svozil, P. Hobza and J. Šponer, *Phys. Chem. Chem.*

Phys., 2010, **12**, 3522-3534.

253. S. A. Smith, K. E. Hand, M. L. Love, G. Hill and D. H. Magers, *J. Comput. Chem.*, 2013, **34**, 558-565.

254. E. H. Song, Z. Wen and Q. Jiang, *J. Phys. Chem. C.*, 2011, **115**, 3678-3683.

255. Y. Zhao, N. E. Schultz and D. Truhlar, *Journal*, 2005.

256. J.-D. Chai and M. Head-Gordon, *J. Chem. Phys.*, 2008, **128**, 084106.

257. S. Grimme, *J. Comput. Chem.*, 2006, **27**, 1787-1799.

258. G. A. Petersson, D. K. Malick, W. G. Wilson, J. W. Ochterski, J. A. Montgomery Jr and M. J. Frisch, *J. Chem. Phys.*, 1998, **109**, 10570-10579.

259. J. Foresman and E. Frish, *Gaussian Inc., Pittsburg, USA*, 1996.

260. F. B. Van Duijneveldt, J. G. van Duijneveldt-van de Rijdt and J. H. van Lenthe, *Chem. Rev.*, 1994, **94**, 1873-1885.

261. R. S. Mulliken, *J. Chem. Phys.*, 1955, **23**, 1833-1840.

262. E. Glendening, J. Badenhoop, A. Reed, J. Carpenter, J. Bohmann, C. Morales, C. Landis and F. Weinhold, *There is no corresponding record for this reference.[Google Scholar]*, 2011.

263. F. Weinhold, C. Landis and E. Glendening, *International reviews in physical chemistry*, 2016, **35**, 399-440.

264. H. Er-Rbib, C. Bouallou and F. Werkoff, *CHEMICAL ENGINEERING*, 2012, **29**.

265. S.-G. Wang, X.-Y. Liao, J. Hu, D.-B. Cao, Y.-W. Li, J. Wang and H. Jiao, *Surf. Sci.*, 2007, **601**, 1271-1284.

266. S. K. Talkhoncheh, M. Haghighi, N. Jodeiri and S. Aghamohammadi, *Journal of Natural Gas Science and Engineering*, 2017, **46**, 699-709.

267. A. G. Bhavani, W. Y. Kim and J. S. Lee, *ACS Catal.*, 2013, **3**, 1537-1544.

268. P. Frontera, A. Macario, A. Aloise, P. L. Antonucci, G. Giordano and J. B. Nagy, *Catal. Today*, 2013, **218-219**, 18-29.

269. M. Rezaei, S. M. Alavi, S. Sahebdelfar, L. Xinmei, L. Qian and Z. F. Yan, *Energy and Fuels*, 2007, **21**, 581-589.

270. J. Niu, J. Ran, X. Du, W. Qi, P. Zhang and L. Yang, *Molecular Catalysis*, 2017, **434**, 206-218.

271. D. Ray, P. M. K. Reddy and C. Subrahmanyam, *Catal. Today*, 2017.

272. H. Peng, Y. Ma, W. Liu, X. Xu, X. Fang, J. Lian, X. Wang, C. Li, W. Zhou and P. Yuan, *Journal of Energy Chemistry*, 2015, **24**, 416-424.

273. R. Dębek, K. Zubek, M. Motak, P. Da Costa and T. Grzybek, *Research on Chemical Intermediates*, 2015, **41**, 9485-9495.

274. F. Meshkani, M. Rezaei and M. Andache, *Journal of Industrial and Engineering Chemistry*, 2014, **20**, 1251-1260.

275. F. Abild-Pedersen, O. Lytken, J. Engbæk, G. Nielsen, I. Chorkendorff and J. K. Nørskov, *Surf. Sci.*, 2005, **590**, 127-137.

276. C.-S. He, L. Gong, J. Zhang, P.-P. He and Y. Mu, *Journal of CO2 Utilization*, 2017, **19**, 157-164.

277. G. Peng, S. Sibener, G. C. Schatz and M. Mavrikakis, *Surf. Sci.*, 2012, **606**, 1050-1055.

278. B. Xing, X.-Y. Pang, G.-C. Wang and Z.-F. Shang, *Journal of Molecular Catalysis A: Chemical*, 2010, **315**, 187-196.

279. Y. Chen, X.-c. Yang, Y.-j. Liu, J.-x. Zhao, Q.-h. Cai and X.-z. Wang, *J. Mol. Graph. Model.*, 2013, **39**, 126-132.

280. Z. Wang, P. Li, Y. Chen, J. Liu, W. Zhang, Z. Guo, M. Dong and Y. Li, *J. Mater. Chem. C*, 2015, **3**, 6301-6306.

281. R. Lv, M. C. Dos Santos, C. Antonelli, S. Feng, K. Fujisawa, A. Berkdemir, R. Cruz-Silva, A. L. Elías, N. Perea-Lopez and F. López-Urías, *Adv. Mater.*, 2014, **26**, 7593-7599.

282. D. Abergel, V. Apalkov, J. Berashevich, K. Ziegler and T. Chakraborty, *Advances in Physics*, 2010, **59**, 261-482.

283. A. C. Neto, F. Guinea, N. M. Peres, K. S. Novoselov and A. K. Geim, *Rev. Mod. Phys.*, 2009, **81**, 109.

284. Y. Son, *Phys. Rev. Lett. https://doi. org/10.1103/PhysRevLett*, 2006, **97**, 216803.

285. X. Yan, X. Cui, B. Li and L.-s. Li, *Nano Lett.*, 2010, **10**, 1869-1873.

286. H. Zheng and W. Duley, *Phys. Rev. B*, 2008, **78**, 045421.

287. M. Frisch, G. Trucks, H. Schlegel, G. Scuseria, M. Robb, J. Cheeseman, G. Scalmani, V. Barone, G. Petersson and H. Nakatsuji, *There is no corresponding record for this reference*.

288. C. Gonzalez and H. B. Schlegel, *J. Chem. Phys.*, 1991, **95**, 5853-5860.

289. J. W. Ochterski, *Gaussian Inc*, 2000, 1-19.

290. M. Chase, C. Davies, J. Downey, D. Frurip, R. Mcdonald and A. Syverud, *J. Phys. Chem. Ref. Data Monograph*, 1998, **9**.

291. E. K. Pokon, M. D. Liptak, S. Feldgus and G. C. Shields, *J. Phys. Chem. A.*, 2001, **105**, 10483-10487.

292. J. A. Montgomery Jr, M. J. Frisch, J. W. Ochterski and G. A. Petersson, *J. Chem. Phys.*, 1999, **110**, 2822-2827.

293. M. F. Fellah and I. Onal, *J. Phys. Chem. C.*, 2010, **114**, 3042-3051.

294. E. V. Starokon, M. V. Parfenov, L. V. Pirutko, S. I. Abornev and G. I. Panov, *J. Phys. Chem. C.*, 2011, **115**, 2155-2161.

295. K. Yoshizawa, *Acc. Chem. Res.*, 2006, **39**, 375-382.

296. S. Grundner, M. A. Markovits, G. Li, M. Tromp, E. A. Pidko, E. J. Hensen, A. Jentys, M. Sanchez-Sanchez and J. A. Lercher, *Nat. Commun.*, 2015, **6**, 7546.

297. D. R. Cooper, B. D'Anjou, N. Ghattamaneni, B. Harack, M. Hilke, A. Horth, N. Majlis, M. Massicotte, L. Vandsburger and E. Whiteway, *ISRN Condensed Matter Physics*, 2012, **2012**.

298. H. Shin, S. Kang, J. Koo, H. Lee, J. Kim and Y. Kwon, *J. Chem. Phys.*, 2014, **140**, 114702.

299. R. Zacharia, H. Ulbricht and T. Hertel, *Phys. Rev. B*, 2004, **69**, 155406.

300. S. Lebègue, J. Harl, T. Gould, J. Ángyán, G. Kresse and J. Dobson, *Phys. Rev. Lett.*, 2010, **105**, 196401.

301. X. Liu, Y. Sui, T. Duan, C. Meng and Y. Han, *Phys. Chem. Chem. Phys.*, 2014, **16**, 23584-23593.

302. Y. Chen, B. Gao, J.-X. Zhao, Q.-H. Cai and H.-G. Fu, *J. Mol. Model.*, 2012, **18**, 2043-2054.

303. M. D. Esrafili, F. Sharifi and L. Dinparast, *J. Mol. Graph. Model.*, 2017, **77**, 143-152.

304. Y. Tang, X. Dai, Z. Yang, Z. Liu, L. Pan, D. Ma and Z. Lu, *Carbon*, 2014, **71**, 139-149.

305. M. Rafique, Y. Shuai and N. Hussain, *Physica E.*, 2017.

306. A. Zandiatashbar, G.-H. Lee, S. J. An, S. Lee, N. Mathew, M. Terrones, T. Hayashi, C. R. Picu, J. Hone and N. Koratkar, *Nat. Commun.*, 2014, **5**, 3186.

307. W. Ju, A. Bagger, G.-P. Hao, A. S. Varela, I. Sinev, V. Bon, B. R. Cuenya, S. Kaskel, J. Rossmeisl and P. Strasser, *Nat. Commun.*, 2017, **8**, 944.

308. B. Guo, Q. Liu, E. Chen, H. Zhu, L. Fang and J. R. Gong, *Nano Lett.*, 2010, **10**, 4975-4980.
309. W. Liang, J. Chen, Y. Liu and S. Chen, *ACS Catal.*, 2014, **4**, 4170-4177.
310. S. Kattel and G. Wang, *J. Mater. Chem. A*, 2013, **1**.
311. Y. Zou, F. Li, Z. Zhu, M. Zhao, X. Xu and X. Su, *Euro. Phys. J. B*, 2011, **81**, 475-479.
312. E. Cruz-Silva, F. Lopez-Urias, E. Munoz-Sandoval, B. G. Sumpter, H. Terrones, J.-C. Charlier, V. Meunier and M. Terrones, *ACS Nano*, 2009, **3**, 1913-1921.
313. P. Nematollahi and E. C. Neyts, *Appl. Surf. Sci.*, 2018, **439**, 934-945.
314. S. Lin, J. Huang and X. Gao, *Phys. Chem. Chem. Phys.*, 2015, **17**, 22097-22105.
315. Y. Tang, Z. Shen, Y. Ma, W. Chen, D. Ma, M. Zhao and X. Dai, *Materials Chemistry and Physics*, 2018, **207**, 11-22.
316. P. Zhang, X. Chen, J. Lian and Q. Jiang, *J. Phys. Chem. C.*, 2012, **116**, 17572-17579.
317. S. Kattel, P. Atanassov and B. Kiefer, *Phys. Chem. Chem. Phys.*, 2013, **15**, 148-153.
318. U. I. Koslowski, I. Abs-Wurmbach, S. Fiechter and P. Bogdanoff, *J. Phys. Chem. C.*, 2008, **112**, 15356-15366.
319. U. I. Kramm, J. Herranz, N. Larouche, T. M. Arruda, M. Lefèvre, F. Jaouen, P. Bogdanoff, S. Fiechter, I. Abs-Wurmbach and S. Mukerjee, *Phys. Chem. Chem. Phys.*, 2012, **14**, 11673-11688.
320. L. Zhu, W. Zhang, J. Zhu and D. Cheng, *Carbon*, 2017, **116**, 201-209.
321. S. Impeng, P. Khongpracha, C. Warakulwit, B. Jansang, J. Sirijaraensre, M. Ehara and J. Limtrakul, *RSC Adv.*, 2014, **4**, 12572-12578.
322. G. Altinay, M. Citir and R. B. Metz, *J. Phys. Chem. A.*, 2010, **114**, 5104-5112.
323. M. F. Fellah and I. Onal, *J. Phys. Chem. C.*, 2012, **116**, 13616-13622.
324. J. S. Woertink, P. J. Smeets, M. H. Groothaert, M. A. Vance, B. F. Sels, R. A. Schoonheydt and E. I. Solomon, *Proceedings of the National Academy of Sciences*, 2009, **106**, 18908-18913.
325. W. Liang, A. T. Bell, M. Head-Gordon and A. K. Chakraborty, *J. Phys. Chem. B.*, 2004, **108**, 4362-4368.
326. P. Pantu, S. Pabchanda and J. Limtrakul, *ChemPhysChem*, 2004, **5**, 1901-1906.
327. K. Yoshizawa, Y. Shiota, T. Yumura and T. Yamabe, *J. Phys. Chem. B.*, 2000, **104**, 734-740.
328. S. Impeng, P. Khongpracha, J. Sirijaraensre, B. Jansang, M. Ehara and J. Limtrakul, *RSC Adv.*, 2015, **5**, 97918-97927.
329. A. D. Mayernick and M. J. Janik, *J. Phys. Chem. C.*, 2008, **112**, 14955-14964.
330. A. D. Mayernick and M. J. Janik, *J. Catal.*, 2011, **278**, 16-25.
331. Z. Lu, G. Xu, C. He, T. Wang, L. Yang, Z. Yang and D. Ma, *Carbon*, 2015, **84**, 500-508.
332. M. Yano, Y. K. Yap, M. Okamoto, M. Onda, M. Yoshimura, Y. Mori and T. Sasaki, *Jpn. J. Appl. Phys.*, 2000, **39**, L300.
333. Y. Wang, J. Zhang, G. Huang, X. Yao and Q. Shao, *J. Mol. Model.*, 2014, **20**, 2536.
334. S. Lin, X. Ye and J. Huang, *Phys. Chem. Chem. Phys.*, 2015, **17**, 888-895.
335. K. Bleakley and P. Hu, *J. Am. Chem. Soc.*, 1999, **121**, 7644-7652.
336. E. Kuipers, A. Vardi, A. Danon and A. Amirav, *Phys. Rev. Lett.*, 1991, **66**, 116.
337. Y.-H. Lu, M. Zhou, C. Zhang and Y.-P. Feng, *J. Phys. Chem. C.*, 2009, **113**, 20156-20160.
338. J.-x. Zhao, Y. Chen and H.-g. Fu, *Theor. Chem. Acc.*, 2012, **131**, 1242.

339. Z. Liu, Q. Xue, T. Zhang, Y. Tao, C. Ling and M. Shan, *J. Phys. Chem. C.*, 2013, **117**, 9332-9339.

340. J.-w. Feng, Y.-J. Liu and J.-x. Zhao, *J. Mol. Model.*, 2014, **20**, 1-7.

341. P. Nematollahi and M. D. Esrafili, *New J. Chem.*, 2016, **40**, 2775-2784.

342. S. Pornsatitworakul, S. Phikulthai, S. Namuangruk and B. Boekfa, 2015.

343. B. Wang and S. Pantelides, *Phys. Rev. B*, 2011, **83**, 245403.

344. Y. Li, Z. Zhou and J. Zhao, *Nanotechnology*, 2008, **19**, 015202.

345. B. Xiao, X.-f. Yu and Y.-h. Ding, *RSC Adv.*, 2014, **4**, 22688-22696.

346. A. Zobelli, A. Gloter, C. Ewels and C. Colliex, *Phys. Rev. B*, 2008, **77**, 045410.

347. J. D. Blakemore, R. H. Crabtree and G. W. Brudvig, *Chem. Rev.*, 2015, **115**, 12974-13005.

348. H. Kim, J. Park, I. Park, K. Jin, S. E. Jerng, S. H. Kim, K. T. Nam and K. Kang, *Nat. Commun.*, 2015, **6**, 8253.

349. H. Fei, J. Dong, M. J. Arellano-Jiménez, G. Ye, N. D. Kim, E. L. Samuel, Z. Peng, Z. Zhu, F. Qin and J. Bao, *Nat. Commun.*, 2015, **6**, 8668.

350. H. Fei, Y. Yang, Z. Peng, G. Ruan, Q. Zhong, L. Li, E. L. Samuel and J. M. Tour, *ACS Appl. Mater. Interfaces*, 2015, **7**, 8083-8087.

351. Z. Wang, S. Xiao, Z. Zhu, X. Long, X. Zheng, X. Lu and S. Yang, *ACS Appl. Mater. Interfaces*, 2015, **7**, 4048-4055.

352. X. Zou, X. Huang, A. Goswami, R. Silva, B. R. Sathe, E. Mikmeková and T. Asefa, *Angew. Chem.*, 2014, **53**, 4372-4376.

353. S. Kattel and G. Wang, *J. Mater. Chem. A*, 2013, **1**, 10790-10797.

354. Y. Zheng, Y. Jiao, J. Chen, J. Liu, J. Liang, A. Du, W. Zhang, Z. Zhu, S. C. Smith and M. Jaroniec, *J. Am. Chem. Soc.*, 2011, **133**, 20116-20119.

355. V. D. Dasireddy, D. Hanzel, K. Bharuth-Ram and B. Likozar, *RSC Adv.*, 2019, **9**, 30989-31003.

356. T. Lu and F. Chen, *J. Comput. Chem.*, 2012, **33**, 580-592.

357. A. A. Latimer, H. Aljama, A. Kakekhani, J. S. Yoo, A. Kulkarni, C. Tsai, M. Garcia-Melchor, F. Abild-Pedersen and J. K. Nørskov, *Phys. Chem. Chem. Phys.*, 2017, **19**, 3575-3581.

358. X. Zhang, Z. Yang, Z. Lu and W. Wang, *Carbon*, 2018.

359. F. Gao, G.-L. Zhao, Z. Wang, D. Bagayoko and D.-J. Liu, *Catal. Commun.*, 2015, **62**, 79-82.

360. N. K. Jaiswal and P. Srivastava, *Solid State Commun.*, 2012, **152**, 1489-1492.

361. E. J. Santos, D. Sánchez-Portal and A. Ayuela, *Phys. Rev. B*, 2010, **81**, 125433.

362. L. Tsetseris, B. Wang and S. Pantelides, *Phys. Rev. B*, 2014, **89**, 035411.

363. M. Wang and Z. Wang, *RSC Adv.*, 2017, **7**, 48819-48824.

364. M. D. Esrafili and S. Asadollahi, *Appl. Surf. Sci.*, 2019, **463**, 526-534.

365. X. Zhang, Z. Lu and Z. Yang, *Journal of Molecular Catalysis A: Chemical*, 2016, **417**, 28-35.

366. F. Li, H. Shu, C. Hu, Z. Shi, X. Liu, P. Liang and X. Chen, *ACS Appl. Mater. Interfaces*, 2015, **7**, 27405-27413.

367. W. Wong, W. R. W. Daud, A. B. Mohamad, A. A. H. Kadhum, K. S. Loh and E. Majlan, *Int. J. Hydrogen Energ.*, 2013, **38**, 9370-9386.

368. K. Niu, B. Yang, J. Cui, J. Jin, X. Fu, Q. Zhao and J. Zhang, *J. Power Sources*, 2013, **243**, 65-71.

369. V. B. Parambhath, R. Nagar and S. Ramaprabhu, *Langmuir*, 2012, **28**, 7826-7833.

370. J. Zhang, Z. Wang and Z. Zhu, *J. Power Sources*, 2014, **255**, 65-69.

371. S. Kattel and G. Wang, *J. Phys. Chem. Lett.*, 2014, **5**, 452-456.

372. L. Panchakarla, K. Subrahmanyam, S. Saha, A. Govindaraj, H. Krishnamurthy, U. Waghmare and C. Rao, *Adv. Mater.*, 2009, **21**, 4726-4730.

373. P. Nematollahi and M. D. Esrafili, *RSC Adv.*, 2016, **6**, 59091-59099.

374. J. Yuan, W. Zhang, X. Li and J. Yang, *ChemComm*, 2018, **54**, 2284-2287.

375. A. Junkaew, S. Namuangruk, P. Maitarad and M. Ehara, *RSC Adv.*, 2018, **8**, 22322-22330.

376. J. C. Da Silva, R. C. Pennifold, J. N. Harvey and W. R. Rocha, *Dalton Transactions*, 2016, **45**, 2492-2504.

377. A. A. Latimer, A. R. Kulkarni, H. Aljama, J. H. Montoya, J. S. Yoo, C. Tsai, F. Abild-Pedersen, F. Studt and J. K. Nørskov, *Nat. Mater.*, 2017, **16**, 225.

378. C. Hammond, M. M. Forde, M. H. Ab Rahim, A. Thetford, Q. He, R. L. Jenkins, N. Dimitratos, J. A. Lopez-Sanchez, N. F. Dummer and D. M. Murphy, *Angew. Chem.*, 2012, **51**, 5129-5133.

379. A. A. Latimer, A. Kakekhani, A. R. Kulkarni and J. K. Nørskov, *ACS Catal.*, 2018, **8**, 6894-6907.

380. Y. Tang, Z. Liu, W. Chen, Z. Shen, D. Ma and X. Dai, *Int. J. Hydrogen Energ.*, 2016, **41**, 13197-13207.

381. T. Pham, E. Leggesse and J. Jiang, *Catal. Sci. Technol*, 2015, **5**, 4064-4071.